Advancing Microwave Imaging Algorithms and Techniques

by

Nozhan Bayat

A Thesis submitted to the Faculty of Graduate Studies of
The University of Manitoba
in partial fulfilment of the requirements of the degree of

DOCTOR OF PHILOSOPHY

Department of Electrical and Computer Engineering
University of Manitoba
Winnipeg, Manitoba, Canada

Abstract

This dissertation studies and develops novel techniques and algorithms in the area of microwave imaging (MWI). In MWI, the objective is to create a (quantitative) image of the dielectric profile of the object of interest (OI) in a non-destructive fashion. To this end, the OI is interrogated using non-ionizing and relatively low-power microwaves which are generated by some antennas. These incident microwaves will then interact with the OI, and consequently scattered electromagnetic fields will arise which contain information about the OI. These scattered fields will be collected, and then processed to extract their information so as to create the final image. This process is often referred to as the *inversion* of the scattered field data to *reconstruct* the OI's dielectric profile.

Currently, MWI faces some challenges that limit its capability to become a widely-accepted imaging tool. Three of these challenges are: (i) lack of fundamental understanding about the relation between the measured scattered fields and the achievable image accuracy and resolution, (ii) insufficient image accuracy and resolution for some applications, and (iii) difficulty to collect sufficient measured data due to various practical limitations. The main focus of this dissertation is to investigate and develop techniques and algorithms in an attempt to address these three challenges.

This dissertation begins by introducing the concept of 'best' possible reconstruction from given MWI configurations. This concept is important since if the best possible reconstruction fails to provide the features of interest, the actual blind reconstruction will not be able to provide these features either. To improve the achievable reconstruction, one option is to inject prior information into the algorithm. To this end, a fully automated inversion algorithm is presented that is able to incorporate prior spatial (structural) information about the OI. The proposed algorithm, which is capable of working with both complete and partially-available prior spatial information, is evaluated against synthetic and experimental data sets.

A central part of MWI data collection, i.e., transmit and receive patterns of the antennas, is then considered. To this end, the use of focused near-field (NF) beams for illumination of

the OI is first addressed. Using a NF plate and a Bessel beam launcher simulated in ANSYS HFSS, it will be shown that focused NF beams can suppress the effects of undesired regions under the Born approximation. Moreover, based on the relation between the electromagnetic inverse scattering and inverse source problems, it will be discussed how this focused approach can reduce the number of required measured data points. Then, the simultaneous use of focused transmit and receive patterns is considered to further suppress the sensitivity of the measured data with respect to undesired regions. In particular, using two NF plates (one for focused transmitting and the other for focused receiving), a single measured data point will be made mainly sensitive to a subwavelength cell within the imaging domain under some constraints and assumptions, namely, one-dimensional objects, limited working distance, and a localized approximation. This is different than typical MWI where one measured data point is sensitive to all the subwavelength cells within the imaging domain.

Finally, it should be noted that this dissertation is structured based on the grouped manuscript style (i.e., sandwich thesis). Therefore, Chapters 2 to 5 are either the peer-reviewed or under-review journal papers of the candidate. Due to this, some general concepts are repeated throughout this dissertation.

Acronyms and Symbols

Herein, two tables are presented. The first table lists some of the important acronyms used in this thesis, and the second lists some of the important symbols.

Acronym	Description
MWT	Microwave tomography.
MWI	Microwave imaging.
OI	Object of interest.
ROI	Region of interest.
TM	Transverse magnetic.
MR-GNI	Multiplicative regularized Gauss-Newton inversion.
MR-CSI	Multiplicative regularized contrast source inversion.
Tikh-GNI	Gauss-Newton inversion using Tikhonov regularization.
SP-GNI	Gauss-Newton inversion using spatial priors regularization.
SVD	Singular value decomposition.
1D	One-dimensional.
2D	Two-dimensional.
3D	Three-dimensional.
MRI	Magnetic resonance imaging.
SNR	Signal-to-noise ratio.
CNFR	Cylindrical near-field range.
SNFR	Spherical near-field range.

Symbol	Description
$\hat{x}$, $\hat{y}$, $\hat{z}$	Unit vectors along x, y and z directions.
j	Imaginary unit ($j^2 = -1$).
$\mathcal{D}$	Imaging domain.
$\mathcal{S}$	Measurement domain.
$\boldsymbol{p}$	Position vector in the measurement domain $\mathcal{S}$.
$\boldsymbol{q}$	Position vector in the imaging domain $\mathcal{D}$.
$\boldsymbol{r}$	Position vector in the measurement domain $\mathcal{S}$.
$\boldsymbol{r}'$	Position vector in the imaging domain $\mathcal{D}$.
$g(.,.)$	Green's function of the background medium.
k_b	Wavenumber of the background medium.
λ	Wavelength of the operation in the background medium.
E^{inc}	Incident electric field (electric field in the absence of the object of interest).
E	Total electric field (electric field in the presence of the object of interest).
E^{scat}	Scattered electric field ($E^{\text{scat}} \triangleq E - E^{\text{inc}}$).
E^{meas}	Measured scattered electric field on the measurement domain $\mathcal{S}$.
$(.)^H$	Hermitian operator (complex conjugate transpose).
$\|\|x\|\|$	L_2 norm of the vector x, defined as $\|\|x\|\| \triangleq \sqrt{x^H x}$.
$\odot$	Hadamard product (element-wise multiplication).
$(.)^{-1}$	Inverse operator.
Re	Real-part operator.
Im	Imaginary-part operator.
$\chi(\boldsymbol{q})$	dielectric contrast of the object of interest at location $\boldsymbol{q}$.
$\epsilon_r(\boldsymbol{q})$	Relative complex permittivity of the object of interest at location $\boldsymbol{q}$.
ϵ_b	Relative complex permittivity of the background medium.
S_{11}	Voltage reflection coefficient at the input port (of the antenna).

Acknowledgments

First, I would like to thank my academic advisor, Prof. Puyan Mojabi, for all of his support, encouragement, and time during my PhD studies.

I would also like to express my appreciation to my PhD examining committee, Prof. Gregory Bridges and Prof. Shaun Lui from the University of Manitoba as well as my external examiner, Prof. Natalia K. Nikolova from McMaster University for their time and efforts in the evaluation and improvement of this work.

I would also like extend my gratitude to Natural Sciences and Engineering Research Council of Canada, the University of Manitoba Graduate Fellowship, and the University of Manitoba GETS Program for their financial support as well as the Canadian Microelectronics Corporation (CMC) for the provision of ANSYS Campus Solution.

Last but not least, my biggest thank-you goes to my parents: Masoud and Nahid.

To my parents

Contents

1

Introduction

This chapter begins with providing an overview of microwave imaging (MWI). Then, some of the associated challenges to improve the achievable accuracy and resolution of this imaging modality will be described. An overview of some proposed solutions to overcome these challenges, which are the novelties of this thesis, will then follow. At the end of this chapter, the outline of this thesis will be presented.

1.1 Microwave Imaging

Microwave imaging (MWI) is an imaging method aiming at the characterization of the dielectric profile[1] of an object of interest (OI). Characterizing the dielectric profile means finding the quantitative values of the OI's dielectric properties at different locations. This is done by illuminating the OI by incident electromagnetic fields at the microwave frequency

[1] The utilized term "profile" is to indicate that the dielectric properties can have spatial variations.

range[2], collecting the resulting *scattered* electromagnetic fields outside the OI, and then processing (inverting) these *scattered* fields to yield an image of the OI's dielectric profile. For example, let us consider one of the experimental data sets collected by the Institut Fresnel in France: the so-called *FoamTwinDielTM* target [1]. Figure 1.1 depicts the experimental setup used to interrogate this target[3]. The cross section of this target, shown in Figure 1.2(a), consists of three circular dielectric cylinders[4].

Now, let us consider how the measured scattered fields from this target are inverted to yield an image of its dielectric profile. The inversion process is iterative, and the inversion algorithm tries to iteratively minimize the discrepancy between the simulated scattered fields due to a predicted dielectric profile and the measured scattered fields. Each of these predictions (reconstructions) forms an image until the inversion algorithm converges to the final image. For example, in Figures 1.2(b)-(h), we have shown seven images of this target where the last one corresponds to the image obtained when the inversion algorithm converges[5]. As can be seen in Figure 1.2(b), at the first iteration, the inversion algorithm does not detect the presence of the target within the imaging domain. However, as the inversion algorithm moves to next iterations (see Figures 1.2(c)-(h)), the presence of the target becomes more and more visible. At the last iteration of this example, i.e., at the 12^{th} iteration shown in Figure 1.2(h), the reconstruction result shows a good agreement with the actual dielectric properties of the OI.

[2] The microwave frequency range is from 300 MHz to 300 GHz which corresponds to 1 m to 1 mm operational (free space) wavelength, respectively. It is worth mentioning that the microwave frequency range that is suitable for microwave biomedical applications such as breast imaging is typically from 600 MHz to 8 GHz which is a trade-off between the achievable penetration depth and spatial resolution.

[3] This target was interrogated from 18 different angles, and then the resulting scattered fields were collected at 241 data points per transmitter at 9 different frequencies ranging from 2 GHz to 10 GHz with the increment of 1 GHz. The schematic that demonstrates the required movements for collecting these experimental data is shown in Figure 1.1(b).

[4] Two of these cylinders have a diameter of 31 mm, and a relative permittivity of $\epsilon_r = 3 \pm 0.3$. The other cylinder has a diameter of 80 mm and a relative permittivity of $\epsilon_r = 1.45 \pm 0.15$.

[5] Herein, we have utilized the multiplicative regularized Gauss-Newton inversion (MR-GNI) algorithm to invert the $5 - 10$ GHz data sets (six frequencies) simultaneously [2, 3]. For all of the reconstruction results shown here the imaging domain has the size of 15×15 cm^2 discretized into 61×61 cells.

Also, it is worth emphasizing that these images are accompanied by colorbars which demonstrate the quantitative values of dielectric properties. Therefore, MWI is a quantitative imaging modality. For example, if we look at Figure 1.2(h), we see three main colors in the image, which can be compared against the colorbar to understand the associated relative permittivity (dielectric constant) values. As can be seen, the dark blue color corresponds to a relative permittivity of one which is for the air. The blue color corresponds to a relative permittivity of about 1.5 which is for the larger cylinder, and finally the red color corresponds to a relative permittivity of 3.3 which is for the smaller cylinders. As can be seen, the inversion algorithm has reconstructed shape, location, and the dielectric properties (relative permittivity values) at each location. The initial guess for this algorithm is trivial; i.e., in the beginning of this algorithm, it is assumed that the medium everywhere is air. Finally, we note that in this example, a cross-section of the OI has been reconstructed. For this reason, we may also refer to this as microwave tomography (MWT). Note that the word tomography is derived from Ancient Greek and consists of two parts: '$\tau\acute{o}\mu o\varsigma$' tomos meaning "slice, section" and '$\gamma\rho\acute{\alpha}\varphi\omega$' graphó meaning "to write" [4].

Now we take a closer look at the data collection procedure to define some important terms. To this end, let us begin by noting that due to the fact that the non-ionizing data collection is performed *outside* the OI, this imaging technique is considered as a non-destructive imaging tool. Obtaining the scattered data involves the following two steps. In the first step shown in Figure 1.3(a), the OI which resides in the imaging domain[6] is successively illuminated by some known electromagnetic fields (e.g., electromagnetic fields generated from some antenna elements) and the resulting field data are then captured by some receivers located *outside* the OI. These field data are referred to as the *total* field data. In the second step shown in Figure 1.3(b), the same procedure is performed but in the absence of the OI. These

[6] The imaging domain is the geometrical domain that contains the OI. Note that the measured data are collected outside the imaging domain.

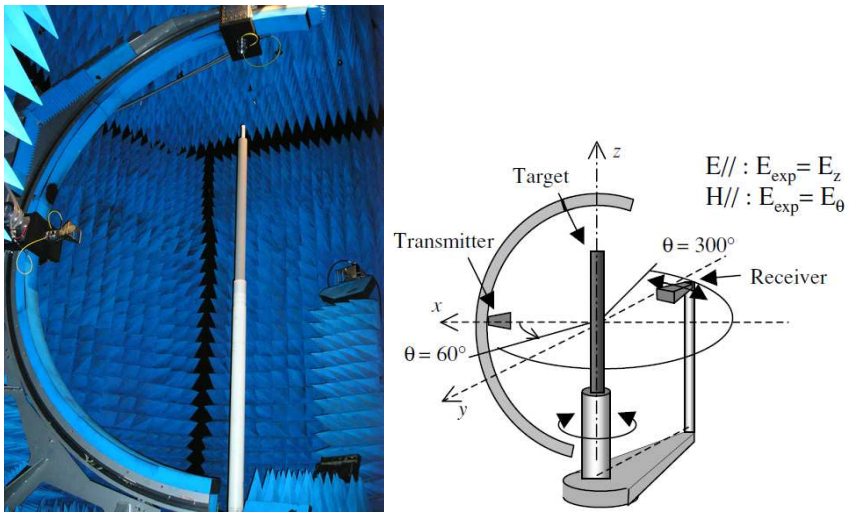

(a) Experimental setup (b) Schematic of the experimental setup

Fig. 1.1: (a) Free space scattering measurement facility of Institut Fresnel and (b) demonstration of the experiment performed by Institut Fresnel. These figures have been taken from [1] ©[2005] Inverse Problems.

field data are referred to as the *incident* field data. Having these two field data sets (i.e., the *total* and *incident* field data), the scattered field data which represent the signature of the OI are obtained by the subtraction of the total field data from the incident field data. That is $\boldsymbol{E}^{\text{scat}} \triangleq \boldsymbol{E} - \boldsymbol{E}^{\text{inc}}$ where $\boldsymbol{E}^{\text{scat}}$, $\boldsymbol{E}$, and $\boldsymbol{E}^{\text{inc}}$ denote the scattered, total, and incident fields respectively. These scattered field data contain information about the dielectric properties of the OI that will later be processed (inverted) to reconstruct the OI's dielectric profile which is the ultimate goal of this imaging technique. This data processing often involves calibrating the collected scattered field data properly and then applying an appropriate inversion algorithms to these data. The inversion algorithm then retrieves the information about the OI that are encoded in the scattered data and finally reconstructs the OI's dielectric profile.

MWI can be formulated as an electromagnetic inverse problem that needs to be solved in order to retrieve[7] the OI's dielectric properties. The use of the term "inverse" lies in the fact

[7] Within the context of this thesis, the terms "retrieve" and "reconstruct" are used interchangeably, and mean finding the internal dielectric properties of the OI from external microwave measurements.

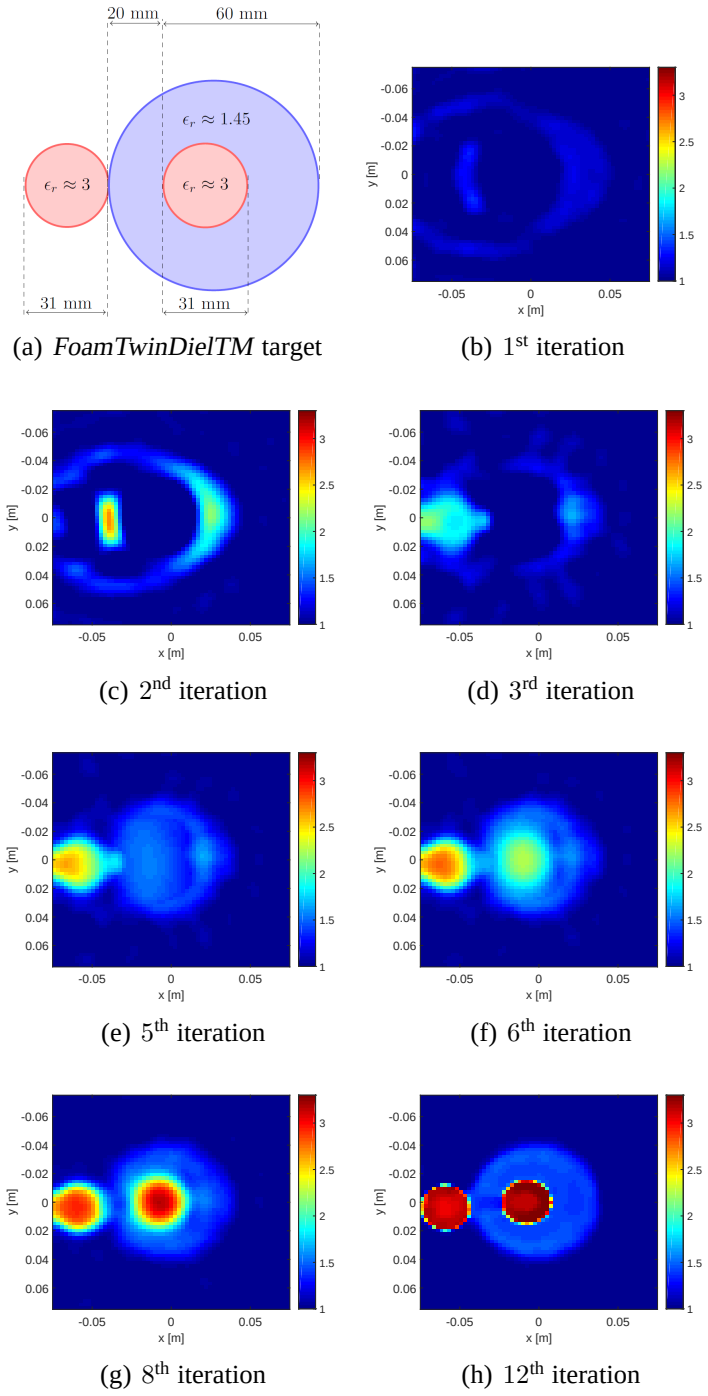

(a) *FoamTwinDielTM* target (b) 1st iteration

(c) 2nd iteration (d) 3rd iteration

(e) 5th iteration (f) 6th iteration

(g) 8th iteration (h) 12th iteration

Fig. 1.2: (a) Cross-section of *FoamTwinDielTM* target from which Institut Fresnel collected an experimental data set. (ϵ_r denotes the relative permittivity (dielectric constant) of the object.) (b)-(h) The inversion of this data set ($5 - 10$ GHz) at different iterations of an inversion algorithm with the last iteration being the 12^{th} iteration.

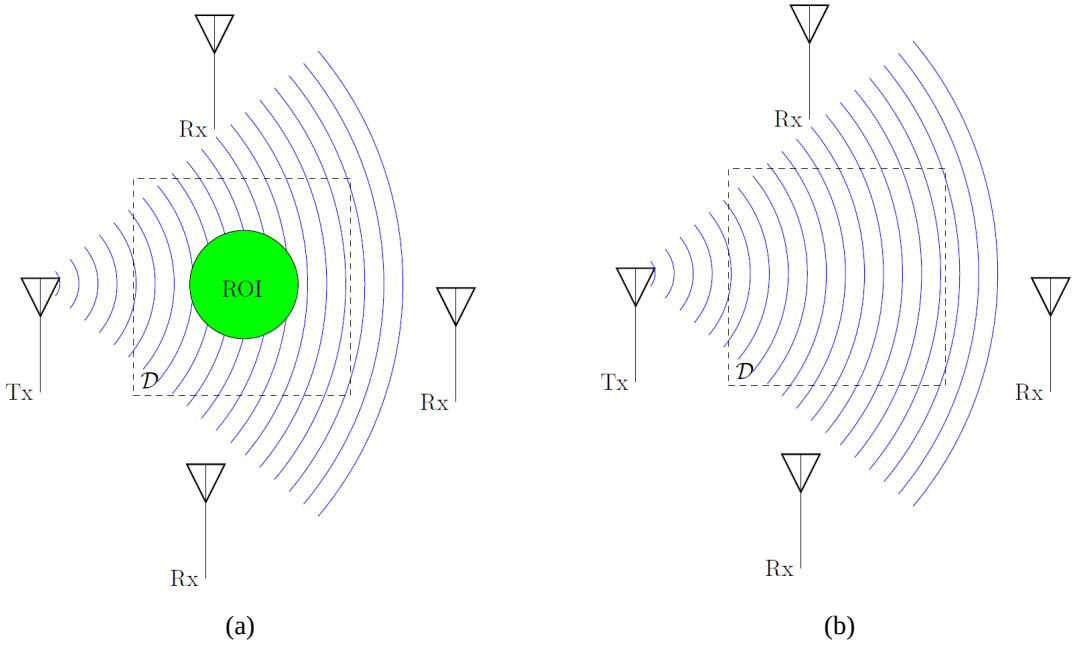

Fig. 1.3: MWI setup for the measurement of (a) the total field E and (b) the incident field E^{inc}. The subtraction of these two measurements is the scattered field E^{scat}. (Tx denotes the transmitter, Rx denotes the receiver, and ROI denotes the region of interest to be imaged.)

that the goal of this problem is to infer the internal properties of the OI from exterior data. Noting that the OI is the *cause* for having a certain scattered field, we can also interpret this inverse problem as retrieving the *cause* from its *effects* [5]. This point of view can be better understood by observing the so-called *data equation* which governs the information flow from the imaging domain (denoted by $\mathcal{D}$) to the external measurement domain (denoted by $\mathcal{S}$) on which the data collection is performed for the two-dimensional (2D) scalar inverse problem [6, Section II][8]

$$\overbrace{E^{\text{scat}}(\boldsymbol{r} \in \mathcal{S})}^{\text{measured data}} = k_b^2 \int_{\mathcal{D}} \overbrace{g(\boldsymbol{r} \in \mathcal{S}, \boldsymbol{r}\,' \in \mathcal{D}) E(\boldsymbol{r}\,' \in \mathcal{D})}^{\text{transfer function}} \frac{\overbrace{\epsilon(\boldsymbol{r}\,')}^{\text{unknown}} - \epsilon_b}{\epsilon_b} d\boldsymbol{r}\,'. \tag{1.1}$$

[8] In 2D scalar MWI, also known as 2D TM MWI, the illumination of the OI is performed by the electric field component that is perpendicular to the imaging domain (imaging plane) which encapsulates the OI. (E.g., the z component of the electric field will be utilized for the interrogation of the OI if the imaging domain resides in the xy plane.) This is perhaps the most popular form of MWI in the literature.

Note that the above equation needs to be repeated for each transmitter as the induced field in the OI will change depending on the transmitting antenna. Before starting to discuss this integral equation, let us note that this equation links two different geometrical domains: (*i*) the imaging domain $\mathcal{D}$, and (*ii*) the measurement domain $\mathcal{S}$. In the above integral equation, $E^{\text{scat}}(\boldsymbol{r})$ represents the collected scattered field at the receiver location $\boldsymbol{r}$ which belongs to $\mathcal{S}$. The $g(\boldsymbol{r}, \boldsymbol{r}\,')$ is Green's function[9] of the known background medium[10]. This known homogeneous background medium has a relative complex permittivity[11] of ϵ_b. In (1.1), $E(\boldsymbol{r}\,')$ represents the total field within the imaging domain which is defined as the field distribution within the imaging domain in the presence of the OI. Also, k_b is the wavenumber of the background medium[12]. Finally, $\epsilon(\boldsymbol{r}\,')$ denotes the OI's relative complex permittivity that we are looking for in this inverse problem, i.e., the actual unknown of the problem. It should be reminded that the OI's relative complex permittivity $\epsilon(\boldsymbol{r}\,')$ can be a function of $\boldsymbol{r}\,'$ which is the position vector spanning the imaging domain $\mathcal{D}$. Consequently, the relative complex permittivity of the OI can vary with respect to the spatial variation. Thus, we use the term relative complex permittivity "profile" to indicate that ϵ can change as a function of position. Also, note that in the data equation, the term $\frac{\epsilon(\boldsymbol{r}\,')-\epsilon_b}{\epsilon_b}$ is often defined as the contrast of the OI's dielectric profile (denotes by χ), i.e., $\chi(\boldsymbol{r}\,') \triangleq \frac{\epsilon(\boldsymbol{r}\,')-\epsilon_b}{\epsilon_b}$. Herein, we refer to χ as the relative complex permittivity contrast profile, or dielectric contrast profile, or simply the contrast.

It should also be emphasized that the data equation, in fact, represents multiple equations.

[9] The Green's function represents the response of the imaging system in the absence of the OI due to a Driac delta excitation.

[10] The background medium is a medium in which the OI has been immersed. This medium can be air or any matching fluid that suits the MWI application. (E.g., water or oil can be a matching fluid for biomedical applications.)

[11] The relative complex permittivity is defined as $\epsilon = \epsilon_r' - j\frac{\sigma}{\omega\epsilon_0}$ where ϵ_r' and σ represent the relative permittivity and the conductivity of this complex value at the angular frequency of ω respectively. Also $j^2 = -1$.

[12] The wavenumber of the background medium is $k_b = \omega\sqrt{\mu_0\epsilon_0\epsilon_b}$ where μ_0 and ϵ_0 are the permeability and permittivity of vacuum, and ϵ_b is the relative permittivity of the background medium in which the OI resides. (Note that the background medium is assumed to be nonmagnetic in this thesis, i.e., $\mu_r = 1$.)

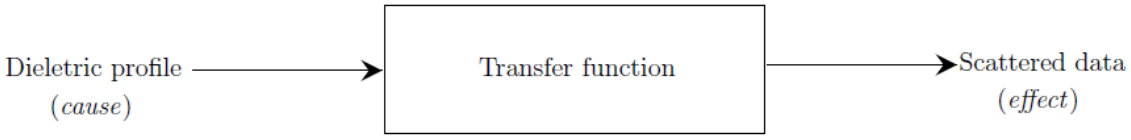

Fig. 1.4: Demonstration of the data equation (1.1) in the form of a transfer function. Note that the transfer function itself is dependent on the input.

For example, if we change the angle of illumination, the internal total field in the OI, i.e., $E(\boldsymbol{r}\,')$, will change. Similarly, if we change the receiving position, the vector $\boldsymbol{r}$ will change, and thus Green's function $g(\boldsymbol{r}, \boldsymbol{r}\,')$ will change. Finally, the change of the frequency will also affect this equation.

The data equation may be interpreted as an equation that a transfer function operates on the unknown quantity and yields the measured data. However, it should be noted that $E(\boldsymbol{r}\,')$, which is a component of this transfer function, is itself a function of the unknown quantity through the so-called *domain equation*[13],

$$E(\boldsymbol{r} \in \mathcal{D}) = E^{\text{inc}}(\boldsymbol{r} \in \mathcal{D}) + k_b^2 \int_{\mathcal{D}} g(\boldsymbol{r} \in \mathcal{D}, \boldsymbol{r}\,' \in \mathcal{D})\, E(\boldsymbol{r}\,' \in \mathcal{D}) \chi(\boldsymbol{r}\,' \in \mathcal{D})\, d\boldsymbol{r}', \quad (1.2)$$

where both $\boldsymbol{r}$ and $\boldsymbol{r}\,'$ belong to the imaging domain $\mathcal{D}$. As can be understood from (1.2), $E(\boldsymbol{r})$ that partially governs the aforementioned transfer function in (1.1) is itself a function of the unknown quantity $\chi(\boldsymbol{r}\,')$. That is why, in practice, (1.1) is often solved in an iterative fashion by updating $E(\boldsymbol{r}\,')$ (thus, updating the transfer function) as well as $\chi(\boldsymbol{r}\,')$ at each iteration. Alternatively, one may also assume some simplified forms of $E(\boldsymbol{r}\,')$ such as

[13] This nonlinear relation between E and χ makes our problem a nonlinear inverse problem.

approximating it with $E^{\text{inc}}(\boldsymbol{r}\,')$[14], and then solve the resulting linearized inverse problem[15].

MWI has several potential applications such as industrial non-destructive testing, biomedical diagnosis, security screening, through wall imaging, as well as remote sensing of oil spills, soil moisture, and sea ice [5, 7–19]. Particularly, the capability of MWI to provide quantitative images of the OI can be useful for clinical applications, e.g., to evaluate the effectiveness of cancer treatment [20]. Moreover, due to the fact that in MWI we are using non-ionizing radiation, as opposed to x-ray computed tomography and also due to its cheaper operational costs compared to magnetic resonance imaging (MRI), this imaging tool can be beneficial for frequent large-scale monitoring applications. On the other hand, MWI can also be utilized in conjunction with other imaging modalities, e.g., with ultrasound tomography or magnetic resonance imaging for the detection and diagnosis purposes [21–23]. However, all of these benefits come with challenges, some of which will be discussed in the next section.

1.2 Novelties and Contributions

The above section briefly introduced MWI and its applications. We now describe three of the main challenges facing this imaging modality. Each of these challenges will be stated in the form of a question. After each question, an approach will be presented which can be thought as a possible solution to overcome the stated challenges. These solutions are basically the novelties and research contributions of this thesis. (The list of the candidate's publications that is directly related to this thesis can be found in Appendix A.)

[14] This approximation is known as the Born approximation.
[15] The reconstruction result presented in Figure 1.2(b) was obtained under the Born approximation.

1.2.1 Challenge I

One of the main challenges in the design of an MWI system is to know what the best possible reconstruction that one can hope to achieve from the given MWI system for a typical OI[16] is. This is important since if the best possible reconstruction fails to provide the features of interest (e.g., a required spatial resolution level), then the designer will know that the system needs to be re-designed so that the best possible reconstruction associated with the new system can provide the details of interest. To understand the importance of this best possible reconstruction, let us assume that an inversion from an MWI system fails to provide the details of interest. At this point, we do not know if the problem is with the incapability of the inversion algorithm to retrieve all the information contents from the measured data[17], or the problem lies in the fact that we did not have enough measured data in the first place[18]. In summary, to enhance the achievable resolution and accuracy from MWI, we need to first develop good understanding about the relation between a set of measured scattered field data and the best possible reconstruction.

In this thesis, we have introduced the concept of "best" possible reconstruction. The process through which the best possible reconstruction of an MWI system can be obtained has been depicted in Figure 1.5. This process needs a numerical calibration object that resemble the features of the OI. This numerical calibration object is placed in the imaging domain in the electromagnetic simulation software and will be interrogated by the utilized antennas in MWI. This step is shown by the forward electromagnetic (EM) solver in Figure 1.5. As shown in Figure 1.5, this forward EM solver[19] is affected by the several design parameters

[16] MWI systems are often designed for specific applications, such as breast cancer imaging systems. Therefore, for a given MWI system, it is reasonable to define a typical OI, or a few typical OIs.

[17] For example, an inversion algorithm that over-regularizes the problem will not be able to use all the information contents of the measured data.

[18] For example, a simple OI may be imaged with a few antennas, say 12 antennas. On the other hand, if we have a more complicated OI, we often need more antennas, say 36 antennas

[19] The forward EM solver solves (1.2) for a given object (i.e., a known χ) and a given excitation (i.e., a

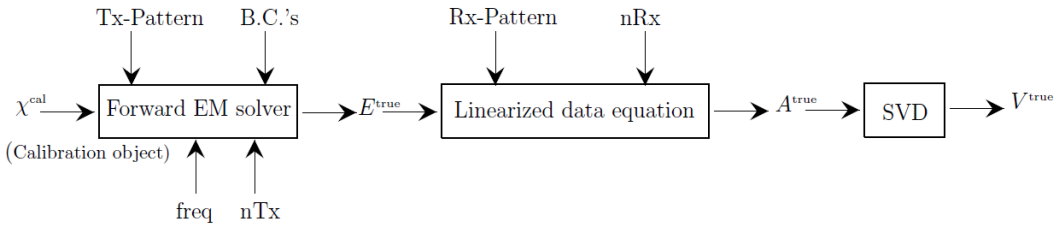

Fig. 1.5: Demonstration of the process through which the best possible reconstruction can be obtained by the use of a numerical calibration object that has a similar dielectric profile as the OI. In this process, the calibration object is placed in the imaging domain and is synthetically interrogated by the antennas of the MWI system. (This step is shown by the forward EM solver block.) This process provides us with the true mapping operator in (1.1) denoted by A^{true}. By taking the SVD of A^{true}, the right singular vectors V^{true} over which the dielectric profile can be expanded for a given MWI system will be obtained.

including illumination patterns (Tx-Pattern), number of illumination angles (nTx), boundary conditions (B.C.'s), and the frequency of operation (freq). When this process, i.e., the forward EM solver process, is completed, the true electric fields within the calibration object denoted by E^{true} are computed. Knowing this true electric field within the calibration object, the data equation (1.1) becomes linearized with a known operator[20]. This known linearized operator has been denoted by A^{true} in Figure 1.5. The superscript "true" in A^{true} is due to the fact that this operator represents the correct mapping operator that we are trying to implicitly reconstruct in the inversion process for a given MWI setup. Using the singular value decomposition (SVD)[21] of the operator A^{true}, the right singular vectors are found.

These right singular vectors create a space in which the best possible reconstructed contrast profile has to lie. Therefore, if these right singular vectors do not possess enough details to

known E^{inc}), and then finds the total field E in the object.

[20] This known operator includes Green's function of the background medium, the background wavenumber k_b, and the computed true electric field.

[21] The SVD of $\boldsymbol{A}_{\boldsymbol{m\times n}}$ is denoted by $\boldsymbol{U\Sigma V}^H$ where the superscript H denotes the Hermitian (complex conjugate transpose) operator, $\boldsymbol{U}$ is an $m \times m$ orthonormal matrix consisting of left singular vectors of the matrix $\boldsymbol{A}$. That is, $\boldsymbol{U}$ is the collection of u_i vectors where u_i denotes the i^{th} left singular vector. In addition, $\boldsymbol{V}$ is an $n \times n$ orthonormal matrix consisting of the right singular vectors of the matrix $\boldsymbol{A}$. That is, $\boldsymbol{V}$ consists of several v_i vectors where v_i denotes the i^{th} right singular vector. Finally, $\boldsymbol{\Sigma}$ is an $m \times n$ rectangular diagonal matrix containing the singular values of the matrix $\boldsymbol{A}$ on its diagonal entries. The i^{th} singular value is denoted by σ_i. These singular values are non-negative real numbers of descending magnitudes; i.e., $\sigma_i > \sigma_{i+1}$.

be able to act as an appropriate basis for the unknown contrast profile, the unknown profile cannot be reconstructed well. To understand this better, let us consider a simple geometrical example. Assume we would like to get the point (1, 1, 1) from the origin in the 3D space but we only have access to two vectors: $\hat{x}$ and $\hat{y}$ which are the unit vectors along the x and y axes. It is then obvious that we can never get to (1, 1, 1) as we do not have access to $\hat{z}$. Then, the best possible point will be (1, 1, 0) using these available vectors. Therefore, in summary, if the right singular vectors are not sufficient for the retrieval of the desired details of the calibration object, we need to change the MWI design parameters (e.g., increase the number of illumination angles) so as to add more right singular vectors with higher spatial frequency contents in order to meet the required resolution and accuracy of the reconstruction.

This introduced concept is a necessary condition that acts as a guideline in the design procedure of MWI systems. In addition, by the use of this concept the effects of several MWI parameters on the achievable resolution and accuracy from this imaging tool can be investigated. This work was published in the *IEEE Transactions on Antennas and Propagation*, and constitutes Chapter 2 of this thesis. We published this paper during my PhD studies but it also includes some aspects of my MSc thesis [24]. In particular, the concept of the best possible reconstruction was developed during my PhD studies.

1.2.2 Challenge II

Another challenge associated with MWI is to understand what can be done in order to improve the accuracy and resolution of the achieved reconstruction if the desired features have not been captured in the best possible reconstruction (or from the actual reconstruction from an imaging algorithm[22]). Broadly speaking, in addition to the signal-to-noise ratio of the

[22] It should be mentioned that the best possible reconstruction may satisfy the required accuracy and resolution but the inversion result does not.

measured data, the achievable accuracy and resolution from MWI depend on two important facts: (*i*) the existence of the required information to achieve the desired resolution and accuracy in the collected data and (*ii*) the capability of the utilized inversion algorithm to retrieve the needed information from the collected data. As was discussed in the previous challenge, the proposed concept of the best possible reconstruction is concerned with the first mentioned fact, i.e., the existence of the information in the collected MWI data. The information content of the collected data can be increased through several methods, e.g, incorporating more transceivers in MWI[23] or performing the data collection process at multiple frequencies[24].

Now, the challenge is that hardware and physical limitations do not allow us to keep adding information to the inversion process through extra measurements. For example, hardware limitations may not enable us to keep adding the number of antennas due to their size and mutual coupling. On the other hand, we might need higher frequencies to reconstruct a small detail. However, these higher frequency electromagnetic waves may not see the internal details due to their limited penetration depth. In such cases, we need a different mechanism to inject extra data to the inversion process. One way to do so is to provide the so-called *virtual* data to MWI. To understand this better, let us consider the example we discussed earlier: getting to the point (1, 1, 1) from the origin when we only have access to $\hat{x}$ and $\hat{y}$ vectors. As noted earlier, this is not possible. Now imagine that we inject $\hat{z}$ vector as the virtual data to the system. We are then able to get to (1, 1, 1) using $\hat{x}$, $\hat{y}$, and $\hat{z}$.

In this thesis, prior information about the OI is injected into the inversion algorithm. There are various forms of prior information. Herein, we consider the prior *structural* information

[23] This increases the sampling resolution of the collected data.

[24] Including the low frequency and high frequency information in the collected data from the OI has its own advantage: performing MWI at lower frequencies leads to a better penetration depth while higher frequencies can result in enhanced resolution.

about the OI[25]. To this end, the most important aspect is how to inject these prior data so that the algorithm is automated and can handle situations where we do not have access to prior information within the whole imaging domain. The details of our proposed method will be discussed in Chapter 3 of this thesis, which is accepted at the journal of *IEEE Transactions on Antennas and Propagation* (in press). In the proposed method, the prior structural information only considers the geometrical aspects of regions in the imaging domain and does not assume any quantitative values associated with each region. It should also be mentioned that the presented algorithms in Chapter 3 are fully automated and do not require any manual adjustments by the user. Moreover, the developed algorithms are capable of working with both complete and partial prior structural information about the OI. The importance this capability will be discussed in Chapter 3.

1.2.3 Challenge III

Let us begin the third challenge by considering a scenario in which we neither have access to sufficient measured data nor have any prior information (virtual data) to use in the inversion process. Then, what can be done in such a scenario?

To answer this question it might be better to first understand the importance of having a balance between the number of collected data points (which are the known quantities of an MWI problem) and the electrical size[26] of the imaging domain (which determines the number of unknowns of that MWI problem). To this end, let us consider the following two examples: the first one is regarding three dimensional (3D) full vectorial MWI[27] and the second one is regarding two-dimensional (2D) scalar MWI.

[25] This structural information can be for example obtained through other high-resolution imaging techniques.
[26] The electrical size is the ratio of the actual dimension with respect to the wavelength of operation.
[27] In contrast to 2D scalar MWI which deals with one component of the electric field, 3D full vectorial MWI considers all three components of the electric field.

Assume a 3D full vectorial MWI system with a 3D imaging domain of $5\lambda_b \times 5\lambda_b \times 5\lambda_b$ where λ_b is the wavelength of operation in the background medium. Suppose that the imaging domain is discretized into 20 cells per wavelength[28] which results in a $100 \times 100 \times 100$ discretized 3D imaging domain that is equivalent of 10^6 complex permittivity unknowns. It should be noted that the vector electric field at each cell is also unknown. This results in having 3×10^6 extra unknowns which are nonlinearly related to 10^6 complex permittivity unknowns. Now, if we are able to accommodate 3 rings of 24 antennas around this 3D imaging domain (total of $3 \times 24 = 72$ antennas) and assuming that when one antenna is in the transmitting mode the rest of the antennas are in the receiving mode, the total number of collected data points[29] will be $72 \times 71 = 5112$[30], which is the number of the known quantities of the corresponding MWI problem to be solved for this imaging system[31]. As can be understood by comparing the number of known and unknown quantities (i.e., 5112 and 10^6 respectively) in this 3D MWI system, there is a significant imbalance between the unknown and known quantities in this imaging system. This can result in degrading the achievable resolution and accuracy in this 3D imaging system[32].

Now, let us consider the similar scenario for 2D scalar MWI: a $5\lambda_b \times 5\lambda_b$ 2D imaging domain similarly discretized into 20 cells per wavelength, thus, resulting in a 100×100 discretized

[28] The rule of thumb of 10 discretized cells per wavelength might not be fine enough in order to resolve the small features of the OI.

[29] The feasibility of collecting these many data points is also dependent on the capability of the utilized switch network in MWI, i.e., the switch network should be able to handle the 72 inputs. However, if we use a network switch that can only take 24 inputs, then the maximum collected data points will be $3 \times 24 \times 23 = 1656$.

[30] It should be noted that in an N-port reciprocal network the number of independent scattering coefficients will be equal to $\frac{(N+1)N}{2}$ [5]. This is also the case for an MWI system with N antennas. In our work, we assumed that s_{ii} data are not measured and only s_{ij} data (for $i \neq j$) are measured and inverted. In addition, we assume that both s_{ij} and s_{ji} are used for inversion as their associated induced contrast sources within the OI are different. Note that s_{ij} data are often converted to field values using a calibration technique. In our case, the simulated data are field data and the experimental inversion uses field values obtained from measured s_{ij} data.

[31] Using more antennas in 3D MWI is challenging due to some physical restrictions such as the placement of the OI and the size of the antennas as well as their mutual coupling.

[32] Of course, this significant imbalance can be alleviated by the use of regularization techniques which introduce virtual data, e.g., the use of Laplacian regularizer assumes that these unknowns vary smoothly within the imaging domain.

imaging domain. We will then have 10^4 complex permittivity unknowns. It should be noted that we also have 10^4 extra complex unknowns for the normal component of the electric field to the imaging domain which are nonlinearly related to 10^4 complex permittivity unknowns. (As noted earlier in 2D scalar MWI only one component of the electric field, i.e., the one that is perpendicular to the imaging domain, is assumed to be the dominant component.) Assuming that we can fit 24 antennas on a ring surrounding the 2D imaging domain (similar to the 3D case but only having one ring of antennas), we will have $24 \times 23 = 552$ data points which are the known quantities of the corresponding 2D scalar MWI problem.

As can be seen, the imbalance between the number of known and unknown quantities has been improved when 2D scalar MWI is utilized instead of 3D full vectorial MWI[33]. This can be better understood by comparing the ratios of the unknowns to knowns for these two examples of MWI. In 3D full vectorial MWI, the ratio of the unknown to known quantities is about 196 (i.e., $\frac{10^6}{5112}$), whereas in 2D scalar MWI this number is about 18 (i.e., $\frac{10^4}{552}$). Therefore, shrinking the imaging domain from 3D to 2D has helped us in alleviating this issue: improving the balance between the known and unknown quantities, and potentially enhancing the achievable accuracy and resolution from this imaging tool.

As can be seen for both 2D scalar MWI and 3D full vectorial MWI, we often have more unknowns than knowns. One way to handle this issue is to inject virtual information as we discussed under challenge II. We also note that typical regularization schemes can also be viewed as methods of adding some generic forms of virtual information. For example, let us consider the under-determined system of equations $\boldsymbol{A}x = b$ mapping the unknown quantity x to the measured data b where $\boldsymbol{A} \in \mathbb{C}^{552\times 10000}$ and $b \in \mathbb{C}^{552}$. This system of equations,

[33] For 2D scalar MWI to be acceptable, one of the main assumptions is to have $\frac{\partial \epsilon}{\partial z} \to 0$ when the imaging domain lies in the xy plane. This assumption has been previously used for breast and forearm imaging, but in any case it does introduce modeling errors to the inversion algorithm. On the other hand, 3D full vectorial MWI reduces this modeling error, but as noted above suffers from increased imbalance between the known and unknown quantities.

when used with standard Tikhonov regularization[34], turns into the following least squares problem

$$x_\beta = \arg\min_x \left\| \begin{bmatrix} \boldsymbol{A} \\ \beta \boldsymbol{I} \end{bmatrix} x - \begin{bmatrix} b \\ 0 \end{bmatrix} \right\|^2 \tag{1.3}$$

where $\|.\|$ denotes the L_2 norm, β^2 is the regularization weight, $\boldsymbol{I}$ is the identity matrix, x_β is the regularized solution and $\arg\min_x$ denotes minimization over x [25]. It should be noted that the matrix $\boldsymbol{A}$ has been augmented with the identity matrix to form a new matrix with the dimension of $\mathbb{C}^{10552\times 10000}$. From an information point of view, our original measured data points have been virtually increased to 10552 by the use of a regularization operator to deal with 10000 unknowns. However, this might not be always ideal as the information coming through these regularization techniques are very generic.

Another way to handle the challenge of having too many unknowns and limited knowns is to further decrease the number of unknowns. This thesis suggests the use of the transmit and receive patterns of the utilized antennas toward this goal. This will now be briefly discussed.

We have proposed to use one of the MWI's design parameters, namely, the incident field distribution within the imaging domain as a tool to reduce the number of unknowns to be retrieved. In other words, this thesis suggests that one can take advantage of the incident field distribution to partially control the sensitivity of the measured data with respect to different regions within the imaging domain and consequently be able to suppress the effects of some parts of the imaging domain on the collected data. This can be viewed as having less number of unknowns within the imaging domain. Therefore, one immediate advantage

[34] In the standard Tikhonov regularization method, we solve $\boldsymbol{A}x = b$ by minimizing $\|\boldsymbol{A}x - b\|^2$ and $\|x\|^2$ over x simultaneously. That is, we find x by minimizing $\|\boldsymbol{A}x - b\|^2 + \beta^2 \|x\|^2$ where β^2 is a real number called the regularization weight.

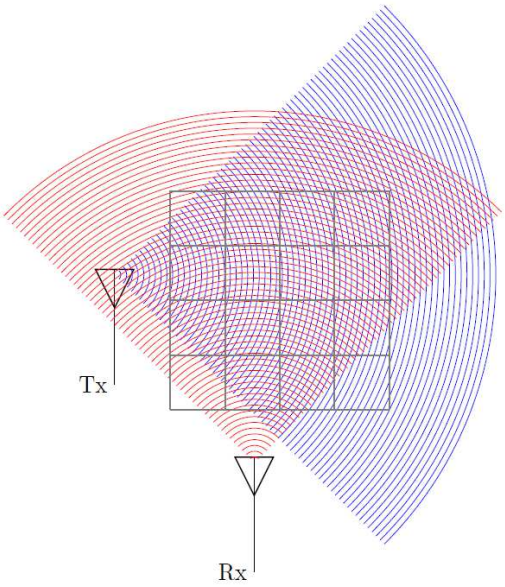

(a) Non-focused transceivers

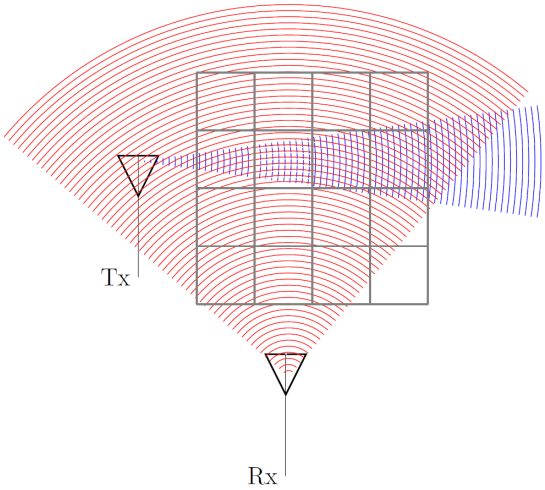

(b) Focused transmitter, non-focused receiver

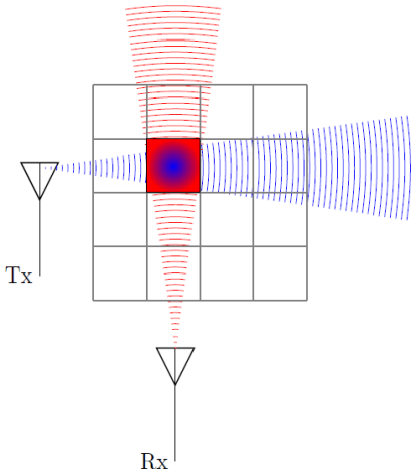

(c) Focused transceivers

Fig. 1.6: MWI setup with three modes of transceiving: (a) demonstrates the mode in which non-focused transmitter and receiver have been used, (b) depicts the setup that incorporates the focused transmitter while using non-focused receiver, and (c) represents the mode in which focused transmitter and receiver have been utilized for the interrogation of the imaging domain. (Tx denotes the transmitter, and Rx denotes the receiver. 4×4 square grid denotes the imaging domain of the MWI system.)

of this method is to have an improved balance between the known and unknown quantities in MWI that can potentially lead to improvement of the achievable accuracy and resolution

of MWI[35][36]. The incident field distribution in MWI is directly related to the properties of the antenna with which the OI is irradiated. One of the main challenges is the fact that the OI is placed close to the antenna (i.e., in the near-field zone of the antenna, and not in its far-field zone[37]). Therefore, the near-field (NF) distribution of the antenna needs to be considered in the design procedure of MWI[38].

Inspired by recent developments in tailoring the NF distributions of radiators, we have suggested to use a focused NF distribution (as opposed to a non-focused one) for the illumination of the OI in order to reduce the effects of the regions outside the region of interest (ROI)[39] on the collected data in MWI. To better understand this, we have demonstrated the proposed idea in Figures 1.6(a) and (b) where the former shows the non-focused NF distribution and the latter depicts the focused NF distribution. As can be seen, when the antenna with a focused incident distribution is utilized in MWI, mainly 4 cells out of 16 cells within the imaging domain are illuminated. On the other hand, the use of a non-focused transmitter

[35] This approach will provide more potential advantages including: (*i*) enabling the use of simpler inversion techniques, (*ii*) reducing the modeling errors, and (*iii*) mitigating the non-uniqueness issue associated with MWI. Note that the MWI problem can be thought as multiple inverse source problems. This is due to the fact that every time that the OI is illuminated, a set of contrast sources is induced in the OI which acts as the source for the scattered field data. It is well-known that the inverse source problem has a non-unique solution due to non-radiating sources [26, 27]. It should be pointed out that in MWI the non-uniqueness of the inverse source problem is generally alleviated through the use of multiple illuminations. This is due to the fact that the contrast sources arising from multiple illuminations have to share one common factor which is the unknown OI's dielectric contrast [26].

[36] In addition, we have previously shown that the use of a focused incident field can enhance the singular value dynamic of the ill-posed problem; see the author's MSc thesis [24].

[37] The far-field zone of an antenna starts from a distance away from the antenna, say $r_{\rm FF}$, and then goes to infinity. In the far-field zone, the fields radiated by the antenna can be approximated by plane waves. To find $r_{\rm FF}$, we often need to find the largest value between the following two quantities: (*i*) $2D^2/\lambda$ and (*ii*) 10λ where D is the largest dimension of the antenna and λ is the wavelength of operation in the medium. For small antennas, the first quantity, i.e., 10λ is the largest number, and therefore for small antennas, the far-field zone starts from 10λ. In other words, for small antennas, the near-field zone will cover distances that are smaller than 10λ from the antenna. On the other hand, for large antennas, the second quantity, i.e., $2D^2/\lambda$ will be the dominant value [24].

[38] The use of near-field (NF) antenna(s) as opposed to far-field (FF) antenna(s) is one of the novelties of this thesis as to the best of our knowledge this is the first time that an antenna designed from a given desired NF distribution has been investigated for MWI.

[39] In the terminology of this thesis, we refer to the subset of the imaging domain that we would like to make the collected data sensitive to as the region of interest (ROI).

results in the illumination of the whole imaging domain[40]. This method has been presented and discussed in details in Chapter 4, which has been published in the journal of *Sensors* (special issue of Microwave Imaging and Detection). Additionally, in the author's opinion, the use of a focused incident NF distribution is important for some MWI applications since it may be viewed as a smaller ruler with which finer details of the OI can be seen.[41] However, this aspect still needs further investigation and our proof is limited to one example in this thesis.

Finally, in this thesis, we have considered another degree of freedom in MWI design, i.e., the receiving pattern of the antennas. This thesis suggests that using receiving patterns in conjunction with transmitting patterns can be helpful to further tailor the sensitivity of the collected data with respect to the ROI.

In Chapter 5, we will show that using these two degrees of freedom (i.e., transmit and receive patterns) concurrently can be viewed as an MWI hardware design aspect[42] that provides a mechanism to further suppress the sensitivity of the measured data with respect to the regions outside the ROI. This can be better understood by the comparison of Figures 1.6(a) and (c) that depict the two modes of transceivers, i.e., non-focused transceivers and focused transceivers in MWI. In the non-focused MWI setup demonstrated in Figure 1.6(a), the receiver is sensitive to all the 16 cells in the 4×4 grid. However, let us now consider the focused transceivers as shown in Figure 1.6(c). Under a localized approximation[43] (e.g., the Born approximation), the receiver is now sensitive to a fewer cells compared to the

[40] Note that due to multiple scattering events within the OI a focused incident field does not necessarily result in the focused total field within the OI.

[41] Note that this is different than the numerical aperture within the context of Abbé's diffraction limit. In this method, our purpose is to confine the geometrical support of contrast sources suing focused beams.

[42] It is important in MWI design to make sure that we have taken into the account both of *hardware parameters*, e.g, incorporated transceivers in MWI and *software parameters*, e.g., utilized inversion algorithm, completely. This is due to the fact that for any application there is a trade off between the requirements in each of these two categories that can lead us to the optimum design for MWI.

[43] The utilized localized approximation is discussed in Chapter 5.

previous cases. As noted earlier, this simplified demonstration has been provided for better understanding of the proposed method and does not take into account phenomena such as multiple scattering events within the OI. The details of our investigation for this method is presented in Chapter 5. This work is currently under review.

1.3 Outline

This chapter described the scope of my thesis and its roadmap. The second chapter of this thesis, Chapter 2, is a peer-reviewed journal paper that includes the research work of my MSc and PhD studies. In this paper, a mathematical framework is introduced with which the achievable accuracy and resolution from MWI can be analyzed. The main contribution of my PhD research work in this paper was the introduction of the concept of the best possible reconstruction which is a necessary condition that needs to be satisfied in the design procedure of MWI systems. Therefore, the discussion on the topic of the best possible reconstruction in Chapter 2 should be viewed as part of my PhD contributions, and the remaining parts of this chapter should be viewed as the background information. Chapter 3, which is one of the accepted (in press) papers of the candidate, is concerned with the MWI inversion algorithm development. This chapter proposes a method to inject virtual data into the MWI algorithms in order to improve their achievable accuracy and resolution. In the proposed method, the prior structural information about the OI has been incorporated in the utilized imaging algorithms, i.e., the MWI software. The developed algorithms in this chapter are able to work with both complete and partial structural information about the OI. On the other hand, Chapter 4 is a peer-reviewed journal paper that mainly focuses on the MWI hardware aspect. In this chapter, the advantages of using focused incident near-field (NF) distributions in MWI are discussed. These advantages include suppressing the sensitivity of the collected data with respect to the regions outside the ROI. In Chapter 5, it is demonstrated

that the simultaneous use of receiver and transmitter with focused patterns can be beneficial in tailoring the sensitivity of the collected data with respect to the regions outside the ROI even more. (Note that both of these two parameters are related to the hardware aspect in MWI.) This chapter, which is an under-review journal paper, also discusses that the use of focused receiving patterns in conjunction with transmitting patterns, which can be useful in making the reconstruction with simpler inversion algorithms more accurate. In Chapter 5, it is demonstrated that the MWI hardware (i.e., incorporated antennas in the system) can be as useful as MWI software (i.e., utilized imaging algorithms) in improving the achievable accuracy and resolution from MWI. Specifically, in Chapter 5, we have suggested that instead of using the transceivers to solely interrogate the OI, we can take advantage of their transmitting and receiving patterns to tailor the sensitivity of the scattered field data with respect to the unknowns.

In summary, this thesis is structured based on the grouped manuscript style (i.e., sandwich thesis). Therefore, Chapters 2 to 5 are the candidate's peer-reviewed or under-review journal papers. These papers collectively contribute toward the goal of this PhD thesis as described in Section 1.2. Following is the list of these papers in the order of their appearance in this thesis:

- **Nozhan Bayat** and Puyan Mojabi, "A Mathematical Framework to Analyze the Achievable Resolution from Microwave Tomography," *IEEE Transactions on Antenna and Propagation*, vol. 64, no. 4, pp. 1484-1489 , 2016.

- **Nozhan Bayat** and Puyan Mojabi, "Incorporating Spatial Priors in Microwave Imaging via Multiplicative Regularization," Accepted to be published in *IEEE Transactions on Antenna and Propagation*, pp. 1-12, 2019 (Manuscript ID. AP1905-0924.R1), in press.

- **Nozhan Bayat** and Puyan Mojabi, "On the Use of Focused Incident Near-Field Distributions in Microwave Imaging," *Sensors*, vol. 18, no. 9, pp. 1-26, 2018.

- **Nozhan Bayat** and Puyan Mojabi, "Focused One-Dimensional Microwave Imaging by Near-Field Plates," Under-review.

Chapter 6 summarizes the works that have been done in this dissertation and the future avenues that can be pursued in this research area. Finally, it should be noted that this dissertation includes eight appendices entitled Appendix A to Appendix H, which are mainly the appendices of the author's published, accepted or submitted journal papers.

2

Concept of Best Possible Reconstruction

This chapter encloses a peer-reviewed journal paper published in *IEEE Transactions on Antennas and Propagation* that consists of the author's work during his MSc and PhD studies[1]. As has been stated in Section 1.2.1, one of the main challenges that MWI faces is to understand the best possible reconstruction that we can achieve from a given MWI system with specific designed parameters, e.g., the minimum number of transceivers which needs to be incorporated into an MWI system in order to achieve a desired image resolution. This chapter proposes the concept of the best possible reconstruction in order to address this issue.

Herein, a mathematical framework that can be utilized to evaluate the effects of different MWI parameters such as the frequency of operation and number of transceivers within the system has been introduced. The main contribution of the author's PhD work in this paper is the introduction of the concept of best possible reconstruction[2]. This concept can act as a tool

[1]

[2] This concept is introduced in Section 2.4 of this paper and then it has been evaluated in the Results section

in the design procedure of MWI systems using which the designer can evaluate the effects of different MWI's parameters on the best achievable reconstruction accuracy and resolution. In other words, this concept serves as a *necessary* condition to be checked prior to the actual hardware design. It should be mentioned that even if the best possible reconstruction is successful in providing desired details about the object being imaged, there is no guarantee that these desired features will be retrieved during the actual inversion process. The abstract of this paper is as follows, which will then be accompanied by the remaining sections of the paper.

Abstract. A mathematical framework is proposed to investigate how different parameters affect the achievable resolution from microwave tomography (MWT). This framework attempts to incorporate multiple scattering events within the object of interest (OI) into its analysis by taking into account the effect of the induced total field within the OI. To this end, a linearized operator, which maps the OI's permittivity profile to the measured data, is first constructed. The framework then revolves around the number of the right singular vectors of this operator, and their spatial frequency contents that can be utilized in reconstruction. Furthermore, this framework is used to introduce the 'best' possible reconstruction that can be achieved in a given MWT system when imaging a typical OI. This concept can then provide some insights and guidelines for MWT system design.

2.1 Introduction

Microwave tomography (MWT) is an imaging method that creates quantitative images of the dielectric profile of an object of interest (OI). This imaging modality offers several potential applications ranging from industrial non-destructive evaluation to biomedical imag-

against synthetic data sets as well as the Conclusions Section. The remaining part of this chapter should be treated as the background materials as they are related to the author's MSc work.

ing [16, 28–30]. To make MWT a viable imaging method, it is important to have solid understanding about its achievable resolution limit for different measurement scenarios and different OIs. To this end, it is important to have a mathematical framework using which such analysis on the achievable resolution can be performed. In an earlier work [31], a mathematical framework for studying the achievable resolution from linear inversion methods was presented. The authors of [31] then investigated why the choice of nonlinear inversion algorithms can result in enhanced resolution compared to the use of linear inversion methods. In contrast to [31], this paper attempts to provide a mathematical framework directly for nonlinear inversion algorithms. A few other papers, e.g., [32, 33], have quantified the resolution achievable from a given experimental MWT system for a few targets. In contrast to those papers, this paper does not aim to quantify the achievable resolution from a given experimental system, but attempts to provide a mathematical framework using which the achievable resolution limit from any MWT systems can be better studied. The core of the framework proposed in this paper is borrowed from a mathematical framework that was recently used to solve the discretized linear Fredholm integral equation of the first kind [34]. In this paper, this framework is adapted to the discretized nonlinear integral equation associated with the MWT problem. As noted above, the proposed framework attempts to take into account the nonlinearity of the MWT problem in its resolution analysis, thus, providing more accurate understanding of the achievable resolution from MWT compared to the aforementioned works. In addition, based on this framework, two different concepts will be introduced, namely, the direct expansion of the contrast profile and the ‘best’ possible reconstruction, which can be used to provide some guidelines and insights on how to design an MWT system. Throughout this paper, we assume that the wave propagation inside the MWT chamber is two-dimensional transverse magnetic.

2.2 Nonlinearity and Resolution

Let's consider the so-called MWT data equation that maps the dielectric profile of the OI, located within the imaging domain $\mathcal{D}$, to the scattered data measured outside $\mathcal{D}$ as

$$E^{\text{scat}}(\boldsymbol{p}) = k_b^2 \int_{\mathcal{D}} g(\boldsymbol{p}, \boldsymbol{q}) E(\boldsymbol{q}) \chi(\boldsymbol{q}) d\boldsymbol{q}, \tag{2.1}$$

where $E^{\text{scat}}(\boldsymbol{p})$ is the scattered electric field at the measurement domain, k_b is the wavenumber of the background medium, $\chi(\boldsymbol{q})$ is the unknown dielectric contrast profile of the OI. The position vectors $\boldsymbol{p}$ and $\boldsymbol{q}$ span the measurement and imaging domains respectively, and $g(\boldsymbol{p}, \boldsymbol{q})$ is Green's function of the background medium. The total field inside the imaging domain is denoted by $E(\boldsymbol{q})$. The contrast profile $\chi(\boldsymbol{q})$ of the OI is defined as $\chi(\boldsymbol{q}) = (\epsilon(\boldsymbol{q}) - \epsilon_b)/\epsilon_b$ where $\epsilon(\boldsymbol{q})$ is the unknown relative permittivity profile of the OI, and ϵ_b is the known relative permittivity of the background medium. To analyze the achievable resolution from MWT, we need to analyze the operator that maps the unknown contrast profile, $\chi(\boldsymbol{q})$, to the measured scattered data, $E^{\text{scat}}(\boldsymbol{p})$. As can be seen from (2.1), this operator depends on both the Green's function $g(\boldsymbol{p}, \boldsymbol{q})$ and the total field within the imaging domain $E(\boldsymbol{q})$. In other words, the information flow from the imaging domain to the measurement domain is mainly controlled by these two functions. The main challenge in analyzing this operator is that the total field $E(\boldsymbol{q})$, which partially defines this operator, is itself nonlinearly related to the unknown $\chi(\boldsymbol{q})$. This makes this operator dependent on the OI. (This is one of the reasons that different resolving abilities have been observed for the same experimental MWT system when imaging different OIs; e.g., see [32].) Based on the above discussion, it can be concluded that the measured data is nonlinearly related to the unknown contrast. Therefore, our first step toward providing a mathematical framework is to decide how to handle this nonlinearity.

Herein, we aim to linearize (2.1) without imposing significant approximations on $E(\boldsymbol{q})$. That is, we would like to incorporate as many multiple scattering events as possible into our analysis. To this end, we use the following procedure.

1. The measured data $E^{\text{scat}}(\boldsymbol{p})$ is inverted using a nonlinear inversion algorithm. A nonlinear inversion algorithm iteratively attempts to model multiple scattering events within the OI. Herein, the multiplicative regularized Gauss-Newton inversion (MR-GNI) algorithm [2, 35] is used as the nonlinear inversion algorithm.

2. The total field $E(\boldsymbol{q})$ at the last iteration of the MR-GNI algorithm is calculated. This calculated total field is denoted by $\bar{E}(\boldsymbol{q})$. For a given inversion algorithm, assuming that the regularization weight is chosen properly, this calculated total field will be the most accurate estimate of the multiple scattering events within the OI that this inversion algorithm can recover.

3. This calculated total field will then be used in (2.1) to linearize the data equation with respect to $\chi(\boldsymbol{q})$. That is, the linearized equation will be

$$\overbrace{E^{\text{scat}}(\boldsymbol{p})}^{\text{known measured data}} = \overbrace{k_b^2 \int_{\mathcal{D}} g(\boldsymbol{p},\boldsymbol{q})\bar{E}(\boldsymbol{q})}^{\text{known linearized operator}} \overbrace{\chi(\boldsymbol{q})}^{\text{unknown}} \, d\boldsymbol{q}. \tag{2.2}$$

We now have a linearized map between the unknown dielectric profile and the measured data. (It should be noted that this type of linearization has been previously used for image enhancement of MWT final reconstructions [36].) We now need to analyze this linearized operator in conjunction with the measured data in order to understand how different parameters affect the achievable resolution. To this end, we discretize (2.2) as $\boldsymbol{A}\chi = b$ where b is a complex vector of length m containing the measured data points, χ is a complex vector of length n containing the contrast values at each discretized cell of the imaging domain, and $\boldsymbol{A}$ is a $m \times n$ complex matrix, which is the discretized form of the integral equation operator in

(2.2). As can be seen, the matrix $\boldsymbol{A}$ depends on Green's function of the background medium and the total field $\bar{E}$. Using the singular value decomposition (SVD) of the matrix $\boldsymbol{A}$, the discretized contrast χ can be written as [37]

$$\chi = \sum_{i=1}^{\min(m,n)} \frac{u_i^H b}{\sigma_i} v_i, \tag{2.3}$$

where u_i and v_i are the left and right singular vectors of $\boldsymbol{A}$ respectively and σ_i is the ith singular value[3]. Note that the upper limit of the above summation is $\min(m, n)$ to exclude the zero singular values from the summation. This indicates that the solution χ lies within the space of the first $\min(m, n)$ right singular vectors v_i, and is equal to the summation of these right singular vectors, each of which weighted by $u_i^H b/\sigma_i$. Finally, we note that when a regularization scheme is used in an inversion algorithm, it is more appropriate to consider the SVD of the augmented operator that accounts for the presence of the regularizer. However, this will make the analysis more complicated and also dependent on the utilized regularization scheme. In this work, we have not taken this into account.

2.3 MWT Resolution Analysis

The key idea behind using (2.3) for resolution analysis lies within the fact that the right singular vectors v_i have properties similar to the Fourier series' basis functions. Specifically, right singular vectors v_i of small indices i have mainly low spatial frequency components; as the index i increases, v_i will then have higher spatial frequency contents [34]. Therefore, as the index i increases, the summation (2.3) will try to incorporate more high spatial frequencies into the solution χ. To use this idea in the rest of this paper, we need to have a tool to evaluate the spatial frequency contents of right singular vectors in different measure-

[3] These singular values are non-negative real numbers of descending magnitudes; i.e., $\sigma_i > \sigma_{i+1}$.

ment scenarios. To this end, we use the power spectrum of the right singular vectors as used in [34]. Herein, to be able to compare the spatial frequency contents of the power spectra of different v_i within the same plot, we choose to plot only one cut of $|\tilde{v}_i(f_x, f_y)|^2$ for each v_i. (f_x and f_y are spatial frequency indices and $\tilde{v}$ denotes the Fourier transform of v.) Specifically, we plot $|\tilde{v}_i(f_x, f_y = 0)|^2$ against different f_x and i indices. As will be seen later, this plot is similar to a rotated "V" letter where the apex of the "V" represents the zero spatial frequency component. As the index i increases, the aperture of the "V" increases; thus, incorporating higher spatial frequency components. It is therefore clear that incorporating as many v_i as possible into the reconstructed χ is desirable so as to achieve a high resolution image. We now need to address the number of right singular vectors that can be incorporated into the reconstructed contrast χ. From (2.3), it might be mistakenly concluded that we can always incorporate $\min(m, n)$ right singular vectors into the reconstructed contrast. However, this is not the case due to the ill-posedness of the problem which results in the blow up of the coefficients $u_i^H b/\sigma_i$ for large i indices [37]. Therefore, although it is critical to incorporate v_is with large i indices into the reconstructed contrast, we cannot include all the v_is due to the instability of the associated mathematical problem. This indicates that the final solution will suffer from not having some high spatial frequency components. If those high spatial frequency components are needed to successfully reconstruct a feature in the OI, that feature will not be properly shown in the reconstructed image. We now need a tool to determine how fast $u_i^H b/\sigma_i$ coefficients blow up. This is important because the faster these coefficients blow up, the smaller number of v_is can be used in the reconstruction. To this end, we simply plot the magnitude of the coefficients $u_i^H b/\sigma_i$ versus the index i. This plot in conjunction with the power spectrum plot enables us to compare different scenarios for MWT applications in terms of the achievable resolution.

2.4 Direct Expansion and 'Best' Possible Reconstruction

As noted above, the number of right singular vectors used in the expansion of the reconstructed profile needs to be truncated to deal with the ill-posedness of the problem. At this point, it is important to be able to check what we could have reconstructed if we were able to use all the $\min(m, n)$ right singular vectors in the reconstruction. To this end, we project the true contrast profile, denoted by χ^{true}, into the space spanned by all the $\min(m, n)$ right singular vectors. The result of this projection, which we refer to as the direct expansion of the contrast profile, is denoted by $\chi^{\forall v_i}$, and will be $\chi^{\forall v_i} = \sum_{i=1}^{\min(m,n)} (v_i^H \chi^{\text{true}}) v_i$. Once $\chi^{\forall v_i}$ is calculated, $\epsilon_r^{\forall v_i}$ can be easily obtained.

It is also worthwhile to discuss a simple method for the evaluation of the 'best' possible reconstruction of an OI in a given MWT setup. This is important since we first need to confirm whether or not this 'best' possible reconstruction can resolve the features of interest prior to inversion. In fact, if the 'best' possible reconstruction cannot achieve the required resolution level, the data inversion will not be able to resolve these features either. As will be seen later, this can provide some insights on how to design an MWT system to achieve a desired resolution level. To find the 'best' possible reconstruction, we first give the true contrast χ^{true} to the forward solver to generate the true total field within the OI. This true total field is denoted by E^{true}. We can now linearize the data equation by utilizing E^{true} instead of $\bar{E}$ in (2.2). This new linearized operator is then referred to as $\boldsymbol{A}^{\text{true}}$. The true contrast profile is then projected into the space spanned by the first $\min(m, n)$ right singular vectors of $\boldsymbol{A}^{\text{true}}$, denoted by v_i^{true}. The result of this projection, which we refer to as the 'best' possible reconstruction χ^{best}, will have a mathematical expression similar to that of $\chi^{\forall v_i}$ with only one difference: v_i^{true} will be used instead of v_i. Once χ^{best} is obtained, ϵ_r^{best} can be easily found. We note that χ^{best} is not necessarily the same as χ^{true} since χ^{best} can only lie within the space of the first $\min(m, n)$ right singular vectors; however, χ^{true} may have components

which lie within the space of the right singular vectors with indices greater than $\min(m, n)$. As also noted earlier, if ϵ_r^{best} cannot achieve the desired resolution level, the inversion of the data cannot achieve the desired resolution level either. This is due to the fact that obtaining ϵ_r^{best} is based on knowing the true total field within the OI; however, in an inversion process we can only aim to have an $\bar{E}$ that is as close as possible to E^{true}. (As will be discussed later, this idea can be used to design application-specific MWT systems.)

2.5 Results

We now apply the above framework to both synthetic and experimental data sets. The synthetic data is collected from a target, which we refer to as the *E*-target. This target, shown in Figure 2.1(a), has been previously used in other publications; e.g., in [32, 33]. Similar to [32], we assume that the *E*-target is lossless and has a relative permittivity of 2.3 within our frequency range of interest. (For all the results presented in this paper, the inversion algorithm starts with an initial guess of zero contrast.) Before starting our analysis, it is important to make sure that the number of utilized transceivers is sufficient for the 'best' possible reconstruction to resolve the features of this OI. In our simulations, we assume that all the antennas are equally spaced around a circle with the radius of 0.15 m. Now, if the number of antennas is nTx, the total number of collected scattering data points will be $nTx \times (nTx - 1)$[4]. We now choose three possible nTx, namely, 8, 16 and 24 at the frequency of 5 GHz. The 'best' possible reconstructed profile, ϵ_r^{best}, for each of these cases has been shown in Figure 2.1(b)-(d). As can be seen, the 'best' possible reconstructed profile fails to resolve these features when nTx is 8. Thus, if 8 transmitters are used for imaging this target, the reconstruction will also fail. Herein, we choose the number of transmitters to be 16 unless otherwise stated. As can be seen, the concept of ϵ_r^{best} provides some guideline

[4] See Footnote 30 in Chapter 1 for a detailed explanation.

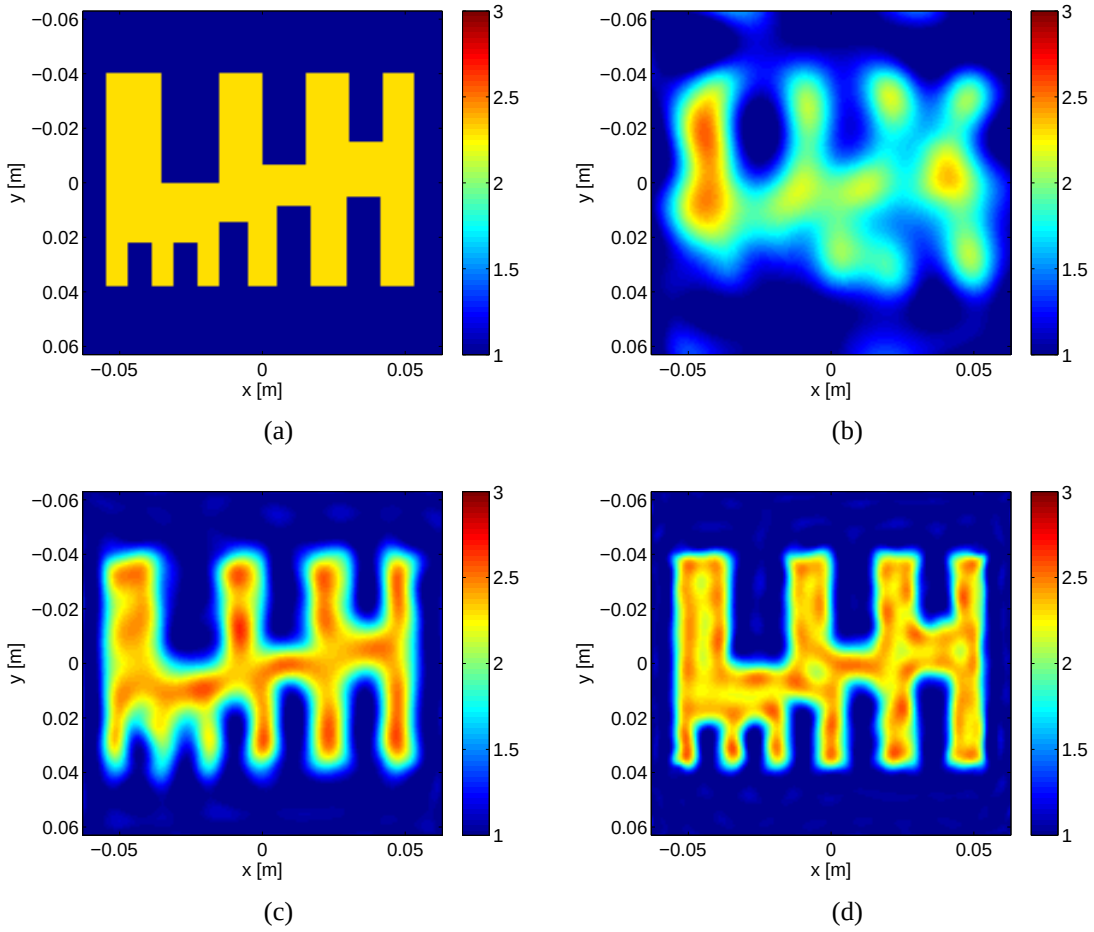

Fig. 2.1: (a) Real part of the true relative complex permittivity profile. (b)-(d) 'Best' possible reconstruction, ϵ_r^{best}, when the number of antennas is set to 8, 16, and 24 respectively. ($f = 5$ GHz)

for the MWT system design; e.g., by avoiding 8 transmitters for this measurement configuration when imaging objects similar to this E-target. To generate the synthetic data set to be inverted, we discretize the E-target into 150×150 cells within a 12.6×12.6 cm^2 domain. (Unless otherwise stated, we assume that the transmitters are line sources.) In all the examples concerning the inversion of this synthetic data set, the inversion domain is 14×14 cm^2 that is discretized into 100×100 cells. Let's start by studying the role of noise in the achievable resolution at $f = 5$ GHz. To study the effect of noise, we add synthetic noise to our data set based on the formula given in [38]. Specifically, we consider four

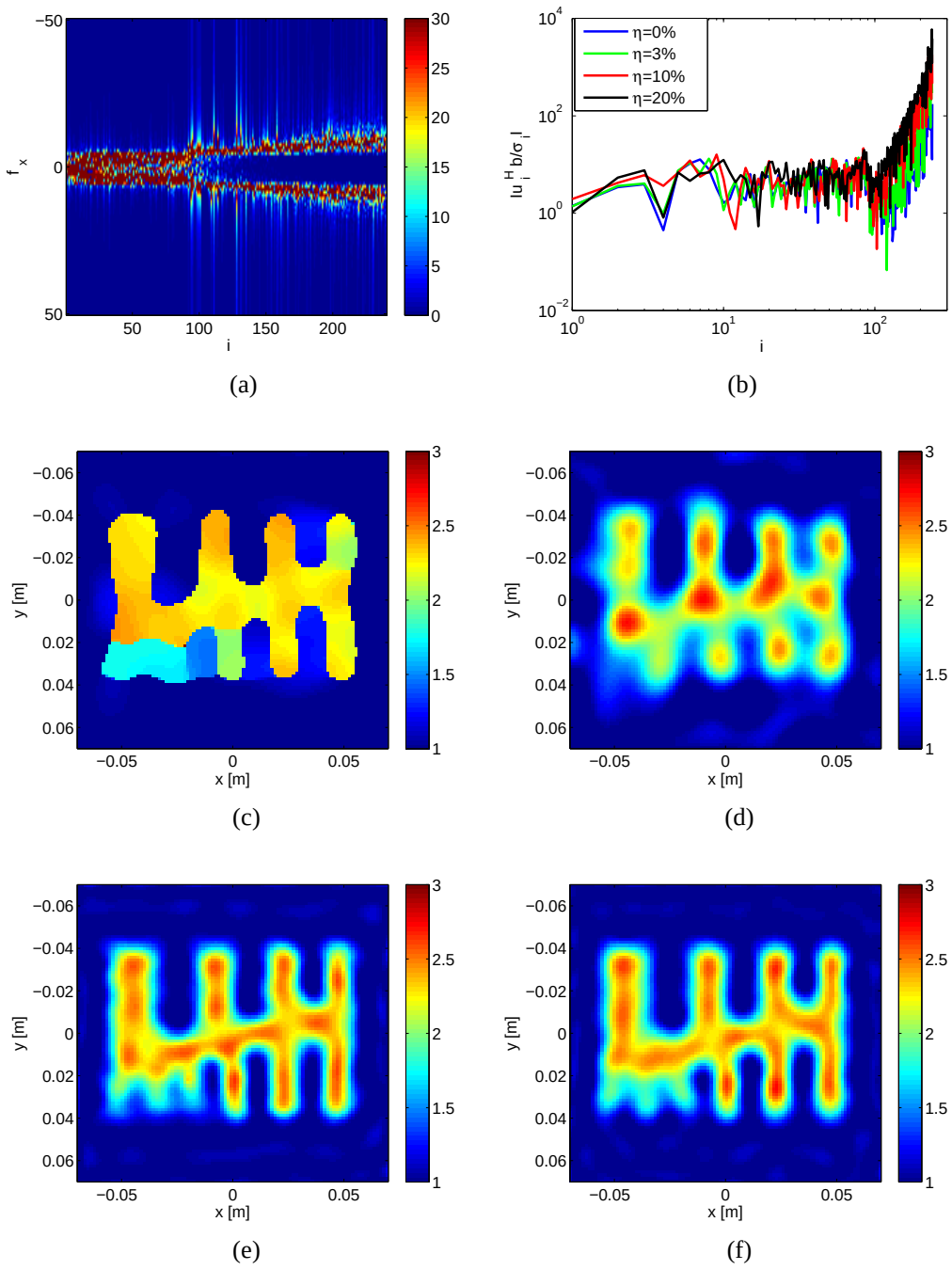

Fig. 2.2: (a) Power spectrum $|\tilde{v}_i(f_x, f_y = 0)|^2$ at $\eta = 0\%$. (Each column of this image represents the power spectrum of a given v_i with respect to f_x.) (b) Variation of $|u_i^H b|/\sigma_i$ for four different noise levels. (c)-(d) Reconstructed real part of the permittivity profile for $\eta = 0\%$ and $\eta = 20\%$ respectively. (e)-(f) Direct expansion of the real part of the permittivity profile for $\eta = 0\%$ and $\eta = 20\%$ respectively. ($nTx = 16$ and $f = 5$ GHz.)

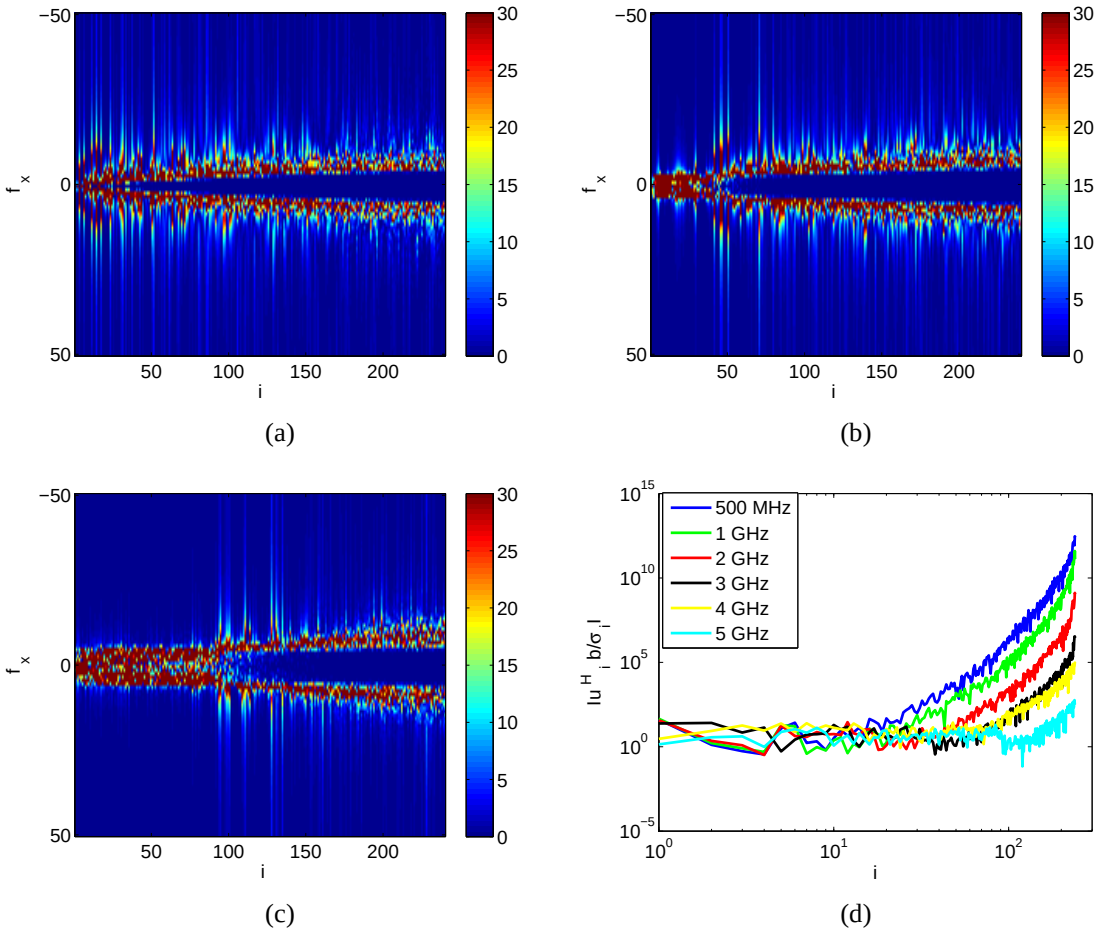

Fig. 2.3: (a)-(c) Power spectra $|\tilde{v}_i(f_x, f_y = 0)|^2$ at 500 MHz, 3 GHz, and 5 GHz respectively; (d) Variation of $|u_i^H b|/\sigma_i$ at six different frequencies. ($nTx = 16$ and $\eta = 3\%$.)

different noise levels: $\eta = 0\%,\ 3\%,\ 10\%$, and 20%. The power spectrum of the right singular vectors when the noise level is 0% is shown in Figure 2.2(a). (Note that $\min(m, n)$ is 240 for this example.) Although not shown, the power spectra corresponding to the other three noise levels have similar spatial frequency contents as the one shown in Figure 2.2(a). Also, as can be seen in Figure 2.2(a), the power spectrum looks like a horizontal "V" letter as pointed out earlier. Now, the question to be answered is whether or not we can use all these spatial frequency components in the reconstruction of χ. To answer this question we plot $|u_i^H b|/\sigma_i$, which are the coefficients of the summation (2.3); see Figure 2.2(b). As can be seen in Figure 2.2(b), as the noise level increases, these coefficients tend to blow up at

smaller i indices; thus, less number of v_is can be incorporated into the reconstructed χ to avoid instability. Consequently, as the noise level increases, less high spatial frequency content can be incorporated into the solution; therefore, the achievable resolution will degrade as the noise level increases. (Note that even for $\eta = 0\%$ we still have some numerical noise, e.g., round-off error.)

Now, let's take a look at the reconstruction of this target. The reconstructed permittivity profiles, denoted by $\epsilon_r^{\text{recons}}$, have been shown in the middle row of Figure 2.2 for the two noise levels. (The reconstructed imaginary part of this lossless target is small, and not shown here.) As can be seen, as the noise level increases, the reconstruction accuracy suffers. In this example, the three small fingers in the bottom left of the true object have not been reconstructed at any of these noise levels. Also, for the noise level of 20%, the finger in the bottom left of the target starts to disappear, and also the two fingers in the bottom right of the target start to combine into one bigger finger. The direct expansion of the reconstructed real-part of the permittivity is shown in the last row of Figure 2.2 for $\eta = 0\%$ and $\eta = 20\%$. As opposed to the reconstructed profiles, these direct expansions have resolved the three small fingers in the bottom left of the OI. (Note that the discretization of ϵ_r^{true} used to create the direct expansion is chosen to be different than the one used to create the synthetic data set so as to avoid the inverse crime.) The above observation is very important. It shows that in the example considered here, the noise level is the main reason for not being able to resolve the three small fingers in the OI. This is due to the fact that the presence of noise limits the number of v_is that can be used in the expansion of the unknown profile. In other words, the presence of noise limits the dimension of the space into which the unknown profile is projected. As also noted earlier, the presence of the regularizer affects the singular vectors into which $\epsilon_r^{\text{recons}}$ is pojected; however, this is not the case for $\epsilon_r^{\forall v_i}$. This explains why $\epsilon_r^{\text{recons}}$ at $\eta = 0\%$ is more homogeneous than its corresponding $\epsilon_r^{\forall v_i}$; compare Figures 2.2(c) and (e). We now consider the effect of the frequency of operation on the achievable resolution. Similar to the previous

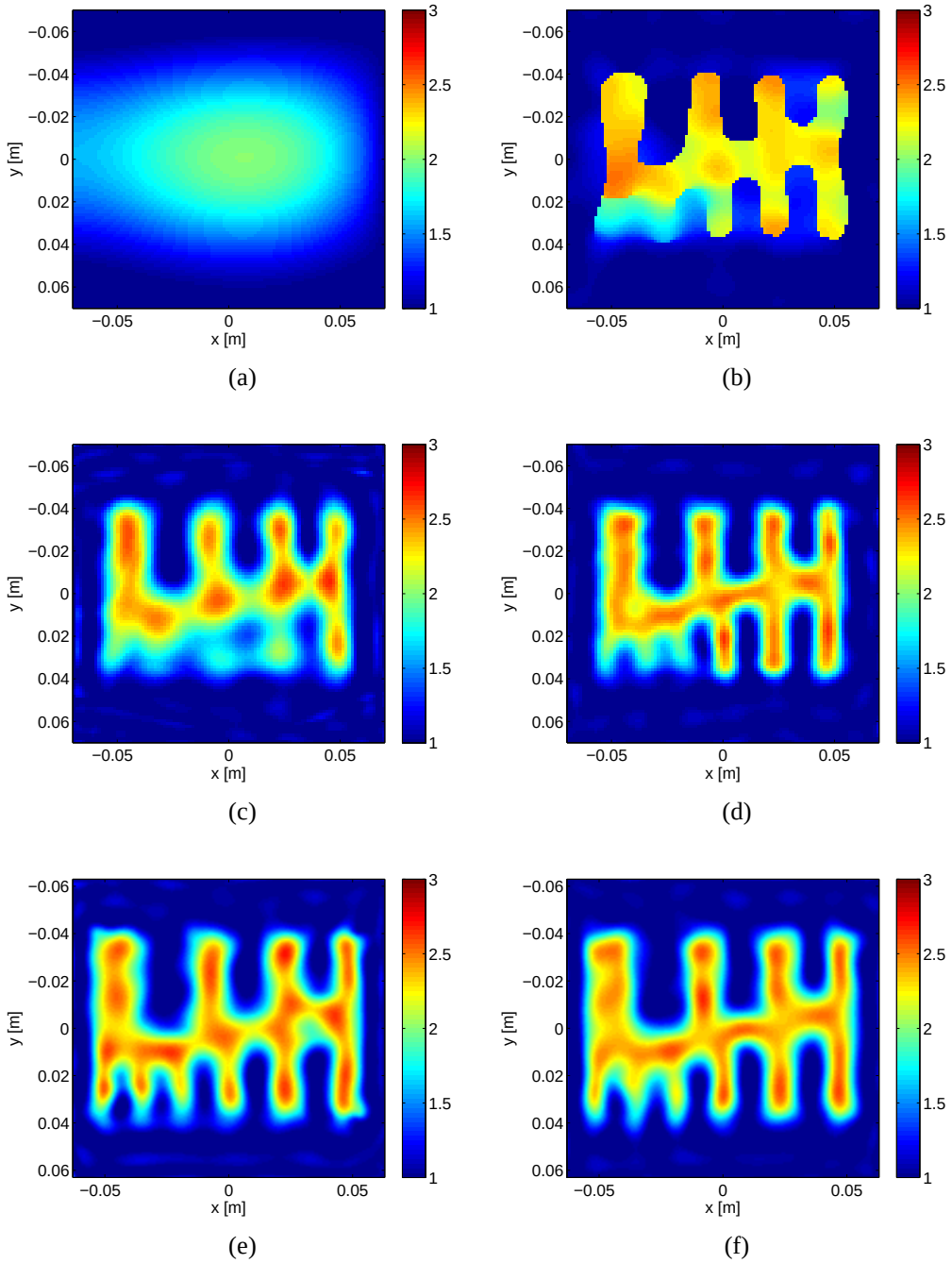

Fig. 2.4: (a)-(b) Reconstructed real part of the permittivity profile at 500 MHz and 5 GHz respectively; (c)-(d) Direct expansion of the real part of the permittivity profile at 500 MHz and 5 GHz respectively; (e)-(f) 'Best' possible reconstruction at 500 MHz and 5 GHz respectively ($nTx = 16$ and $\eta = 3\%$.)

example, we assume that the OI is irradiated by 16 transceivers. However, in this section, we fix the noise level η to be 3%. The frequency is then changed from 500 MHz to 5 GHz. Let's first take a look at the power spectra $|\tilde{v}_i(f_x, f_y = 0)|^2$ at three different frequencies that are shown in Figure 2.3(a)-(c). As can be seen, as the index i increases, the amount of high spatial frequency contents within v_i is generally increased in the form of a horizontal "V" letter. Now, let's consider how many of these right singular vectors can be used in the reconstruction of the unknown profile. This can be understood by plotting the coefficients $|u_i^H b|/\sigma_i$ versus the index i. As can be seen in Figure 2.3(d), as the frequency increases, these coefficients tend to blow up at a larger index i. That is, as the frequency of operation increases, the reconstructed profile has the chance to lie within a space of v_is having a larger dimension, thus, having the chance to resolve more features. The reconstruction results at 500 MHz and 5 GHz are shown in Figure 2.4(a) and (b), respectively. As can be seen, as the frequency increases, we have better reconstruction. This is consistent with our observation regarding the ability to incorporate more right singular vectors into the expansion of the reconstructed contrast as the frequency increases. Now, let's consider what we could have achieved if we were able to use all the right singular vectors at these two frequencies. That is, we'd like to address what $\epsilon_r^{\forall i}$ would be for 500 MHz and 5 GHz. This has been shown in Figure 2.4(c) and (d). As can be seen, for each frequency, $\epsilon_r^{\forall i}$ is better than its corresponding $\epsilon_r^{\text{recons}}$. This is, of course, due to the fact that $\epsilon_r^{\text{recons}}$ cannot utilize all the right singular vectors whereas we have used all the right singular vectors[5]to create $\epsilon_r^{\forall v_i}$. It is now worthwhile to consider the 'best' possible reconstruction at these two frequencies as shown in Figure 2.4(e) and (f). As opposed to the reconstructed profile and the direct expansion, the three small fingers are visible in the 'best' possible reconstruction at both frequencies. Having this in mind, and noting that the 'best' possible reconstruction relies on the true total field in the object, as opposed to the reconstructed (estimated) total field in the case of the

[5] Herein, we have utilized all the right singular vectors up to $\min(m, n)$ of the reconstructed matrix $\boldsymbol{A}$ to create the $\epsilon_r^{\forall v_i}$.

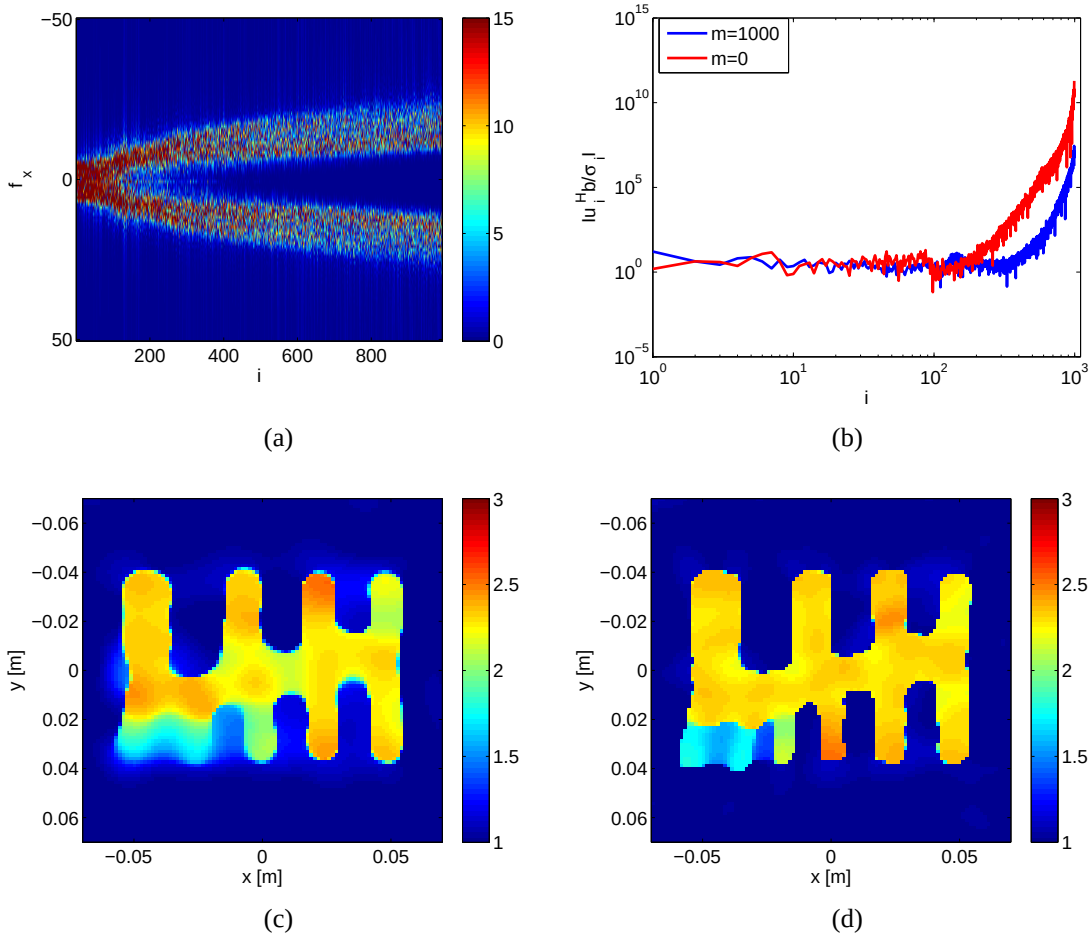

Fig. 2.5: (a) Power spectrum $|\tilde{v}_i(f_x, f_y = 0)|^2$ for $m = 1000$; (b) Variation of $|u_i^H b|/\sigma_i$ for $m = 0$ and $m = 1000$; (c)-(d) Reconstructed real-part of the permittivity profile for $m = 0$ and $m = 1000$ respectively. ($nTx = 32$, $f = 5$ GHz, and $\eta = 3\%$.)

direct expansion, it can be concluded that the accurate recovery of the total field in the OI (or, equivalently, the multiple scattering events within the OI) is very important in achieving a high resolution image.

In all the previous examples, we have assumed that the incident field distribution by which the OI is illuminated has the distribution of a line source. We now consider the use of a focused incident field distribution, which can be modelled by multiplying the incident field distribution of the line source by $\cos^m \psi$ where ψ is the angle between the boresight axis

of the transmitter and the line that connects the transmitter to the observation point [39][6]. The parameter m controls the focusing level; the larger m, the more focused incident field distribution. Now, let's assume that 32 transceivers are utilized to collect the scattering data set. Herein, we consider single-frequency inversion at 5 GHz when the noise level is set to 3%. The power spectrum plot for $m = 1000$ is shown in Figure 2.5(a). The power spectrum for $m = 0$ is similar to that of $m = 1000$, and is not shown here. In addition, as shown in Figure 2.5(b), the coefficients $|u_i^H b|/\sigma_i$ blow up for larger i when $m = 1000$ as compared to the case when $m = 0$.[7] This indicates that with the increased focusing level, we are now able to utilize more right singular vectors to reconstruct the unknown contrast. This should now demonstrates itself in the reconstructed permittivity using these two different focusing levels, shown in Figure 2.5(c) and (d). As can be seen, the three small fingers in the bottom left of the profile are visible when $m = 1000$; but, they are not visible when $m = 0$.

We now consider the experimental *FoamTwinDielTM* data set collected by the Fresnel Institute [1]. The target consists of three dielectric circular cylinders. Two of these cylinders have a diameter of 31 mm, and a relative permittivity of 3 ± 0.3. The other cylinder has a diameter of 80 mm and a relative permittivity of 1.45 ± 0.15. This target is irradiated from 18 different angles, and the resulting scattering field is collected at 241 points at 9 different frequencies ranging from 2 GHz to 10 GHz with the step of 1 GHz. Let's first observe the power spectra corresponding to the single-frequency (2 GHz) and multiple-frequency inversion of this data set, shown in Figure 2.6(a) and (b). As can be seen, the multiple-frequency inversion provides higher spatial frequency contents compared to the single-frequency inversion. Also, the coefficients $|u_i^H b|/\sigma_i$ associated with the multiple-frequency inversion blow up later compared to those associated with the 2 GHz inversion (not shown here). Conse-

[6] This focusing parameter denoted by m should not be confused with the number of measured data points which has also been denoted by m and has been used in several places in this chapter in the form of $\min(m, n)$.

[7] Note that such large focusing m values may not be practical. For example, see the note on the working distance in Chapter 5. Herein, we have used such large focusing m values merely for the sake of discussion.

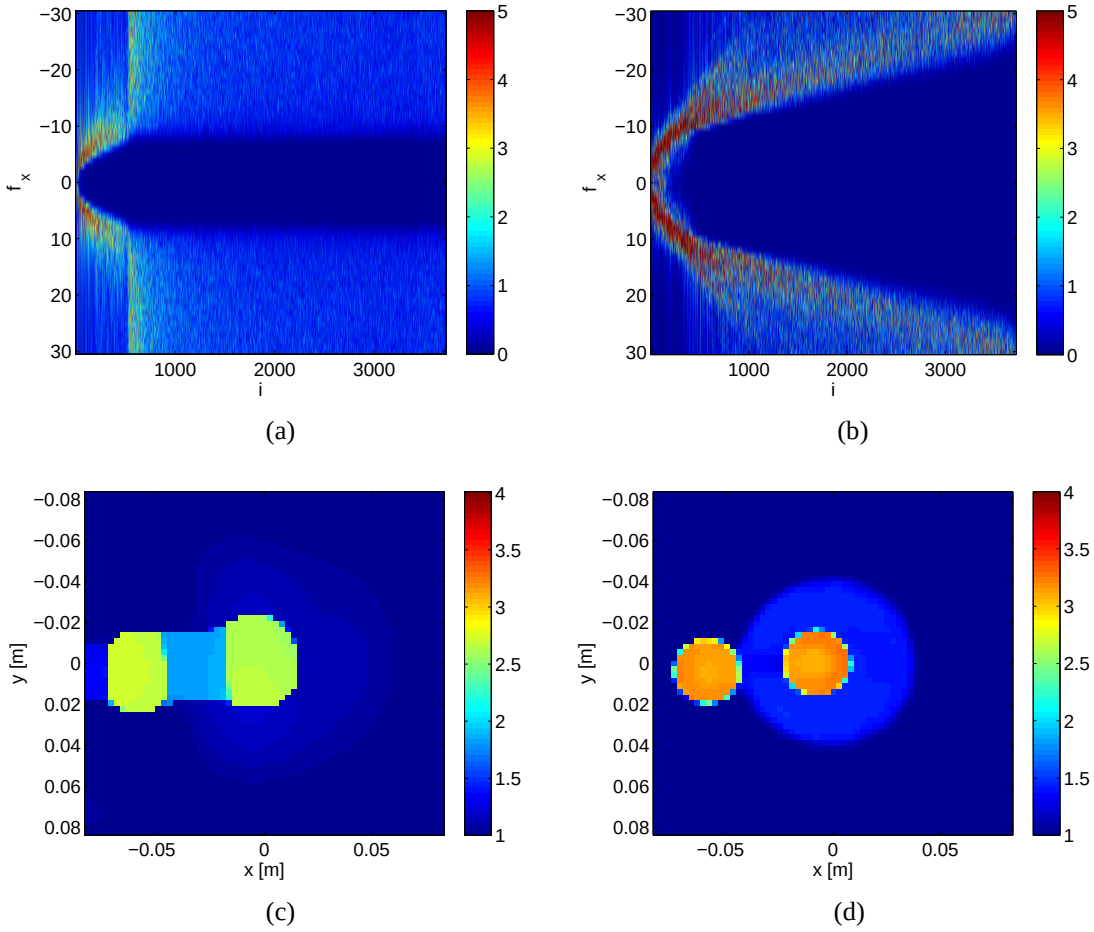

Fig. 2.6: *FoamTwinDielTM* experimental data: (a)-(b) Power spectra $|\tilde{v}_i(f_x, f_y = 0)|^2$ for 2 GHz and multiple-frequency inversion respectively; (c)-(d) Reconstructed real-part of the permittivity profile for 2 GHz and multiple-frequency inversion respectively.

quently, the multiple-frequency inversion can utilize more high spatial frequency contents, thus, resulting in enhanced reconstruction, as can be seen and compared in Figure 2.6(c) and (d).

2.6 Discussion and Conclusion

We have proposed a mathematical framework to analyze the achievable resolution from MWT. Based on this framework, the effect of different parameters on the achievable resolution can be investigated. As noted earlier, the information flow from the OI to the measurement domain is partially governed by the induced total field within the OI; thus, the information flow depends on the OI's permittivity profile as well. Since the OI's permittivity profile is the actual unknown of the problem, predicting the achievable resolution for an arbitrary OI is not feasible using the proposed framework (or, perhaps, any framework). In other words, performing resolution analysis should be focused on application-specific scenarios for which a numerical calibration object, or a few numerical calibration objects, can be defined. These calibration objects, which should resemble the overall dielectric profiles of the objects to be imaged, can then be utilized in conjunction with this framework to infer the achievable resolution.

Based on the proposed framework, the following procedure can be suggested so as to determine the MWT system parameters given a desired resolution. First, a numerical calibration object is defined, which serves as ϵ_r^{true}. The next step will be to find ϵ_r^{best}. If ϵ_r^{best} does not capture the required resolution level, more scattering data needs to be collected, e.g., using more transceivers or frequencies until ϵ_r^{best} captures the required resolution level. Therefore, the concept of ϵ_r^{best} provides some guidelines, and acts as a necessary condition for the MWT system design. Having ensured that ϵ_r^{best} meets the required resolution level, the collected scattering data can then be inverted to find $\epsilon_r^{\text{recons}}$ and $\epsilon_r^{\forall i}$. If $\epsilon_r^{\text{recons}}$ does not capture the required resolution level, but $\epsilon_r^{\forall i}$ does, this might be an indication that more right singular vectors should be incorporated into $\epsilon_r^{\text{recons}}$. One way to achieve this is to decrease the degree of the ill-posedness of the problem, e.g., by reducing the overall noise of the data, using more focused incident field distributions, etc. If neither $\epsilon_r^{\text{recons}}$ nor $\epsilon_r^{\forall i}$ can reconstruct the

resolution level of interest, that may indicate that the reconstructed total field distribution within the OI, $\bar{E}$, is not sufficiently close to the true total field within the OI, E^{true}. This might be handled by reducing the overall noise, which includes measurement noise, calibration error, regularization error, round-off error, modelling error, etc. However, some sources of the overall noise, e.g., round-off error, cannot be completely removed. If after all these efforts, $\epsilon_r^{\text{recons}}$ is still not able to meet the desired resolution level, the MWT system design needs to be iteratively modified until $\epsilon_r^{\text{recons}}$ is satisfactory. This iterative modification often includes either collecting more scattering data or utilizing *a priori* information about the OI ('virtual' data) in the inversion algorithm.

3

Multiplicative Regularization to Incorporate Spatial Priors

This chapter encloses an accepted journal paper in *IEEE Transactions on Antennas and Propagation*[1]. As has been mentioned in Section 1.2.2, one of the challenges facing MWI is the lack of sufficient achievable accuracy and resolution from this imaging tool to become commercial in some applications (e.g., biomedical imaging). One way to enhance the achievable accuracy and resolution from MWI is to inject more information about the object being imaged into the inversion algorithm. In this chapter, one of these methods, i.e., incorporating prior structural information into the inversion algorithm, is considered. (For example, this type of prior information can be obtained through another imaging modality such as MRI.)

To this end, a fully automated inversion algorithm is proposed that can incorporate spatial

[1]

priors (SP) information about the imaging domain in order to improve the achievable reconstruction accuracy. As will be seen, the proposed algorithm is capable of working with both fully-available and partially-available spatial priors. In summary, the proposed algorithm has the following two main advantages in comparison with the existing algorithms.

- The proposed algorithm uses a multiplicative regularization term to incorporate spatial priors. The weight of this regularization is automatically determined.
- The proposed algorithm uses an additional layer of regularization in order to deal with the absence of spatial priors within sub-regions of the imaging domain.

The abstract of this paper is as follows, and then the remaining sections of this paper are presented.

Abstract. This paper presents a microwave imaging algorithm that can incorporate prior structural information, also known as spatial priors (SP), about the object being imaged to enhance the achievable image quantitative accuracy. This algorithm (i) is fully automated, and (ii) can work with both complete and partially-available structural information. The core idea of this imaging algorithm is to use a multiplicative regularization term to incorporate SP, and a second one to handle the lack of structural information in a given part of the imaging domain. This algorithm, which has been implemented for the two-dimensional transverse magnetic case, is evaluated against single-frequency and multiple-frequency synthetic and experimental microwave imaging data sets.

3.1 Introduction

Microwave imaging (MWI) can be used to create a quantitative image of the complex permittivity profile of an object of interest (OI). MWI is currently being investigated for several applications such as biomedical imaging and industrial monitoring applications, e.g., see [5, 7, 9, 13, 40]. In MWI, the OI is often surrounded by several antennas. Each antenna successively illuminates the OI with the remaining antennas collecting the emanating fields. The resulting scattered fields are then processed (inverted) by an inverse scattering algorithm to create (reconstruct) a quantitative complex permittivity image of the OI [41]. For successful imaging, electromagnetic waves need to sufficiently penetrate into the OI for effective interrogation of the OI. This requirement limits the maximum frequency of operation. (For example, frequencies around 1 to 2 GHz have been mainly considered for microwave breast imaging.) Subsequently, this maximum frequency constraint can limit the achievable spatial resolution. Therefore, inverse scattering algorithms (or, simply referred to as inversion algorithms herein) may not be able to reconstruct the complex permittivity of small regions (e.g., a small tumour) but instead may reconstruct an *effective* permittivity of a larger region enclosing that small region. This will ultimately make the diagnosis based on the complex permittivity value difficult.

To handle this challenge, it has been suggested that high-resolution *structural* information, also known as *spatial* information, can be first obtained from a high-resolution imaging modality, e.g., magnetic resonance imaging (MRI) and ultrasound tomography. This structural information, which divides the imaging domain into various regions with unknown complex permittivity values, can then be fed as prior information to microwave imaging algorithms so that the complex permittivity associated within each region can be more accurately reconstructed [22, 42–46]. In this paper, we refer to this structural prior information as prior spatial information or simply as *spatial priors* (SP). One way to incorporate these SP

into an inversion algorithm is to include them as a penalty term (regularization term) so that this penalty term favours similar complex permittivity values within each region in the optimization process [44, 45]. On the other hand, SP may also be incorporated into an inversion algorithm in other ways; e.g., in [47], the SP were utilized to create a numerical inhomogeneous background (instead of the actual background) for the microwave imaging problem. Then, the inversion algorithm iteratively builds upon this numerical background to converge to an appropriate complex permittivity image. In contrast to the penalty-term approach, the numerical background approach requires the user to assign initial complex permittivity values to each region of the SP to form this numerical background. In this paper, we use the penalty-term approach, and therefore, we do not require any prior information about the complex permittivity values. Thus, we always start our inversion with a trivial initial guess (zero dielectric contrast).

Inspired by the work presented in [45], we have recently developed a multiplicative regularized Gauss-Newton inversion algorithm that incorporates SP [48]. Our proposed algorithm has two important features. 1) It does not require the SP to be available over the whole imaging domain. That is, the proposed algorithm can handle *partially*-available SP. This can be useful for biomedical imaging applications where the SP may not be available in a subdomain which is suspicious to have a tumour. 2) Due to the multiplicative implementation of the SP penalty term, this algorithm is fully automated, and the user does not need to set any parameters such as the regularization weight. (This is important in *nonlinear* inversion algorithms as choosing an appropriate regularization weight can be quite challenging.) In this paper, we present this algorithm in details, and evaluate its performance against synthetic and experimental data sets. This paper is structured as follows. We start with a problem statement followed by a section motivating why the proposed approach is useful. We then present the mathematical formulation of our algorithm followed by a section on its synthetic and experimental evaluation, and finally present our conclusions. The time dependency of

$\exp(j\omega t)$ where $j^2 = -1$ is considered throughout this paper, and the implementation of the proposed algorithm is for the two-dimensional (2D) transverse magnetic (TM) case.[2]

3.2 Problem Statement

Assume we have (i) a set of microwave scattered field data collected from the illuminated imaging domain which can be either at a single frequency or at multiple frequencies, and (ii) a set of spatial priors (SP) which can either include spatial information about the whole imaging domain (referred to as *complete* SP), or include spatial information merely about a part of the imaging domain (referred to as *partial* SP). The goal is then to develop an automated electromagnetic inverse scattering algorithm that can benefit from these complete or partial spatial priors to reconstruct the complex permittivity profile of the imaging domain.

3.3 Motivation

Let us now motivate the utilization of complete and partial SP in MWI using a synthetic example. Consider the lossless OI (referred to as the "W" target) shown in Figure 3.1(a) at the frequency of 1 GHz. This OI consists of three small fingers mounted on a rectangular base with three different relative permittivities ϵ_r as 2.0, 3.0, and 4.0. (This object is lossless, and therefore the imaginary part of its complex permittivity profile is zero; i.e., $\text{Im}(\epsilon_r) = 0$.) The separation between two adjacent fingers is $\lambda_b/10$ where $\lambda_b = 0.3$ m is the wavelength in the background medium (air). We illuminate this OI with 32 transceivers, and invert the resulting scattered data using two different 'blind'[3] inversion algorithms: the multiplica-

[2] In the context of MWI, the 2D TM inversion is referred to imaging a cross section where the incident and scattered electric fields are assumed to be perpendicular to this cross section.

[3] In the context of this paper, 'blind' inversion algorithms refer to those algorithms that do not assume any specific prior information about the object being imaged. As will be seen later, we have used three blind

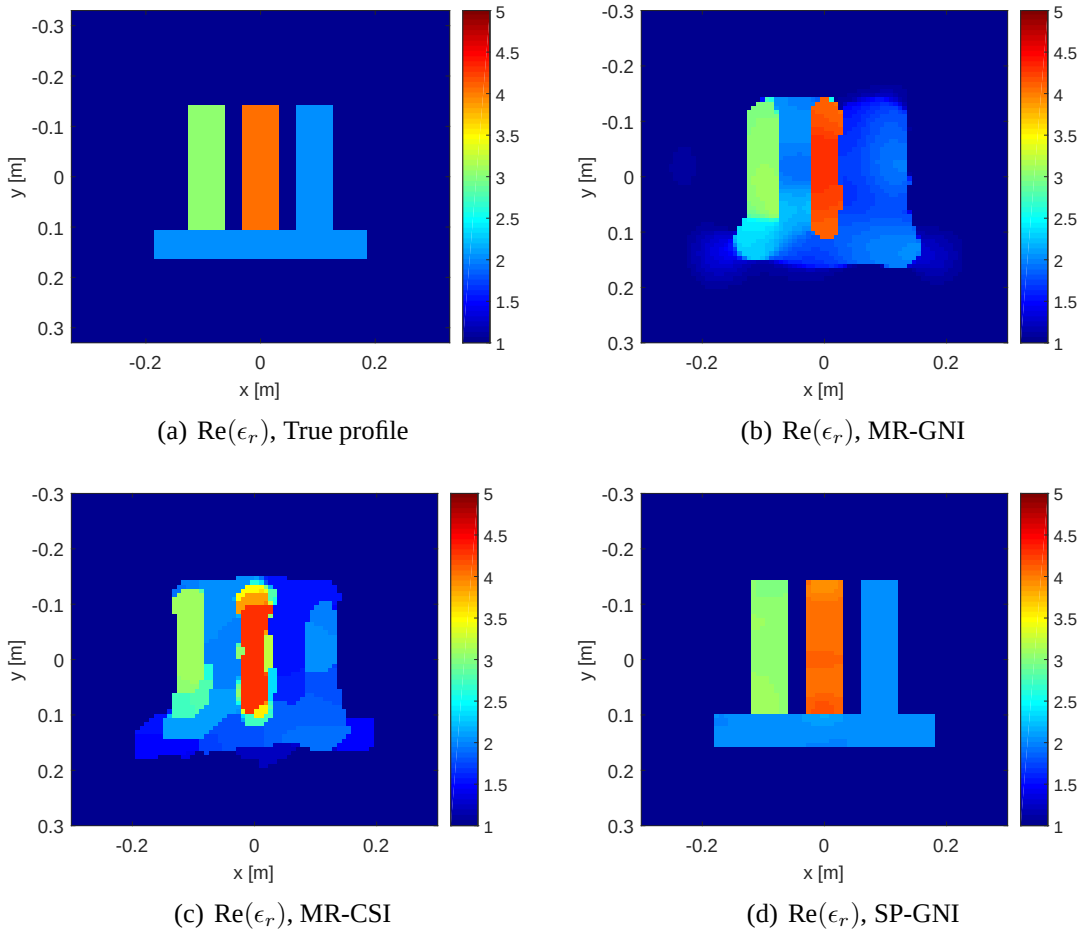

(a) Re(ϵ_r), True profile

(b) Re(ϵ_r), MR-GNI

(c) Re(ϵ_r), MR-CSI

(d) Re(ϵ_r), SP-GNI

Fig. 3.1: (a) The true relative permittivity profile of the lossless object of interest (OI), which is referred to as the "W" target (1st form). Its adjacent fingers are separated by $\lambda_b/10$ where λ_b is the wavelength in the background medium (air). The reconstructed images obtained by the (b) MR-GNI algorithm, (c) MR-CSI algorithm, and finally (d) the proposed algorithm (SP-GNI) when using the complete spatial priors (SP).

tive regularized Gauss-Newton inversion (MR-GNI) algorithm [2, 3] and the multiplicative regularized contrast source inversion (MR-CSI) algorithm [49, 50], with the reconstructed relative permittivity results shown in Figures 3.1(b) and (c) respectively. (The details of this study will be presented in Section 3.5.1.) As can be seen, due to the limited achievable spatial resolution, the relative permittivity values of these three fingers cannot be reconstructed well. Therefore, diagnosis based on the reconstructed permittivity values can be difficult. If

inversion algorithms in this paper: MR-GNI, MR-CSI, and Tikh-GNI algorithms.

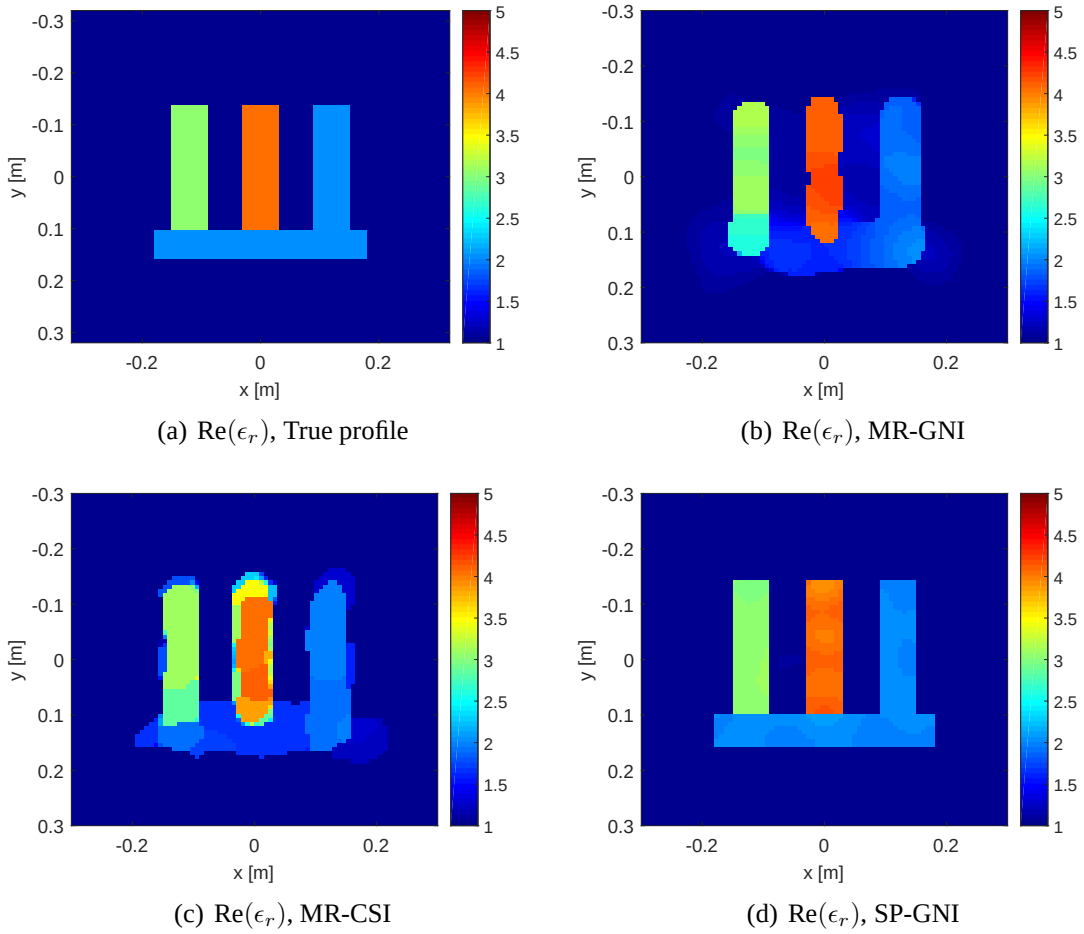

(a) Re(ϵ_r), True profile

(b) Re(ϵ_r), MR-GNI

(c) Re(ϵ_r), MR-CSI

(d) Re(ϵ_r), SP-GNI

Fig. 3.2: (a) The true relative permittivity profile of the lossless object of interest (OI), which is referred to as the "W" target (2nd form). Its adjacent fingers are now separated by $\lambda_b/5$. The reconstructed images obtained by the (b) MR-GNI algorithm, (c) MR-CSI algorithm, and finally (d) the proposed algorithm (SP-GNI) when using the complete spatial priors (SP).

we now utilize our proposed inversion algorithm with the complete SP, the image shown in Figure 3.1(d) is obtained which accurately reconstructs the relative permittivity values.

It is instructive to note that if the fingers are separated by $\lambda_b/5$ as shown in Figure 3.2(a) (as opposed to $\lambda_b/10$ in the previous case), the reconstruction results using the MR-GNI and MR-CSI algorithms (blind inversion algorithms) as well as the proposed algorithm become more similar as shown in Figures 3.2(b)-(d). Finally, let us consider a more difficult

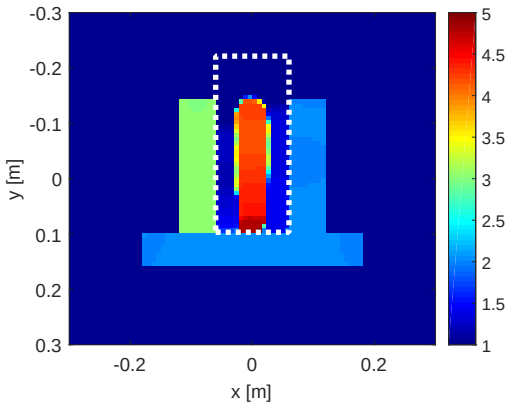

Fig. 3.3: Use of *partial* spatial priors (SP) to reconstruct the relative permittivity of the "W" target when the separation between the fingers is $\lambda_b/10$ (1st form). The white dotted rectangle has been superimposed on the reconstructed image to show the area in which we have no prior spatial information; i.e., the SP is assumed to be available everywhere *except* inside the white dashed box. (As will be seen later, the MRSP-GNI algorithm has been used to reconstruct this image.)

scenario where we have partial SP, which include structural information about the whole imaging domain *except* within the white dotted rectangle shown in Figure 3.3. The proposed algorithm can handle the partial SP, and yields the reconstructed relative permittivity shown in Figure 3.3. As can be seen, this algorithm, without having access to the SP in the white dotted rectangle, can successfully reconstruct the finger within this rectangle and can also reconstruct the relative permittivity values of the other two fingers. Furthermore, note that the utilized partial SP do not include any information about the separation between the fingers; however, the proposed algorithm is still able to reconstruct the separation between the fingers using the available partial SP.

3.4 Mathematical Formulation

Herein, we first review the fundamentals of the MR-GNI algorithm [35], [2, 3]. The reason for having this review is that the proposed algorithm is built upon the MR-GNI framework.

We then discuss the proposed SP multiplicative regularizer, using which we develop the so-called SP-GNI and MRSP-GNI algorithms.

3.4.1 Review: Data Misfit Cost Functional

The MWI problem is often cast as an optimization problem. The core of the optimization is the so-called data misfit cost functional, often defined as the L_2 norm discrepancy between the measured scattered data and the simulated scattered data due to a given contrast χ. The contrast χ is the *unknown* complex permittivity contrast profile defined as

$$\chi(\boldsymbol{r}) \triangleq \frac{\epsilon(\mathbf{r}) - \epsilon_b}{\epsilon_b}, \tag{3.1}$$

where $\mathbf{r}$ is the position vector in the imaging domain, $\epsilon(\mathbf{r})$ is the unknown relative complex permittivity of the OI, and ϵ_b is the known homogeneous relative complex permittivity of the background medium. Denoting the measured scattered data by E^{meas} and the simulated scattered data due to a contrast χ by $E^{\text{scat}}(\chi)$, the data misfit cost functional is defined as

$$\mathcal{C}^{\text{LS}}(\chi_n) = \eta \left\| E^{\text{meas}} - E^{\text{scat}}(\chi) \right\|^2, \tag{3.2}$$

where $\|.\|$ denotes the L_2 norm, and $\eta = (\|E^{\text{meas}}\|^2)^{-1}$ is the normalization factor. (In the above cost functional, the summation over the number of transceiver has been dropped for the simplicity of notation.)

3.4.2 Review: GNI Algorithm

In the Gauss-Newton inversion (GNI), the contrast is iteratively updated by minimizing the data misfit cost functional. At the nth iteration of the GNI algorithm, we update the contrast

as

$$\chi_{n+1} \;=\; \chi_n + \nu_n \Delta\chi_n, \tag{3.3}$$

where χ_n is the known estimate of the contrast profile available at the nth iteration, $\Delta\chi_n$ is the correction to be found, and ν_n is an appropriate step length.[4] The correction $\Delta\chi_n$ is found by solving

$$\mathbf{H}_n \Delta\chi_n = -g_n, \tag{3.4}$$

where $\mathbf{H}_n$ and g_n are the Hessian matrix and the gradient vector of the cost functional at the nth iteration of the algorithm respectively.[5] The Hessian matrix and the gradient vector at the nth iteration are calculated based on the Jacobian (sensitivity) matrix at the nth iteration which is often denoted by $\mathbf{J}_n$.[6] Then, (3.4) becomes

$$[\mathbf{J}_n^H \mathbf{J}_n]\Delta\chi_n = -\mathbf{J}_n^H d_n \tag{3.5}$$

where the superscript H denotes the Hermitian (complex conjugate transpose) operator, and the discrepancy vector d_n at the nth iteration is $d_n \;=\; E^{\text{scat}}(\chi_n) - E^{\text{meas}}$.

3.4.3 Review: MR-GNI Algorithm

It is known that (3.5) is ill-posed and needs to be regularized. To this end, the MR-GNI algorithm directly regularizes the data misfit cost functional using the so-called weighted L_2 norm total variation multiplicative regularizer [35], [2, 53, 54], which we refer to as MR in this paper. The MR is represented by the following cost functional which changes at each

[4] To determine an appropriate step length ν_n, we utilize the method presented in [51, Section. 6].

[5] In the calculation of $\mathbf{H}_n$, the second derivative of the scattered field with respect to χ, i.e., $\partial^2 E^{\text{scat}}/\partial\chi^2$, is neglected; thus, this algorithm is named GNI. See see [52, Appendix D.1] for the derivation of this second derivative.

[6] The Jacobian matrix represents the first derivative of the scattered field at the receivers with respect to the contrast, i.e., $\partial E^{\text{scat}}/\partial\chi$; for its derivation, see [52, Appendix D.1].

iteration of the algorithm (thus, having the subscript n)

$$\mathcal{C}_n^{\mathrm{MR}}(\chi) = \frac{1}{A}\int_D \frac{|\nabla\chi(\mathbf{r})|^2 + \delta_n^2}{|\nabla\chi_n(\mathbf{r})|^2 + \delta_n^2} d\mathbf{s} \tag{3.6}$$

where $\int_D$ is the integral over the imaging domain D, A is the area of the imaging domain, δ_n^2 is a steering parameter given in [2, 35, 53], and ∇ is the gradient operator. The data misfit cost functional is then regularized as

$$\mathcal{C}_n(\chi) = \mathcal{C}^{\mathrm{LS}}(\chi)\, \mathcal{C}_n^{\mathrm{MR}}(\chi). \tag{3.7}$$

Due to the presence of this MR, (3.5) will change into a regularized form as

$$[\mathbf{J}_n^H \mathbf{J}_n + \beta_n \mathcal{L}_n]\Delta\chi_n = -\mathbf{J}_n^H d_n - \beta_n \mathcal{L}_n \chi_n \tag{3.8}$$

where $\mathcal{L}_n$ and β_n are the resulting regularization operator and its weight at the nth iteration. The operator $\mathcal{L}_n$ when acting on a vector of appropriate size x is given by

$$\mathcal{L}_n x \triangleq -\frac{1}{A}\nabla \cdot [\frac{1}{|\nabla\chi_n(\mathbf{r})|^2 + \delta_n^2}\nabla x] \tag{3.9}$$

where '$\nabla\cdot$' is the divergence operator. In addition, the regularization weight is $\beta_n = \mathcal{C}^{\mathrm{LS}}(\chi_n)/\eta$. In summary, the two features of the MR-GNI algorithm are as follows. (i) The regularization operator $\mathcal{L}_n$ has both edge-preserving and smoothing properties. (ii) This algorithm is fully automated, e.g., the regularization weight β_n is automatically determined by the algorithm. (For more comparative discussions, see [54, 55].)

3.4.4 SP-GNI Algorithm

3.4.4.1 General Idea

Assume that there exist SP about the OI. Herein, we incorporate SP into the GNI algorithm using a multiplicative regularization term. Similarly to [45], our regularizer favours the equality of the complex permittivity values of the pixels (discretized cells) located in the same region. To better understand this, consider Figure 3.4 where three regions (purple, pink, and yellow regions) are shown in a 3×3 discretized imaging domain with each cell representing a contrast value (χ_1 to χ_9). In the same figure, consider the system of equations $\mathbf{A}\chi = \mathbf{0}$ where its first row simply enforces χ_1 and χ_4 to have the same value through $\chi_1 - \chi_4 = 0$. Similarly, the other rows establish the equality between complex permittivity values in the other two regions (pink and yellow). It is, therefore, clear that minimizing $\|\mathbf{A}\chi\|^2$ in conjunction with the data misfit cost functional, and assuming an appropriate relative (regularization) weight, can take into account the SP in the inversion process [45].

3.4.4.2 Multiplicative Implementation

Herein, we incorporate SP in the form of a multiplicative regularization term, and therefore minimize

$$\mathcal{C}_n(\chi) = \mathcal{C}^{\mathrm{LS}}(\chi)\, \mathcal{C}_n^{\mathrm{SP}}(\chi), \tag{3.10}$$

where the SP multiplicative regularization at the nth iteration of the GNI algorithm is given as

$$\mathcal{C}_n^{\mathrm{SP}}(\chi) = \frac{\|p \odot (\mathbf{A}\chi)\|^2 + \gamma_n^2}{\|p \odot (\mathbf{A}\chi_n)\|^2 + \gamma_n^2}. \tag{3.11}$$

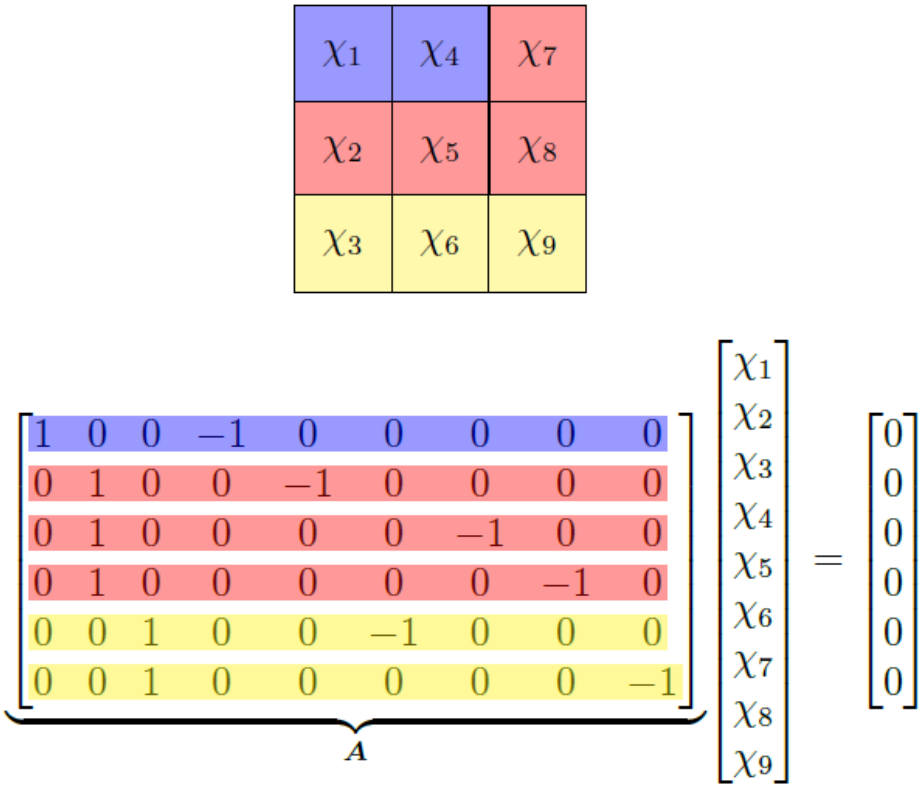

Fig. 3.4: (Top) A 3×3 discretized imaging domain consisting of three spatial regions: purple, pink, and yellow. (Bottom) A matrix equation, $\mathbf{A}\chi = \mathbf{0}$ that enforces the equality of the contrast values located in the same region. The color of each row is the same as the color of the corresponding region. For example, the first row of this matrix (the purple row) enforces the equality of χ_1 and χ_4 in the purple region.

In this SP cost functional, γ_n^2 is a steering parameter, and p is a confidence vector with elements between 0 and 1 (i.e., $0 \leq p_i \leq 1$) that represents our confidence level regarding SP at different parts of the imaging domain. (The choice of γ_n^2 and p will be discussed later.) In addition, the operator $\odot$ is the Hadamard product which represents the element-wise multiplication of the corresponding elements of two vectors of the same length. With the use of this SP regularization term, (3.5) will change into the following regularized form

$$[\mathbf{J}_n^H \mathbf{J}_n + \beta_n \mathcal{S}_n]\Delta\chi_n = -\mathbf{J}_n^H d_n - \beta_n \mathcal{S}_n \chi_n \tag{3.12}$$

The regularization operator at the nth iteration of the algorithm is then $\mathcal{S}_n$. This operator when acting on a vector of appropriate size, e.g., the vector x, is defined as

$$\mathcal{S}_n x \triangleq \big[\frac{1}{\|p \odot (\mathbf{A}\chi_n)\|^2 + \gamma_n^2}\big]\mathbf{A}^H(p \odot (p \odot (\mathbf{A}x))). \tag{3.13}$$

As can be seen, due to the multiplicative implementation of this SP, the regularization weight at the nth iteration is automatically set to $\beta_n = \mathcal{C}^{\text{LS}}(\chi_n)/\eta$. We refer to this algorithm as the SP-GNI algorithm in this paper.

3.4.4.3 Justification

Let us now justify why minimizing (3.10) can take into account the SP. For simplicity, consider that we have full confidence about the SP in the whole imaging domain (i.e., assume p is a vector of ones). Then, it can be shown that minimizing (3.10) using the GNI algorithm is the same as minimizing the following cost functional

$$\mathcal{C}_n(\chi) = \mathcal{C}^{\text{LS}}(\chi) + \tau_n \|\mathbf{A}\chi\|^2 \tag{3.14}$$

where the weight τ_n will be

$$\tau_n = \frac{\eta\beta_n}{\|\mathbf{A}\chi_n\|^2 + \gamma_n^2}. \tag{3.15}$$

Noting that minimizing $\|\mathbf{A}\chi\|^2$ is equivalent to enforcing the SP, it can be seen that (3.14) enforces both the data misfit cost functional and the SP. In addition, noting that minimizing (3.10) is equivalent to (3.14), we can conclude that our proposed SP-GNI algorithm enforces both the measured scattered data and the SP.

3.4.4.4 Parameters

There is one positive real parameter in the SP regularizer that needs to be set, i.e., γ_n^2. To set up this parameter, we follow a similar approach as used in the choice of δ_n^2 in (3.6). As noted in [2, 35, 53, 54], δ_n^2 is chosen to be $\mathcal{C}^{\text{LS}}(\chi_n)/(\Delta x \Delta y)$ where $\Delta x \Delta y$ is the area of a discretized cell in the imaging domain lying in the xy plane. The presence of $\mathcal{C}^{\text{LS}}(\chi_n)$ in this expression results in having smaller δ_n^2 values as the inversion algorithm gets closer to the solution. The presence of $\Delta x \Delta y$ in the denominator of δ_n^2 can be justified by noting that δ_n^2 should be added to $|\nabla \chi_n|^2$, see (3.6). The calculation of $\nabla \chi_n$ requires one division by Δx in the $\hat{x}$ direction, and another one by Δy in the $\hat{y}$ direction. Based on this observation δ_n^2 is chosen to have the $\Delta x \Delta y$ component in its denominator to be somehow consistent with $|\nabla \chi_n|^2$. Similar to the above, we choose γ_n^2 to be $\mathcal{C}^{\text{LS}}(\chi_n)\, \ell$ where ℓ is the length of the contrast vector χ. Note that γ_n^2 should be added to $\|p \odot (\mathbf{A}\chi_n)\|^2$ as opposed to $|\nabla \chi_n|^2$. Since this norm value is somehow related to the length of the vector χ_n, we have decided to include ℓ in the expression of γ_n^2. (Compared to our conference paper on this topic [48], we have changed the choice of γ_n^2.) In addition, as noted earlier, the vector p is chosen to represent the confidence vector corresponding to different regions of SP. In this paper, the elements of the vector p have been chosen to be either zero (no SP at a particular region), or 1.[7]

3.4.5 MRSP-GNI Algorithm

If SP regarding a sub-region within the imaging domain is not available, the SP regularizer $\mathcal{S}_n$ will not be applied to that sub-region, leaving that part of the imaging domain un-

[7] Based on our numerical evaluations not presented in this paper, some non-zero choices of p (e.g., $p_i = 0.5$) have had similar performance as $p_i = 1$. We speculate that this is due to the presence of the same p vector in the numerator and denominator of the operator $\mathcal{S}_n$.

regularized. Thus, the inversion algorithm may yield un-reliable (unstable) results. This can be better understood in the extreme case of not having any reliable prior spatial information. In this case, p will be a zero vector, and therefore $\mathcal{C}_n^{\text{SP}}(\chi)$ reduces to 1, and $\mathcal{C}_n(\chi)$ in (3.10) becomes equal to $\mathcal{C}^{\text{LS}}(\chi)$. Thus, we again arrive at our un-regularized cost functional. This demonstrates the weakness of the SP-GNI algorithm, and other similar algorithms, when we do not have access to SP over the whole imaging domain.

3.4.5.1 Approach

To enable the SP-GNI algorithm to handle *partial* SP, we propose to use a second layer of regularization in conjunction with the SP regularization term.[8] To this end, we minimize

$$\mathcal{C}_n(\chi) = \mathcal{C}^{\text{LS}}(\chi)\, \mathcal{C}_n^{\text{MR}}(\chi)\, \mathcal{C}_n^{\text{SP}}(\chi). \tag{3.16}$$

Then, (3.12) will become

$$\begin{aligned}[\mathbf{J}_n^H \mathbf{J}_n + \beta_n \mathcal{L}_n + \beta_n \mathcal{S}_n]\Delta\chi_n = \\ - \mathbf{J}_n^H d_n - \beta_n \mathcal{L}_n \chi_n - \beta_n \mathcal{S}_n \chi_n.\end{aligned} \tag{3.17}$$

As can be seen, we now have two regularization operators: $\mathcal{L}_n$ defined in (3.9) and $\mathcal{S}_n$ defined in (3.13). It is instructive to note that if we have no SP at all, p will be a zero vector, which makes $\mathcal{S}_n$ a zero operator; therefore, (3.17) will turn into (3.8), which is still properly regularized due to the presence of $\mathcal{L}_n$.

[8] The idea of using a second layer of regularization has also been utilized with another type of prior information: when the prior information is the complex permittivity values of the OI, and the objective is to reconstruct the geometrical shape of the OI [56]. This type of inversion algorithms is often referred to as shape and location reconstruction.

3.4.6 Multiple-Frequency MRSP-GNI Algorithm

To develop the MRSP-GNI for *simultaneous* multiple-frequency inversion[9], we first need to consider our assumption regarding how complex permittivity values change with respect to the frequency. We consider the complex permittivity at the frequency of f to be in the form of $\epsilon = \epsilon_r - j\frac{\sigma}{2\pi f \epsilon_0}$ where the real-valued ϵ_r and σ (conductivity) are assumed to be constant with respect to f within the frequency bandwidth of interest. Based on this assumption which was also used in [58], within the frequency bandwidth of operation, the real part of the complex permittivity does not change with respect to the frequency whereas its imaginary part does. (This is a simple model; more accurate models such as the Debye model are also available [29].) To be able to incorporate the variation of the complex permittivities of the OI and the background medium with respect to f, our multiple-frequency MRSP-GNI algorithm performs the optimization with respect to the real and imaginary parts of χ, denoted by χ_R and χ_I respectively. Furthermore, since based on the above complex permittivity model, the contrast profiles at different frequencies are related, we can formulate the cost functional merely based on $\chi_{R,(1)}$ and $\chi_{I,(1)}$ which denote the real and imaginary parts of the contrast at the lowest frequency f_1. To this end, we need to be able to calculate the derivative of the scattered field at the kth frequency with respect to $\chi_{R,(1)}$ and $\chi_{I,(1)}$. This can be done using the chain rule by the frequency-dependent coefficients $\xi_{(k)}$ and $\zeta_{(k)}$ as

$$\begin{aligned}
\frac{\partial E_k^{\text{scat}}}{\partial \chi_{R,(1)}} &= \xi_{(k)} \frac{\partial E_k^{\text{scat}}}{\partial \chi_{R,(k)}}, \text{ where } \xi_{(k)} = \frac{\epsilon_b'^2 + \epsilon_b''^2}{\epsilon_b'^2 + (\frac{f_1}{f_k})^2 \epsilon_b''^2} \\
\frac{\partial E_k^{\text{scat}}}{\partial \chi_{I,(1)}} &= \zeta_{(k)} \frac{\partial E_k^{\text{scat}}}{\partial \chi_{I,(k)}}, \text{ where } \zeta_{(k)} = \frac{f_1}{f_k} \xi_{(k)}
\end{aligned} \tag{3.18}$$

[9] In contrast to the frequency hopping technique [57] in which the inversion at a single lower frequency is used as an initial guess for the inversion of the next higher frequency data set, the simultaneous inversion approach inverts the whole multiple frequency data set together. Based on our experience, simultaneous frequency inversion often outperforms frequency hopping inversion.

where the relative complex permittivity of the background medium at f_1 is denoted by $\epsilon_b = \epsilon_b' - j\epsilon_b''$ where $\epsilon_b'' = \frac{\sigma_b}{2\pi f_1 \epsilon_0}$.

Herein, for the simplicity of notation, we refer to $\chi_{R,(1)}$ and $\chi_{I,(1)}$ as χ_R and χ_I. Therefore, we can use the same cost functional as (3.16) but replace the data misfit cost functional with its multiple-frequency form as

$$\mathcal{C}^{\text{LS}}(\chi_R, \chi_I) \triangleq \sum_{k=1}^{K} \alpha_{(k)} \left\| E_{(k)}^{\text{meas}} - E_{(k)}^{\text{scat}} \right\|^2 \tag{3.19}$$

where k denotes the frequency index with the total number of frequencies set to K. Similar to [35], the normalization factor $\alpha_{(k)}$ is chosen to be

$$\alpha_{(k)} = \frac{1}{\left\| E_{(k)}^{\text{meas}} \right\|^2} \frac{f_k^{-2}}{\sum_{s=1}^{K} f_s^{-2}}. \tag{3.20}$$

The real and imaginary parts of the contrast at the nth iteration are updated by applying the correction $\Delta\chi_{R,n}$ and $\Delta\chi_{I,n}$.[10] These corrections are found by solving

$$\begin{bmatrix} \mathbf{H}_{11,n} & \mathbf{H}_{12,n} \\ \mathbf{H}_{21,n} & \mathbf{H}_{22,n} \end{bmatrix} \begin{bmatrix} \Delta\chi_{R,n} \\ \Delta\chi_{I,n} \end{bmatrix} = - \begin{bmatrix} g_{1,n} \\ g_{2,n} \end{bmatrix} \tag{3.21}$$

[10] Note that the subscript n which does not have parentheses is for the GNI iteration number. On the other hand, the subscript (k) with parentheses, which has been dropped for the simplicity of notation, is for the frequency index.

where the block Hessian matrices can be found as[11]

$$\begin{aligned}
\mathbf{H}_{11,n} &= \Big[\sum_{k=1}^{K} \alpha_{(k)}\xi_{(k)}^2 \mathrm{Re}\big[\mathbf{J}_{n,(k)}^H \mathbf{J}_{n,(k)}\big]\Big] + \beta_n \mathcal{L}_n + \beta_n \mathcal{S}_n \\
\mathbf{H}_{12,n} &= -\sum_{k=1}^{K} \alpha_{(k)}\xi_{(k)}\zeta_{(k)} \mathrm{Im}\big[\mathbf{J}_{n,(k)}^H \mathbf{J}_{n,(k)}\big] \\
\mathbf{H}_{21,n} &= \sum_{k=1}^{K} \alpha_{(k)}\xi_{(k)}\zeta_{(k)} \mathrm{Im}\big[\mathbf{J}_{n,(k)}^H \mathbf{J}_{n,(k)}\big] \\
\mathbf{H}_{22,n} &= \Big[\sum_{k=1}^{K} \alpha_{(k)}\zeta_{(k)}^2 \mathrm{Re}\big[\mathbf{J}_{n,(k)}^H \mathbf{J}_{n,(k)}\big]\Big] + \beta_n \mathcal{L}_n + \beta_n \mathcal{S}_n.
\end{aligned} \tag{3.22}$$

In addition, the two concatenated gradient vectors in (3.21) are

$$\begin{aligned}
g_{1,n} &= \Big[\sum_{k=1}^{K} \alpha_{(k)}\xi_{(k)} \mathrm{Re}\big[\mathbf{J}_{n,(k)}^H d_{n,(k)}\big]\Big] + \mathcal{L}_n \chi_{R,n} + \mathcal{S}_n \chi_{R,n} \\
g_{2,n} &= \Big[\sum_{k=1}^{K} \alpha_{(k)}\zeta_{(k)} \mathrm{Im}\big[\mathbf{J}_{n,(k)}^H d_{n,(k)}\big]\Big] + \mathcal{L}_n \chi_{I,n} + \mathcal{S}_n \chi_{I,n}
\end{aligned} \tag{3.23}$$

where the frequency-dependent discrepancy vector $d_{n,(k)}$ is the same as d_n in Section 3.4.2 which is evaluated at the kth frequency.

3.5 Results and Discussion

Herein, we evaluate the proposed SP-GNI and MRSP-GNI algorithms for two synthetic examples and an experimental one[12]. These evaluations are performed for complete and partial SP. To be able to better understand the advantages of using SP, all these data sets are also inverted with no prior information (using 'blind' inversion algorithms such as the

[11] For the derivation of the Hessian matrix for the single-frequency data misfit cost functional with respect to the real and imaginary parts of the contrast, see the Appendix in [59].

[12] The performance of these algorithms have been studied for the experimental forearm data set as well, see Appendix D). As this study was preliminary we did not include them in the main body of the thesis.

MR-GNI algorithm). For all the synthetic test cases, SP are generated on the same grid as the imaging grid, which is different than the grid used to generate the synthetic data to be inverted. Finally, as noted in Section 3.4.4, for all the inversion using SP, the elements of the vector p are set to be either 1 or 0.

3.5.1 Synthetic Example: "W" Target

This is the same example considered in Section 3.3. Herein, we provide details on how the inversion was performed. At 1 GHz, the "W" target is interrogated by 32 transceivers (line sources) which are placed on a circle having a radius of $2\lambda_b$, where λ_b is the wavelength in the background medium. (The centre of this measurement circle is at the centre of the imaging domain.) When one antenna transmits, the remaining antennas receive, thus collecting $32 \times 31 = 992$ complex data points. This scattered data set was created using a method of moments (MoM) solver where the OI was placed in a 66×66 cm^2 domain discretized into 91×91 square cells. Once the data set is created, we added 3% noise to it according to the formula presented in [38]. For all the inversion algorithms, the imaging domain is chosen to be a 60×60 cm^2 domain discretized into 80×80 square cells. As described in Section 3.3, we consider two forms of this "W" target. (i) In the first form, which is shown in Figure 3.1(a), the separation between the adjacent fingers is set to $\lambda_b/10$. (ii) In the second form, we have increased the separation to $\lambda_b/5$ as shown in Figure 3.2(a).

3.5.1.1 Inversion with No Prior Information

As described in Section 3.3, the MR-GNI and MR-CSI algorithms suffer from limited achievable resolution for the first form of the target, but perform well for its second form where the separation between the fingers are doubled: compared Figure 3.1(b)-c with Fig-

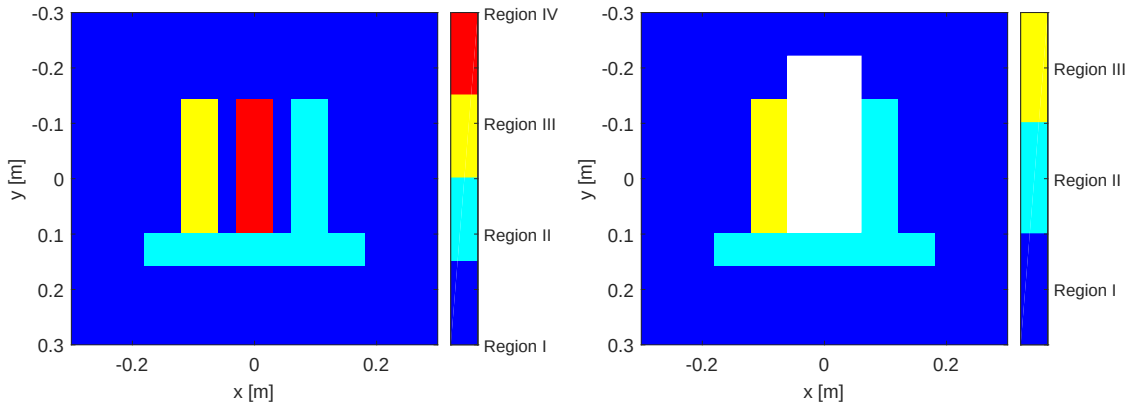

(a) Complete spatial priors (SP) (b) Partial spatial priors (SP)

Fig. 3.5: (a) Complete spatial priors (SP) for the "W" target (first form) depicting four regions within the imaging domain. (b) Partial spatial priors for the "W" target (first form) where no spatial priors are available within the white box. Note that the number of regions in the partial SP has now been decreased from four to three.

ure 3.2(b)-(c). Note that we have only shown the reconstructed real parts of the reconstructed complex permittivity. The reconstructed imaginary parts are small, and thus are not shown here for brevity.

3.5.1.2 Inversion with the Complete SP

The complete SP for the first form of this target is shown in Figure 3.5(a). As can be seen, the SP identify four regions tagged by Regions I to IV in the image colorbar without making any assumptions about their complex permittivity values. The SP-GNI algorithm then takes these SP, and reconstructs the quantitative relative permittivities as shown in Figure 3.1(d). Similarly, the SP for the second form of this target is created (not shown here) and fed to the SP-GNI algorithm with the reconstruction result shown in Figure 3.2(d). As expected, the SP is enforced successfully, and the reconstructed relative permittivity values are more accurate than the blind inversion results considered above. We have also used the complete SP with the MRSP-GNI algorithm, which resulted in similar reconstructions as the SP-GNI

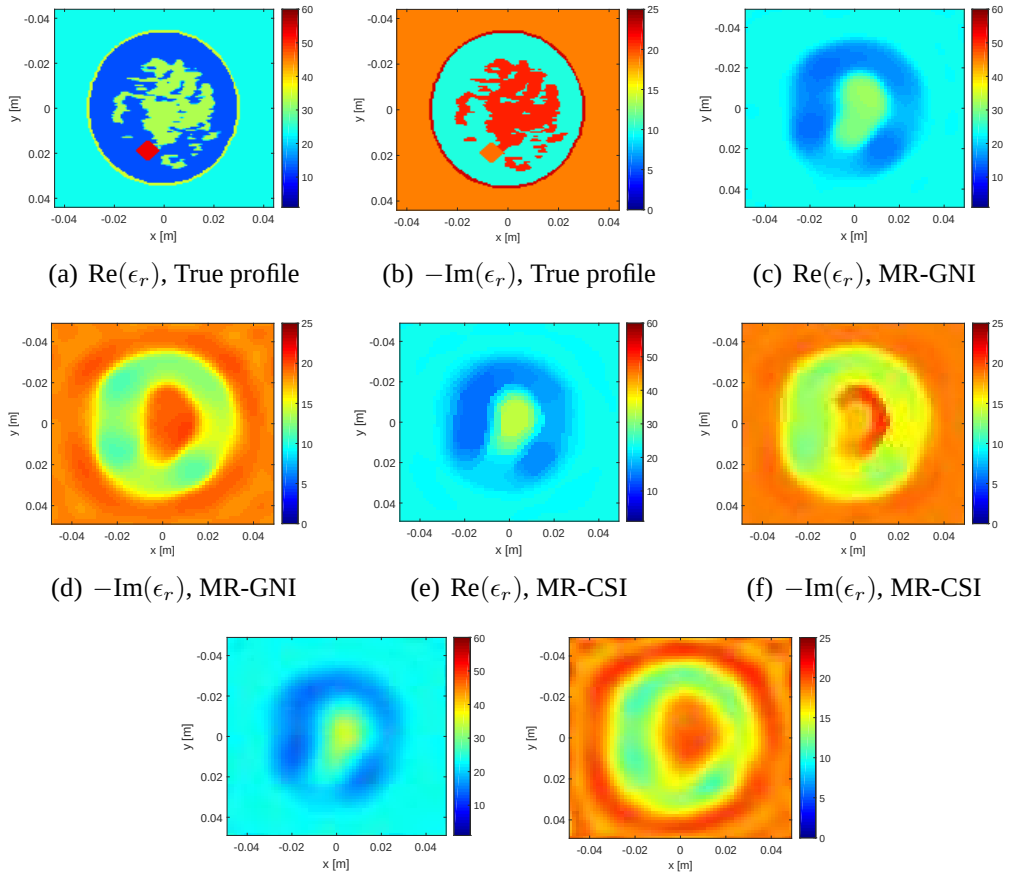

(a) Re(ϵ_r), True profile (b) $-$Im(ϵ_r), True profile (c) Re(ϵ_r), MR-GNI

(d) $-$Im(ϵ_r), MR-GNI (e) Re(ϵ_r), MR-CSI (f) $-$Im(ϵ_r), MR-CSI

(g) Re(ϵ_r), Tikh-GNI (h) $-$Im(ϵ_r), Tikh-GNI

Fig. 3.6: (a)-(b) True real and imaginary parts of the relative complex permittivity of the numerical breast model at 1.1 GHz. (The tumour has a diameter of approximately $0.15\lambda_b$ and has been assigned a relative complex permittivity of the $53.4 - j18.8$.) Single-frequency blind inversion results obtained using the (c)-(d) MR-GNI algorithms, (e)-(f) MR-CSI algorithm, and finally (g)-(h) Tikh-GNI algorithm.

algorithm, and thus are not shown here.

3.5.1.3 Inversion with the Partial SP

Finally, we evaluate the performance of the algorithm for the first form of the target (i.e., $\lambda_b/10$ separation between the adjacent fingers) when we have only access to *partial* SP. The partial SP to be used are shown in Figure 3.5(b) where the *white box* shows the region

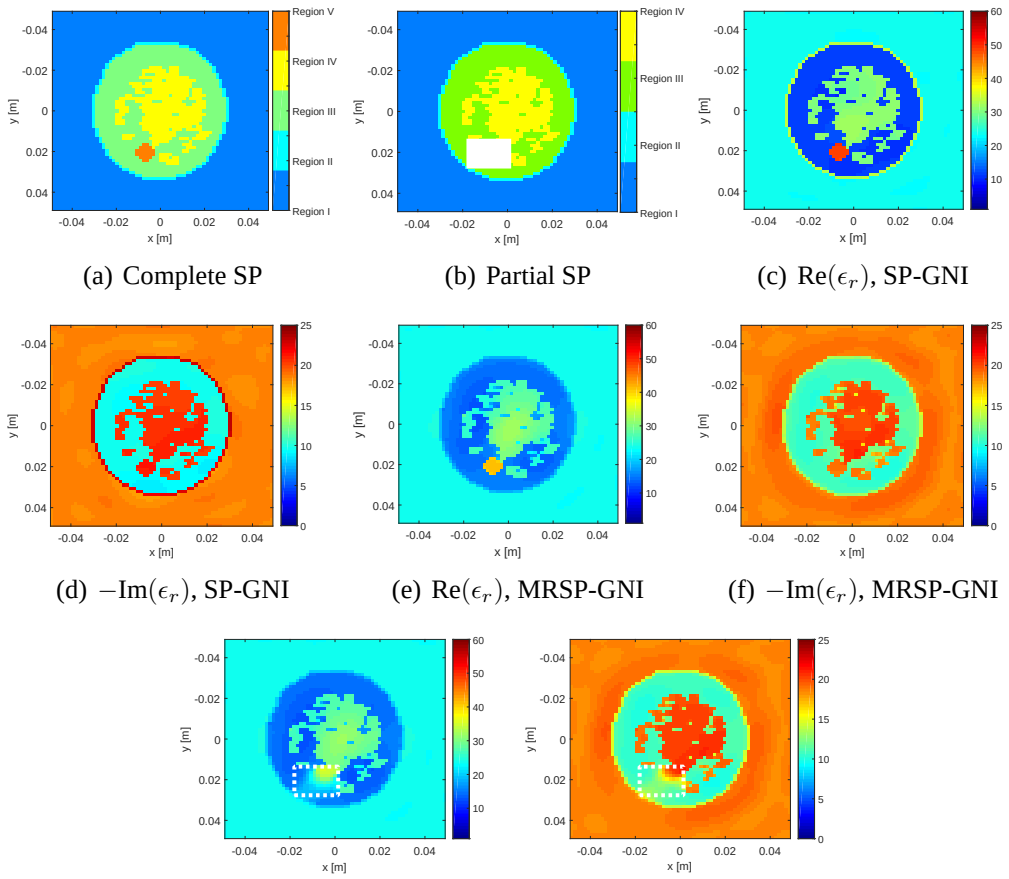

(a) Complete SP (b) Partial SP (c) Re(ϵ_r), SP-GNI

(d) $-$Im(ϵ_r), SP-GNI (e) Re(ϵ_r), MRSP-GNI (f) $-$Im(ϵ_r), MRSP-GNI

(g) Re(ϵ_r), MRSP-GNI (Partial SP) (h) $-$Im(ϵ_r), MRSP-GNI (Partial SP)

Fig. 3.7: (a) The complete spatial priors (SP) for the breast model showing the existence of five regions within the imaging domain. (b) The partial SP with the white box showing the region in which there are no spatial priors. Single-frequency (1.1 GHz) inversion: the reconstructed real and imaginary parts using the (c)-(d) SP-GNI with the complete SP, (e)-(f) MRSP-GNI algorithm with the complete SP, and finally (g)-(h) MRSP-GNI algorithm with the partial SP. (The dashed white lines indicate the region in which there are no SP available.)

in which we do not have any prior spatial information. As can be seen by comparing the colorbar of the partial SP with that of the complete SP (Figure 3.5(b) vs Figure 3.5(a)), the partial SP includes only three regions as opposed to four regions. As expected, the SP-GNI cannot successfully handle this scenario due to the absence of regularization for the pixels located within the white box (not shown here). On the other hand, the MRSP-GNI successfully handles the partial SP with its reconstruction shown in Figure 3.3 where we

Tab. 3.1: The relative complex permittivity of the breast model at 1.1 GHz according to [40] where the relative complex permittivity is denoted by $\epsilon_r = \epsilon' - j\epsilon''$.

Tissue	ϵ' **(real part)**	ϵ'' **(imaginary part)**
Background	23.3	-18.46
Skin	35.0	-23.00
Fat	12.6	-10.13
Fibro	32.7	-20.92
Tumor	53.4	-18.80

have used dashed white lines to indicate the domain in which there were no SP available. It is worthwhile to remind that the reason behind the success of the MRSP-GNI algorithm in handling the partial SP lies in its use of two layers of regularization.

3.5.1.4 Inversion with imperfect SP

In addition to the complete and partial SP, we have tested the sensitivity of our proposed algorithm with respect to imperfect SP. See Appendix B for more details.

3.5.2 Synthetic Example: Numerical Breast Phantom

The OI is a transverse cross section of a MRI-derived numerical breast phantom provided by the University of Wisconsin Cross-Disciplinary Electromagnetics Laboratory (UWCEM) [60, 61]. The real and imaginary parts of the true numerical breast model at 1.1 GHz are shown in Figures 3.6(a)-(b) respectively. (We have used MATLAB function *interpn* to reduce the resolution of this model.) As can be seen, this phantom consists of skin, fat, tumour, and fibroglandular tissues. The assigned complex permittivity values for each tissue type at 1.1 GHz are listed in Table 3.1. To generate the synthetic scattered data to be inverted, we have created the breast model on a 8.8×8.8 cm^2 domain discretized into a 142×142 grid. The breast model was irradiated by 36 transceivers located on a circle of radius 12 cm, thus,

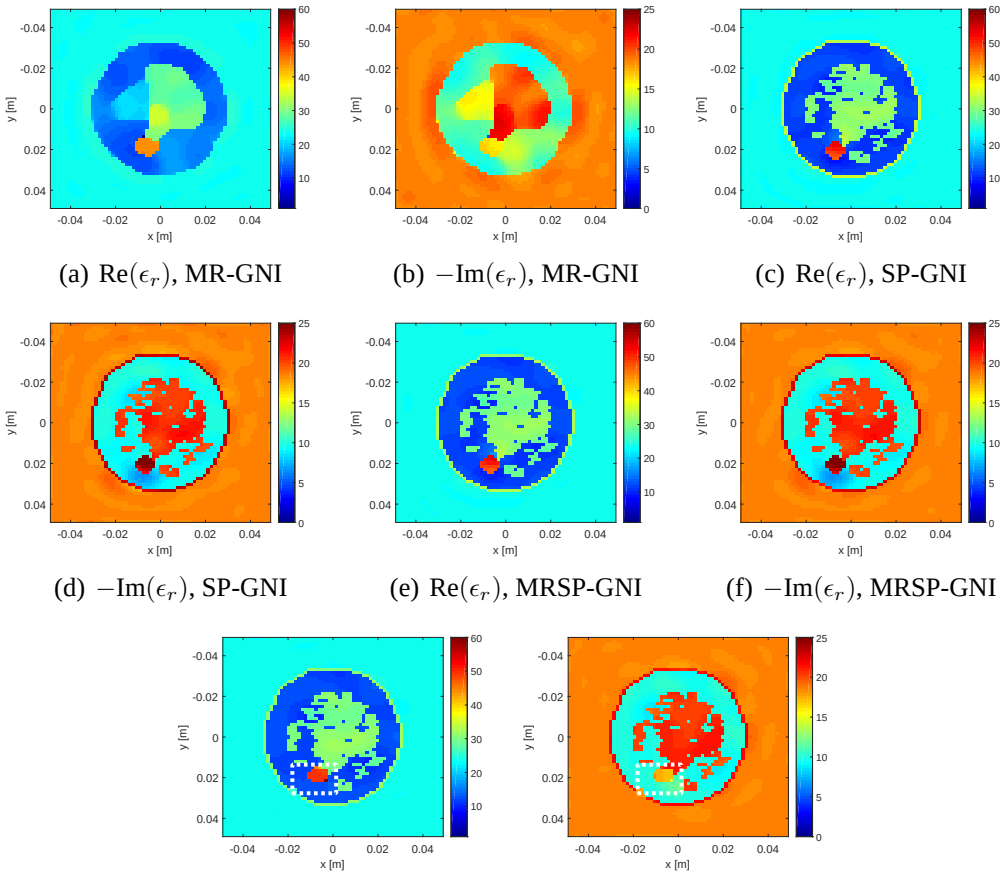

(a) Re(ϵ_r), MR-GNI (b) $-$Im(ϵ_r), MR-GNI (c) Re(ϵ_r), SP-GNI

(d) $-$Im(ϵ_r), SP-GNI (e) Re(ϵ_r), MRSP-GNI (f) $-$Im(ϵ_r), MRSP-GNI

(g) Re(ϵ_r), MRSP-GNI (Partial SP) (h) $-$Im(ϵ_r), MRSP-GNI (Partial SP)

Fig. 3.8: Multiple-frequency inversion (at 1.1, 1.5 and 2 GHz). Reconstructed real and imaginary parts using the (a)-(b) MR-GNI algorithm (blind inversion), (c)-(d) SP-GNI algorithm with the complete SP, (e)-(f) MRSP-GNI algorithm with the complete SP, and finally (g)-(h) MRSP-GNI algorithm with the partial SP. (The dashed white lines indicate the region in which there are no SP available.)

having $36 \times 35 = 1260$ complex data points at a single frequency. Similar to the previous case, the synthetic data is generated by an MoM solver at 1.1 GHz with 3% noise added to the data. For all cases, the inversion is performed on a 9.8×9.8 cm^2 domain discretized into a 65×65 grid.

3.5.2.1 Inversion with No Prior Information

We first invert this data set using the MR-GNI and MR-CSI algorithms that do not use any prior spatial information. These blind reconstruction results are shown in Figures 3.6(c)-(f). As can be seen, the tumour cannot be resolved at this frequency. (Note that that diameter of the tumor is about $0.15\lambda_b$ where λ_b is the wavelength in the background medium at 1.1 GHz.) To further investigate the inversion of this data set without any prior spatial information, we invert it by the GNI algorithm using Tikhonov regularization, which we refer to as *Tikh-GNI* algorithm. (For the details regarding the implementation of our Tikh-GNI algorithm, see Appendix C.) The reconstruction result using the Tikh-GNI algorithm, shown in Figures 3.6(g)-(h), is consistent with the MR-GNI and MR-CSI results, and is incapable of resolving the tumour.

3.5.2.2 Inversion with the Complete SP

The complete SP regarding this breast model is shown in Figure 3.7(a). The inversion of this data set in conjunction with this complete SP has been shown using the SP-GNI and MRSP-GNI algorithms in Figure 3.7(c)-(f). As can be seen, both the SP-GNI and MRSP-GNI provide more accurate reconstruction of the complex permittivity values of the breast model compared to the blind inversion algorithms considered above. Furthermore, the SP-GNI algorithm provides more accurate complex permittivity reconstruction than the MRSP-GNI: the reconstructed complex permittivity of the tumour is about $48.64 - j21.15$ using the SP-GNI, and is about $40.93 - j18.92$ using the MRSP-GNI algorithm. In addition, the skin layer is visible in the SP-GNI reconstruction whereas it is not in the MRSP-GNI reconstruction. The outperformance of the SP-GNI algorithm compared to the MRSP-GNI algorithm is due to the fact that the MRSP-GNI algorithm is using two layers of regularization which work

together to reconstruct the OI. However, in this case, the use of the second layer of regularization is not needed since we have access to the complete SP. To better understand this, we need to recall that the second layer of regularization is a generic MR that has smoothing (Laplacian operator), and edge-preserving properties. Therefore, the smoothing property of this extra regularization might result in losing the skin layer in the reconstruction, and/or smoothing out the tumour into the fibroglandular tissues. This can be seen by comparing the real part reconstruction using the SP-GNI, shown in Figure 3.7(c), with that using the MRSP-GNI, shown in Figure 3.7(e).

3.5.2.3 Inversion with the Partial SP

Let us assume that we know the SP everywhere except in an area around the tumour, which has been shown with a white rectangular box in Figure 3.7(b). As we already noted, the SP-GNI algorithm cannot handle this case since it cannot apply any regularization scheme for the cells inside the white box. Therefore, for this case, we use the MRSP-GNI which is equipped with two regularization schemes. The reconstruction using the MRSP-GNI for the partial SP has been shown in Figure 3.7(g)-(h). In this figure, we have identified the region in which we have no SP with a dashed white rectangle. Although the MRSP-GNI cannot reconstruct the complex permittivity value of the tumour in this region, it is still capable of yielding a stable reconstruction.

3.5.2.4 Multiple-Frequency Inversion with No Prior Information

In order to improve the accuracy of the reconstructed image, we now consider multiple-frequency inversion at the following three frequencies: 1.1 GHz, 1.5 GHz and 2 GHz. Similar to the previous cases, we first invert this multiple-frequency data set without us-

ing any spatial prior information with the result shown in Figures 3.8(a)-(b). Comparison of this multiple-frequency reconstruction with its single-frequency counterparts, e.g., see Figure 3.6(c)-(d), clearly demonstrates the improvement of achievable resolution and quantitative accuracy due to the incorporation higher frequency scattering data. (Note that the frequency of operation is still not high enough to be able to reconstruct the geometrical details of fibroglandular tissues.)

3.5.2.5 Multiple-Frequency Inversion with the Complete SP

Using the complete SP shown in Figure 3.7(a), the SP-GNI and MRSP-GNI algorithms result in the reconstructions shown in Figure 3.8(c)-(f). As expected, the structural information are now utilized, and also the overall quantitative accuracy is reasonable. The reconstructed complex permittivity of the tumour using the SP-GNI and MRSP-GNI algorithms are about $48.86 - j24.26$ and $48.38 - j24.49$ respectively; thus, the reconstructed permittivity has an undershoot in the real part and an overshoot in the imaginary part. On the other hand, the reconstructed complex permittivity of the tumour using the MR-GNI algorithm considered above was about $44.29 - j16.35$ (undershoot in both real and imaginary parts). As can be seen, since the scattered data contained high-frequency information, all of these reconstructions have resulted in reasonable quantitative accuracy.[13]

3.5.2.6 Multiple-Frequency Inversion with the Partial SP

We again consider the partial SP shown in Figure 3.7(b) where there are no spatial information in the white box. (The white box encloses the tumour.) The SP-GNI algorithm cannot

[13] The overshoot and undershoot in the reconstructed permittivity can be related to the regularization weight. For example, an over-regularized problem (i.e., using too much regularization weight) might result in a solution that is an under-estimate of the true solution. This can be better understood by studying the *L*-curve associated with ill-posed problems [62].

handle this partial SP due to the absence of any regularization applied to the white box region. However, as can be seen in Figure 3.8(g)-(h), the MRSP-GNI can successfully use the partial SP, and not only reconstructs the complex permittivity where the SP is available but also reconstructs the complex permittivity where the SP is not available (i.e., the white box area which is shown by the dashed white lines in Figure 3.8(g)-(h).) In particular, the reconstructed complex permittivity of the tumour using this method is about $49.20 - j17.23$. A counter-intuitive observation is that the reconstructed complex permittivity value of the tumour using the MRSP-GNI with the partial SP is more accurate than that using the MRSP-GNI (and SP-GNI) with the complete SP. We have two speculations regarding this observation. First, in addition to the complex permittivity value, the shape of the reconstructed object matters in its scattering signature. For example, if the inversion algorithm mistakenly reconstructs the shape of an OI smaller than its true size, the reconstruct contrast may then overshoot to compensate for the smaller reconstructed size. (As can be seen, the shape of the reconstructed tumour is different in the partial SP inversion as compared to the complete SP inversion.) Second, there are always some errors in the SP since it is generated in a grid that is different than that of the true object.

3.5.3 Experimental Example: FoamDielIntTM Date Set

We consider one of the experimental data sets that has been collected by the Fresnel Institute [1], known as *FoamDielIntTM*. This target, shown in Figure 3.9(a), consists of two dielectric circular cylinders. The larger cylinder has a diameter of 80 mm and a relative permittivity of 1.45 ± 0.15. The smaller cylinder shown in red has a diameter of 31 mm and a relative permittivity of 3 ± 0.3. This target is irradiated from 8 different angles and the resulting scattered field is collected at 241 points at 9 different frequencies ranging from 2 GHz to 10 GHz with a 1 GHz increment. The measured data points are located on a two-

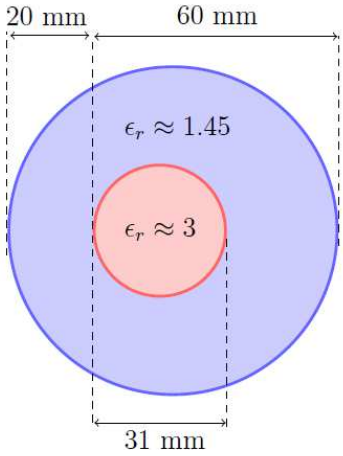

(a) *FoamDielIntTM* target

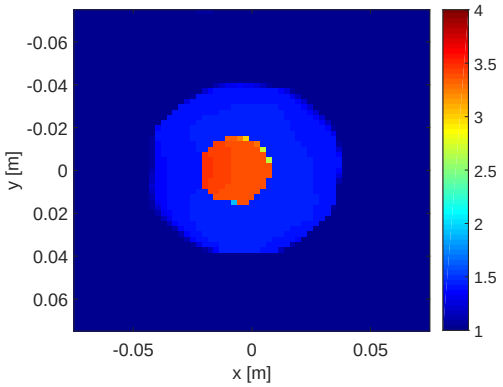

(b) Re(ϵ_r), 5 GHz MR-GNI

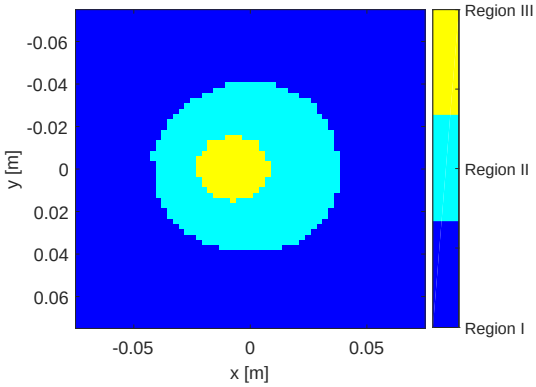

(c) Complete SP

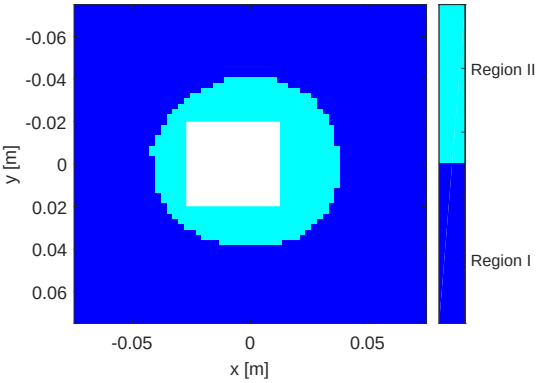

(d) Partial SP

Fig. 3.9: (a) *FoamDielIntTM* target from the Fresnel institute, (b) blind inversion at 5 GHz (no prior information) using the MR-GNI algorithm, (c) the complete spatial priors (SP) showing three regions within the imaging domain, which were derived from the blind 5 GHz inversion, and (d) the partial SP with the white box showing the region in which we have no spatial priors.

third of a ring with a radius of 1.67 m. For all of the reconstruction results presented in this section, the imaging domain has the size of 15×15 cm^2 discretized into 61×61 cells.

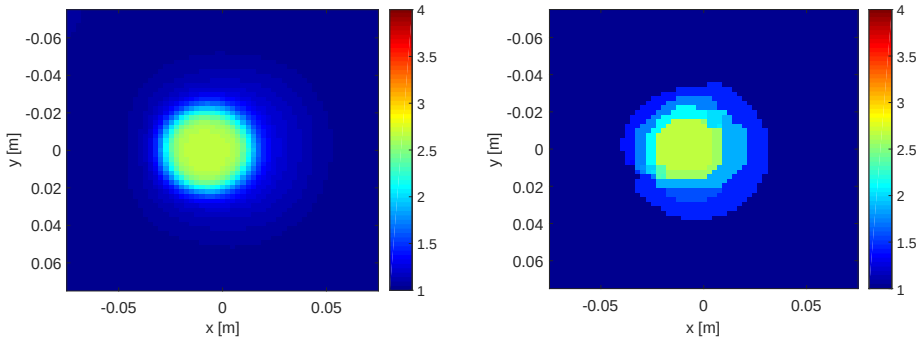

(a) 2 GHz MR-GNI (b) 2 GHz MR-CSI

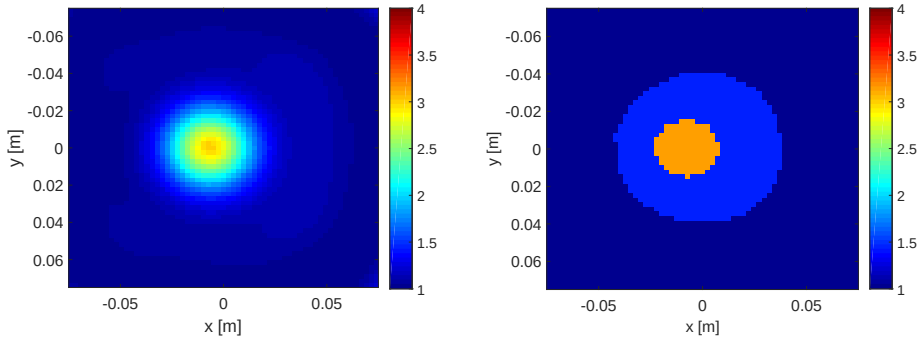

(c) 2 GHz Tikh-GNI (d) 2 GHz SP-GNI

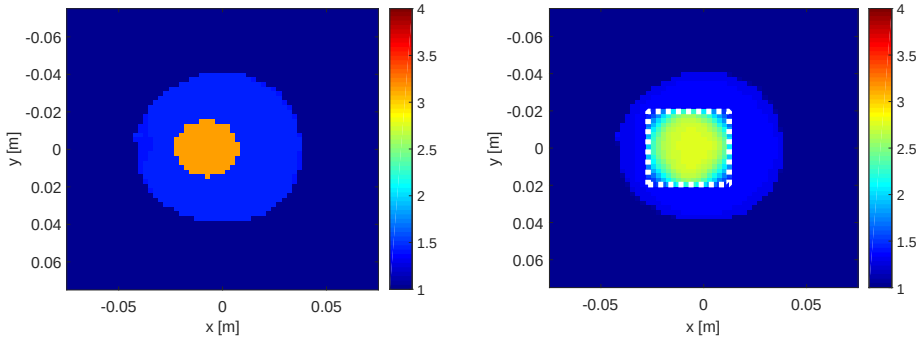

(e) 2 GHz MRSP-GNI (f) 2 GHz MRSP-GNI (Partial SP)

Fig. 3.10: 2 GHz inversion results where the reconstructions of the real parts of relative complex permittivity profile, $\mathrm{Re}(\epsilon_r)$, are shown. (The reconstructed imaginary parts are small, and are not shown here for brevity.) (a) blind inversion using the MR-GNI algorithm, (b) blind inversion using the MR-CSI algorithm, (c) blind inversion using the Tikh-GNI algorithm, (d) SP-GNI algorithm with the complete SP, (e) MRSP-GNI algorithm with the complete SP, and (f) MRSP-GNI with the partial SP. (The dashed white lines indicate the region in which there are no SP available.)

3.5.3.1 Approach

We first use a higher frequency data set (5 GHz) to merely create spatial priors about this target, and then use these obtained spatial priors to invert a lower frequency data set (2 GHz). In a practical scenario, the SP is expected to be provided by a different higher-resolution imaging modality. However, herein, we simply use a higher frequency data set to create an image to imitate a high-resolution image obtained from a different imaging modality such as MRI or ultrasound tomography.

3.5.3.2 Obtaining the Complete SP

To obtain our SP, we perform a high-frequency (5 GHz) blind inversion as shown in Figure 3.9(b). This quantitative image was then fed to the MATLAB function *kmeans* in the form of $kmeans(\text{image}, 3)$. The number 3 in the argument of *kmeans* function indicates the number of regions that exist within the imaging domain, including the background medium. The output of this MATLAB function is a matrix filled with 0, 1, and 2 that represents the existence of three regions inside the imaging domain. We have then tagged these values with the names BackGr, Foam, and dielectric as shown in the colorbar of Figure 3.9(c), which serves as our complete SP.

3.5.3.3 Creating the Partial SP

We have created partial SP as shown in Figure 3.9(d) from the complete SP. As can be seen in the partial SP, we have no spatial priors in the white box. Note that this white box encloses the internal cylinder.

3.5.3.4 Inversion with No Prior Information

Before showing the inversion using the SP at the lowest frequency (2 GHz), let us first check the inversion at this frequency without any prior information. The reconstructions using the MR-GNI, MR-CSI, and Tikh-GNI algorithms have been shown in Figure 3.10(a)-(c). (The reconstructed imaginary parts are small due to the lossless nature of the target; thus, they are not shown for brevity.) As can be seen, these images do not accurately reconstruct the permittivity values of the two cylinders.

3.5.3.5 Inversion with the Complete SP

We now use the complete SP with the SP-GNI and MRSP-GNI algorithms. The reconstruction results shown in Figure 3.10(d)-(e) clearly show the two cylinders with accurate permittivity values.

3.5.3.6 Inversion with the Partial SP

Finally, we consider the partial SP shown in Figure 3.9(d). Similar to all the previous cases, the SP-GNI cannot handle the absence of prior information in the white box. On the other hand, the MRSP-GNI is capable of handling the partial SP with the reconstruction result shown in Figure 3.10(f). As can be seen, the presence of the internal dielectric cylinder is clear. In addition, the reconstructed permittivity of the internal cylinder, over which we had no spatial priors, is similar to that of the blind inversion shown in Figure 3.9(a). (The undershoot in the reconstructed complex permittivity value of the internal cylinder is probably due to the over-estimate of the reconstructed size of this internal cylinder.)

3.6 Conclusion

We have presented a multiplicatively regularized Gauss-Newton inversion algorithm that is capable of incorporating prior spatial information about the object being imaged. An important aspect of this algorithm (MRSP-GNI algorithm) is that it can handle *partial* prior spatial information. This was achieved by creating two layers of regularization, one of which incorporates the prior spatial information, and the other is a generic regularization to handle the lack of prior information in a given region. This can be useful for biomedical imaging applications since we might not have any prior spatial information in a region which is suspicious to be the location of a tumour.

In addition, this algorithm is automated; that is, it does not require the user to input any parameters, e.g., an appropriate regularization weight, at the start of the inversion process. This is important since inversion algorithms are often applied to various data sets collected from various objects under different signal-to-noise ratios. Thus, each measurement scenario may require a different regularization weight. Therefore, it is desirable to have a mechanism to *automatically* choose an appropriate regularization weight. Similar to other published multiplicative regularization approaches, this algorithm also has the same advantage of setting its own parameters in an automated fashion.

Finally, the incorporation of spatial priors in microwave imaging can be useful when blind inversion algorithms are incapable of reconstructing the features of interest. This might happen for example (i) when the feature size is small compared to the wavelength of operation (e.g., about one-tenth of a wavelength), or (ii) when we do not have sufficient transceivers to illuminate and collect the resulting scattered fields from sufficient angles.

4

On the Use of Focused Incident Near-Field Beams

This chapter encloses a peer-reviewed journal paper published in *Sensors* that consists of the author's work during his PhD studies[1]. In this chapter, the effects of an antenna near-field (NF) distribution as one of the MWI's design parameters on the achievable accuracy is evaluated. This study is particularly important due to the following two reasons.

- **Near-field distribution vs far-field pattern**. Most of the NF MWI systems, to the best of the author's knowledge, utilize far-field (FF) antennas such as horn, dipole, and open-ended waveguide antennas for the illumination of the object of interest (OI). These antennas are referred to as FF antennas due to the fact that they are mainly designed based on their FF operational criteria. However, in NF MWI, the incident NF distribution of the utilized antennas plays the main role. This is due to the fact that the OI is placed in the NF zone of the antennas.

[1] Nozhan Bayat and Puyan Mojabi, "On the Use of Focused Incident Near-Field Distributions in Microwave Imaging," *Sensors*, vol. 18, no. 9, pp. 1-26, 2018.

- **Focused vs non-focused near-field beams**. We study the effects of using focused NF beams compared with the use of non-focused NF beams for the illumination of the OI. It is shown that the use of focused NF beams can be effective in suppressing undesired scatterers (i.e., the unknown objects whose dielectric properties are not of our interest).

To this end, as will be seen, we utilize two NF antennas: (i) a near-field plate and (ii) a Bessel beam launcher. These antennas are referred to as NF antennas as they have been designed to have specific properties in their NF zone. Through several ANSYS HFSS simulation studies, we demonstrate that the sensitivity of the collected data can be reduced with respect to the regions outside our region of interest. Moreover, it is discussed that the use of focused incident NF distributions can reduce the number of required collected data points.

The abstract of this paper is as follows, after which the remaining sections of this paper are presented.

Abstract. We consider the use of focused incident near-field (NF) beams to interrogate the object of interest (OI) in NF microwave imaging (MWI). To this end, we first discuss how focused NF beams can be advantageously utilized to suppress scattering effects from the neighbouring objects whose unknown dielectric properties are not of interest (i.e., undesired scatterers). We then discuss how this approach can also be helpful in reducing the required measured data points to perform imaging. Driven by the relation between the electromagnetic inverse source and inverse scattering problems, our approach emphasizes the importance of tailoring the induced contrast sources in the imaging domain through the utilized incident NF beams. To demonstrate this idea, we consider two recently-proposed NF beams, and simulate them for imaging applications. The first one is a subwavelength focused NF beam generated by a passive NF plate, and the other is a Bessel beam generated by a

leaky radial waveguide. Simple imaging examples are considered to explore the potential advantages of this approach, in particular, toward mainly *seeing* the object of interest, and not the unknown undesired scatterers. The scope of this paper is limited to homogeneous dielectric objects for which the induced total field distributions in the interrogated objects are similar to the incident field distributions (e.g., those that satisfy the Born approximation). Simple inversion results for focused and non-focused beams are presented accompanied by discussions comparing the achieved reconstructed values.

4.1 Introduction

Microwave imaging (MWI) is an imaging technique that can be used to produce a quantitative image of the dielectric profile of the object of interest (OI) by solving the corresponding electromagnetic inverse problem. In MWI, the OI is illuminated by incident electromagnetic fields at the microwave frequency range, and the resulting scattered fields are processed (inverted) to create (reconstruct) the OI's dielectric profile image. This processing often involves calibrating the measured data and applying an appropriate inversion algorithm to this calibrated measured data. This imaging tool has the potential to be utilized for different applications such as breast cancer detection, stroke diagnosis, through wall imaging, security screening, and industrial non-destructive evaluation [5, 7–15]. MWI can also be used in conjunction with other imaging tools, e.g., with magnetic resonance imaging or ultrasound tomography [21–23]. In addition, MWI can be performed in the time domain or frequency domain, with the latter being the focus of this paper. Moreover, in some applications, reconstructing the magnetic properties is also of interest (e.g., in [63]); herein, we only consider non-magnetic objects.

MWI can be performed in at least three fashions: (i) 1-D (line reconstruction; e.g., [19]),

(ii) 2-D (cross section reconstruction; e.g., [53]), and (iii) 3-D (volumetric reconstruction; e.g., [64]). This is often determined based on several factors such as the application area, data collection process, and the amount of measured data. For some applications including biomedical imaging, it is desirable to enhance the achievable reconstruction accuracy from MWI. To this end, in addition to the development of appropriate inversion algorithms and regularization techniques, e.g., [3, 54, 65, 66], several other techniques have been suggested to further improve the achievable image accuracy from MWI. For example, these include (i) using prior spatial information about the OI [67–69], (ii) using prior information about the permittivity values or the expected ratio between the real and imaginary parts of the OI's complex permittivity [70, 71], (iii) increasing the number of transceivers and frequencies of operation [72], (iv) improving the signal to noise ratio (SNR) of the system [73], (v) appropriate data calibration techniques [5, 74], (vi) enhanced modeling of the imaging system in the inversion algorithm [75]. All of the above techniques may be classified under the following two categories. The first category aims to increase the *overall* SNR with noise being either the actual noise or the modeling error. (Modeling error is defined as any discrepancies between the actual imaging setup and the numerical model used in the inversion algorithm.) On the other hand, the second category aims to enrich the information content of the data to be used for inversion; this is done by increasing the number of measurements and incorporating prior information (virtual data) about the OI.

The work presented in this paper aims to suppress the effect of *undesired* scatterers in the inversion process. To this end, we begin by defining undesired scatterers as any scatterers within the imaging chamber that we are *not* interested in finding their *unknown* dielectric properties. Considering the scattered fields due to these undesired scatterers as unwanted signals, or *noise*, the topic of this paper, therefore, falls under the first category above: i.e., enhancing the overall SNR. Note that the undesired scatterer and the OI might be two distinct objects, or they can be attached to each other. For example, in 2D (cross-sectional) imaging

of a 3D object, e.g., breast, the irradiating antenna not only illuminates the cross-section of interest but also illuminates other cross-sections. These other cross sections are then undesired scatterers with respect to the cross section to be imaged. Herein, we investigate how tailoring the incident field can be helpful toward suppressing such undesired scattering effects. Since the focus of this paper is on the incident field (and, not the total field), the scope of this work is limited to imaging scenarios in which the induced fields in the dielectric objects are similar to the incident fields. (This is mainly associated with low-contrast and electrically small objects.) In addition, for simplicity, we have also limited the scope of this work to homogeneous lossless OIs and undesired scatterers.

A key aspect which is considered in this paper is that the OI is often placed electrically close to the antenna system, i.e., in its near-field (NF) zone, so as to make the imaging system more compact and also to enrich the information content of the measured data. (NF data collection increases the chance of capturing evanescent waves which contain high spatial resolution information about the OI.) Several NF MWI systems have been developed; however, to the best of our knowledge, all of them utilize standard "far-field (FF) antennas". Herein, the term "FF antennas" has been used to indicate standard antennas such as dipoles, monopoles, Vivaldi, open ended waveguides which have not been specifically designed to achieve a certain NF distribution. (Some of these FF antennas have been modified, e.g., with a dielectric inclusion, to enhance their NF focusing [6, 76].) All of these FF antennas have important advantages, e.g., their compactness, ease of modelling in the inversion algorithm, bandwidth, and the ability to easily operate in matching fluids. However, it is beneficial for near-field MWI to investigate antennas which are specifically designed to achieve desired NF distributions: in NF MWI, it is the incident NF of the antenna, *not* its FF pattern, that interrogates the OI. As a follow-up to our previous work where we have discussed that the choice of the incident field distribution can affect the achievable reconstruction [39, 72], we now discuss and demonstrate that a focused incident NF can be used advantageously in NF

MWI to suppress undesired scattering events. The idea behind this paper is therefore simple: making sure that the *spotlight* of the antenna is on the OI, and not on the undesired scatterers. To this end, we will utilize a NF plate and a Bessel beam launcher to demonstrate the potential advantages of using a focused incident NF beam in MWI. (We have recently presented a concise form of this idea in [77].) We also note that there exist other techniques for focusing the fields into a hotspot, e.g., using an antenna array configuration [78–80]. The focus of this paper is not to compare these focusing techniques; we just note that the radiators used in this paper do not require array feeding networks or array signal processing.

Finally, in this paper, we use the terms *focused* instead of *directive*, and *distribution* instead of *pattern* since the terms *directivity* and *pattern* describe FF properties of antennas, and are more appropriate for the FF zone. We also utilize *NF distributions* and *NF beams* interchangeably. In addition, hereafter, we refer to NF MWI simply as MWI for brevity. It should also be noted that the time-dependency of $\exp(j\omega t)$ is implicitly assumed throughout this paper.

4.2 Motivation

Incorporating unknown undesired scatterers in the inversion process requires that we (*i*) include them as extra unknowns in the inversion algorithm, and subsequently (*ii*) ensure that more scattering data are collected to compensate for the resulting increase in the number of unknowns. However, we may not be able to meet these two conditions in certain cases. To understand this better, it is important to discuss the "sufficient" amount of data needed for successful inversion. To this end, we begin by reviewing how the MWI problem, which is an inverse scattering problem, is related to the inverse source problem. (In the inverse source problem, the goal is to find the equivalent currents that generate the measured elec-

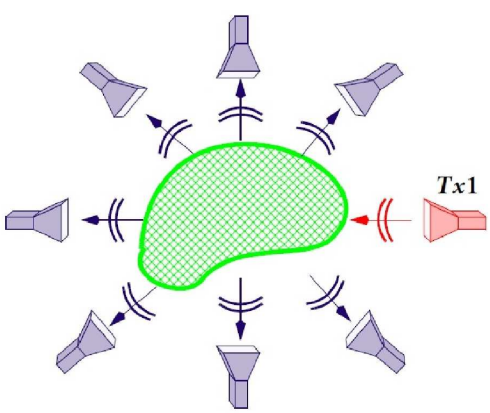

(a) MWI problem for ***Tx1***

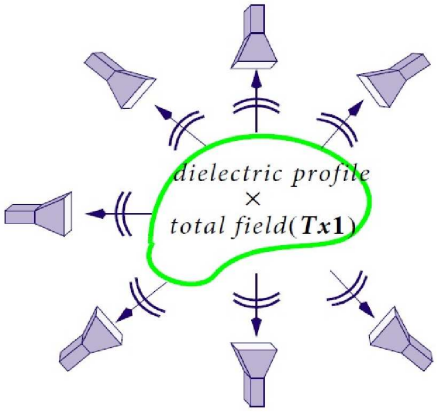

(b) Inverse source problem corresponding to ***Tx1***

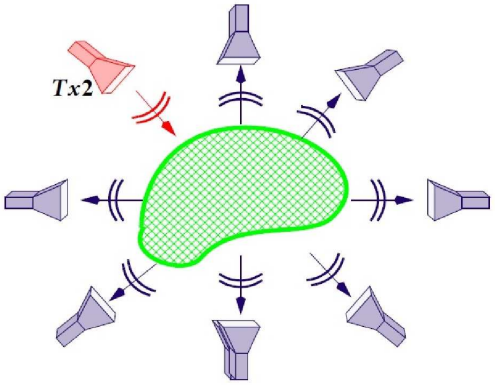

(c) MWI problem for ***Tx2***

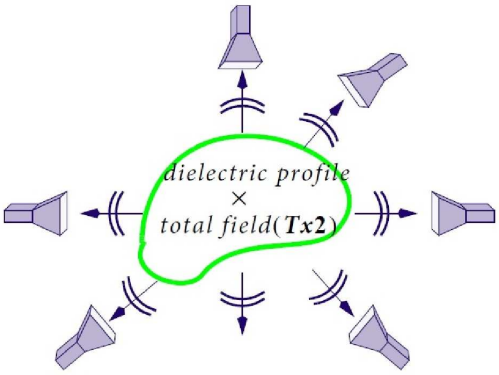

(d) Inverse source problem corresponding to ***Tx2***

Fig. 4.1: Demonstration of the relation between the MWI and inverse source problems. (a) represents the MWI problem when the OI is interrogated by the transmitter ***Tx1*** (red antenna) while the other antennas (grey antennas) act as receivers. (b) represents the equivalent inverse source problem for (a) in which ***Tx1*** has been replaced by contrast sources in the geometrical domain of the OI. Similarly (c) and (d) demonstrate the same concept but for a different transmitter: ***Tx2***.

tromagnetic fields.) Once this relation is established, the amount of information needed for successful inversion can be better understood from NF antenna measurements' point of view. We then address how the choice of the NF distribution can be utilized advantageously to suppress the scattering from undesired scatterers in an attempt to alleviate the necessity of including them as extra unknowns in the inversion process.

4.2.1 The relation between the MWI and inverse source problems

Consider Figure 4.1(a) in which the dashed green region represents the OI surrounded by multiple antennas. As can be seen, the antenna denoted by $Tx1$ irradiates the OI. The other antennas surrounding the OI act as receivers, and collect the resulting *total* field data $\boldsymbol{E}$. The incident field $\boldsymbol{E}^{\text{inc}}$, i.e., the field in the absence of the OI, is also collected in a separate experiment by the same antennas. Having both the total and incident fields, the scattered field can then be obtained as $\boldsymbol{E}^{\text{scat}} \triangleq \boldsymbol{E} - \boldsymbol{E}^{\text{inc}}$. Equivalently, this scattered field can be thought as the field radiated by a new set of currents, often referred to as *contrast sources* [81] which radiate in the background medium. These contrast sources are confined within the OI's geometrical domain; i.e., they are zero outside the OI's geometrical support. This is shown in Figure 4.1(b) where the actual illuminating antenna $Tx1$ is replaced by contrast sources within the OI's geometrical domain. As shown in this figure, these contrast sources depend on the multiplication of the OI's dielectric contrast profile and the induced total field within the OI due to $Tx1$. These contrast sources are then written as $\boldsymbol{w}(\boldsymbol{r}) = \chi(\boldsymbol{r})\boldsymbol{E}(\boldsymbol{r})$ [81] where χ is the dielectric contrast profile of the OI, $\boldsymbol{E}$ is the total field induced in the OI due to a given transmitter (in this case, $Tx1$), and $\boldsymbol{r}$ is the location vector. Note that the dielectric contrast profile is defined as

$$\chi(\boldsymbol{r}) \triangleq \frac{\epsilon(\boldsymbol{r}) - \epsilon_b}{\epsilon_b} \tag{4.1}$$

where $\epsilon(\boldsymbol{r})$ is the relative permittivity of the OI, and ϵ_b is the relative homogeneous permittivity of the background medium. (In this paper, the background medium is air.) As can be seen from the above discussion, the MWI problem in Figure 4.1(a) has now been cast as an electromagnetic inverse source problem shown in Figure 4.1(b), with its unknown quantity being these contrast sources. (This well-known relation can also be found in other references, e.g., see [82].) To minimize the null space of the associated inverse problem, the OI

may be illuminated from multiple angles. This has been demonstrated in Figure 4.1(c) in which a different transmitter ($Tx2$) now illuminates the OI. Similarly, this is equivalent to the inverse source problem depicted in Figure 4.1(d); however, the new unknown contrast sources in this case are different than the ones in Figure 4.1(b) as the total field induced in the OI is now due to $Tx2$, instead of $Tx1$. Based on this discussion, the MWI problem can be thought as the summation of multiple inverse source problems whose unknown contrast sources share one common component: the dielectric profile of the OI. For a more detailed discussion on this topic, see for example [83]. (As also noted by other authors, this analogy has been used to develop the contrast source inversion algorithm [81].)

4.2.2 Suppressing undesired scattering effects

Based on the above discussion, it can be understood that the contrast sources induced in the OI can be considered as the *cause* for the scattered field data, similar to the current distribution of an antenna being the cause for its radiation pattern. More specifically, the scattered field at a given receiver due to a given transmitter can be thought as the weighted summation of all the contrast sources induced at different locations within the OI's geometrical domain. (This is parallel to the concept of antenna arrays in which the field at a given location in space is the weighted summation of the effects of all the single antenna elements.) This can be better understood by observing the so-called *data equation* [50] which maps the contrast sources from the imaging domain D to the scattered field on the measurement domain S for the 2D scalar problem

$$\boldsymbol{E}^{\text{scat}}(\boldsymbol{r} \in S) = k_b^2 \int_D g(\boldsymbol{r} \in S, \boldsymbol{r}\,' \in D)\, \boldsymbol{w}(r\,' \in D)\, d\boldsymbol{r}'. \tag{4.2}$$

The above equation indicates that the scattered field at the receiver location $\boldsymbol{r}$ is affected by all the contrast sources weighted by Green's function g of the background medium and the

background wavenumber k_b. Therefore, one way to not *see* a specific part of the imaging domain, e.g., an undesired scatterer, is to ensure that the contrast sources induced in the undesired scatterer are small, and are ideally zero. Due to the fact that the dielectric profile within the imaging domain is unknown, we are not able to fully control the distribution of contrast sources within the imaging domain. However, since the contrast sources are affected by the incident NF distribution, $\boldsymbol{E}^{\text{inc}}$, through the so-called *domain equation* [50],

$$\boldsymbol{w}(\boldsymbol{r} \in D) = \chi(\boldsymbol{r} \in D)\boldsymbol{E}^{\text{inc}}(\boldsymbol{r} \in D) + k_b^2 \int_{\mathcal{D}} g(\boldsymbol{r} \in D, \boldsymbol{r}\,' \in D)\, \boldsymbol{w}(r\,' \in D)\, d\boldsymbol{r}', \quad (4.3)$$

we can use the incident NF distribution to *partially* control the distribution of the contrast sources.

The idea to be pursued here has been demonstrated in Figure 4.2 where a focused incident NF in Figure 4.2(a) and a non-focused one in Figure 4.2(b) irradiate three distinct dielectric objects, with the central green one represents the OI, and the other two black ones represent the undesired scatterers. Due to the fact that the incident NF in Figure 4.2(a) is more focused toward the OI, the contrast sources within the undesired scatterers are more *likely* to be weaker in Figure 4.2(a), and subsequently, the scattered data collected by the grey receiver in Figure 4.2(a) is more likely to contain less information about the undesired scatterers as compared to the grey receiver shown in Figure 4.2(b). Therefore, if the main purpose is to see the OI (central object), Figure 4.2(a) offers an advantageous measurement scenario as the received signal is mainly due to the OI. We will investigate this further in Section 4.3 of this paper. (This is similar to our approach toward justifying an appropriate incident field for 2D transverse magnetic inversion [6].) Note that there exist situations in which focusing the incident field in one spot does not result in weaker contrast sources elsewhere; however, for situations where Born approximation is valid ($\boldsymbol{E} \approx \boldsymbol{E}^{\text{inc}}$ thus $\boldsymbol{w} = \chi\boldsymbol{E} \approx \chi\boldsymbol{E}^{\text{inc}}$) focusing the incident field into a spotlight will weaken the contrast sources at other areas. That is why

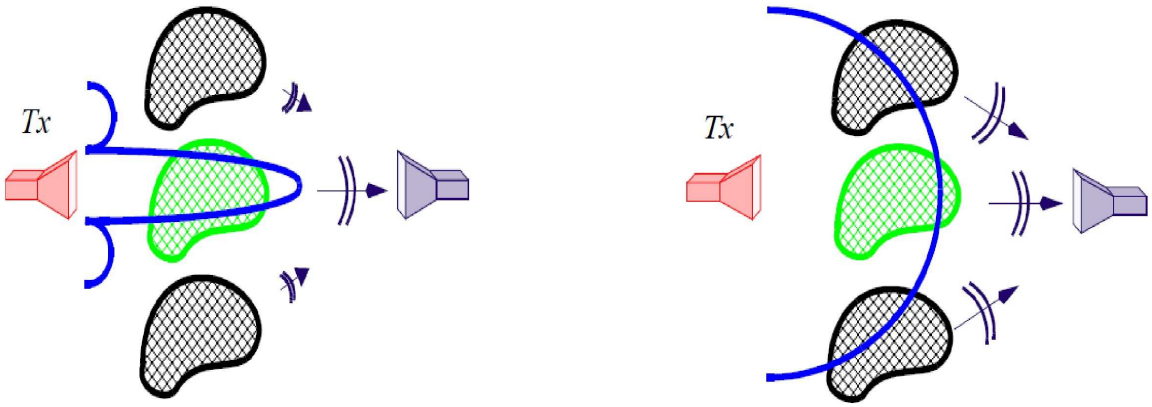

(a) Focused NF distribution (b) Non-focused NF distribution

Fig. 4.2: (a) represents the scenario in which a focused NF beam is used for irradiation of the OI (central green object). (b) represents the scenario in which a non-focused NF beam is used for irradiation. The side black objects are the undesired scatterers.

we have limited the scope of this paper to scenarios in which the total and incident fields share similar distributions.

It is also important to note that in some situations, the use of a focused incident field has a disadvantage compared to a non-focused one. In particular, if the transmitter in Figure 4.2 can vertically move up and down to scan the OI, then at some elevations the focused incident field will not irradiate the OI. On the other hand, the non-focused incident field might still be able to irradiate the OI due to its wider NF beam. This will result in the loss of some useful information for the focused incident field. One remedy for this situation is to steer the antenna toward the OI when we move the antenna vertically up and down to ensure that the focused beam always see the OI. (This is similar to the concept of stripmap and spotlight modes in synthetic aperture radars.)

4.2.3 Sufficient measured data

In the previous section, we discussed suppressing the effect of undesired scatterers to avoid including them as unknowns in the inversion algorithm. As noted earlier, if we decide to include undesired scatterers as part of the unknowns in the inversion process, we need to ensure that sufficient measured data are collected to reconstruct not only the OI but also the undesired scatterers. We now rely on Section 4.2.1 to further discuss this in an intuitive fashion. To this end, let us first note that the equivalent inverse source problems corresponding to the MWI problem (see Figure 4.1) are, in fact, antenna characterization problems which we often encounter in NF antenna measurement techniques. (In NF antenna measurement techniques, antenna characterization or diagnostics deals with finding the equivalent currents of the antenna under test from NF antenna measurements.) This is due to the fact that each set of these contrast sources can be thought as an unknown *antenna* radiating the measured scattered fields. From the theory of cylindrical and spherical NF antenna measurements [84], it is known that the number of required measured data points depends on both the wavelength of operation (λ) and the electrical size of the antenna. Noting the relation between the MWI and inverse source problems, it can be understood that the required sampling resolution for MWI will similarly depend on the size of the OI and the wavelength of operation. We also note that in NF antenna measurements, the above criteria are used to find the fields *outside* the measurement domain (i.e., for performing NF to FF transformation), which is easier than reconstructing the fields interior to the measurement domain. For example, the required angular and vertical data sampling resolutions for a cylindrical NF antenna measurement system is [85]

$$\Delta\varphi = \frac{\lambda}{2(a+\lambda)} \quad \text{and} \quad \Delta z = \frac{\lambda}{2} \tag{4.4}$$

where a is the radius of the smallest cylinder that encloses the antenna under test. It is worthwhile to note that the above sampling resolution requires collecting two orthogonal field components at each measurement location, which are tangential to the measurement surface, i.e., E_φ and E_z in the cylindrical coordinates where the axis of the measurement cylinder is assumed to be on the z axis. (In MWI, often one field component is collected at each measurement location, in most implementation E_z.)

Based on the above discussion and the similarity of the inverse scattering and inverse source problems, the parameter a in MWI can be thought as the smallest cylinder that encloses the OI and undesired scatterers. Therefore, it can be easily understood that the larger a with respect to the wavelength, the more measured data are necessary for performing successful inversion. (We re-emphasize that this approach is only being used to develop some intuitive understanding about the MWI data sampling resolution, and should not be considered as an exact governing formula for the MWI problem. For a more detailed discussion on retrievable information, see [86].) If we are not able to provide the inversion algorithm with sufficient information content (e.g., due to the physical size of the antennas or strong mutual coupling between them), an alternative option will be to reduce the number of unknowns, e.g., by *not* seeing some parts of the original imaging domain. Therefore, although 3D full-vectorial inverse scattering algorithms are the most accurate option for inverting the measured data as practical systems and objects are all 3D structures, it is still important to simplify the inversion process for the cases where the amount of measured data cannot support the retrieval of many unknowns associated with 3D full-vectorial inversion. For example, each *voxel* of a discretized imaging domain will have four complex unknowns in 3D full vectorial inversion: E_x, E_y, E_z, and the OI's complex permittivity. Therefore, for a $100 \times 100 \times 100$ discretized imaging domain, we will therefore have 4×10^6 complex unknowns. (Regularization techniques are helpful in providing *vitual* data, e.g., enforcing smoothness by the Laplacian regularizer, that partially handle this huge number of unknowns.)

4.2.4 A synthetic test case

To demonstrate the concept above, we perform the following simulation study in which the utilized incident field is a numerical model, and does not represent an actual field. (In Section 4.3, we will focus on simulated fields due to practical NF antennas.) In this example, we consider a two-dimensional transverse magnetic MWI. The true dielectric profile considered is shown in Figure 4.3(a) which consists of four lossless scatterers in the xy plane. It is assumed that the two light blue circular scatters with the relative permittivity of 2.0 are the OI, and the other two (the yellow and red ones) with the relative permittivity of 2.5 and 3.0 are the undesired scatterers. The true profile was created on a 18×18 cm^2 domain discretized into 100×100 square pixels. The frequency of operation is assumed to be 5 GHz. Two types of incident fields are considered to illuminate the imaging domain: the first one is an omnidirectional line source incident field, and the other is a focused incident field as shown in Figures 4.3(b) and (c) respectively. The mathematical expression for the omnidirectional line source is $\boldsymbol{E}^{\text{inc}} = \hat{z}\frac{1}{4j}H_0^2(k_b|\boldsymbol{r}-\boldsymbol{r}'|)$ where $\boldsymbol{r}$ represents the transmitter location, $\boldsymbol{r}'$ represents the observation point within the imaging domain, and $j^2 = -1$. In addition, H_0^2 is the zeroth order Hankel function of the second kind. The focused incident field is then *modeled* (not, an actual field) by multiplying this omnidirectional incident field by $\cos^m \psi$ where ψ is the angle between the boresight axis of the antenna and the line connecting the antenna to the observation point in the imaging domain; e.g., see [72]. (The parameter m, which controls the focusing level, is set to be 300 here.) For all the antennas, the boresight axis is the line that connects the antenna to the centre of the imaging domain.

We consider two types of measurement domains: (1) a full circle and (2) a circular sector. In the first one, we place 22 antennas evenly distributed on a circle of 14 cm radius around the imaging domain as shown in Figure 4.3(d). In the second scheme, we distribute these 22 antennas on two opposite 60° sectors of the same measurement circle as shown in Fig-

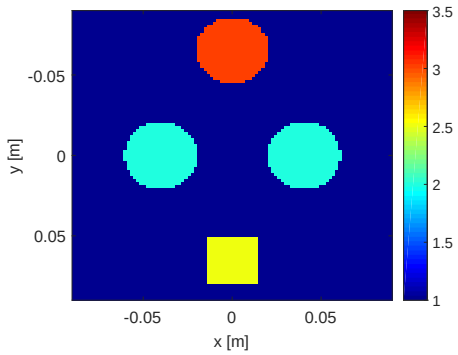

(a) True relative permittivity.

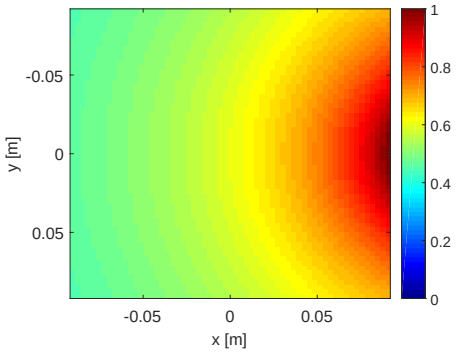

(b) Non-focused (omnidirectional) NF distribution

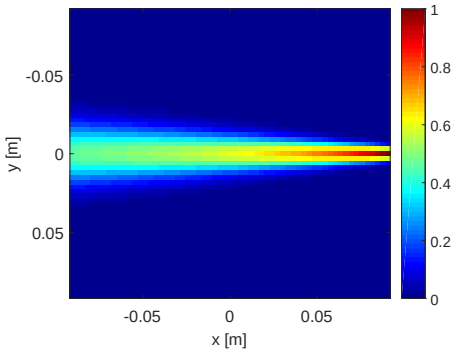

(c) Focused NF distribution

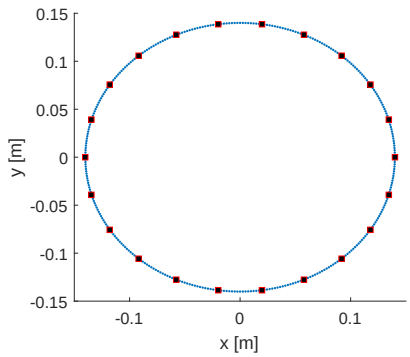

(d) Distribution of antennas on a circle

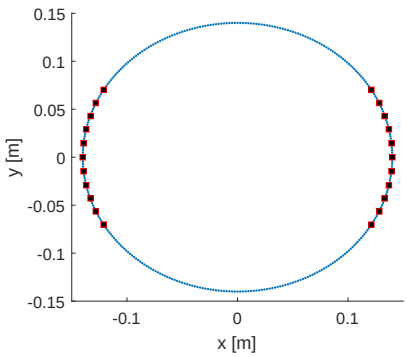

(e) Distribution of antennas on two circular sectors

Fig. 4.3: (a) represents the true relative permittivity profile. The two light blue circles are assumed to be the OI, and the other two side objects (red and yellow) are the undesired scatterers. (b) and (c) represent the non-focused (omnidirectional) and focused incident fields respectively which are used to irradiate the imaging domain. (e) and (f) represents two type of data collection schemes with antennas located either on a full circle or on a two circular sectors respectively.

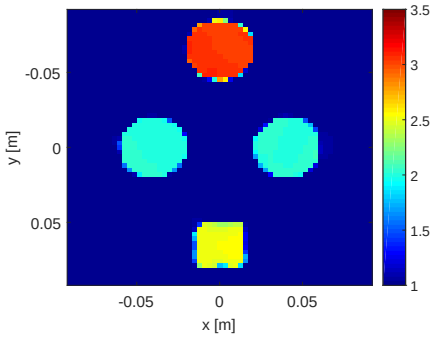

(a) Reconstruction using the omnidirectional incident field for the full circular measurement domain

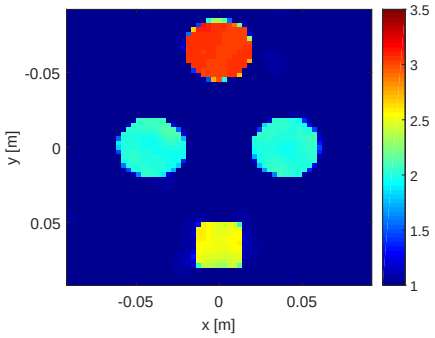

(b) Reconstruction using the focused incident field for the full circular measurement domain

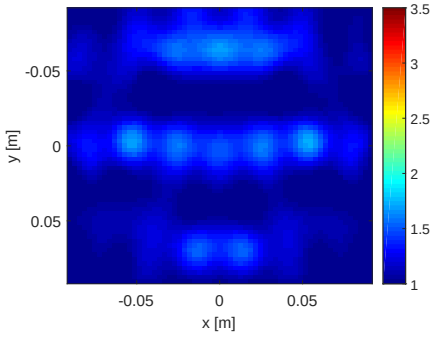

(c) Reconstruction using the omnidirectional incident field for the circular sector measurement domain

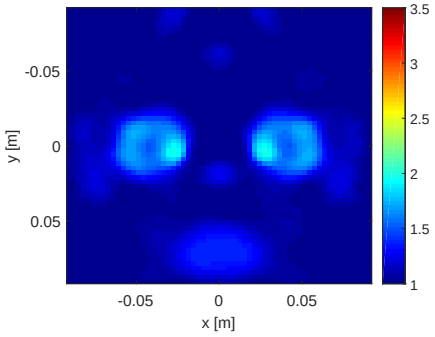

(d) Reconstruction using the focused incident field for the circular sector measurement domain

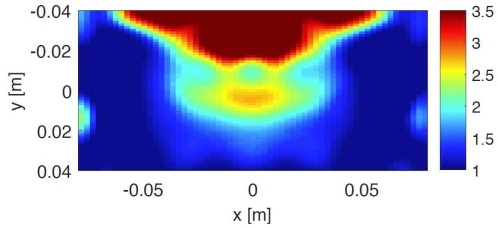

(e) Reconstruction using the omnidirectional incident field for the circular sector measurement domain for the smaller imaging domain

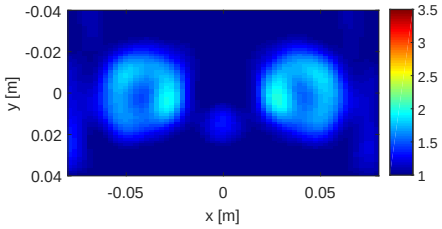

(f) Reconstruction using the focused incident field for the circular sector measurement domain for the smaller imaging domain

Fig. 4.4: (a) and (b) represent the inversion of the data collected on the full circular measurement domain for two cases: omnidirectional and focused incident fields respectively. (c) and (d) represent the inversion of the data collected on the circular sector measurement domain for two cases: omnidirectional and focused incident fields respectively. (e) and (f) represent the inversion of the data collected on the circular sector measurement domain for two cases, omnidirectional and focused incident fields respectively with the smaller imaging domain that only includes the OI, and not the undesired scatterers.

ure 4.3(e). Based on the analogy with the cylindrical NF antenna measurements noted in Section 4.2.3, the use of the circular sector measurement domain will not be as good as the full circular one; however, in some applications, we have to use this type of limited-view configurations as we may not have a full 360° access around the imaging domain.

The irradiation of the imaging domain is performed using either the omnidirectional incident field or the focused one. In the irradiation process, when one antenna transmits, all the antennas including the transmit antenna collect the scattered field data. This scattered data is synthetically generated by a method of moment forward solver, and 3% noise is added to this data according to the formula shown in [38]. The inversion of the noisy scattered data is then performed by the multiplicative regularized Gauss-Newton inversion (MR-GNI) algorithm [2, 3, 53] on an imaging domain with the size of 18.4×18.4 cm^2 discretized into 61×61 cells.

The inversion results for the full circular measurement domain with the omnidirectional and focused incident fields are shown in Figures 4.4(a) and (b) respectively. As can be seen, both images have good reconstruction accuracy. Next, we consider the circular sector measurement domain: its inversion results for the omnidirectional and focused incident fields are shown in Figures 4.4(c) and (d) respectively. As can be seen, both images are poor due to suffering from limited view angles. However, it can be noticed that the use of the focused incident field enables us to at least see the OI (i.e., the two circular scatterers). This is due to the fact that the focused incident fields in this data collection configuration mainly see the OI, and not the undesired scatterers, and therefore, the measured scattered data on the circular sector measurement domain are mainly due to the OI. From a mathematical point of view, the use of the focused incident field has made the scattered field data less sensitive to the unknown undesired scatterers, and therefore the inversion algorithm can work with less informative data.

To investigate this further, we make the imaging domain smaller by shrinking it into a rectangular imaging domain of the size 16×8 cm^2 discretized into 61×61 cells so as to only enclose the OI, and not the undesired scatterers. This will then completely ignore the presence of the undesired scatterers in the inversion algorithm. The inversion of the data collected on the circular sectors for this smaller imaging domain for the two incident field types are shown in Figures 4.4(e) and (f). As can be seen, the inversion of the data due to the omnidirectional incident field is now even poorer since ignoring the presence of the undesired scatterers has resulted in significant modelling error in the inversion algorithm. However, as expected, the inversion of the data collected on the circular sectors due to the focused incident field still shows the overall geometry of the OI due to the data being less sensitive to the undesired scatterers. Finally, we note that in this example, the beams of the focused incident fields are always toward the centre of the imaging domain, see the definition for $\cos^m \psi$ above. If, for example, the focused beams of the transmitting antennas were all parallel to the x axis, some incident fields (i.e., those corresponding to the antennas at the top and bottom ends of the circular sectors) might not even interact with the OI, thus, reducing the information content of the data. (Of course, this is not an issue with omnidirectional incident fields.)

4.3 NF Beams and Results

The example presented in Section 4.2.4 utilized a numerically modelled incident field. In this section, we consider realistic incident NF distributions. To this end, we consider two antenna systems that are able to create NF focusing: (1) a NF plate which can create a subwavelength focused NF distribution on a line (line focusing) [87] and (2) a Bessel beam launcher which is able to generate spot focused NF distribution (spot focusing) and maintain it over a distance away from the launcher [88]. Herein, we use these two antennas to illuminate the OI so as to demonstrate the idea presented in the previous section. It should

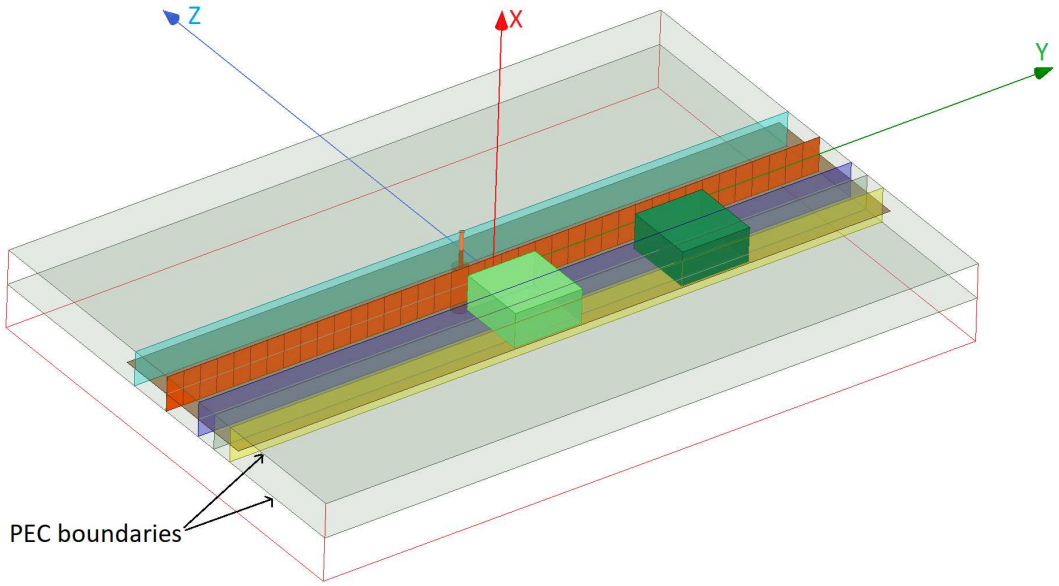

Fig. 4.5: The simulated NF plate setup . The NF plate (orange plane), introduced in [87], is excited from the back by the inner conductor (orange cylinder) of a coaxial cable which lies on the excitation plane (light blue plane). This structure then illuminates the OI (light green dielectric box) and the undesired scatterer (dark green dielectric box). The dark blue and yellow planes show the focal plane and the receivers' plane respectively. The two dielectric boxes have the same size of $\lambda/20 \times \lambda/10 \times \lambda/10$ along x, y, and z directions, and have the same relative permittivity.

be noted that all the results presented herein have been simulated using ANSYS HFSS.

4.3.1 Interrogation of objects by the NF plate

The NF plate test setup, shown in Figures 4.5 and 4.6, includes a thin passive plate with the length of about λ (orange plane) in the y direction that consists of multiple capacitive elements and is placed within a parallel plate waveguide with the height of λ/20; see [87] for the details regarding this NF plate. At the frequency of 1 GHz, this passive NF plate is excited by the cylindrical waves emanating from the inner conductor of a coaxial cable that has been extended into the parallel plate waveguide. The excitation source is shown by an orange cylinder on the excitation plane (light blue plane) in Figures 4.5 and 4.6. (The NF

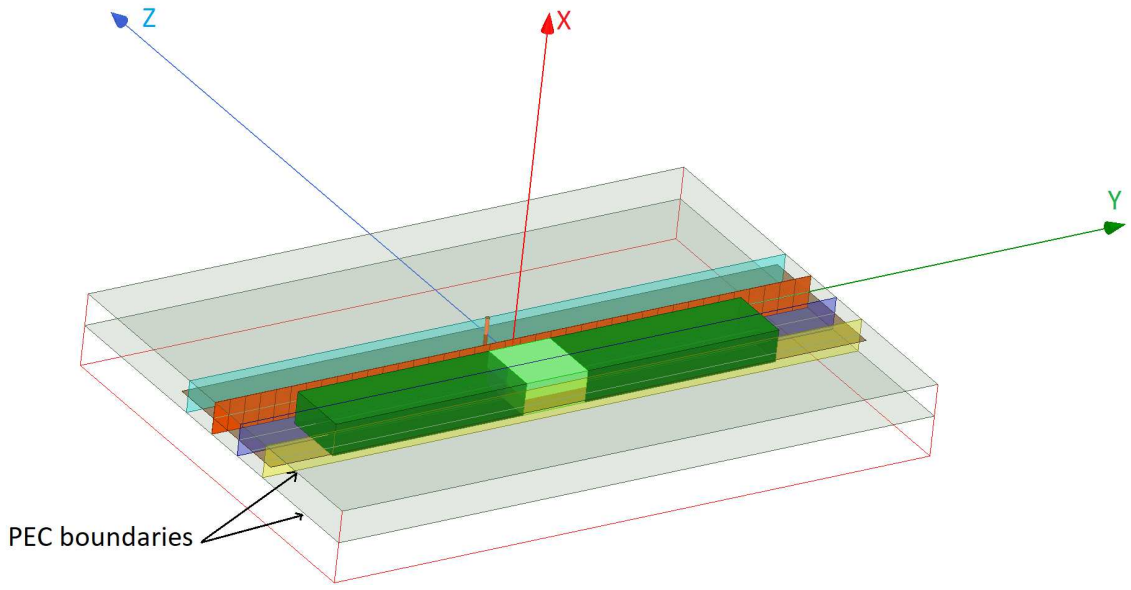

Fig. 4.6: The simulated NF plate (orange plane) setup with a dielectric slab in front of it. The dielectric slab has the size of $\lambda/20 \times 2\lambda/3 \times \lambda/10$. The description of the excitation and receiver planes are the same as Figure 4.5. The dielectric slab consists of an OI and two undesired scatterers. The OI is the light green box, and the two undesired scatterers attached to the OI are the dark green boxes.

plate has the same separation of $\lambda/15$ from the excitation and focal planes.) Once illuminated by the impinging cylindrical waves, the NF plate creates a highly oscillating electromagnetic fields at the plate that subsequently results in a focused NF beam at the focal plane. As noted in [87], the NF plate is designed by back-propagating the desired focused NF distribution at the focal plane toward the NF plate to find the required field on the NF plate, then calculating the required surface impedance profile needed to support the existence of this field, and finally implementing this surface. Our simulated NF plate resulted in about $\lambda/12$ beamwidth on the focal plane, and was not a perfect *sinc* function compared to the one reported in [87], which also had a narrower beamwidth of $\lambda/18$. We also note that this NF plate can be regarded as an electromagnetic metasurface which transforms a given non-focused field into a desired focused one.[2]

[2] In this work, the NF plate is simulated in ANSYS HFSS using impedance sheets.

All of the simulation case studies for the NF plate setup are performed under one of the following two configurations: (*i) Configuration I* is the configuration in which the NF plate is present within the parallel plate waveguide to create a focused NF distribution, and (*ii*) *Configuration II* is the configuration that the NF plate is removed from the imaging setup in order to reduce the focusing of the NF distribution. (That is, Configuration II is obtained by removing the orange NF plate in Figures 4.5 and 4.6.) For each of these two configurations, four different case studies are considered. The utilized objects (OI and the undesired scatterer) in all four case studies have the same relative permittivity of 1.50. In the first three case studies, the objects are dielectric boxes with the same dimensions of $\lambda/20 \times \lambda/10 \times \lambda/10$ along x, y, and z directions respectively, while in the fourth case study we elongate our dielectric box in the y direction, thus creating a dielectric slab with the dimension of $\lambda/20 \times 2\lambda/3 \times \lambda/10$ with the same relative permittivity of 1.50. In all these four cases, the separation between the closest facet of the dielectric objects to the NF plate is about $\lambda/60$. In addition, although our simulated configurations suffer from large $|S_{11}|$ values, these values are close to each other, thus making the comparison of the two configurations reasonable.

The four case studies are illustrated with figures in Appendix F. In Case I, as can be seen in Figure F.1(a) in Appendix F, the only object present in the system is the OI that is placed exactly at the center with respect to the NF plate. In Case II (Figure 4.5), both the light and dark green dielectric boxes are present in the system. In both of these cases, the light green dielectric box represents the OI while the dark green dielectric box in Case II represents the undesired scatterer which is located $\lambda/4$ away from the center. Case III only consists of the undesired scatterer, as shown in Figure F.1(c). Finally, in Case IV (Figure 4.6), we have a dielectric slab that consists of an OI and two undesired scatterers. The OI, the light green box in Figure 4.6, has the same size and dielectric property as the OI in Cases I and II. Two undesired scatterers, the dark green boxes in Figure 4.6, have the same dielectric property as the OI. (The size of each of these undesired scatterers is $\lambda/20 \times 17\lambda/60 \times \lambda/10$.)

Having defined our two configurations (i.e., presence and absence of the NF plate) and four case studies per configuration, we now irradiate these four different cases under each configuration, and then collect the resulting fields at the receivers' locations. The receivers are located along the line of intersection between the yellow and brown planes in Figures 4.5 and 4.6. This receiver line is parallel to the y axis, and is separated from the NF plate by about $\lambda/7.5$. (Note that the receivers' locations is not on the focal plane; the focal plane, which is $\lambda/15$ away from the NF plate, passes through the center of the objects.) The fields collected by the receivers in the presence of the objects are referred to as the total NF data. Subtracting the incident NF at the receivers' locations from the total NF data, we find the *scattered NF data*. Analysis of the scattered NF data is the focus of the next section.

4.3.1.1 Analysis of the scattered NF data

Herein, we discuss our observations from the comparison of the scattered NF data for the four case studies under both configurations. Prior to this, let us take a look at the magnitude of the incident NF distribution at the receivers' locations for both configurations in Figures 4.7(a) and (b) which represent the presence and absence of the NF plate respectively. As can be seen, the presence of the NF plate has created a focused NF distribution. It should be noted that the focused incident field does not have the shape of the *sinc* function as expected based on the design presented in [87]. We speculate two reasons for this. First, the *sinc* behavior is to be expected at the focal plane whereas our receivers' line is not on the focal plane. Second, our simulated structure can still be optimized; however, since our purpose is to study the performance of a more focused beam as compared to a non-focused one, the achieved incident field serves this purpose, which can be seen by comparing Figures 4.7(a) and (b).

We now begin by comparing the scattered NF data for Cases I and II under our two con-

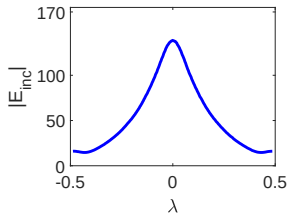

(a) Configuration I, incident NF

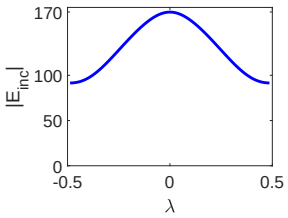

(b) Configuration II, incident NF

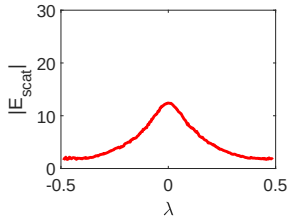

(c) Configuration I, Case I

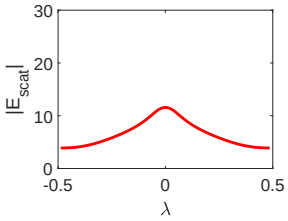

(d) Configuration II, Case I

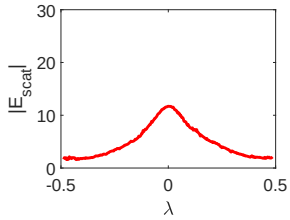

(e) Configuration I, Case II

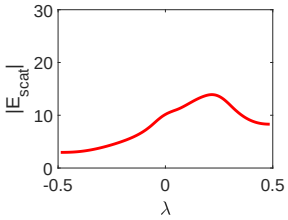

(f) Configuration II, Case II

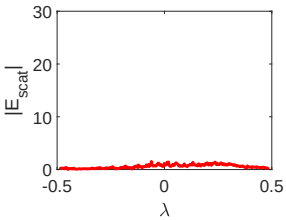

(g) Configuration I, Case III

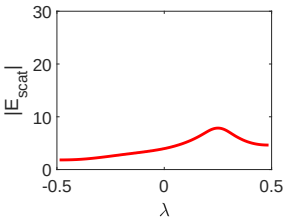

(h) Configuration II, Case III

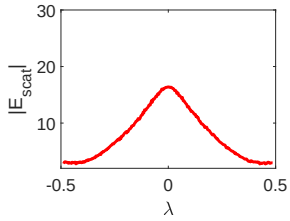

(i) Configuration I, Case IV

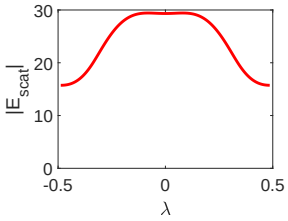

(j) Configuration II, Case IV

Fig. 4.7: Configuration I represents the presence of the NF plate, and Configuration II represents its absence. (a)-(b) show the incident NF distributions at the receivers' locations. (c)-(j) Scattered NF data under the two configurations for Cases I to IV.

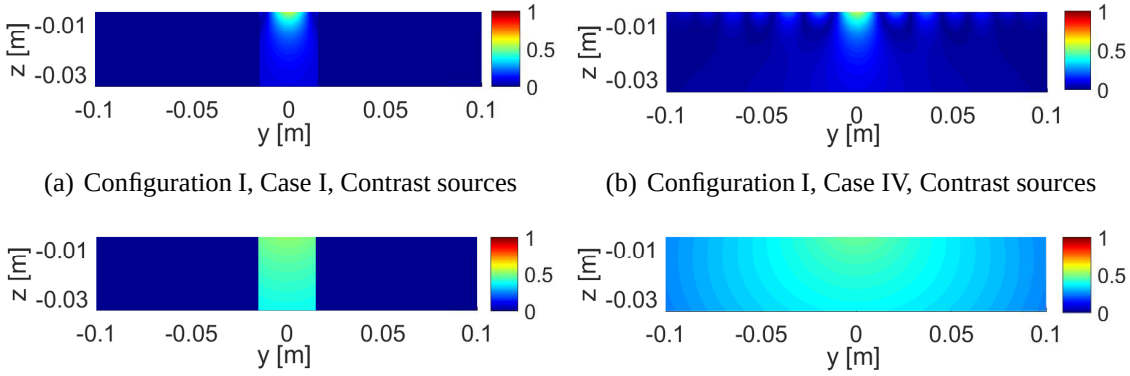

(a) Configuration I, Case I, Contrast sources

(b) Configuration I, Case IV, Contrast sources

(c) Configuration II, Case I, Contrast sources

(d) Configuration II, Case IV, Contrast sources

Fig. 4.8: Induced contrast sources (their magnitudes) for Cases I and IV for both configurations: with the NF plate (Configuration I), and without the NF plate (Configuration II). The contrast sources in each configuration have been normalized with respect to the maximum of the incident field at that configuration.

figurations. Figures 4.7(c) and (e) show the scattered NF data for these two cases under Configuration I. As can be seen by comparing Figures 4.7(c) and (e), the presence of the undesired scatterer has barely changed the scattered NF data. In other words, the imaging system employing this focused incident NF distribution is not very sensitive to the undesired scatterer. On the other hand, the scattered NF data for Configuration II (when the NF plate is removed) have been shown in Figures 4.7(d) and (f): as can be seen, the effect of the undesired scatterer is now completely visible in the scattered NF data, and has shifted the maximum of the scattered NF data in Figure 4.7(f). To further verify this, we consider Case III where only the undesired scatterer is present. The scattered NF data for this case under Configurations I and II have been shown in Figures 4.7(g) and (h): as can be seen, the scattered NF data obtained in the presence of the NF plate (Configuration I) has much smaller magnitude compared to that obtained in the absence of the NF plate (Configuration II). In conclusion, the presence of the undesired scatterer is less “seen” by the receivers when the utilized irradiating source is the focused incident NF beam.

As noted earlier, in Case IV, we elongate the light green dielectric box; see the new elon-

gated light green dielectric box in Figure 4.6, which we refer to as the dielectric slab. The resulting scattered NF data for this dielectric slab have been shown in Figures 4.7(i) and (j). Comparing Figures 4.7(c) and 4.7(i) for Configuration I and also comparing Figures 4.7(d) and (j) for Configuration II shows that elongating the dielectric box under Configuration I has not changed the resulting scattered NF data as much as that under Configuration II. In other words, the effects of elongating the OI is less visible with the NF plate present. To justify this, one may take a look at the induced contrast sources for Cases I and IV under both configurations as shown in Figure 4.8, and observe that the contrast sources associated with Cases I and IV undergo less changes in Configuration I compared to that in Configuration II. We speculate that this is important for 2D inversion (tomographic inversion) of 3D targets as signals arising from anywhere other than the cross section of interest contribute to the modelling error.

4.3.1.2 Inversion results

Now, let us consider inverting the scattered NF data collected using the NF plate setup. The choice of the inversion algorithm depends on many parameters including the number of measured NF data points. In MWI, it is often desirable to choose a nonlinear inversion algorithm (e.g., contrast source inversion or Gauss-Newton inversion methods) in which the OI's dielectric profile is iteratively reconstructed. However, these nonlinear inversion algorithms are better suited when the OI is illuminated from different angles of incidence. (That is why we used a nonlinear inversion algorithm in Section 4.2.4.) As in Section 4.3.1.1, we have only illuminated the OI from one direction, the choice of nonlinear inversion algorithms is not appropriate. Therefore, we use a linear inversion algorithm in order to reconstruct the complex permittivity of the OI. In our linearized inversion approach, we assume that the scattered NF data is related to the unknown dielectric contrast χ linearly. That is, $\boldsymbol{E}^{scat} = \mathcal{L}(\chi)$

Tab. 4.1: The reconstructed OI's permittivity for Cases I and II under the two configurations.

Cases	**Calibration object's permittivity**	**Configuration I**	**Configuration II**
Case I	1.20	$1.90 - j0.29$	$1.74 - j0.04$
Case II	1.20	$1.89 - j0.32$	$1.58 - j0.25$
Case I	1.50	$1.65 - j0.03$	$1.71 - j0.01$
Case II	1.50	$1.66 - j0.01$	$1.57 - j0.23$

where $\mathcal{L}$ is a linear operator. As can be seen from (4.2), this linear operator depends on both Green's function of the system and the total field induced in the object. To determine $\mathcal{L}$, we use a calibration object similar to the method presented in [5]. Herein, for simplicity, we reconstruct one relative complex permittivity value for the OI. In addition, we limit the data collection scheme to only one data point behind the centre of the OI on the receiver domain. Thus, the operator $\mathcal{L}$ simply becomes a complex number which is multiplied by the contrast to output the scattered NF value at the single measurement point. In other words, $\mathcal{L}$ becomes the slope of the line that linearizes the relation between the scattered NF data and the contrast around the contrast of the calibration object. Denoting the dielectric contrast of the calibration object as χ^c, $\mathcal{L}$ simply becomes $\boldsymbol{E}^{scat}(\chi^c)/\chi^c$ where $\boldsymbol{E}^{scat}(\chi^c)$ is the scattered NF data due to the known calibration object. Once this $\mathcal{L}$ is found, the unknown contrast can be found as $\chi = \boldsymbol{E}^{scat}/\mathcal{L}$.

Now, consider the reconstruction of the permittivity value of the OI for the MWI setup shown in Figure 4.5 under our two configurations (with and without the NF plate) for Case studies I and II. We consider the same dielectric boxes (with the size of $\lambda/20 \times \lambda/10 \times \lambda/10$) as presented earlier in Figure 4.5 as the OI and undesired scatterer, but now with a relative permittivity of 1.70, instead of 1.50. (As will be seen, the permittivity of 1.50 will be used as one of the calibration objects.) The inversion results for Configurations I and II for two different calibration objects (having the same size as the OI) are reported in Table 4.1. As can be seen, the inversion results for Cases I and II under the focused incident field

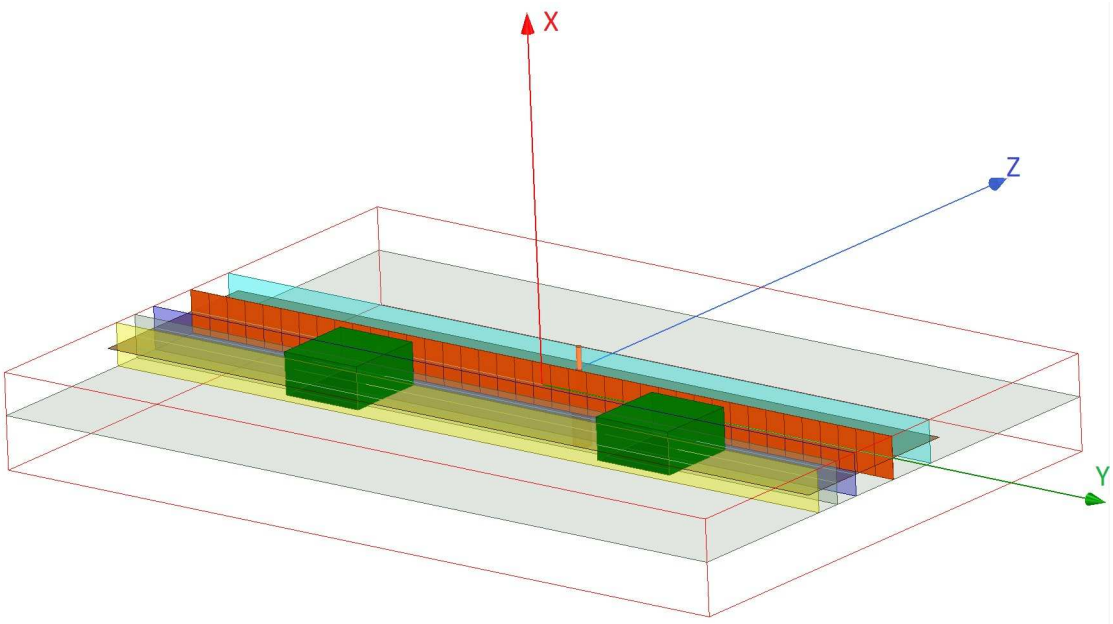

Fig. 4.9: Separation resolution study. The simulated NF plate (orange plane) setup with two dielectric objects (dark green dielectric boxes) separated by about 0.13λ from each other. (In the figure, this separation has been *exaggerated* by a larger distance for illustration clarity.) The objects have the same size of $\lambda/20 \times \lambda/10 \times \lambda/10$ along the x, y, and z directions, and have the same relative permittivity of 1.50. The description of the excitation and receiver planes are the same as Figure 4.5.

illumination (Configuration I) do not change as much as those under Configuration II. (For example, compare the change from $1.90 - j0.29$ to $1.89 - j0.32$ with the stronger change from $1.74 - j0.04$ to $1.58 - j0.25$.) This demonstrates that Configuration I is less sensitive to the presence of the undesired scatterer. It should also be noted that the inversion result of Configuration II are more accurate. We speculate that this is due to the fact that the total fields in the calibration object and that in the OI are closer to each other for the non-focused incident beam, thus, making the utilized linear inversion algorithm more suitable for Configuration II.

4.3.1.3 Separation resolution study

We now study the effect of using a focused incident NF distribution on the achievable separation resolution for one test case under the same two configurations described above. This case study for Configuration I is shown in Figure 4.9. As can be seen, there are two dielectric objects (the two dark green dielectric boxes in Figure 4.9) that have been placed approximately 0.13λ apart from each other in front of the NF plate. These two dielectric objects have the same relative permittivity of 1.50 and the same size of $\lambda/20 \times \lambda/10 \times \lambda/10$ in the x, y, and z directions with the distance between their closest facet to the NF plate being about $\lambda/60$.

To perform this study, we assume that the NF plate moves along the y direction to scan the two objects in the following three steps. Initially, its main beam is directly toward the first dielectric object, then the main beam is moved directly toward the gap between the two objects, and finally its main beam will be directly toward the second object. Similar to the previous section, this will constitute our Configuration I; for configuration II, we assume the same procedure but without the NF plate. In each of these three steps, the scattered NF data are collected on the receivers' line residing on the yellow plane. For each of these steps, we have a set of distinct receivers which are mainly within the main beam of the NF plate. (The details of these steps and our simulation details are described in Appendix F.)

We now discuss the obtained scattered NF data from this simulation study which have been depicted in Figures 4.10(a) and (b). As can be seen from Figure 4.10(a), the gap between the two dielectric boxes is detectable directly from the scattered NF data when the focused incident NF distribution is utilized. However, this is not the case when the NF plate is removed in Configuration II; this can be seen from Figure 4.10(b). As can be seen in Figures 4.10(a) and (b), the magnitude of the scattered NF data at the center of the figure, which is asso-

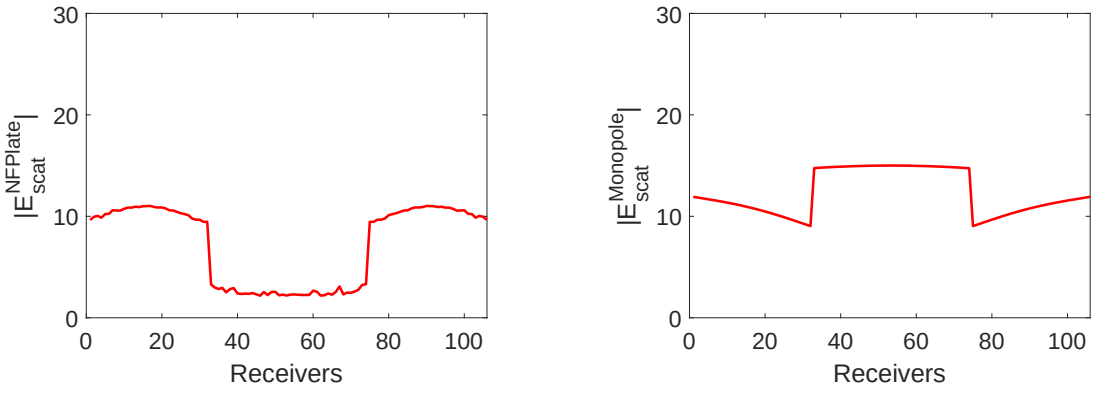

(a) Scattered NF data, Configuration I

(b) Scattered NF data, Configuration II

Fig. 4.10: Separation resolution study. Scattered NF data for (a) Configuration I and (b) Configuration II.

ciated with the gap between the two dielectric objects, is *minimum* for Configuration I and *maximum* for Configuration II. Based on the concept of contrast sources that was explained earlier in Section 4.2.1, this can be explained as follows. In Configuration I, when the NF plate directly illuminates the gap, it will not induce significant contrast sources in the two dielectric objects. Therefore, the resulting scattered signal will be small. On the other hand, when the gap is illuminated in the absence of the NF plate (i.e., Configuration II), more contrast sources will be induced in the two dielectric objects due to the wider illuminating beam. Due to the symmetry of the objects, the induced contrast sources in the two objects will be in-phase. Therefore, the resulting two contrast sources can be thought as a two-element in-phase antenna array that subsequently generates a radiation peak toward its broadside ($-\hat{z}$ direction in Figure 4.10). This, therefore, justifies why the maximum of the scattered NF data in Configuration II occurs at the center of the Figure 4.10(b). (The central receiver corresponds to the broadside direction.)

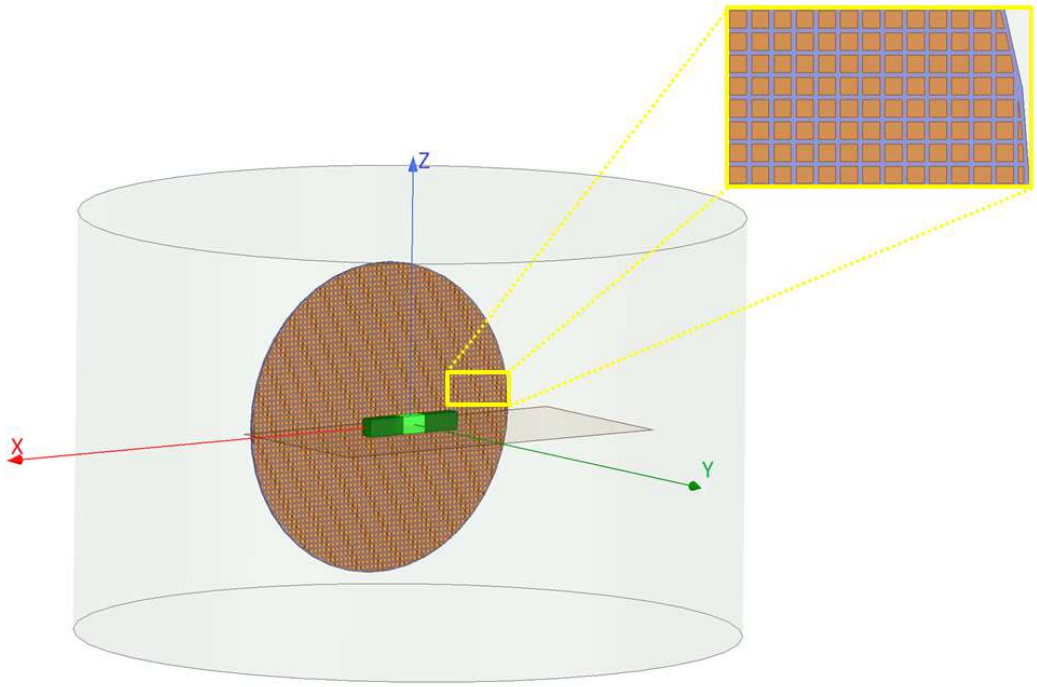

Fig. 4.11: The simulated Bessel beam launcher setup. The Bessel beam launcher (orange circular structure), introduced in [88], is parallel to the *xz* plane. A more detailed view of the capacitive sheet is shown in the inset. The brown plane (*xy* plane) contains the cross section of three dielectric boxes, all of which have the same relative permittivity of two. This figure represents our Case II study where the light green dielectric box, with the size of $\lambda/2 \times \lambda/4 \times \lambda/3$, represents the OI, and the two dark green dielectric boxes, with the size of $3\lambda/4 \times \lambda/4 \times \lambda/3$, serve as the undesired scatterers.

4.3.2 Interrogation of objects by the Bessel beam launcher

In the previous section, the idea of suppressing undesired scattering effects for MWI was studied using the NF plate. One limitation of this study lies in the fact that the OI and the undesired scatterer(s) are located on one line. This was due to the fact that the utilized NF plate provides 1D focusing. To consider more general cases, we have simulated the Bessel beam launcher presented in [88, 89] by the use of ANSYS HFSS so as to apply it to MWI applications. This Bessel beam launcher, shown in orange in Figures 4.11 and

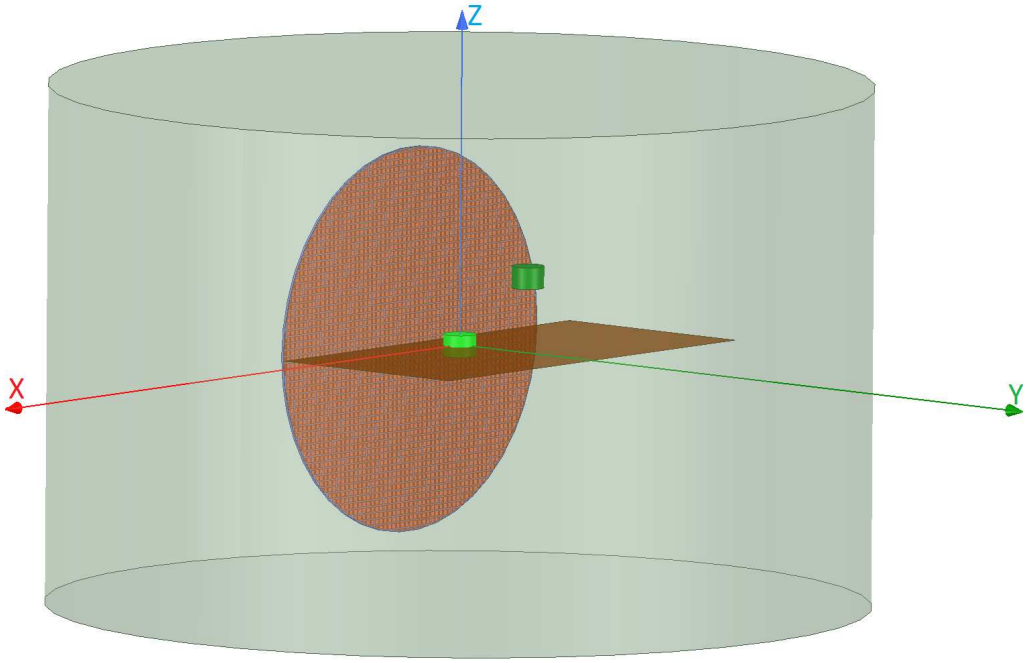

Fig. 4.12: The simulated Bessel beam launcher setup. This represents Case IV where the light green circular cylinder (with the radius of $\lambda/4$ and the height of $\lambda/3$) represents the OI and the dark green circular cylinder, with the same size and dielectric properties as the OI, represents the undesired scatterer.

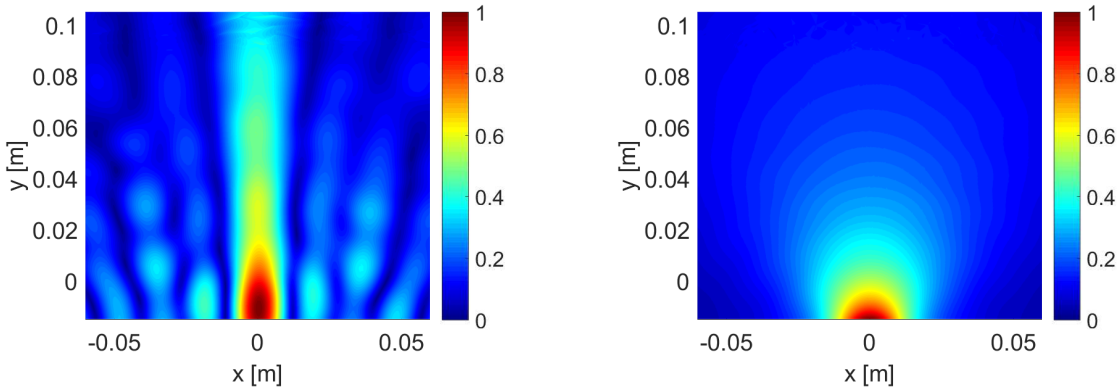

(a) Configuration I, incident NF distribution

(b) Configuration II, incident NF distribution

Fig. 4.13: Normalized magnitude of the incident NF distribution for (a) Configuration I (Bessel beam) and (b) Configuration II (dipole).

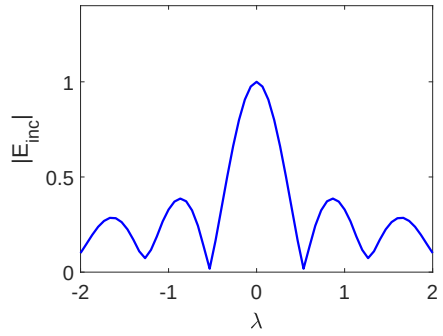

(a) Configuration I, incident NF at the receivers

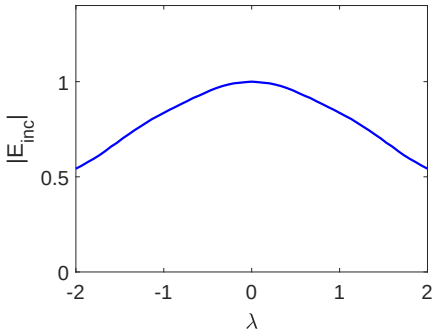

(b) Configuration II, incident NF at the receivers

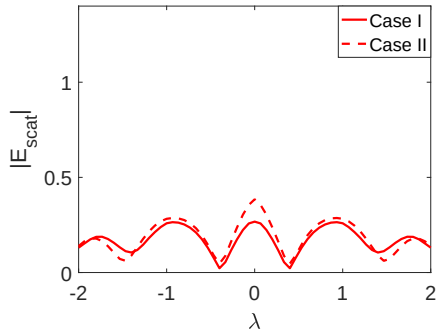

(c) Configuration I, scattered NF for Cases I & II

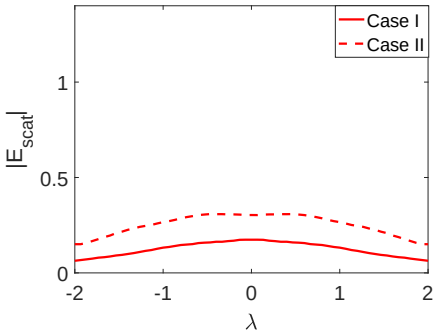

(d) Configuration II, scattered NF for Cases I & II

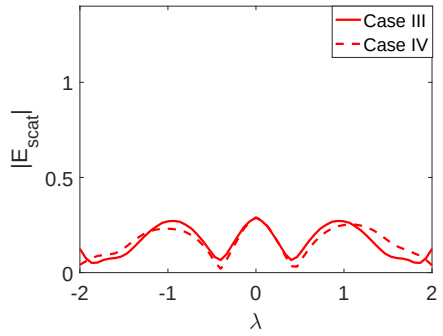

(e) Configuration I, scattered NF for Cases III & IV

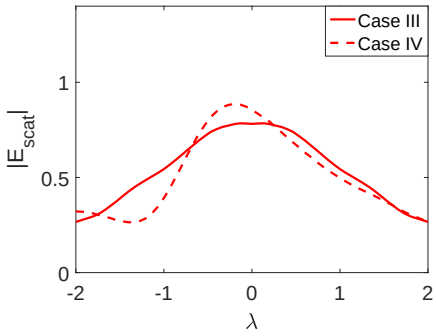

(f) Configuration II, scattered NF for Cases III & IV

Fig. 4.14: (a)-(b) normalized magnitude of the incident NF at the receiver line; (c)-(f) scattered NF at the receiver line for Configurations I and II regarding Case I (single small box), Case II (elongated box consisting of an OI and two undesired scatterers), Case III (single small cylinder) and Case IV (small cylinder with an offset extra undesired scatterer) respectively. In Configuration I, these fields correspond to the $\hat{y}$ component of the electric field, and in Configuration II, they correspond to the $\hat{x}$ component of the electric field.

4.12, is a planar structure capable of focusing electromagnetic fields into a 2D spot in front of the launcher and then maintains this focused beam over some distance away from the launcher. This distance is referred to as the non-diffracting zone of the launcher, after which the focused beam starts to diffract [88]. (The non-diffractive zone of this launcher is about 2.1λ [89].) This launcher utilizes a leaky radial waveguide in order to generate the Bessel beam [88]. This waveguide consists of a capacitive impedance sheet located over a ground plane (separated by 1 mm) which is fed by a coaxial cable. This capacitive impedance sheet is made of square patch elements (with the length of less than $\lambda/10$ printed on both sides of a substrate with $\epsilon_r = 6.15$ and the height of $h = 0.127$ mm. The diameter of this launcher is about 6λ and its frequency of operation is 10 GHz [89]. The simulated Bessel beam launcher is capable of generating electric field whose normal component, the $\hat{y}$ direction in Figures 4.11 and 4.12, is a truncated zeroth-order Bessel function of the first kind, and has a first-null beamwidth of less than λ. That is, theoretically, the incident field in the $\hat{y}$ direction will be in the form of [88]

$$E_y = J_0(k_{xz}\sqrt{x^2 + z^2})e^{-jk_y y} \tag{4.5}$$

where J_0 is the zeroth-order Bessel function of the first kind, and $k_{xz}^2 + k_y^2 = k_b^2$ where k_{xz} is the transverse wavenumber, k_y is the normal wavenumber, and k_b is the wavenumber in the background medium (free space in our case).

Similar to the NF plate case, we consider two configurations. Configuration I uses the Bessel beam launcher to irradiate the objects. On the other hand, in Configuration II, a dipole antenna replaces the Bessel beam launcher to serve as our non-focused incident beam, see Figure F.4 in Appendix F. For each of these configurations, we consider four case studies. In Case I, a rectangular dielectric box with the relative permittivity of two and the size of $\lambda/2 \times \lambda/4 \times \lambda/3$ is placed at the center of the launcher and about λ away from the

launcher (similarly, about λ away from the dipole antenna in Configuration II) as shown in Figure F.3(a). Case II not only considers the light green box as the OI, but also includes the two undesired scatterers, the dark green boxes in Figure 4.11, attached to the OI. These undesired scatterers have the same relative permittivity as the OI, each of which with the size of $3\lambda/4 \times \lambda/4 \times \lambda/3$. Case III, see Figure F.3(c), includes a new OI that is a circular dielectric cylinder with the relative permittivity of four, height of $\lambda/3$, and the radius of $\lambda/4$ located about λ away from the center of the Bessel beam launcher. Finally, Case IV adds this dark green dielectric cylinder as an undesired scatterer to Case III. Figure 4.12 shows Case IV where the light and dark green cylinders represent the OI and undesired scatterer respectively. In Case IV, the OI and undesired scatterer have the same dielectric property, and the undesired scatterer is offset by $(\lambda, \lambda/2, \lambda)$ with respect to the center of the OI. (The center of the OI is the origin of the coordinates.)

Finally, It should be noted that all the simulations concerning Configuration II (i.e., in the absence of the Bessel beam launcher) have been preformed assuming that the dipole is horizontally oriented along the x axis. Since neither a horizontal dipole nor a vertical one can generate a dominant E_y component (similar to the Bessel beam launcher), we have oriented the dipole along the x axis so that a dominant E_x can be achieved in Configuration II. This enables us to compare two different incident fields (focus and non-focused ones) with their dominant electric field components lying in the imaging plane (xy plane), similar to the transverse electric microwave tomography.

4.3.2.1 Analysis of the scattered NF data

The incident NF beams within the xy plane for Configurations I and II are shown in Figures 4.13(a) and (b). In addition, the measurement domain (receivers' locations) is taken to be a line in the xy plane and parallel to the x axis, which is 2λ away from the OI's center.

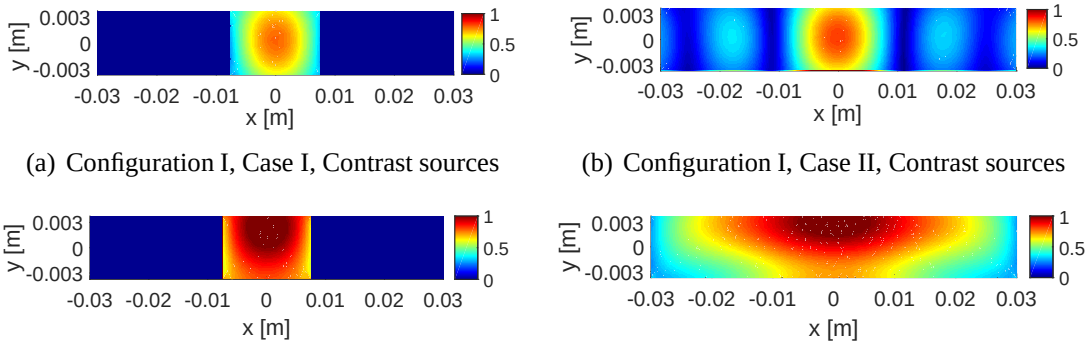

(a) Configuration I, Case I, Contrast sources

(b) Configuration I, Case II, Contrast sources

(c) Configuration II, Case I, Contrast sources

(d) Configuration II, Case II, Contrast sources

Fig. 4.15: Induced contrast sources (their magnitudes) for Cases I and II for both configurations: using the Bessel beam launcher (Configuration I), and using the dipole antenna (Configuration II). The contrast sources in each configuration have been normalized with respect to the maximum of the incident field at that configuration.

Over this line, we have distributed 61 receivers which are evenly spaced. The incident NFs on the measurement domain have also been plotted in Figures 4.14(a) and (b). (Note that the first-null beamwidth of the Bessel beam in Figure 4.14(a) is about λ.) The scattered NF data (i.e., the scattered fields at the receivers' locations) for Cases I to IV for both configurations are shown in Figures 4.14(c) to (f). As can be seen in these figures, the change in the scattered NF data due to the introduction of the undesired scatterer is less in Configuration I than that in Configuration II. Based on the discussion presented in Section 4.2.2, we speculate that this is due to the fact that the induced contrast sources have undergone less changes in Configuration I when the undesired scatterers were introduced. This has been demonstrated in Figure 4.15 where the contrast sources for both configurations regarding Cases I and II have been plotted: as can be seen, the contrast sources in Case I and II are more similar under Configuration I. (Also, note that the contrast sources $\boldsymbol{w}$ outside the box in Case I for both configurations are exactly zero since the contrast χ outside the box is zero.)

4.3.2.2 Inversion results

A simple linear inversion algorithm, the same as the one used in Section 4.3.1.2, is employed to invert the scattered NF data. To this end, we utilize a known calibration object with a complex relative permittivity value close to that of the OI. Using this calibration object, we linearize the nonlinear inverse scattering problem, and then reconstruct the complex permittivity of the OI using one measured data point located at $(0, 2\lambda, 0)$, which is directly behind the OI.

Now, let us first consider the inversion results for Cases I and II under our two configurations. As listed in Table 4.2, the calibration object has a relative permittivity of 1.50 and the size of $\lambda/2 \times \lambda/4 \times \lambda/3$ (same size as the OI in Cases I and II). The achieved reconstructed value (real and imaginary parts) under Configuration I shows less changes compared to those under Configuration II when we go from Case I to Case II. However, as can be seen the inversion results under Configuration I are quantitatively less accurate. The same observation holds when comparing the reconstructed values for Cases III and IV under the two configurations, see Table 4.2. That is, under Configuration I, when we go from Case III to Case IV, the reconstructed value shows smaller changes. However, quantitatively, Configuration II yields more accurate results.

The observation that the reconstructed values under Configuration I undergo less changes when the undesired scatterers are introduced indicates that Configuration I has provided less sensitivity to the presence of these undesired scatterers. However, it is important to discuss why the reconstructed permittivity under Configuration I is less accurate. Herein, we present a few speculations to justify this. First, the linearized inversion approach assumes that the total field in the calibration object and the OI are identical. We speculate that this assumption is more accurate for the dipole antenna due to having a broader and more uniform beam.

Tab. 4.2: The inversion results for Cases I to IV under the two configurations: with the Bessel beam (Configuration I) and the dipole antenna (Configuration II).

Cases	**Calibration object's permittivity**	**Configuration I**	**Configuration II**
Case I	1.50	$1.51 - j0.11$	$2.00 - j0.13$
Case II	1.50	$1.61 - j0.01$	$2.16 - j1.30$
Case III	3.50	$3.52 - j0.16$	$3.58 - j0.63$
Case IV	3.50	$3.54 - j0.18$	$3.77 - j0.88$

(Note that a given inversion algorithm can be more suitable to a given measurement setup depending on its assumptions.) Second, the Bessel beam has the so-called "self-healing" property [90, 91], which could reduce the sensitivity of the data to the unknown permittivity. Third, the polarization of the Bessel beam launcher used for imaging is $\hat{y}$ and that of the dipole is $\hat{x}$. Therefore, the induced contrast sources in the OI can be thought as some dipole antennas oriented in the $\hat{y}$ and $\hat{x}$ directions for Configurations I and II respectively. The measured data point, located at $(0, 2\lambda, 0)$, will then be mainly along the axes of these dipoles in Configuration I and along the broadside of these dipoles in Configuration II. This could also result in less sensitivity for Configuration I.

4.4 Discussion and Conclusions

Broadly speaking, this paper proposes that tailoring the contrast sources induced in the objects can be used advantageously in MWI. This approach has the potential to suppress (or, enhance) the sensitivity of the measured data with respect to specific regions of the imaging domain, e.g., a region which requires more accurate assessment. It was noted that we do not have full control over tailoring contrast sources since the induced total fields within the objects are dependent on the objects' unknown dielectric properties. Due to this difficulty, we have limited the scope of this paper to scenarios in which the induced total field distributions inside homogeneous objects are similar to the illuminating incident field distributions. For

the cases where this (Born) assumption does not hold, one option is to utilize an estimate of the dielectric profile of the objects (which might be obtained via a different imaging modality), and then use this prior knowledge to create an incident field distribution that results in a desired total field distribution in the objects.

We also noted the importance of tailoring the incident NF beam of the irradiating antenna, as opposed to its FF pattern, for NF MWI. In this paper, we have investigated two NF beams for imaging which satisfy our desired property: a focused NF distribution. We envision that the area of electromagnetic metasurfaces will offer a systematic tool to synthesize appropriate incident NF distributions to be utilized for imaging (e.g., see [92]). This is due to the fact that metasurfaces can transform a given excitation electromagnetic field to a desired one by imposing appropriate surface boundary conditions [93]. In addition, in this work, we did not consider tailoring the polarization of the incident field for the benefit of imaging, which can also be pursued in future.

In this paper, we have only considered focused NF beams with the purpose of minimizing the sensitivity of the collected scattering data to undesired scatterers. However, depending on the application area and purpose, one can employ incident NF beams of different distributions to optimize the retrieval of various features of interest. In addition, within the scope of our assumptions, we have intuitively discussed that this focused NF beam approach can limit the geometrical support of the induced contrast sources, and can therefore result in less required measured data points as compared to scenarios in which wider NF beams are utilized. In addition, one of the other potential advantages of focused NF beams, which has not been investigated here, is the ability to enhance the SNR of the measured data. In some applications, such as those which operate in lossy medium, enhancement of the SNR is critical to enhance the achievable reconstruction accuracy and resolution.

In summary, this paper demonstrated that the use of focused NF beams can suppress some

undesired scattering effects. From a broader point of view, the main message of this paper is the suggestion that the incident NF beam, as an MWI system design component, can be advantageously utilized to optimize some imaging aspects, and not just to irradiate the objects.

5

Focused One-Dimensional Microwave Imaging by Near-Field Plates

This chapter encloses a submitted journal paper of the author's PhD work that is currently under review. In Chapter 4, we have discussed that the use of focused incident NF distributions (as one of the parameters in MWI hardware design) can help us suppress the sensitivity of the collected data with respect to a subset of the imaging domain. It was shown that this leads to having less number of unknowns.

Herein, we propose to use another degree of freedom in addition to what has been considered in the previous chapter in order to improve the achievable accuracy and resolution. In particular, in this chapter, the use of focused receiving patterns in conjunction with focused transmitting patterns is considered. As will be discussed and demonstrated in this chapter, the simultaneous use of focused transmit and receive patterns can further alleviate the sensitivity of the collected data with respect to undesired regions. Consequently, the number of unknowns can be reduced drastically. In particular, using the proposed setup, it is shown

that we are able to reconstruct the complex permittivity of a subwavelength discretized pixel (referred to as a cell) from one single data point[1]. As will be seen, this comes with its own limitations that will also be discussed in this chapter.

The abstract of this submitted paper is first presented followed by its sections.

Abstract. The use of subwavelength focused transmit and receive patterns is considered in microwave imaging. To this end, a subwavelength focused near-field (NF) beam, generated by a NF plate, is utilized to illuminate a one-dimensional (1D) object of interest. A second NF plate, whose excitation point coincides with the focal point of the former NF plate, is then used to collect the emanating scattered field. Using these two focused beams and under a localized approximation, it is shown that a single scattered data point can be made mainly sensitive to the complex permittivity value at a subwavelength cell for 1D objects being imaged. This is in contrast to standard microwave imaging where a given measured scattered data point is typically sensitive to the complex permittivity values within the whole imaging domain. Although this study is valid within some major constraints (i.e., 1D objects, a limited working distance for NF plates, and a localized approximation), it demonstrates that the transmit and receive patterns of antennas can affect the governing equations of microwave imaging, and therefore can be utilized as two extra degrees of freedom in the design of microwave imaging systems.

5.1 Introduction

Microwave imaging (MWI) works by irradiating the object of interest (OI) by incident microwaves, and then measuring the emanating scattered fields outside the OI to infer the OI's

[1] As will be seen in this chapter, this method has its own constraints and limitations, namely, 1D objects of interest, limited working distance of near-field plates, and the use of a localized approximation.

internal complex permittivity profile [5, 7–10, 12–14, 66, 94, 95]. The scattered field data are obtained by subtracting the measured incident fields (i.e., external fields in the absence of the OI) from the measured total fields (i.e., external fields in the presence of the OI). The process of creating a quantitative image of the OI's internal complex permittivity profile from the measured external scattered field data is often referred to as the *inversion* of the data to *reconstruct* (or, to retrieve) the OI's complex permittivity profile. MWI may be performed in the time-domain or frequency-domain; herein, we consider frequency-domain MWI where time-harmonic incident microwaves are used to illuminate the OI.

5.1.1 Inverse Scattering versus Inverse Source

MWI inversion belongs to the class of electromagnetic inverse scattering problems as its main objective is to reconstruct a physical property (i.e., complex permittivity) of a passive scatterer. This is in contrast to electromagnetic inverse source problems where the goal is to reconstruct the equivalent currents of an active source, e.g., reconstructing the equivalent currents of an antenna under test from its measured radiated electromagnetic fields [96, 97]. The relation between the inverse scattering and inverse source problems can be understood from the electromagnetic volume equivalence principle. Based on this principle, an inverse scattering problem where the OI is illuminated from multiple directions can be cast as several inverse source problems that share a common property [98, 99]. This is based on the fact that scattered field data can be thought as the fields generated by volume equivalent current densities that replace the actual OI. In the context of MWI, these volume equivalent currents are often represented by the so-called *contrast sources*, which only exist within the geometrical support of the OI, and are zero otherwise [81]. These contrast sources are related to the unknown complex permittivity contrast of the OI and the unknown total field within the OI.

5.1.2 MWI Challenges

MWI inversion is challenging (at least) for the following three reasons. 1) The measured scattered data at a given receiver due to a given transmitter is typically related to the unknown complex permittivity values and the unknown induced total fields *everywhere* within the whole imaging domain. That is, one measured data point is sensitive to many unknowns. This requires the use of many transmit-receive pairs to reconstruct these many unknowns, which can be challenging in practice. 2) The unknown complex permittivity values and the unknown induced total fields within the OI are nonlinearly related to each other. This is due to multiple scattering events occurring within the imaging domain. This makes the mathematical problem nonlinear, and the inversion algorithm needs to be able to retrieve these multiple scattering events through an iterative process. 3) Due to the so-called smoothing effects [37] of Green's functions of conventional MWI systems (e.g., free space Green's function), the effects of higher spatial frequency components of the OI's contrast sources are dampened in the measured scattered data. This is reflected in the small singular values of Green's function operator mapping the contrast sources to the resulting external scattered field data. This leads to an ill-posed mathematical problem which makes the inversion process unstable; i.e., a small change in the measured scattered data can result in significant changes in the reconstruction result [100]. Appropriate regularization algorithms [54] need to be utilized to stabilize the inversion process. A major difficulty with the use of regularization techniques for this nonlinear problem is to ensure that appropriate regularization weights have been used.

5.1.3 Inverse Scattering Algorithms

Although the inverse scattering problem associated with MWI faces the above challenges, inverse scattering algorithms (or, simply inversion algorithms) offer the following two significant advantages for MWI. 1) They can achieve *quantitative* images of the OI's relative complex permittivity profile. 2) They can achieve sub-diffraction (super-resolution) images *even* when the scattered data are collected in the far-field zone [31]. This has already been verified by applying different inverse scattering algorithms to several experimentally collected data sets, e.g., see [32, 33, 101]. For example, in several cases in MWI, inverse scattering algorithms seem to be able to reconstruct a separation resolution of about $\lambda/8$ where λ is the wavelength in the background medium. However, this is not a general rule as the achievable result depends on several other factors such as the number of utilized transceivers and their locations, the OI's complex permittivity profile, signal-to-noise ratio of the measured data, etc; e.g., the achievable separation resolution worsens when imaging more complicated OIs, e.g., see [32, 33]. The main reason for achieving super-resolution using inverse scattering algorithms has been attributed to the ability of these algorithms to take into account multiple scattering events within the OI. Noting that multiple scattering events can convert evanescent waves to propagating waves [102], it has been speculated that unraveling the multiple scattering events by the inversion algorithm may enable the retrieval of high spatial information about the OI [103–105]. Although inverse scattering algorithms have successfully reconstructed many synthetic and experimental test cases, they are currently unable to ensure that a certain image quantitative accuracy and resolution can be obtained for a given OI due to the nonlinearity of the MWI problem. For example, upon reconstruction of their final image, they cannot make sure that a given region of interest which is suspicious to be cancerous has been reconstructed with a certain spatial resolution.

5.1.4 Evanescent Field Based Devices

As noted above, inverse scattering algorithms achieve super-resolution images of *scatterers* via sophisticated data processing (*software*). We now consider a different class of methods that achieves super-resolution images of active *sources* using *hardware*. That is, this class of methods solve electromagnetic inverse source problems directly at the hardware level, without the use of inverse source algorithms. An example of these hardware methods is the seminal work of Pendry on superlenses [106] where it was shown that both propagating waves and evanescent waves diverging from a point source converge back to a focal point when a negative refractive index (NRI) material is placed between the source and the focal point. Based on this, Pendry concluded that sub-diffraction imaging of sources (inverse source) can be performed using these volumetric superlenses. Later on, Grbic and Eleftheriades experimentally demonstrated this idea with a two-dimensional (2D) microwave transmission-line metamaterial [107]. However, as noted in [108] and references therein, the existence of an NRI material is accompanied by dispersion and loss which practically limits its imaging distance and resolution. To alleviate dispersion and loss, and also to make the fabrication process simpler, there have been recent progress in creating sub-diffraction focal spots using surfaces (structures whose thickness is small compared to the wavelength) as opposed to volumetric metamaterials. These surfaces have been referred to as near-field plates or metascreens. In particular, in [109], it was theoretically shown that using the so-called radiationless interference, subwavelength focusing can be achieved using near-field (NF) plates. This idea was then experimentally demonstrated in [87] where microwaves emanating from a cylindrical source was focused to a (half-power beamwidth) spot of approximately $\lambda/20$. Since this class of hardware systems utilizes evanescent waves, we use the same terminology used in [108, 110] and refer to them as evanescent field based devices.

5.1.5 Motivation

The development of MWI hardware systems has been focused on antenna and microwave circuit design to irradiate the OI and record the emanating fields while reducing the mutual coupling between co-resident antennas, choosing appropriate matching fluids, and maintaining a high dynamic range. Although several groups have contributed to the development of MWI hardware systems, the main effort in the MWI research community has remained focused on the development of the software aspect of this modality, namely, inverse scattering algorithms.[2]

On the other hand, recent advances in evanescent field based devices, such as the NIR superlens, has shown the possibility of (perfect) reconstruction of an active source merely based on a hardware system, and *without* utilizing an inverse source algorithm.[3] Since inverse scattering and inverse source problems are related, this raises the following question: *can we similarly design an MWI hardware system that facilitates the reconstruction of the complex permittivity values at subwavelength levels?* To this end, Okhmatovski *et. al.* used Green's functions of an NRI volumetric lens [112] and a Maxwell fish-eye lens [113] (instead of Green's function of free space), and developed an approach to retrieve the complex permittivity values in MWI. In their work, the use of these focusing Green's functions simplified the recovery of unknown contrast sources at subwavelength levels within the discretized OI. Once these contrast sources were found, the complex permittivity values at different cells were obtained.

Similarly, the main purpose of our paper is to demonstrate that the hardware aspect of MWI can facilitate the inversion process. The idea behind our approach is to use evanescent field

[2] Other forms of MWI algorithms such as radar-based algorithms are also available and have their own advantages; however they are outside the scope of this paper.

[3] As another example, the use of a hardware system to solve a Fredholm integral equation of the second kind has been recently demonstrated in [111].

based devices to provide subwavelength focused transmit *and* receive patterns for MWI.[4] Under some constraints and approximations to be described later, we use these focused beams to make a single measured scattered data point mainly sensitive to the complex permittivity value at a given subwavelength cell. Therefore, within our constraints and approximations, this will be a hardware system whose output (a single measured data point) is approximately related to the unknown complex permittivity value at a subwavelength cell. Although due to our constraints and limitations (i.e., 1D objects, limited working distance of NF plates, and a localized approximation) the utilized hardware system does not hold promise for practical MWI applications, this paper demonstrates the important role that transmit and receive patterns can play in MWI applications.

This paper is structured as follows. Section 5.2 presents the problem statement. Section 5.3 reviews the two main governing equations of MWI with some remarks on the achievable resolution and accuracy using inverse scattering algorithms. Our methodology, which relies on simplifying the standard MWI governing equations due to the use of focused transmit and receive patterns, is then presented in Section 5.4. Full wave simulation studies are presented in Section 5.5 to evaluate the proposed idea. The inversion results will be presented in Section 5.6, followed by some conclusions and remarks in Section 5.7. Finally, we note that the far-field term "pattern" is loosely used in this paper since MWI is often performed in the NF zone, and the utilized evanescent field based device is also for the NF zone. However, for simplicity, we use the terms "pattern", "NF distribution", and "NF beam" interchangeably throughout this paper. The time-dependency of $\exp(j\omega t)$ is also implicitly assumed in this paper.

[4] Note that the use of focused transmit patterns have also been investigated for focused microwave thermal therapy, e.g., using an antenna array [114], and also for microwave imaging to suppress undesired scattering effects [99].

5.2 Problem Statement

We consider the simultaneous use of focused transmit and receive patterns in MWI to investigate if a *single* measured data point can be made mainly sensitive to the complex permittivity value at a *single* subwavelength cell. If this could be achieved, we would essentially have a non-invasive probe whose measured data is directly related to the complex permittivity value at that subwavelength cell.[5] This is in contrast to standard MWI where a single measured data point is related to several unknown complex permittivity values within the whole OI. To this end, our approach is to have a subwavelength focused transmit *and* receive patterns that simultaneously look at a subwavelength cell within the imaging domain. To visualize this, consider the transmit and receive patterns with respect to a square imaging domain discretized into 4×4 cells as shown in Figure 5.1 for four different configurations where Configuration IV represents the case with more focused transmit (blue) and receive (red) patterns.

We emphasize that the above objective is, in general, *not* possible due to scattering events within the OI. As will be seen later, the reason that we can (to some extent) achieve this objective is due to 1) utilizing subwavelength focused transmit and receive patterns, 2) considering 1D OIs, and 3) applying a localized approximation. Despite the fact that our objective is pursued within this limited framework, our broader goal is to demonstrate that the transmit and receive patterns are two degrees of freedom that can affect the MWI's governing equations, and can be useful in tailoring the sensitivity of the MWI data with respect to unknown complex permittivity profile. This is important as to the best of our knowledge, these two degrees of freedom have not been taken advantage of in the the design of MWI

[5] In [112, 113], to find the complex permittivity value at a specific subwavelength cell, it is still necessary to perform multiple measurements. In other words, in these two works, although there is a one-to-one correspondence between a given measured scattered data point and the contrast source in a given subwavelength cell, this one-to-one correspondence does not hold between the measured data point and the complex permittivity value in that subwavelength cell.

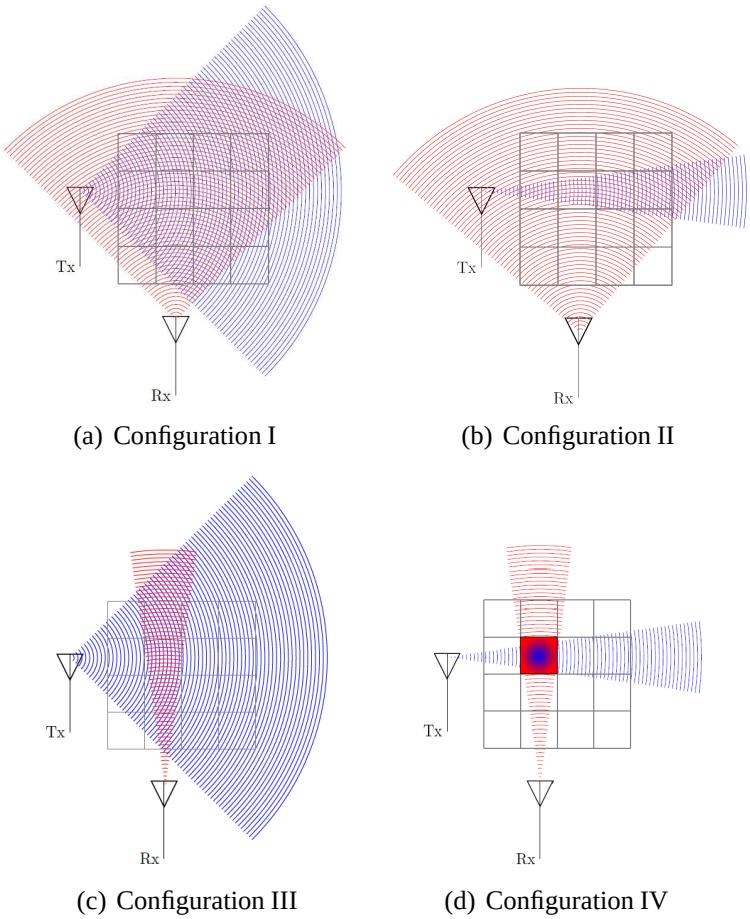

(a) Configuration I (b) Configuration II

(c) Configuration III (d) Configuration IV

Fig. 5.1: The transmit pattern (Tx) shown in blue and the receive pattern (Rx) shown in red *together* tailor the sensitivity of the measured data with respect to the complex permittivity values within the imaging domain. (The imaging domain has been depicted by a 4×4 discretized square.) Configuration IV depicts the scenario where the transmit and receive patterns are more focused.

systems.

To this end, inspired by the promise of easier fabrication, low profile, and light weight of NF plates as compared to NIR volumetric lenses, we use two NF plates in our setup, one as the transmitter to illuminate the OI and the other as the receiver to collect the resulting scattered field. This investigation is performed by full wave simulation of these NF plates along with the OI using ANSYS HFSS. For each OI, one single scattered data point is collected using HFSS. The location of this data point coincides with the focal point of the

receiving NF plate. This single data point will then be inverted in a 2D scalar fashion[6] to retrieve the complex permittivity at a certain subwavelength cell. This subwavelength cell coincides with the focal point of the transmitting NF plate. Finally, we note the following major constraint in our study. The utilized NF plates (practically) suffer from having a limited working distance; i.e., the distance between the focal spot and the NF plate is small compared to the wavelength [108]. In addition, the NF plates provide 1D focusing. Due to these limitations, we have restricted ourselves to 1D OIs (small thickness), as opposed to 2D OIs shown in Figure 5.1 or 3D OIs.

5.3 Review: Microwave Imaging

The main purpose of this section is to review the two main governing equations of MWI: the so-called data and domain equations. Let us consider a non-magnetic OI with an unknown relative complex permittivity profile $\epsilon(\boldsymbol{q})$ where $\boldsymbol{q}$ is the position vector spanning the imaging domain D. In addition, we denote the measurement domain S which is located outside D. The position vector $\boldsymbol{p}$ will then span the measurement locations on S. In summary, $\boldsymbol{q} \in D$ and $\boldsymbol{p} \in S$. In MWI, the unknown quantity is often formulated as the unknown contrast profile $\chi(\boldsymbol{q})$ expressed as

$$\chi(\boldsymbol{q}) = \frac{\epsilon(\boldsymbol{q}) - \epsilon_b}{\epsilon_b} \tag{5.1}$$

where ϵ_b is the known relative complex permittivity of the homogeneous background medium. When the OI is illuminated by an incident field of a transmitting antenna, denoted by E^{inc}, the resulting total fields at the receiving antennas located on S are measured, which are referred to as the total field data. The same measurements are repeated in the absence of the

[6] In the 2D scalar inversion, the incident electric field is assumed to be perpendicular to the cross section being imaged. As will be seen later, the utilized NF plates automatically satisfy this assumption.

OI which result in the incident field data. The subtraction of the incident data from the total data results in the scattered field data denoted by $E^{\text{scat}}(\boldsymbol{p})$. These scattered field data, which are often collected for several transmit and receive pairs, are then fed to an inverse scattering algorithm to reconstruct $\chi(\boldsymbol{q})$.

5.3.1 Data and Domain Equations

As noted earlier, the scattered field data can be thought as the fields generated by the so-called contrast sources. These contrast sources, which merely exist within the OI's geometrical support, are denoted by $w(\boldsymbol{q})$ and expressed as

$$w(\boldsymbol{q}) = \chi(\boldsymbol{q})E(\boldsymbol{q}) \tag{5.2}$$

where $E(\boldsymbol{q})$ is the total field in the OI. The data equation then relates these contrast sources to the scattered field data as [58]

$$E^{\text{scat}}(\boldsymbol{p}) = \mathcal{G}_S(w(\boldsymbol{q})) \tag{5.3}$$

where $\mathcal{G}_S$ is a linear operator that links the information within D to the information within S. This operator is defined as follows

$$\mathcal{G}_S(w(\boldsymbol{q})) = k_b^2 \int_D g(\boldsymbol{p} \in S, \boldsymbol{q}) w(\boldsymbol{q}) d\boldsymbol{q} \tag{5.4}$$

where g denotes Green's function of the imaging medium, and k_b is the wavenumber in the background medium.

The other main equation in MWI governs the interactions only within D, and is called the

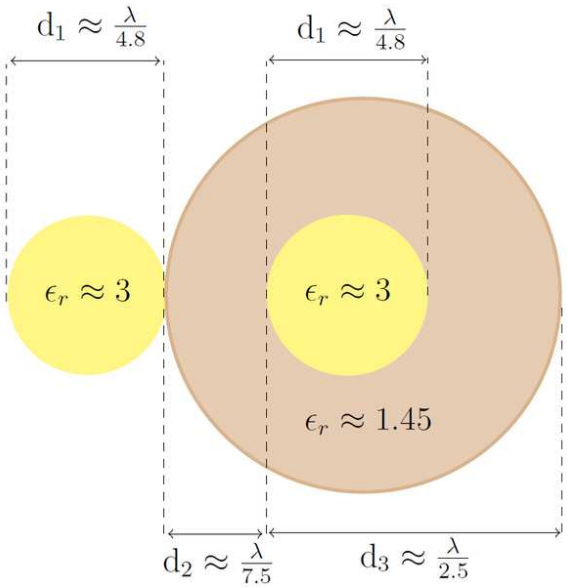

Fig. 5.2: FoamTwinDielTM target used by the Institut Fresnel [1]. The three lengths (i.e. , d_1, d_2, and d_3) shown here are in terms of the free space wavelength at the operational frequency of 2 GHz. (The relative permittivities are about 1.45 and 3.)

domain equation, and is expressed as

$$w(\boldsymbol{q}) = \chi(\boldsymbol{q})E^{\text{inc}}(\boldsymbol{q}) + \chi(\boldsymbol{q})\mathcal{G}_D(w(\boldsymbol{q})) \tag{5.5}$$

where the domain operator $\mathcal{G}_D$ is defined as

$$\mathcal{G}_D(w(\boldsymbol{q})) = k_b^2 \int_D g(\boldsymbol{q} \in D, \boldsymbol{q}')w(\boldsymbol{q}')d\boldsymbol{q}'. \tag{5.6}$$

The equations (5.3) and (5.5) govern the MWI problem. These two equations can be combined into one equation for the main unknown χ as [115]

$$E^{\text{scat}}(\boldsymbol{p}) = \mathcal{G}_S(\chi(\mathcal{I} - \mathcal{G}_D\chi)^{-1}E^{\text{inc}}) \tag{5.7}$$

where $\mathcal{I}$ is the identity operator. The nonlinearity of the inverse scattering problem is evident from the operator $(\mathcal{I} - \mathcal{G}_D\chi)^{-1}$ which is dependent on the unknown χ. Approximating this

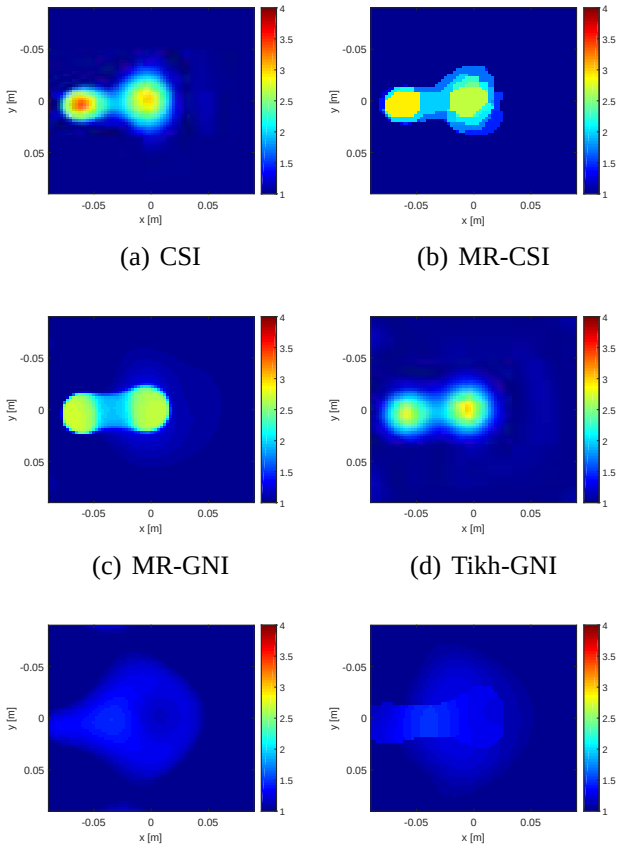

(a) CSI (b) MR-CSI

(c) MR-GNI (d) Tikh-GNI

(e) Born Approximation (f) Born Approximation with MR

Fig. 5.3: The reconstruction of the real-part of the relative complex permittivity of FoamTwinDielTM target at 2 GHz using (a)-(d) four different nonlinear inversion algorithms (CSI, MR-CSI, MR-GNI, and Tikh-GNI respectively), and (e)-(f) using the Born approximation without and with multiplicative regularization (MR).

operator by the first term in its Neumann series expansion, i.e., $(\mathcal{I} - \mathcal{G}_D\chi)^{-1} \approx \mathcal{I}$, results in the famous Born approximation [115], which does not take into account multiple scattering events. On the other hand, the use of nonlinear inversion algorithms can be intuitively thought as including more terms of the Neumann series expansion in an iterative fashion, thus capturing more multiple scattering events.

5.3.2 Resolution and Quantitative Accuracy

For the sake of completeness and to avoid misunderstanding that evanescent field based devices are required to obtain super-resolution in MWI, we briefly review the ability of inverse scattering algorithms in achieving super-resolution. To this end, we consider a widely-used far-field data set: *FoamTwinDielTM* data set from Fresnel Institute [1]. This far-field data set was collected from the dielectric target depicted in Figure 5.2 in an anechoic chamber using 18 transmitters and 241 receivers per transmitter. Herein, we consider the lowest frequency range of this data set, i.e., 2 GHz. At this frequency, the measured data were collected at a radius of about 11.13λ away from the centre of the target. The inversion of these 18×241 data points using four different algorithms, namely (i) contrast source inversion (CSI) [81], (ii) CSI with the weighted L_2 norm total variation multiplicative regularizer (MR), known as MR-CSI [58], (iii) Gauss-Newton inversion using the MR, known as MR-GNI [2, 3] and (iv) GNI using Tikhonov regularization (Tikh-GNI) [51, 116], have been shown in Figure 5.3(a)-(d). As can be seen, the separation $d_2 = \lambda/7.5$ between the two small dielectric cylinders has been successfully resolved using all these inverse scattering algorithms. It is instructive to note the reconstruction under the Born approximation (without and with MR) [38] shown in Figure 5.3(e)-(f) where the separation has not been resolved, and also the dielectric values are not accurate.

5.4 Methodology

We now discuss that the transmit and receive patterns affect the MWI's governing equations. The main idea behind our methodology is to make the data and domain equations mainly *localized* at a sub-region within the whole imaging domain. To this end, we consider an extreme case where the scattered field data from 1D OIs are collected by subwavelength

focused NF beams. For this extreme case, and under our constraints and approximations to be discussed later, we localize the data and domain equation mainly at a subwavelength cell. Then, we use one scattered field data point to reconstruct the complex permittivity at that subwavelength cell. Therefore, we are not reconstructing the complex permittivity values in the whole OI, but merely at a given subwavelength cell.

5.4.1 MWI with a Focused Receiver

Let us start by observing the data equation, see (5.3). This equation states that *all* the contrast sources within the imaging domain D are responsible for generating the scattered field at a given receiver. That is, the scattered field at a given receiver is a weighted summation of these contrast sources. The weights are determined by Green's function of the imaging system, and the summation is performed by integration over the whole imaging domain. Thus, in the discrete form, where the imaging domain is discretized into N subwavelength cells, the data equation can be written as

$$E^{\text{scat}} = \mathcal{G}_S(w) = \sum_{i=1}^{N} \alpha_i w_i \tag{5.8}$$

where w_i is the contrast source at the ith subwavelength cell, and α_i is the weight of this contrast source. (We have dropped the position vectors $\boldsymbol{p}$ and $\boldsymbol{q}$ for simplicity.) At each subwavelength cell, the contrast source is assumed to be uniform. In many MWI case studies where imaging medium is assumed to be free space, α_i will be related to the free space Green's function, and (5.8) implicitly assumes that the receiver has an *omnidirectional* pattern.

Imagine now a scenario that instead of an omnidirectional receiving pattern, we utilize a receiving hardware that has a pattern focused on a subwavelength cell within the imaging

domain, say at the mth cell[7]. Thus, in this scenario, we will have a focused data operator, denoted by $\mathcal{G}_S^{\text{foc}}$, that mainly *sees* the contrast source at the mth cell. Then, the received scattered field can be written as

$$E^{\text{scat}} = \mathcal{G}_S^{\text{foc}}(w) = \sum_{i=1}^{N} \alpha_i^{\text{foc}} w_i \approx \alpha_m^{\text{foc}} w_m \tag{5.9}$$

where w_m is the contrast source at the mth cell toward which the receiving pattern is focused, and α_m^{foc} is its complex coefficient weight. This coefficient is, in fact, related to Green's function of the new system. As can be seen, the focused data operator $\mathcal{G}_S^{\text{foc}}$ now links one measured data point to one contrast source.

Assuming that we know α_m^{foc}, we can then retrieve w_m from a single measured data point E^{scat}. However, finding w_m does *not* mean that we can find the complex permittivity contrast at this subwavelength cell denoted by χ_m. This can be explained by writing the discretized domain equation (5.5) for w_m as

$$w_m = \chi_m E_m^{\text{inc}} + \chi_m \mathcal{G}_D(w) = \chi_m E_m^{\text{inc}} + \chi_m \sum_{i=1}^{N} \beta_i w_i \tag{5.10}$$

where E_m^{inc} is the incident field at the mth cell, which is often assumed to be known in MWI. As can be seen, w_m not only depends on the unknown χ_m but also depends on unknown contrast sources at other cells, each of which weighted by the complex coefficient β_i. Therefore, to find χ_m, we need to know all the contrast sources, as can be seen from

$$\chi_m = \frac{w_m}{E_m^{\text{inc}} + \sum_{i=1}^{N} \beta_i w_i}. \tag{5.11}$$

This may be done by moving the focused receiver to scan all the subwavelength cells within

[7] Since we have considered 1D OIs, the discretization is performed along one direction, e.g., along the y direction in Figure 5.5.

the imaging domain, and then finding each of the contrast sources individually. Once all the contrast sources are obtained, then χ_m can be found using (5.11). We note that this part of our approach (i.e., the use of a focused receiver) is similar to [112, 113] with two upcoming differences: (i) we will use a NF plate for generating a focused NF beam, and (2) we will use full-wave simulations of the NF plate in the presence of the OI, instead of merely considering Green's function of an ideal NIR lens.

5.4.2 MWI with a Focused Receiver and a Focused Transmitter

Let us now consider the use of a focused transmitter having a focused incident field of $E^{\text{inc,foc}}$. In the following analysis, in conjunction with a focused transmitter, we also utilize a localized approximation where the contrast source w is approximated by $\gamma E^{\text{inc,foc}}$ [117]. (The function γ can depend on the contrast function χ and the domain operator $\mathcal{G}_D$.) As noted in [117], the localized approximation $w \approx \gamma E^{\text{inc,foc}}$ can cover different forms of approximations including the Born and extended Born approximations.[8] Assuming that our incident field $E^{\text{inc,foc}}$ is focused on the mth cell (and thus, negligible at other cells)[9], and considering the localized approximation $w \approx \gamma E^{\text{inc,foc}}$, the contrast source at the mth cell, i.e., w_m, is subsequently taken to be the dominant contrast source. Based on this, (5.10) will be approximated as

$$w_m = \chi_m E_m^{\text{inc,foc}} + \chi_m \mathcal{G}_D^{\text{foc}}(w) \approx \chi_m E_m^{\text{inc,foc}} + \chi_m \beta_m^{\text{foc}} w_m \tag{5.12}$$

where $E_m^{\text{inc,foc}}$ denotes the focused incident field at the mth cell, and $\mathcal{G}_D^{\text{foc}}$ denotes the domain operator in the new imaging medium. Note that $\mathcal{G}_D^{\text{foc}}(w)$ has been approximated by $\beta_m^{\text{foc}} w_m$ where β_m^{foc} is a complex number. Therefore, based on (5.12), the contrast source w_m is

[8] In the case of the Born approximation, we have $\gamma = \chi$, and in the case of the extended Born approximation, we have $\gamma = \frac{\chi}{1-\mathcal{G}_D(\chi)}$ [117].

[9] Note that since the NF plates create 1D focusing and the OI is also 1D, this is a valid assumption.

approximated by[10]

$$w_m \approx \gamma E_m^{\text{inc,foc}} \approx \frac{\chi_m}{1-\chi_m \beta_m^{\text{foc}}} E_m^{\text{inc,foc}}. \tag{5.13}$$

Finally, using (5.9) and (5.13), we can obtain χ_m as

$$\chi_m \approx \frac{E^{\text{scat}}}{\alpha_m^{\text{foc}} E_m^{\text{inc,foc}} + \beta_m^{\text{foc}} E^{\text{scat}}}. \tag{5.14}$$

As can be seen, (5.14) directly relates the measured scattered data point to the complex permittivity contrast at the mth subwavelength cell. As will be discussed in Section 5.6.1, α_m^{foc} and β_m^{foc} can be found, and thus, with having a single scattered data point E^{scat}, we will be able to retrieve χ at the mth subwavelength.

5.4.3 Limitation

Note that a subwavelength focused incident field does not necessarily result in having a dominant contrast source at the mth subwavelength cell and negligible contrast sources at the other cells due to scattering events within the OI. This can then invalidate our localized approximation, and consequently invalidate (5.14). Herein, our 1D assumption regarding the OI plays a major role in our ability to employ the above methodology. For general 2D and 3D OIs where (5.14) fails, the main message of the above methodology, i.e., the importance of the transmit and receive patterns, still holds. For example, for a general OI when an overall knowledge about its complex permittivity is available, one might synthesize an incident field to have a focused total field at a sub-region within the whole imaging domain.[11] The receive pattern can then intersect with this illuminated sub-region so that the sensitivity with respect to the overlapped region can be potentially improved.

[10] It is worth noting the similarity between the localized approximation in (5.13) with the extended Born approximation shown in Footnote 8.

[11] For example in [114], the prior knowledge about the complex permittivity image of the OI has been used to synthesize a focused total field in a region within the breast for microwave thermal therapy.

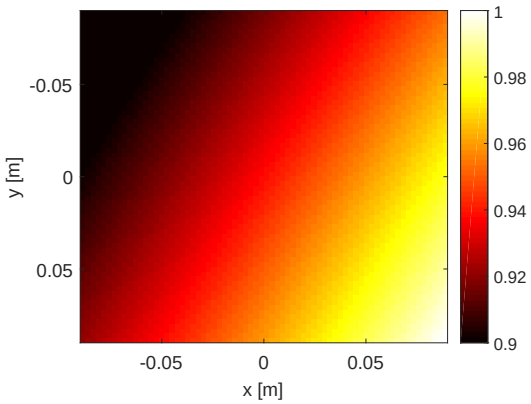

Fig. 5.4: Normalized magnitude of the sensitivity for the *FoamTwinDielTM* target when the transmitter is located at $(11.13\lambda, 0)$ and the receiver is located at $(5.57\lambda, 9.64\lambda)$. The wavelength of operation is $\lambda = 0.15$ m.

5.4.4 Sensitivity

It is instructive to view this focused approach as a way to tailor the sensitivity of the measured data with respect to complex permittivity values at different cells. To this end, let us consider the sensitivity of the scattered field $E^{\text{scat}}(\boldsymbol{p})$ at a receiver located at $\boldsymbol{p}$ due to a given transmitter with respect to the complex permittivity contrast profile $\chi(\boldsymbol{q})$. The variation in the scattered field, denoted by ΔE^{scat}, due to having a $\Delta\chi(\boldsymbol{q})$ perturbation in the contrast profile can be mathematically expressed as

$$\Delta E^{\text{scat}}(\boldsymbol{p}) \approx \frac{\partial E^{\text{scat}}}{\partial \chi}(\Delta\chi(\boldsymbol{q})) \tag{5.15}$$

where $\partial E^{\text{scat}}/\partial\chi$ denotes the *sensitivity* (or, Jacobian) operator that when operates on the perturbation $\Delta\chi$ results in the subsequent variation in the scattered field data. In nonlinear (iterative) inversion algorithms, the sensitivity operator $\partial E^{\text{scat}}/\partial\chi$ is evaluated with respect to the current estimate of the contrast profile. In particular, if we evaluate the derivative at

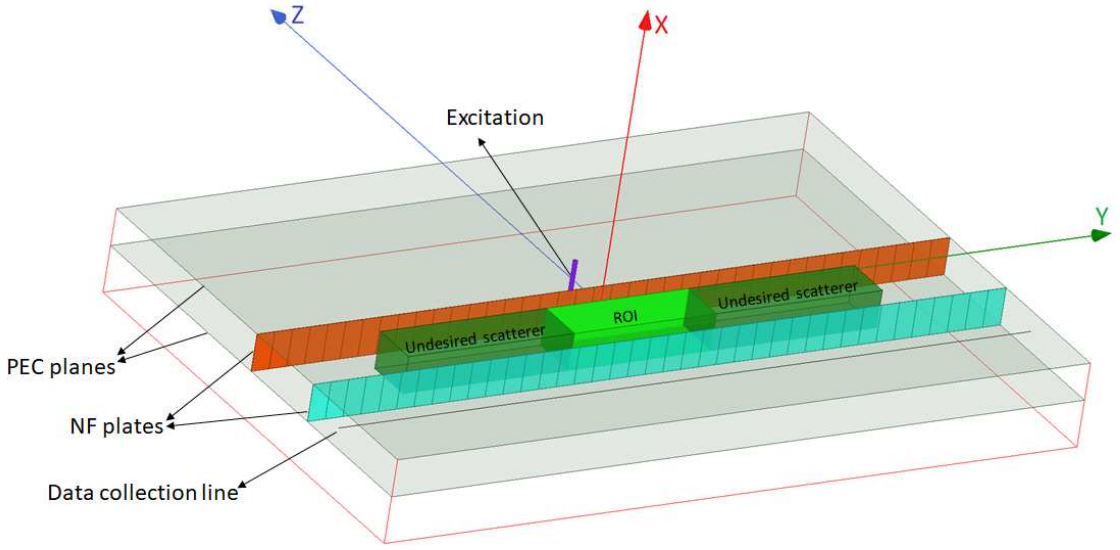

Fig. 5.5: The simulated setup in ANSYS HFSS consisting of two NF plates with a dielectric slab between them. As can be seen, each NF plate is parallel to the y axis, and consists of 39 unit cells, each of which is an appropriate capacitive element [87]. The origin of the coordinates is at the 20th unit cell (the middle unit cell) of the orange NF plate. The purple cylinder which is placed on the z axis at $z = \lambda/15$ is a monopole that excites the orange NF plate. The orange NF plate then creates a focused incident field at its focal point which is located on the z axis at $z = -\lambda/15$ (i.e., at the geometrical centre between the two NF plates). The induced contrast source at this focal point can be thought as an excitation for the light blue NF plate which is located at $z = -2\lambda/15$. The resulting scattered field is then received at the focal point of the light blue NF plate which is located on the z axis at $z = -3\lambda/15$. The data collection line is $z = -3\lambda/15$, and the focal point of the light blue NF plate is located at the intersection of this line with the z axis. The dielectric slab shown in this figure corresponds to Case II (ROI with undesired scatterers) under Configuration IV.

$\chi = 0$ (i.e., sensitivity under the Born approximation), we will have [52, Appendix D.1]

$$\Delta E^{\text{scat}}(\boldsymbol{p}) \approx \frac{\partial E^{\text{scat}}(\boldsymbol{p})}{\partial \chi}\Big|_{\chi=0}(\Delta\chi) = k_b^2 \int_{\mathcal{D}} g(\boldsymbol{p},\boldsymbol{q}) E^{\text{inc}}(\boldsymbol{q}) \Delta\chi(\boldsymbol{q}) d\boldsymbol{q}. \tag{5.16}$$

In a typical (non-focused) MWI system, Green's function $g(\boldsymbol{p},\boldsymbol{q})$ that links a cell within the imaging domain to the receiving point as well as the incident field at different cells within the imaging domain are relatively uniform. Therefore, a given measured data point (say, at location $\boldsymbol{p}$) is typically sensitive to all subwavelength cells within the imaging domain.

This has been demonstrated in Figure 5.4 for the *FoamTwinDielTM* target considered in Section 5.3 where the normalized magnitude of the sensitivity (evaluated at $\chi = 0$) for the receiver located at $(x = 5.57\lambda, y = 9.64\lambda)$ and the transmitter located at $(x = 11.13\lambda, y = 0)$ has been shown. ($\lambda = 0.15$ m.) As can be seen, the normalized sensitivity is close to unity for all the subwavelength cells within the imaging domain. Using the focused receiver and transmitter configuration, (5.16) needs to be modified by replacing g with Green's function of the focusing medium g^{foc}, and by replacing E^{inc} with the focused incident field $E^{\text{inc,foc}}$. Noting that g^{foc} includes the effect of the focused pattern, it can be understood that both the focused transmit and receive patterns can be utilized to tailor the sensitivity distribution.

5.4.5 Non-uniqueness

In the inversion process presented above, we first find w_m from E^{scat} (inverse source), and then we retrieve χ_m. This may raise concerns since it is well-known that an inverse source problem has a non-unique solution, e.g., see [26]. Due to this non-uniqueness, Chew *et. al.* noted that solving for contrast sources in the data equation (5.3), and then using these contrast sources in the domain equation (5.5) to retrieve the complex permittivity contrast is not appropriate [83].[12] Therefore, in general, the contrast sources within the imaging domain should not be directly inverted. However, our case is different as we use a single measured data point to find the contrast source at a single subwavelength cell (not within the whole imaging domain). In other words, as opposed to contrast sources within the whole imaging domain which can take different forms to generate the same scattered field data (non-uniqueness), our unknown contrast source is limited to only one subwavelength cell. Thus, for our case, the unknown contrast source does not have the freedom to take different forms.

[12] Note that this is different than the contrast source inversion [81] method where the data and domain equations are simultaneously utilized, through which the non-uniqueness issue is handled.

5.5 Simulation Study

To implement the above idea, we consider a planar device which can focus electromagnetic waves into a subwavelength spot (cell). As noted in Section 5.1, this planar structure is referred to as a near-field (NF) plate [87]. Herein, we first provide a brief introduction to NF plates and their design procedure. This will then be followed by different ANSYS HFSS simulation studies (Electronic Desktop 2018) to evaluate the proposed idea.

5.5.1 Near-Field (NF) Plates

A NF plate, as explained in [87, 118], is an electrically thin patterned planar structure that acts as a wave transformer, transforming an incident electromagnetic field impinging on its input side to a field on its output side that is focused in a subwavelength region at a NF distance away from the NF plate. The operation of this device is based on Merlin's work [109] that introduced a specific aperture field distribution that converges to a focus away from the aperture. A NF plate is an engineered passive surface that produces this aperture field distribution when illuminated by an incident electromagnetic field. This aperture field distribution consists of highly oscillating fields (predominantly evanescent) that can then be combined constructively and destructively within the NF zone so as to form the desired focused subwavelength pattern on the plane called focal plane [118]. This process has been referred to as the radiationless interference [109] due to its use of the evanescent wave (i.e., non-radiative components of the fields) interference.

Let us now review the design procedure of the NF plate. As described in [118, Chapter 2], the first step is to consider a subwavelength focal pattern on the focal plane. The desired focal pattern is then back-propagated on the surface of the NF plate to find the required

total field on the aperture. The incident field impinging on the NF plate is assumed to be a cylindrical wave, and therefore, the incident field is modelled by a zeroth-order Hankel function of the second kind. Knowing both the incident and total fields on the aperture, the required current density on the NF plate can be found.[13] Once the required current density on the NF plate is known, the impedance profile of the NF plate can be obtained by dividing the required total field on the aperture by the required current density on the aperture. This impedance profile is then discretized into unit cells, and can then be realized, e.g., using the distributed interdigitated capacitors [87]. (In this work, the NF plate is simulated in ANSYS HFSS using impedance sheets.)

5.5.2 Focused Microwave Imaging Setup

The utilized setup, shown in Figure 5.5, includes two thin passive NF plates with the dimensions of about $\lambda \times \lambda/20$ in the y and x directions respectively where λ is the wavelength in the air at the operational frequency of 1 GHz. Both of these two identical NF plates are based on the design and parameters originally presented in [87]: they consist of 39 capacitive unit cells that are placed within a parallel plate waveguide with the height of $\lambda/20$ [87]. The presence of the perfect electric conductor (PEC) of the parallel plate waveguide enables us to study the 2D scalar imaging problem as the electric field will have only one component E_x, and the OI and NF plates can be assumed to be of infinite size along the x direction. (The OI is also electrically thin in the z direction, thus, making it a 1D OI.) As described in the caption of Figure 5.5, each NF plate has an excitation point and a focal point. The focal point of the transmitting NF plate located at $(0, 0, -\lambda/15)$ which coincides with the excitation point of the receiving NF plate. This focal point is the center of the subwavelength

[13] As noted in [118], the required currents density consists of two parts: one for canceling the effect of the incident field on the output side of the NF plate, and the other for creating the required focused field distribution.

Tab. 5.1: Four Data Collection Configurations. (Configuration IV is the main configuration considered herein.)

	Transmit Pattern	Receive Pattern
Configuration I	Omnidirectional	Omnidirectional
Configuration II	Focused	Omnidirectional
Configuration III	Omnidirectional	Focused
Configuration IV	**Focused**	**Focused**

cell at which the complex permittivity will be reconstructed in Section 5.6.

5.5.2.1 Transmitting NF Plate

The orange NF plate can be thought as the transformer that transforms an omnidirectional transmitting pattern into a focused one. This NF plate is illuminated by a monopole, shown by a purple cylinder in Figure 5.5, that has been placed at $z = \lambda/15$ on the z axis behind the transmitting NF plate. This purple monopole has been created by the extension of the inner conductor of a coaxial cable. (The coaxial cable has not been shown in Figure 5.5.) Once illuminated by the monopole, this orange NF plate will then generate a focused incident NF field at its focal point in front of the plate at $z = -\lambda/15$ on the z axis, which is the midpoint between the two NF plates.

5.5.2.2 Receiving NF Plate

The receiving NF plate, i.e., the light blue plate, is separated by $2\lambda/15$ from the transmitting one. This separation is chosen so that the focal point of the transmitting orange NF plate coincides with the excitation point of the receiving NF plate. All the OIs considered in our case studies are placed between these two NF plates.[14] Once the OI is illuminated, contrast

[14] Since the two NF plates are placed electrically close to each other, the width of the OI which is along the z axis in Figure 5.5 will be automatically limited, i.e., 1D objects. To overcome the width limitation, the NF plates need to be designed to have longer working distances. As noted in [108], practical issues such as power

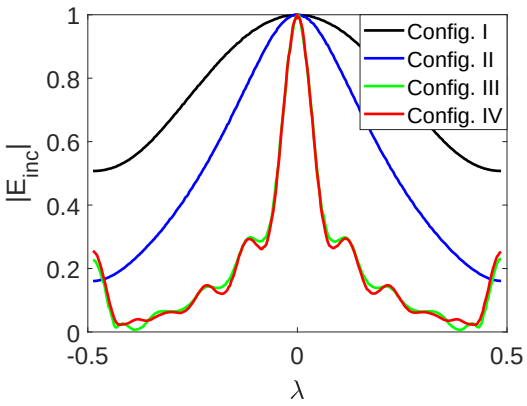

Fig. 5.6: Comparison of the normalized magnitude of the incident field at the data collection line for the four configurations. (Each incident field has been normalized to its own maximum value due to the presence of the reflections from the NF plates.)

sources are induced in the OI, whose corresponding scattered fields will interact with the light blue receiving NF plate, and will then be collected along the data collection line, i.e., $z = -3\lambda/15$ line. (Later on, we will only use one data point for reconstruction.)

5.5.3 Comparison of Four Data Collection Configurations

As noted above, our setup consists of two NF plates. To demonstrate the advantages of our setup, we consider the following three extra configurations. (i) In Configuration I, both of the NF plates are removed from the setup; thus the OI is merely illuminated by the monopole, and the receiver is assumed to be an omnidirectional receiver. (ii) In Configuration II, the orange NF plate, i.e., the one used for the focused transmit pattern, is added to the setup, but the light blue NF plate is removed and therefore the receiver is assumed to be omni-directional. (This configuration is similar to the study performed in [99].) (iii) In Configuration III, the light blue, i.e., the one used for the focused receive pattern is added to the setup while the orange NF plate is removed from the setup, and thus the OI is illuminated

and noise consideration do not allow a working distance of more than $\lambda/4$ [108].

by an omnidirectional pattern [15]. (This will be similar to the use of an NIR lens in [112].) (iv) Finally, Configuration IV is the main set up considered in this paper which includes both the transmitting and receiving NF plates. These four configurations have been summarized in Table 5.1.

5.5.3.1 Incident NF Data

Let us take a look at the normalized magnitude of the incident field data along the data collection line. As can be seen in Figure 5.6, the incident field becomes more focused for Configurations III and IV. This is expected as both Configurations III and IV use a receiving NF plate. A question might arise regarding why the incident field of Configuration II, which uses a transmitting NF plate, is not sufficiently focused. This can be understood by noting that the incident field of Configuration II is supposed to be focused at $(0, 0, -\lambda/15)$, which is not on the data collection line.

5.5.3.2 Scattered NF Data

We now consider the scattered NF data on the data collection line to show that the proposed setup (i.e., Configuration IV) is mainly sensitive to a localized region, which we refer to as the region of interest (ROI). This region of interest is the subwavelength region around the focal point of the transmitting NF plate which coincides with the excitation point of the receiving NF plate, i.e., at the location $(0, 0, -\lambda/15)$. To study the scattered NF data, we first need to place an OI in the space between the two NF plates. To this end, we consider two case studies for each of the four configurations. In Case I, we *merely* place the light green dielectric box denoted by ROI between the two NF plates, see the ROI box in Figure 5.5.

[15] Note that although the monopole antenna is omnidirectional with respect to angular variation in the $y - z$ plane, its pattern on a line (e.g., on the data collection line) is still relatively focused (see Figure 5.6)

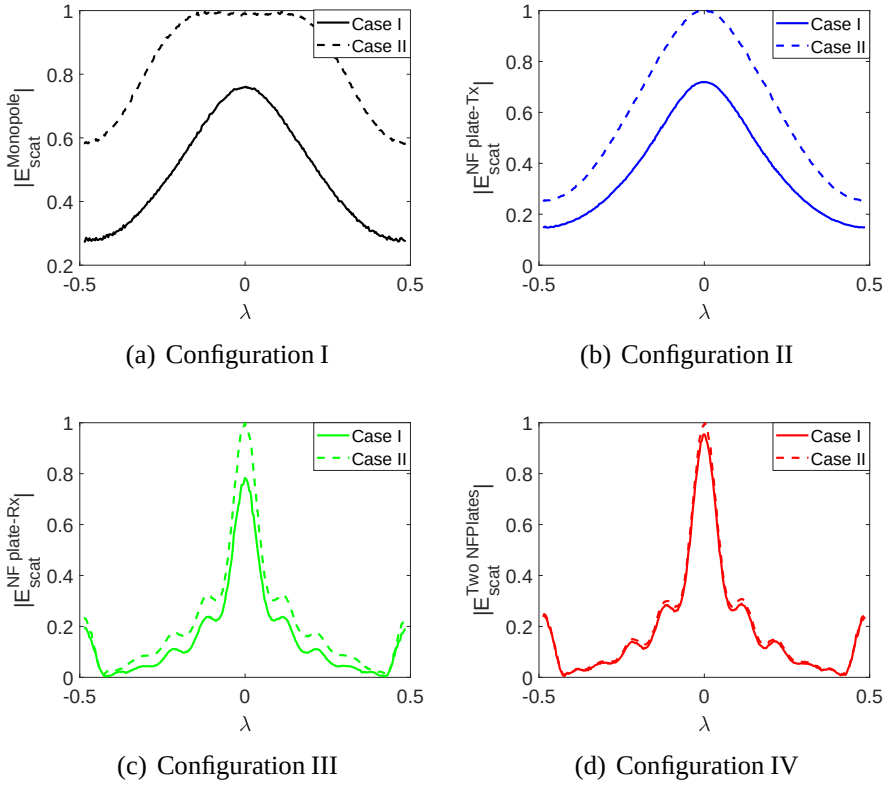

(a) Configuration I (b) Configuration II

(c) Configuration III (d) Configuration IV

Fig. 5.7: The normalized magnitude of the scattered field data for Case I (solid lines) and Case II (dashed lines) under four configurations. Case I includes only the OI located in the ROI, and Case II adds two undesired scatterers to the OI. (a) Configuration I (no NF plates), (b) Configuration II (the orange NF plate),(c) Configuration III (the blue NF plate), and (d) Configuration IV (both NF plates). For each configuration, the scattered data have been normalized to its own Case II.

The geometrical space taken by this object is assumed to be our ROI. In Case II, we attach two other dielectric objects, shown as dark green boxes in Figure 5.5, to this object. We refer to these two dark green dielectric boxes as the undesired scatterers as they are outside the ROI. The main purpose of considering these two Cases is to demonstrate that the scattered NF data for both Case I and Case II are similar under Configuration IV. That is, we aim to show that Configuration IV is mainly sensitive to the ROI, and not to presence of the undesired scatterers.

All of these three dielectric boxes are assumed to have the same relative permittivity of

$\epsilon_r = 4.0$ (lossless) and have the same dimensions of $\lambda/20 \times \lambda/5 \times \lambda/15$ along the x, y, and z directions. Let us now compare the scattered field data for Case I and Case II under our four configurations. The magnitude of the scattered field data have been plotted in Figures 5.7(a)-(d). Noting Figures 5.7(a) and (b), it can be seen that the collected scattered field data change when we add the two undesired scatterers (Case II) to the ROI (Case I). Comparing these two figures, it can also be seen that the scattered data under Configuration II are less sensitive to the changes occurring outside the ROI (i.e., being less sensitive to the presence of the undesired scatterers) as compared to Configuration I due to the use of a focused transmit pattern. (This is similar to the results presented in [99].) We now move on to Configuration III in which we utilize the focused receive pattern. As can be seen in Figure 5.7(c), the scattered field data in Configuration III undergo less changes compared to Configurations I and II. Finally, we consider the scattered field data under Configurations IV in which both of the NF plates are present within the setup. As can be seen in Figure 5.7(d), the concurrent use of the focused transmit and receive pattens has decreased the sensitivity of the scattered data with respect to the undesired scatterers. In other words, the collected data in Configuration IV is mainly sensitive to the ROI.

5.6 Inversion Results

Now that we have studied these four configurations, we will focus on Configuration IV in the rest of this paper. Furthermore, instead of considering the scattered field data on the data collection line, we consider one *single* scattered data point in the middle of the data collection line which corresponds to the focal point of the receiving NF plate as shown in Figure 5.5. Once we have this single scattered data point, E^{scat}, we can use (5.14) to retrieve the complex permittivity value at the focal point of the transmitting NF plate. As required by (5.14), we first need to know α_m^{foc} and β_m^{foc}, which is to be discussed below.

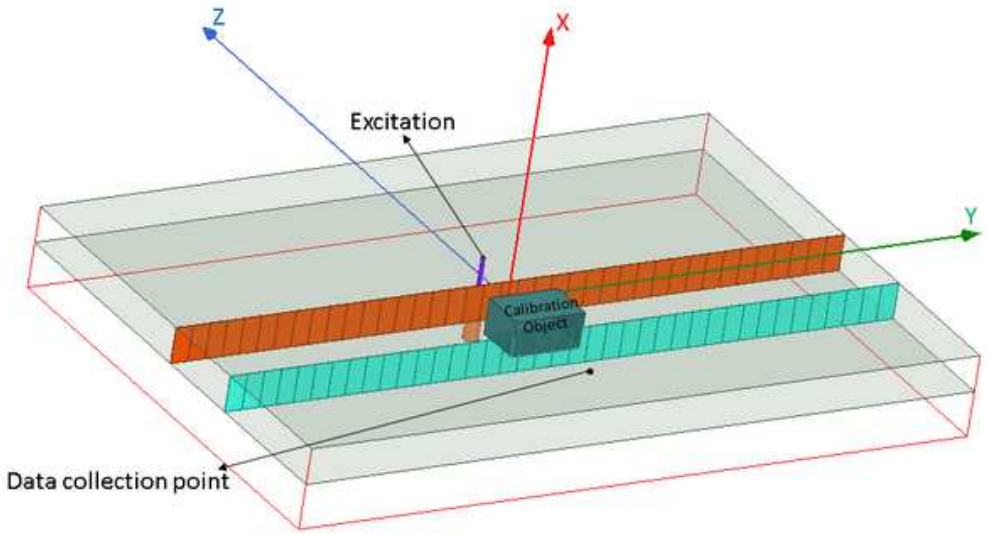

Fig. 5.8: The calibration object is placed between the two NF plates centered at the focal point of the orange NF plate. The known permittivity of this calibration object, along with the scattered field data point at the focal point of the light blue NF plate as well as the total field within the calibration object are used to determine α^{foc} and β^{foc}.

5.6.1 Calibration

As noted in Section 5.3, the two operators $\mathcal{G}_S$ and $\mathcal{G}_D$ govern the MWI equations. Therefore, the knowledge of these two operators are needed for performing inversion. On the other hand, as explained in Section 5.4, when we use subwavelength focused transmit and receive patterns (i.e., Configuration IV), the $\mathcal{G}_S$ operator for our *single* data point can be approximated by one complex number, namely α^{foc}, see (5.9). (We have dropped the subscript m from α_m^{foc} for simplicity.) On the other hand, as can be seen in (5.12), for the focused setup (i.e., Configuration IV), we have approximated the $\mathcal{G}_D$ operator by one complex number β^{foc}. Therefore, for our problem, determining $\mathcal{G}_S$ and $\mathcal{G}_D$ operators reduces to determining two complex numbers, namely α^{foc} and β^{foc}.

To determine α^{foc} and β^{foc}, we have used a calibration object with the relative permittivity of 6.50 and with the size of $\lambda/20 \times \lambda/10 \times \lambda/15$ centered at the focal point of the transmitting

NF plate. Therefore, we now have a calibration *contrast* which is $\chi^{\text{cal}} = 5.50$. (To show the robustness of the calibration procedure with respect to the choice of the permittivity values for the calibration object, see Appendix G.) This calibration object is then placed as shown in Figure 5.8. After being illuminated by the transmitting NF plate, the resulting scattered NF is collected at the data collection point, which is the focal point of the receiving NF plate. This data point is referred to as $E^{\text{scat,cal}}$. Furthermore, the induced total field within the calibration object is recorded at the point $(0, 0, -\lambda/15)$ which is the geometrical centre of the calibrated object. This total field which is denoted by E^{cal} can be used in conjunction with χ^{cal} to determine the calibrated contrast source $w^{\text{cal}} = \chi^{\text{cal}} E^{\text{cal}}$. Noting (5.9), we can then find α^{foc} as

$$\alpha^{\text{foc}} = \frac{E^{\text{scat,cal}}}{w^{\text{cal}}}. \tag{5.17}$$

This α^{foc} will then be used for reconstruction of different objects with different permittivity values and sizes. Finally, the incident field at $(0, 0, -\lambda/15)$ is also obtained and is referred to as $E^{\text{inc,cal}}$. Then, noting (5.12), β^{foc} can be found as

$$\beta^{\text{foc}} = \frac{w^{\text{cal}} - \chi^{\text{cal}} E^{\text{inc,cal}}}{\chi^{\text{cal}} w^{\text{cal}}}. \tag{5.18}$$

Now that we have obtained α^{foc} and β^{foc}, we start reconstructing some OIs in the following three subsections. Note that our focused approach makes the single data point collected at the focal point of the receiving NF plate mainly sensitive to the complex permittivity value at the focal point of the transmitting NF plate. Therefore, using this single complex data point, we recover the complex permittivity value only at the subwavelength cell around the focal point of the transmitting NF plate.

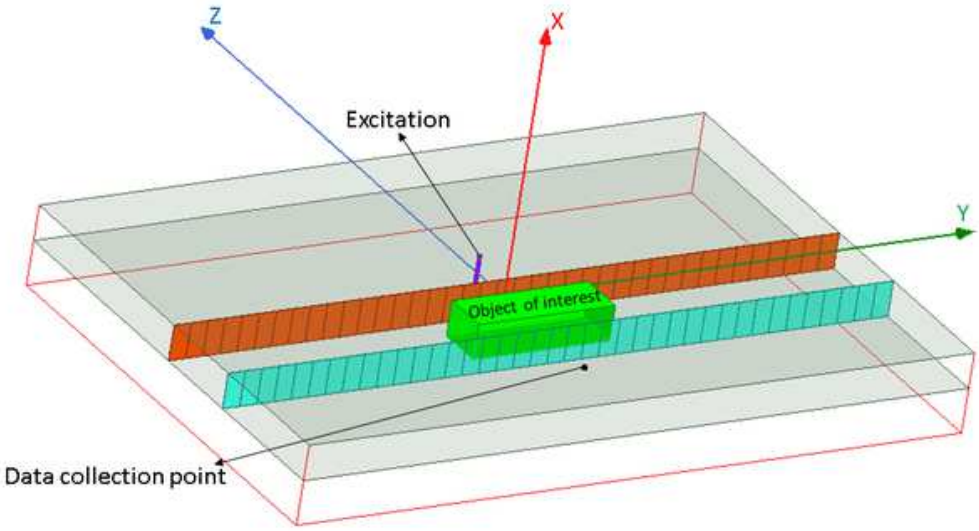

Fig. 5.9: An OI with the dimensions of $\lambda/20 \times \lambda/5 \times \lambda/15$ along the x, y, and z directions has been placed between the two NF plates. Once irradiated, the resulting scattered field is collected at the focal point of the receiving NF plate, i.e., at $(0, 0, -3\lambda/15)$. The relative permittivity of this OI is varied from 5.5 to 10.5 with the increment of 0.5.

5.6.2 Elongated Lossless Object

In this case study, we have considered a rectangular dielectric box with the size of $\lambda/20 \times \lambda/5 \times \lambda/15$ to be the OI. This simulation setup has been demonstrated in Figure 5.9. As can be seen, the size of the OI is twice as the size of the calibration object in the y direction. We consider 11 scenarios for this OI by changing its relative permittivity from 5.5 to 10.5 with an increment of 0.5. In each scenario, the OI is illuminated, and one *single* scattered data point is collected at the focal point of the receiving NF plate. We then use (5.14) to retrieve the contrast of the object at the focal point of the transmitting NF plate. The retrieved and true relative permittivities of the object for these 11 scenarios have been shown in Figure 5.10. As can be seen, there is a good agreement between the true and retrieved values. Although the true object is lossless, the retrieved complex permittivities have small imaginary parts (with a maximum value of 0.22), which have been reported in Table H.1 in Appendix H. We have also observed that if the OI has a small relative permittivity (in particular, below the

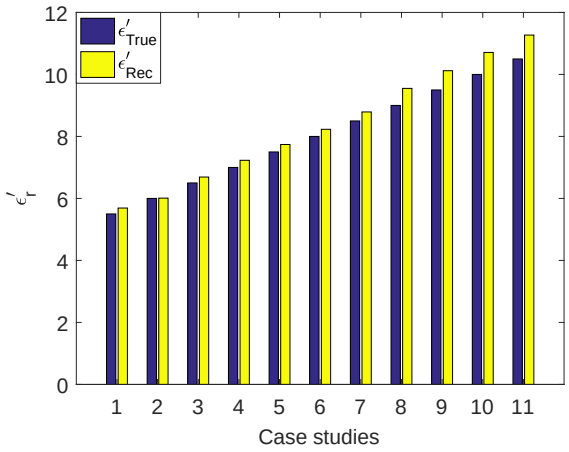

(a) Re(ϵ_r)

Fig. 5.10: The reconstructed real part of the relative permittivity of the OI considered in Figure 5.9 versus its true relative permittivity for 11 case studies. The height of the blue bars shows the true (real) relative permittivity of the OI while the height of the yellow bars depicts the real part of the reconstructed complex permittivity. The horizontal axis of this plot shows the 11 case studies where the true relative permittivity of the OI varies from 5.50 to 10.50 with the increment of 0.50.

relative permittivity of 2.0), the reconstructed result tends to be unreliable. Noting that the induced contrast source at the focal point of the transmitting NF plate serves as the excitation for the receiving NF plate, we speculate that the reason behind this might lie in the small induced contrast source which might not be able to sufficiently excite the receiving NF plate.

5.6.3 Elongated Lossy Object

To further evaluate the performance of this method we have also considered a lossy object with the same size ($\lambda/20 \times \lambda/5 \times \lambda/15$) but now with a relative complex permittivity of $\epsilon_r = 8.00 - j3.00$. Similar to the above, one single scattered data point at the focal point of the receiving NF plate was collected, and then (5.14) was used to retrieve the complex permittivity at the focal point of the transmitting NF plate. The retrieved value is $\epsilon_r = 7.80 - j2.93$, which is in close agreement with the true complex value.

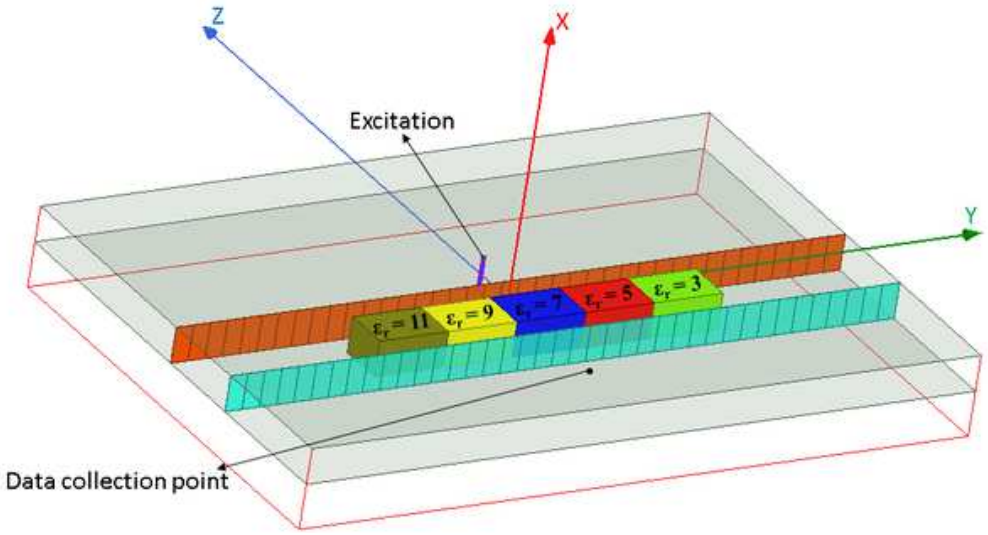

Fig. 5.11: An inhomogeneous object has been placed between the two NF plates. This object consists of five rectangular dielectric cells each of which has the same dimensions of $\lambda/20 \times \lambda/10 \times \lambda/15$ along the x, y, and z directions but with different dielectric permittivities. The scattered data point collected at the focal point of the receiving NF plate is used to retrieve the permittivity value at the focal point of the transmitting NF plate, i.e., the permittivity at the blue cell.

5.6.4 Inhomogeneous Object

We now investigate the performance of the proposed idea when the OI is inhomogeneous as shown in Figure 5.11. The object consists of five cells; each of these cells has the same size of $\lambda/20 \times \lambda/10 \times \lambda/15$ but with five different permittivity values. As can be seen, these five cells have been depicted in five different colors indicating that they have different relative permittivities, namely $\epsilon_r = 3$, 5, 7, 9, and 11. Among these five cells, the blue cell with the relative permittivity of $\epsilon_r = 7.00$ coincides with the focal point of the transmitting NF plate, and therefore it is our region of interest. Similar to the previous example, one scattered data point has been collected at the focal point of the receiving NF plate, and then (5.14) resulted in the retrieved permittivity of $7.83 - 0.08j$, which is in close agreement with the true relative permittivity of 7.00 at the blue cell.

5.7 Conclusions

The main conclusion of this paper is that transmit and receive patterns can affect the MWI's governing equations, and provide two extra degrees of freedom in designing MWI systems. These additional degrees of freedom can be advantageously utilized to create imaging systems whose sensitivity distributions can be tailored based on different requirements. In other words, instead of putting all the efforts in the development of sophisticated inverse scattering software, it is also advantageous to consider developing hardware systems that facilitate the process of complex permittivity retrieval. The appropriate MWI approach may then be reached by a trade-off between the complexity of the inverse scattering software and that of the hardware system.

In particular, in this work, we have used two NF plates which provide subwavelength focused NF beams. Through full-wave simulations of these two NF plates, for 1D objects and under a localized approximation, we have shown that a single scattered data point can be made mainly sensitive to the complex permittivity value at one subwavelength cell. We then showed that the retrieval of the complex permittivity value at that subwavelength cell can be done in an easy manner. Due to the fact that the utilized NF plates suffer from a limited working distance and high reflections, they cannot be utilized in applications such as microwave breast imaging. In addition, the presented localized data and domain equations can also fail when we consider more complicated 2D and 3D objects. Despite these limitations, these NF plates still serve the main purpose of this paper: demonstrating that properly shaping the NF beams of the transmit and receive antennas can be valuable for microwave imaging, and may (to some extent) simplify the process of complex permittivity retrieval by their effects on the MWI's governing equations. In particular, with recent advances in phased array antennas and electromagnetic metasurfaces, tailoring the radiation patterns of antennas for imaging applications can be a promising avenue.

6

Conclusions and Future Work

In this chapter, we first present the conclusions of this dissertation and then propose some future works that can be pursued in this research area. These conclusions are basically the summary of what has been achieved during the author's PhD studies. Herein, each contribution is first presented, followed by its advantages and disadvantages/limitations.

6.1 Conclusions

The main objective of this dissertation was to develop novel techniques and algorithms that can lead to better understanding and improvement of the achievable accuracy and resolution in MWI. For the techniques and algorithms presented in this dissertation, we have provided insight into why these techniques and algorithms can have a positive impact on the achievable MWI reconstruction. This has then followed by some demonstrations through synthetic and experimental case studies. These novel techniques and algorithms basically constitute

the contributions of this PhD dissertation. Now, let us present them in the same order that they have been discussed in this dissertation and then make some remarks regarding their advantages and disadvantages/limitations.

6.1.1 Contributions

- **'Best' possible reconstruction**[1]: The concept of the best possible reconstruction from a given MWI system with specific properties (e.g., an MWI system that uses certain number of transceivers and operates at certain frequency(ies)) is introduced. This concept can serve as a design guideline using which the MWI system designer can evaluate the required specifications of an MWI system that can meet a desired achievable resolution from that MWI system, e.g., the required number of transceivers or the lowest operational frequency(ies) to be incorporated in an MWI system in order to retrieve a specific part of an OI with a certain resolution. Now let us consider the advantage and limitation of this introduced concept.

  - **Advantage**: The best possible reconstruction that has been proposed in this dissertation has been derived from the procedure that considers the multiple scattering events (i.e., nonlinearity of the MWI problem) within an OI. Consequently, it provides a more accurate guideline compared with the methods that do not take into account these multiple scattering events (i.e., methods that consider the simplified MWI problem under the Born approximation). Enabled by this concept, prior to designing an MWI system to image a specific object (e.g., breast) the designer can evaluate what the best possible reconstruction will be. For example, do we have enough information to even have the hope to detect a tumor with

[1] Nozhan Bayat and Puyan Mojabi, "A Mathematical Framework to Analyze the Achievable Resolution from Microwave Tomography," *IEEE Transactions on Antenna and Propagation*, vol. 64, no. 4, pp. 1484-1489, 2016.

the diameter smaller than 5 mm within a given breast? If the best possible reconstruction cannot reconstruct the desired feature, other approaches (e.g., using more transceivers, incorporating prior information) should be considered.

  - **Limitation**: The best possible reconstruction does not take into account the signal-to-noise ratio and the extra information provided by regularization operators as well as practical issues such as mutual coupling between the co-resident antennas.

- **Spatial Priors**[2]: An MWI algorithm that can incorporate spatial (structural) prior information about the OI in order to improve the achievable quantitative accuracy and resolution has been proposed. The spatial priors to be fed to the proposed imaging algorithm can be obtained from other imaging modalities, e.g., MRI. We have utilized single-frequency, multiple-frequency synthetic and experimental data sets in order to evaluate the performance of the proposed algorithm. Now, let us consider the advantage and limitation of this introduced method.

  - **Advantage**: The proposed algorithm is fully automated and does not need the user to change the regularization weight in each iteration during the inversion process. This algorithm is capable of working with both complete and partially-available spatial information about OI (i.e., when we only have access to prior spatial information in some part(s) of the imaging domain). It is worth emphasizing that the purposed algorithm does not require assigning any quantitative values (e.g., relative complex permittivity) to the regions associated with spatial prior information. In short, this algorithm can improve the achievable complex permittivity image from MWI upon its integration with other high resolution imaging modalities.

[2] Nozhan Bayat and Puyan Mojabi, "Incorporating Spatial Priors in Microwave Imaging via Multiplicative Regularization," Accepted to be published in *IEEE Transactions on Antenna and Propagation*, pp. 1-12, 2019 (Manuscript ID. AP1905-0924.R1), in press.

  - **Limitation**: The elements of the confidence vector p considered in the multiplicative regularization term has been mainly evaluated for two values: $p = 1$ (i.e., when we have full confidence about the provided spatial priors) and $p = 0$ (i.e., when there is no prior spatial information in a sub-region). For other values of the confidence vector p such as $p = 0.5$, the algorithm behaves relatively similar to $p = 1$. The reason seems to be due to the regularization operator where $1 \times (\chi_i - \chi_j) = 0$ and $0.5 \times (\chi_i - \chi_j) = 0$ are treated similarly. Based on the proposed implementation of the confidence vector p in the SP regularization term (which takes into account the spatial prior information about the OI) in this dissertation, the values of the confidence vector p will be similar to $p = 1$ for $0 < p < 1$.

- **Focused Transmitting Pattern**[3]: Broadly speaking, we have suggested that the transmitting antenna can be advantageously utilized toward improving the achievable accuracy and resolution from MWI and not merely to interrogate the OI. Specifically, it has been shown that a focused incident near-field (NF) distribution (i.e., focused transmitting pattern) can beneficially be utilized for interrogating the OI. This has been demonstrated through several simulation studies that carried out in ANSYS HFSS software and under the Born approximation. Now, let us consider the advantage and disadvantage of using a focused transmitting antenna in MWI.

  - **Advantage**: Using an antenna with a focused incident NF distribution can suppress the effects of undesired scatterers surrounding the OI on the collected scattered data. Considering the scattered data arising from the undesired scatterer as unwanted signals, the use of a focused incident NF distribution directed toward the OI can improve the signal-to-noise ratio of the collected data. This advan-

[3] Nozhan Bayat and Puyan Mojabi, "On the Use of Focused Incident Near-Field Distributions in Microwave Imaging," *Sensors*, vol. 18, no. 9, pp. 1-26, 2018.

tage of using a focused transmitting pattern can be observed from another point of view which is also beneficial for the inversion procedure. Utilizing focused transmitting pattern directed toward the OI can lead to mainly interrogating the OI and not any other regions within the imaging domain. This can[4] result in having less number of unknowns within the imaging domain. Therefore, a better balance between the number of known quantities (i.e., collected scattered data) and the number of unknown quantities (i.e., number of unknown cells within the imaging domain) can be achieved. We have also noted that having less number of unknowns in the MWI problem can enable us to use simpler inversion techniques which are computationally less expensive.

  - **Disadvantage**: Using a focused transmitting pattern has the drawback of being less sensitive with respect to regions outside the focused beam area. Consequently, if we are not sure about the region that encloses the OI, e.g., a tumor tissue within woman breast, it is often better to use a non-focused transmitting pattern to be able to collect information about the whole imaging domain.

- **Simultaneous Usage of Focused Transmit and Receive Patterns**[5]: It has been discussed that transceivers' transmitting and receiving patterns in MWI can act as two extra degrees of freedom in MWI hardware system design in order to tailor the sensitivity of collected data with respect to different regions within the imaging domain even further compared to the case where we have only used transmitting patterns[6]. As has been discussed earlier, the tailoring of the collected data sensitivity with respect to the different regions within the imaging domain can potentially lead to the improvement of the achievable accuracy and resolution. From a broader point of view, in this approach, we have suggested that the development of MWI's hardware system for

[4] The term *can* has been used here to indicate that this is under the Born approximation and can fail due to multiple scattering events.

[5] Nozhan Bayat and Puyan Mojabi, "Focused Microwave Imaging by Near-Field Plates," Under-review.

[6] This is the method that has been discussed in the previous contribution.

improving some of its aspects, i.e., its achievable accuracy and resolution, can be as important as the development of sophisticated inverse scattering software for the same purpose[7]. Particularly, in this dissertation, we have demonstrated through simulation studies by the use of two NF plates that using focused transmitting and receiving patterns simultaneously can be advantageously employed to focus the sensitivity of the collected data to a sub-wavelength cell in the imaging domain. Although this method is only valid within certain constraints and limitations (1D objects of interest, limited working distance of near-field plates, and the use of a localized approximation), it shows that the use of appropriate transmit and receive patterns can affect (or, simplify) the governing equations (data and domain equations) of microwave imaging. Thus, they can be used as extra degrees of freedom in microwave imaging system design. Now, let us consider the advantage and disadvantage of the simultaneous use of focused transmit and receive patterns in MWI.

- **Advantage**: One of the advantages for concurrently using the focused transmit and receive patterns in MWI is the capability of suppressing the contribution of the unwanted unknown scatterers (i.e., undesired scatterers) on the collected data from this imaging tool. As discussed earlier, this can lead to better balancing between the known and unknown quantities in the MWI problem which can possibly result in more accurate reconstruction. Moreover, under its own constraints, this approach can simplify the complexity of the inversion procedure that needs to retrieve many unknown quantities (i.e., discretized cells within the imaging domain) from the limited number of known quantities (i.e., collected data at the receivers' location). In particular, we have demonstrated that using the proposed method the two mapping operators for the so-called data and domain equations denoted by $\mathcal{G}_S$ and $\mathcal{G}_D$ respectively, can be simplified. This can

[7] Probably, the most suitable MWI design approach can be reached by a trade-off between the complexity of the inverse scattering software and that of the hardware system.

not only improve the accuracy of the achievable reconstruction from this imaging modality but can also make the inversion process of the collected data simpler and faster. In this dissertation, using two NF plates and employing a localized approximation we have shown that the two mapping operators, i.e., $\mathcal{G}_S$ and $\mathcal{G}_D$, can be represented by two complex values rather than two matrices containing multiple complex values when imaging 1D objects.

– **Disadvantage**: The advantage that has been discussed above can be seen as a disadvantage from another point of view. The use of focused transmit and receive patterns simultaneously can result in *unseen* regions[8] from both of the transmitting and receiving points of view. This can be considered as a disadvantage if the regions of interests does not physically lie on (or overlap with) the region that is being interrogated by the transceivers. This might then result in false diagnosis. Therefore, if the rough estimate of the OI's location and electrical size within the imaging domain is unknown, it might be a better approach to incorporate non-focused transmit and receive patterns in MWI in order to first approximately localize the OI. Afterward, the transceivers with the focused transmit and receive patterns can be utilized in order to improve the accuracy of the obtained reconstruction from MWI.

  Another drawback is mainly related to the method through which we have demonstrated the proposed technique (i.e., using two NF plates). The utilized NF plates for our demonstration has a short focal depth (i.e., $\lambda/15$ where λ is the wavelength at the operational frequency of 1 GHz). Therefore, to make the proposed approach more feasible to be employed in real applications, one may need to develop a technique that is able to generate and possibly maintain the focused field in a longer range compared with the utilized NF plates in this dissertation.

[8] The term *unseen* has been used to indicate that the dielectric properties of these regions will not be seen by either the transmitter or by the receiver at microwave frequency of operation.

6.2 Future Work

The research presented in this dissertation can be further pursued on two fronts (*i*) the electromagnetic inverse scattering algorithm development, i.e., MWI software development, and (*ii*) the optimization of the MWI equipment (e.g., the incorporated transceivers in MWI), i.e., MWI hardware development in order to make the this imaging device a more feasible imaging tool to be employed commercially[9].

- **MWI software development**. One of the avenues that can be considered to further pursued in this front is the improvement of the proposed inversion algorithm in this dissertation that can take into account the spatial prior (SP) information of the object being imaged. For instance, due to the limitation that has been explained earlier, the performance of the proposed algorithm has been mainly evaluated against two values of the confidence vectors p (i.e., $p = 1$ and $p = 0$). One can adjust the proposed regularization term (or propose a new regularization term) that more effectively can handle various values of the confidence vector.

  It will also be interesting to extend this algorithm to a 3D full vectorial imaging algorithm and evaluate its performance against different synthetic and experimental data sets. This is particularly important as it can address one of the major challenges facing the 3D full vectorial imaging algorithm: having two many unknowns that need to be retrieved by the use of limited number of known quantities.

  It is worth noting that our *experimental* evaluation of the spatial priors algorithm was limited to simple targets and an MRI image with MWI inversion (an MRI and MWI were not co-registered). Once an imaging system with co-registered ultrasound to-

[9] As mentioned earlier, probably the most appropriate MWI design can be reached by a trade-off between these two fronts, i.e., MWI software and hardware developments.

mography and MWI, or with co-registered MRI and MWI is available[10], this algorithm needs to be tested against more practical data sets.

- **MWI hardware development**. In this dissertation, the use of focused incident NF distributions has been proposed in order to tailor the sensitivity of the collected data at the receiver(s). The advantages of incorporating this proposed technique has been demonstrated synthetically through simulation studies using ANSYS HFSS. The experimental validation of this technique can be considered as a future research area in this front. This experimental validation can include the fabrication of the utilized NF plates in our simulation studies or manufacturing of other illuminators that are able to create a focused incident NF distribution.

  Once an experimental system using focused NF beams is available, several practical imaging parameters can also be investigated, for example, the signal-to-noise ratio (SNR) of the measured data. It is expected that the use of focused NF beams improves the SNR of the measured data. This can be understood as follows. In addition to using the available power more effectively, utilizing a focused incident NF distribution, which is directed toward the OI, mainly lead to the interrogation of the OI and not the surrounding objects that are acting as undesired scatterers. However, the use of non-focused incident NF distributions can result in interrogating the OI as well as the undesired scatterers and consequently having their EM signatures in the collected data. Considering the scattered data generated due to the presence of undesired scatterers as unwanted signals (treated as noise) we can expect that utilizing focused incident NF distributions directed toward the OI result in better SNR.

  In this dissertation, we have considered the effects of two hardware design parameters: transmitting and receiving patterns. This two parameters have been utilized to tailor the sensitivity of the collected data at the receivers with respect to the different

[10] To the best of the author's knowledge, there is one experimental joint MRI-MWI system [23].

regions within the imaging domain. Another parameter using which the sensitivity of the collected data with respect to different regions within the imaging domain can be governed is the polarization of the utilized transceivers. In the future work, we can investigate whether the polarization of the utilized transceivers in MWI (as the two other hardware parameters in MWI) can be utilized advantageously to tailor the sensitivity of the collected data with respect to different regions within the imaging domain.

This concludes my PhD dissertation on the novel techniques and algorithms that can advance microwave imaging modality.

APPENDIX

A

List of Publications

In this Appendix, the author's publications that is directly related to this thesis is being listed.

- **Journal papers**:
  - **Nozhan Bayat** and Puyan Mojabi, "Focused One-Dimensional Microwave Imaging by Near-Field Plates," Under-review.
  - **Nozhan Bayat** and Puyan Mojabi, "Incorporating Spatial Priors in Microwave Imaging via Multiplicative Regularization," Accepted to be published in *IEEE Transactions on Antenna and Propagation*, pp. 1-12, 2019, in press (Manuscript ID. AP1905-0924.R1).
  - **Nozhan Bayat** and Puyan Mojabi, "On the Use of Focused Incident Near-Field Distributions in Microwave Imaging," *Sensors*, vol. 18, no. 9, pp. 1-26, 2018.
  - **Nozhan Bayat** and Puyan Mojabi, "A Mathematical Framework to Analyze the Achievable Resolution from Microwave Tomography," *IEEE Transactions on*

Antenna and Propagation, vol. 64, no. 4, pp. 1484-1489 , 2016[1].

- **Abstract/Conference papers**:
  - Puyan Mojabi and **Nozhan Bayat**, "A Multiplicative Regularizer to Incorporate Prior Spatial Data in Microwave Imaging Reconstruction ," *European Conference on Antennas & Propagation (EuCAP)*, Krakow, Poland, 2019. (**Invited**).
  - Chaitania Narendra, Trevor Brown, **Nozhan Bayat**, and Puyan Mojabi, "Multi-Plane Magnetic Near Field Data Inversion Using the Source Reconstruction Method," *Antenna Technology and Applied Electromagnetics (ANTEM)* , Waterloo, Canada, 2018. (**Invited**)
  - **Nozhan Bayat** and Puyan Mojabi, "Near-Field Microwave Imaging Using Focused Near-Field Beams: An Approach to Mitigate Undesired Scattering Effects," 2^{nd} *International Union of Radio Science Atlantic Radio Science Conference (URSI AT-RASC)*, Gran Canaria, Spain, 2018.
  - Puyan Mojabi, Nariman Firoozy, **Nozhan Bayat**, Trevor Brown, Chaitanya Narendra, Pedram Mojabi, Chen Niu, Tyler Tiede, Thomas Neusitzer, Xiang Li, Ian Jeffrey, Joe LoVetri, and David Barber, "Electromagnetic Inversion for Biomedical Imaging, Antenna Characterization, and Sea Ice Remote Sensing Applications," *International Union of Radio Science Asia-Pacific Radio Science Conference (URSI AP-RASC)*, Seoul, Korea, 2016 (**Invited**).
  - **Nozhan Bayat**, Chen Niu, and Puyan Mojabi, "Synthetic Study of the Use of Bessel Beam Illumination in 2D Microwave Tomography," *IEEE Antennas and Propagation, U.S. National Committee and International Union of Radio Science (USNC-URSI) National Radio Science Meeting*, Fajardo, Puerto Rico, USA, 2016.

[1] The main contribution of the author's PhD work in this paper is the introduction of the concept of best possible reconstruction from a given MWI system with specific properties.

– Puyan Mojabi, **Nozhan Bayat**, Majid Ostadrahimi, Amer Zakaria, Joe LoVetri, "On the Achievable Resolution from Microwave Tomography," 1^{st} *International Union of Radio Science Atlantic Radio Science Conference (URSI AT-RASC)*, Gran Canaria, Spain, 2015. (**Invited**).

B

Sensitivity with Respect to Imperfect Spatial Priors

This appendix is associated with Chapter 3. Evaluating the performance of the proposed inversion algorithm against imperfect SP is challenging and cannot be conclusive as this evaluation depends on various parameters including the type of OI, the type of SP imperfection, the number of measured data points, etc. Herein, we consider two scenarios in which we provide imperfect SP for the reconstruction of the "W" target (with $\lambda_b/10$ separation between the fingers, i.e., the first form of the "W" target).

The SP used in the first scenario is shown in Figure B.1(a) where the SP associated with the rightmost finger is wrong; compare this SP with the correct version in Figure 3.5(a). The MRSP-GNI reconstruction under these imperfect SP (assuming full confidence $p_i = 1$) is shown in Figure B.1(b). As can be seen, the reconstruction of the rightmost finger suffers. However, if we accurately inspect the reconstructed rightmost finger and zoom in, we can see that the MRSP-GNI algorithm has, to some extent, distinguished between the expected

rightmost finger and the artefact due to the imperfect SP. This can be seen by noting that the reconstructed permittivity of the artefact is smaller than the reconstructed permittivity in the region that corresponds to the expected location of the rightmost finger.

In the second scenario, we introduce an extra false region into the SP as shown in Figure B.1(c) which is the extra rectangular region tagged as Region V in the colorbar. The MRSP-GNI reconstruction under this imperfect SP (assuming full confidence $p_i = 1$), shown in Figure B.1(d), is almost the same as the reconstruction under the complete SP shown in Figure 3.1(d). This is expected since adding this extra false region does *not* incorporate false information into the inversion algorithm. The presence of this wrong region (Region V) in the SP simply guides the inversion algorithm to favour equal complex permittivity values in Region V. On the other hand, the presence of Region I in the SP guides the inversion algorithm to favour equal complex permittivity values in Region I. However, due to the fact that our formulation never enforces that the complex permittivity values must be different in different regions, the MRSP-GNI algorithm correctly assigns similar permittivity values to all the pixels in Regions I and V, which satisfies the wrong SP associated with Region V, and the true SP associate with Region I.

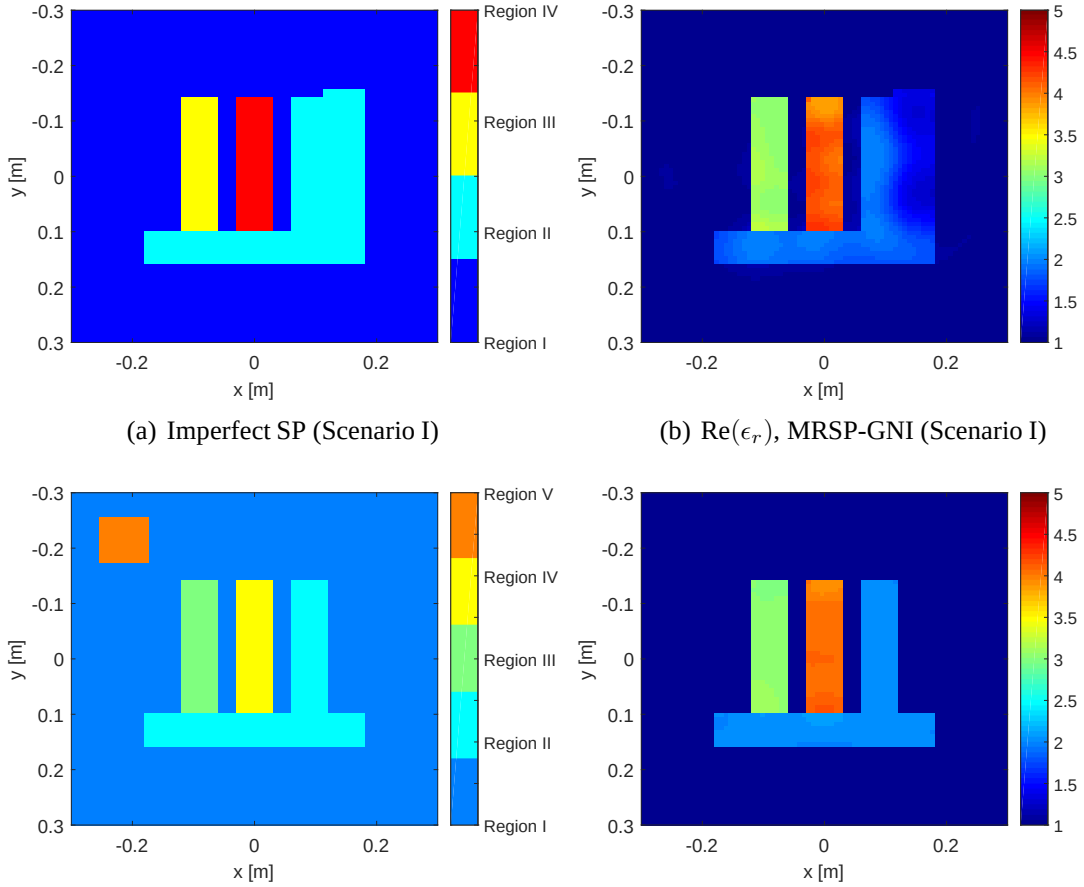

(a) Imperfect SP (Scenario I)

(b) Re(ϵ_r), MRSP-GNI (Scenario I)

(c) Imperfect SP (Scenarion II)

(d) Re(ϵ_r), MRSP-GNI (Scenario II)

Fig. B.1: (a) Imperfect SP (Scenario I) for the "W" target (its first form) where the imperfection is related to the spatial priors for the rightmost finger (exaggerated size). (b) The reconstructed real part of the relative complex permittivity profile using the MRSP-GNI algorithm under these imperfect SP (Scenario I). (c) Imperfect SP (Scenario II) for the "W" target (its first form) where an extra false region can be seen in the top-left of the SP image. (d) The reconstructed real part of the relative complex permittivity profile using the MRSP-GNI under these imperfect SP (Scenario II).

C

Tikh-GNI Implementation

This appendix is associated with Chapter 3. Herein, we present our implementation of the Tikhonov regularization method for the GNI algorithm. Tikhonov regularization has been widely used with the GNI algorithm (and other inversion algorithms) in the form of an additive regularization term. In such methods, the regularization weight needs to be determined by a regularization parameter choice method. To make our Tikhonov implementation automated, and also to be consistent with the multiplicative regularization approach considered in this paper, we use a multiplicative term similar to the one suggested in [51]. That is, at the nth iteration of the GNI algorithm, we minimize

$$\mathcal{C}_n(\chi) = \mathcal{C}^{\text{LS}}(\chi)\, \mathcal{C}_n^{\text{Tikh}}(\chi) \tag{C.1}$$

where the multiplicative Tikhonov regularization is given as

$$\mathcal{C}_n^{\text{Tikh}}(\chi) = \frac{\|\chi\|^2 + \rho_n^2}{\|\chi\|_n^2 + \rho_n^2}. \tag{C.2}$$

In the above cost functional, the steering parameter ρ_n^2, similar to γ_n^2 in (3.11), is chosen to be $\mathcal{C}^{\mathrm{LS}}(\chi_n)\ell$. Minimizing $\mathcal{C}_n(\chi)$ over the contrast, the correction $\Delta\chi_n$ can be found from

$$[\mathbf{J}_n^H\mathbf{J}_n + \beta_n\mathcal{T}_n]\Delta\chi_n = -\mathbf{J}_n^H d_n - \beta_n\mathcal{T}_n\chi_n. \tag{C.3}$$

The regularization operator $\mathcal{T}_n$, when operates on a vector of appropriate size x, is defined as

$$\mathcal{T}_n(x) \triangleq \frac{1}{\|\chi\|_n^2 + \eta_n^2}x. \tag{C.4}$$

As can be seen from (C.3), this multiplicative approach is identical to the following additive Tikhonov regularization approach

$$\mathcal{C}_n(\chi) = \mathcal{C}^{\mathrm{LS}}(\chi) + \kappa_n \|\chi\|^2, \tag{C.5}$$

if the (additive) regularization weight κ_n is chosen to be

$$\kappa_n = \frac{\eta\beta_n}{\|\chi\|_n^2 + \eta_n^2}. \tag{C.6}$$

Herein, we refer to this multiplicative implementation of Tikhonov regularization for the GNI algorithm as the Tikh-GNI algorithm.

D

Spatial Priors for Human Forearm Imaging

This appendix is associated with Chapter 3- This appendix noted in the footnote 12 of Section 3.5. In this Appendix, we have considered the forearm data set at 0.8 GHz with 24 dipole antennas immersed in the matching fluid with the relative complex permittivity of $77 - j17$.[1] Herein, we have utilized the image from magnetic resonance imaging (MRI) of the forearm to extract the structural prior information and then invert the measured MWI data. This MRI image has been depicted in Figure D.1(a). We would like to note the followings.

- The forearm in the MWI system and the MRI system is **not** co-located: *"During the MRI scan, the volunteers were in supine position, resting their forearms on a bed. Thus, the orientation of the arm during the MRI scan was different than during the MWT data collection."* [53].

[1] We acknowledge the Electromagnetic Imaging Laboratory at the University of Manitoba (Prof. LoVetri) for letting us to use this experimental data set in this report. For the details regarding this data set, please see [53, 119].

- Consequently, image registration needs to be performed so that we can use the MRI image for MWI inversion. We have used a very preliminary (*ad hoc*) method to extract prior structural information from the MRI image to be given to the MWI inversion. The details of our preliminary method can be found in the Section D.5 of this Appendix.

- The extracted prior structural information from the MRI image has been shown in Figure D.1(b).

  – As can be seen, the structural prior information consists of 9 regions. These regions can be seen in the colorbar of Figure D.1(b) denoted by Region I to Region IX.

  – Note that we do **not** make any assumptions regarding the complex permittivity values at these 9 regions.

D.1 Reconstruction Results

Let us first note that in all the reconstruction results presented herein, the inversion algorithms start from a trivial initial guess, i.e. the contrast of zero. The reconstructed real parts of the complex permittivity profile by the use of three blind inversion algorithms[2], namely MR-GNI, MR-CSI, and Tikh-GNI, have been shown in Figures D.2(a)-(c). In addition, the reconstructed real part of the complex permittivity profile using MRSP-GNI (i.e., the algorithm that takes into account spatial priors) is shown in Figure D.2(d). Similarly, the reconstructions of the imaginary part of the complex permittivity profile using these four algorithms have been shown in Figures D.3(a)-(d).

[2] Herein, we referred to the algorithms that do not take into account the structural information as the blind inversion algorithms.

D.2 A Note on the Imaginary Part Reconstruction

We speculate that the reason behind the poor reconstruction of the imaginary part as compared to the real part (in all the inversions) is due to the imbalance between the real and imaginary parts of the contrast. In fact, the imaginary part reconstruction can be improved by *balancing* the real and imaginary parts of the contrast. (The *balanced* MR-CSI results have been utilized in [119] whereas the *balanced* MR-GNI results have been utilized in [53].) However, balancing the real and imaginary parts of the contrast requires a different form of prior information which is the average ratio between the real and imaginary parts of the contrast profile. Herein, to avoid an extra piece of prior information, we have not used any balancing in our inversion. To understand this imbalance issue better, let us calculate the contrast of the bone:

$$\chi^{\text{bone}} = \frac{\epsilon_r^{\text{bone}} - \epsilon_r^{\text{background}}}{\epsilon_r^{\text{background}}} = \frac{(13 - j3) - (77 - j17)}{77 - j17} = -0.8308 - j0.0016. \qquad \text{(D.1)}$$

As can be seen, the ratio between the real and imaginary parts of this contrast is

$$\text{ratio} = \frac{-0.8308}{-0.0016} \approx 517. \qquad \text{(D.2)}$$

Therefore, if we apply a regularization method on the complex contrast, say $||\boldsymbol{A}\chi||$, it will be dominated by the real part of the contrast, i.e., $||\boldsymbol{A}\chi_R||$ where $\boldsymbol{A}$ is the regularization operator and χ_R is the real part of the complex contrast χ.

D.3 Comparison

For the sake of quantitative comparison, we have chosen one point in the top bone, and one point in the muscle tissue, and have reported the reconstructed complex permittivity values for each of these algorithms in Table D.1. As can be seen, the main advantage of the MRSP-GNI algorithm has been a slight improvement in the reconstruction of the relative complex permittivity of bones. Other than this, we do not observe significant improvements. However, it is very difficult to judge the performance of the MRSP-GNI algorithm as the utilized spatial priors are not ideal as we do not have a proper image registration between the MRI and MWI. For example, we have only used translational movement of the MRI image to create our spatial priors, and have not used any rotations or scalings at this point.

D.4 Observations

As noted in the paper, MRSP-GNI utilizes two regularization operators: (i) a standard MR, and (ii) a spatial prior (SP) regularizer. Due to this, the MRSP-GNI algorithm can be regarded as a *soft* spatial prior method. This is advantageous when the SP is not very accurate or it is not complete. Due to this *soft* spatial prior technique, some of the regions of the SP are not enforced in the MRSP-GNI algorithm. For example, the MRSP-GNI reconstruction shown in Figure D.2(d) does not show Regions III, VI, VII, VIII, and IX, see Figure D.1(b). This could be a positive aspect in the sense that this algorithm might correctly regard all these regions as muscle (Region IV). In other words, this soft technique can be immune to false regions. On the other hand, it could have negative aspects as well. For example, the bones are expected to have two regions which do not show up in the reconstruction. Finally, we have also used our *hard* spatial prior technique, referred to as the SP-GNI algorithm (not shown here). As expected, the reconstruction of this algorithm enforces the presence of all

9 regions; however, the reconstructed permittivity was not acceptable. We have not fully investigated the reason behind this; but, our speculation is that the utilized spatial priors are not sufficiently accurate for SP-GNI as this algorithm (as opposed to MRSP-GNI) has no other regularization means other than the provided SP.

D.5 Extracting Prior Structural Information from the MRI Image

To obtain the structural information of the forearm, the MRI image was imported into MATLAB and the color indices of different pixels were retrieved. Moreover, the resolution of the discretized MRI image in MATLAB was decreased using the *interpn* function. This image was then compared to blind inversions. Based on this comparison, we performed some translational movements (i.e., movements along the $\hat{x}$ and $\hat{y}$ directions) of the MRI image to merely adjust the overall external contour of the forearm's prior spatial image. We have **not** performed any rotations or scaling. Therefore, our current image registration is limited.

Tab. D.1: Reported Relative Complex permittivity of the Forearm in [53] as well as the reconstructed values though the utilized four inversion algorithms.

Tissue type	$\epsilon_r^{\text{Reported}}$	$\epsilon_r^{\text{MR-GNI}}$	$\epsilon_r^{\text{MR-CSI}}$	$\epsilon_r^{\text{Tikh-GNI}}$	$\epsilon_r^{\text{MRSP-GNI}}$
Bone	13 -3j	35.45 - 13.02j	39.01 - 13.53j	41.38-12.8j	29.86 - 9.69j
Muscle	56 - 20j	66.31 - 21.72j	64.77 - 21.95j	65.33-21.05j	65.05 - 22.78j

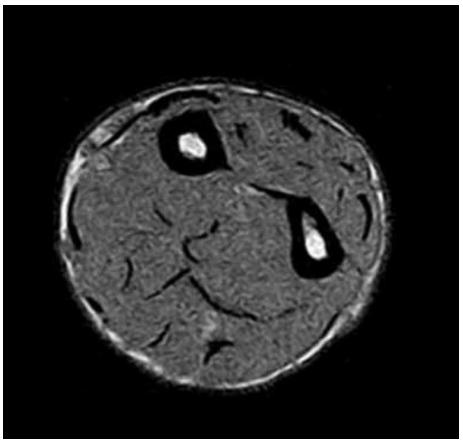

(a) MRI image

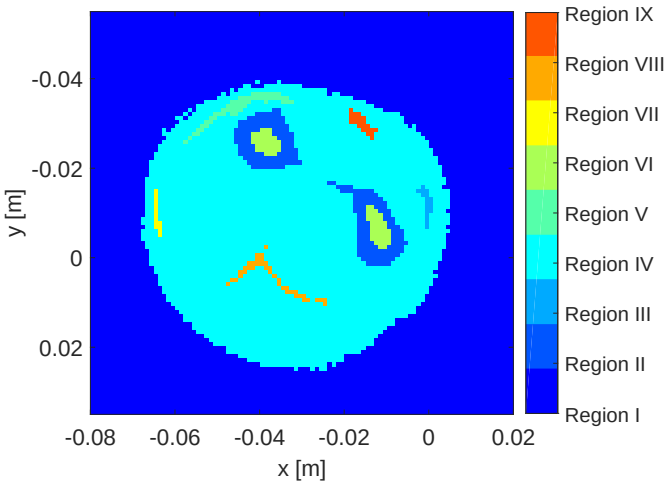

(b) Extracted spatial priors (SP)

Fig. D.1: (a) The MRI image (This MRI image was taken from [53], ©[2013] IEEE). (b) The structural information for this forearm that shows the existence of nine regions within the imaging domain.

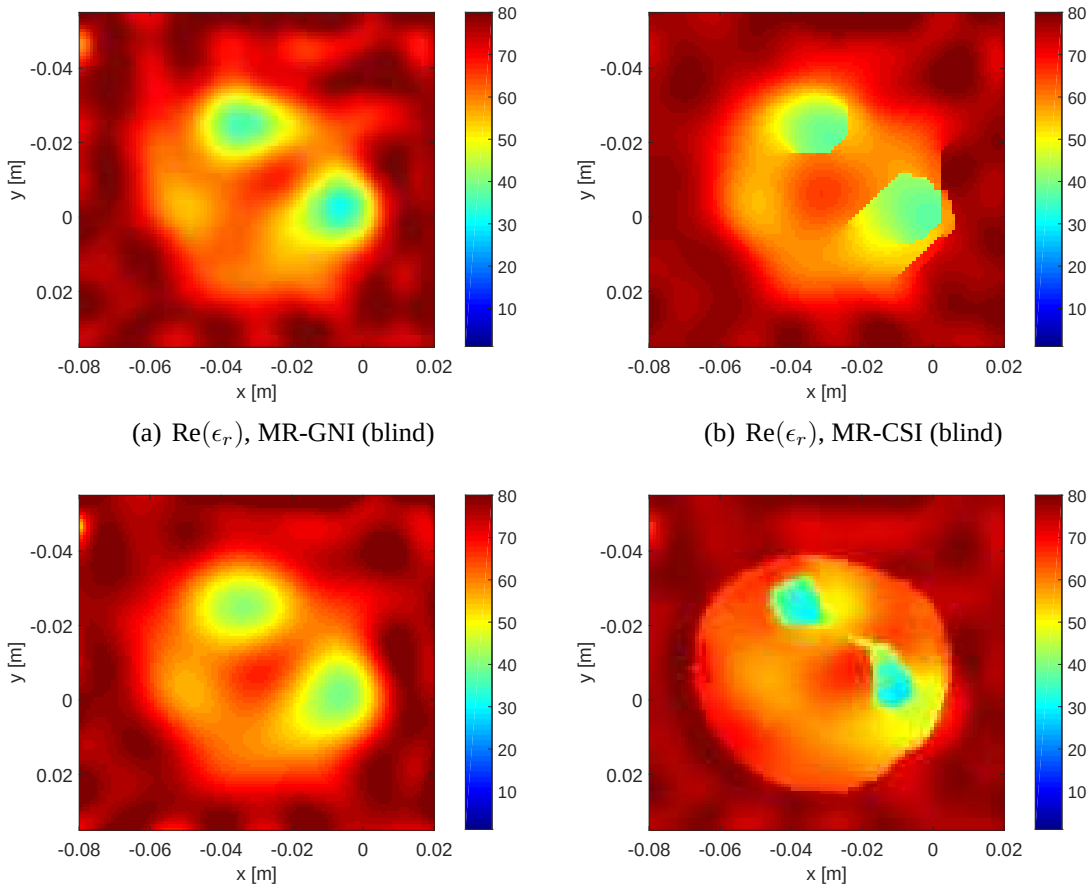

(a) Re(ϵ_r), MR-GNI (blind)

(b) Re(ϵ_r), MR-CSI (blind)

(c) Re(ϵ_r), Tikh-GNI (blind)

(d) Re(ϵ_r), MRSP-GNI (spatial priors)

Fig. D.2: Real-part reconstruction of the complex permittivity of the forearm at 0.8 GHz using the (a) MR-GNI algorithm (blind), (b) MR-CSI algorithm (blind), (c) Tikh-GNI algorithm (blind), and (d) MRSP-GNI algorithm (prior spatials).

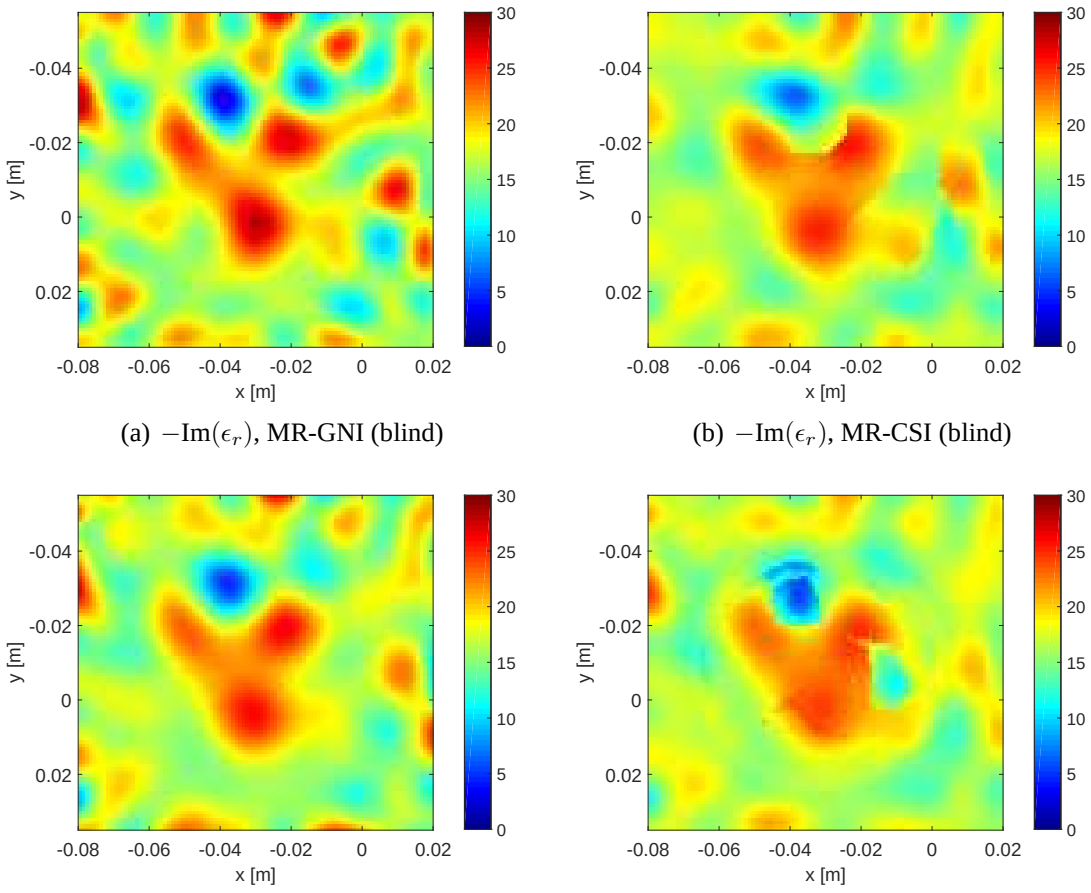

(a) $-\mathrm{Im}(\epsilon_r)$, MR-GNI (blind)

(b) $-\mathrm{Im}(\epsilon_r)$, MR-CSI (blind)

(c) $-\mathrm{Im}(\epsilon_r)$, Tikh-GNI (blind)

(d) $-\mathrm{Im}(\epsilon_r)$, MRSP-GNI (spatial priors)

Fig. D.3: Imaginary-part reconstruction of the complex permittivity of the forearm at 0.8 GHz using the (a) MR-GNI algorithm (blind), (b) MR-CSI algorithm (blind), (c) Tikh-GNI algorithm (blind), and (d) MRSP-GNI algorithm (prior spatials).

E

Simulation Details of the Separation Resolution Study

This appendix is associated with Chapter 4. In this Appendix, we elaborate on how the separation resolution simulation study (see Section 4.3.1.3) was carried out by the use of ANSYS HFSS. To this end, we have placed two dielectric objects with the separation of about 0.13λ from each others in the NF plate setup under Configurations I and II. Due to the simulation setup, it was not possible to keep the two dielectric objects stationary, and then move the NF plate to scan the objects in the three steps as described in Section 4.3.1.3. To handle this, instead of moving the NF plate and keeping the objects stationary, we do the reverse procedure: the two separated objects are moved together parallel to the NF plate in three steps. In Step I, the first dielectric object is located exactly at the center and in front of the NF plate. In Step II, the gap between the two objects is located at the center with respect to the NF plate, and finally in Step III the second dielectric object is placed at the center with respect to the NF plate. The two separated objects at each of these three steps are interrogated, and then the resulting scattered NF data are collected at the receivers' line

(located on the yellow plane in Figure 4.9).

Now, we will explain how the scattered NF data have been collected in each of the above steps. In this study, we have placed the total number of 106 receiving points along the line of intersection between the yellow and brown planes in Figure 4.9. This line, which we refer to as the receivers' line, is parallel to the y axis and has been separated by about $\lambda/7.5$ from the NF plate. At each of the above three steps, only those receivers that reside exactly behind the dielectric object being illuminated (Steps I and III) or the gap being illuminated (Step II) are used for data collection. (In other words, the receiving points used in each step are located mainly within the main beam of the NF plate.) We then plot these three sets of the scattered NF data together to create Figure 4.10(a) for Configuration I and Figure 4.10(b) for Configuration II. Finally, it should be mentioned that due to the symmetry of the NF plate setup as well as the symmetric arrangement of the two dielectric objects, we have obtained the scattered NF data in Step III by flipping the scattered NF data from Step I.

F

Visual Summary of the Different Test Cases

This appendix is associated with Chapter 4. In this Appendix, we show additional figures to better demonstrate the studied test cases in Section 4.3. This illustration starts by the test cases under configuration I considered in Section 4.3.1 as shown in Figures F.1(a)-(d). As noted in the paper, Configuration II for Section 4.3.1 is simply achieved by merely removing the NF plate. Due to this, only one case (Case I) under Configuration II is illustrated herein; see Figure F.2. Next, the test cases considered in Section 4.3.2 are shown in Figures F.3(a)-(d). Configuration II for these test cases are simply achieved by replacing the Bessel beam launcher with a dipole antenna. Due to this, only one test case (Case I) under Configuration II is shown herein; see Figure F.4.

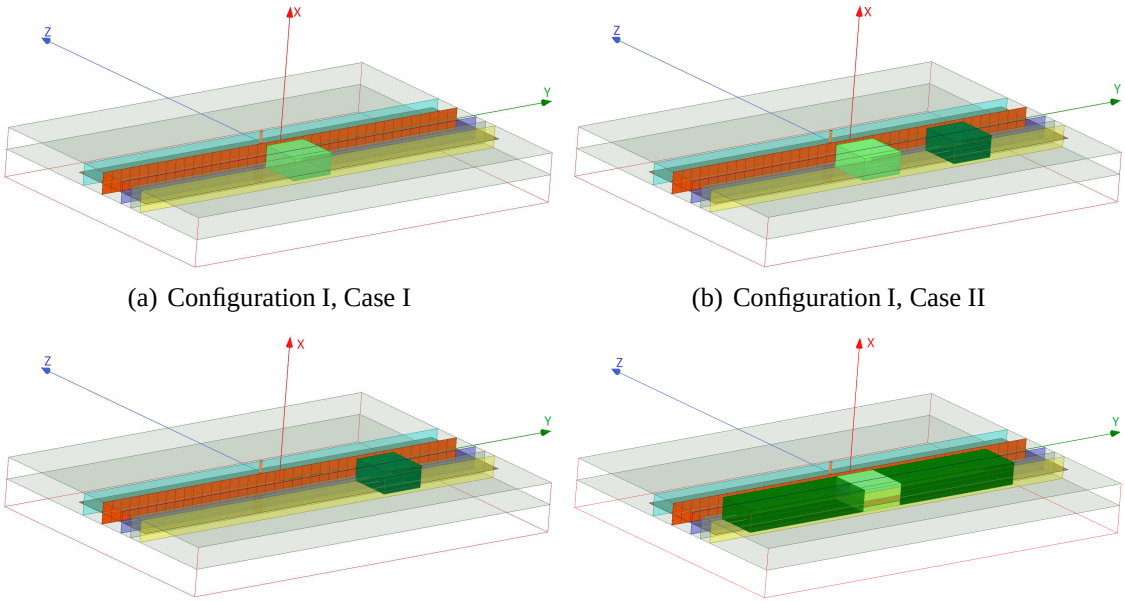

(a) Configuration I, Case I

(b) Configuration I, Case II

(c) Configuration I, Case III

(d) Configuration I, Case IV

Fig. F.1: Summary of different case studies under Configuration I of the NF plate setup.

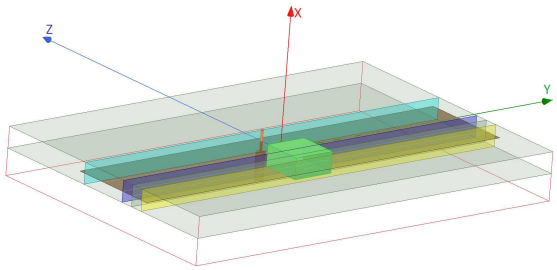

Fig. F.2: Configuration II, which is in the absence of the NF plate, for Case I.

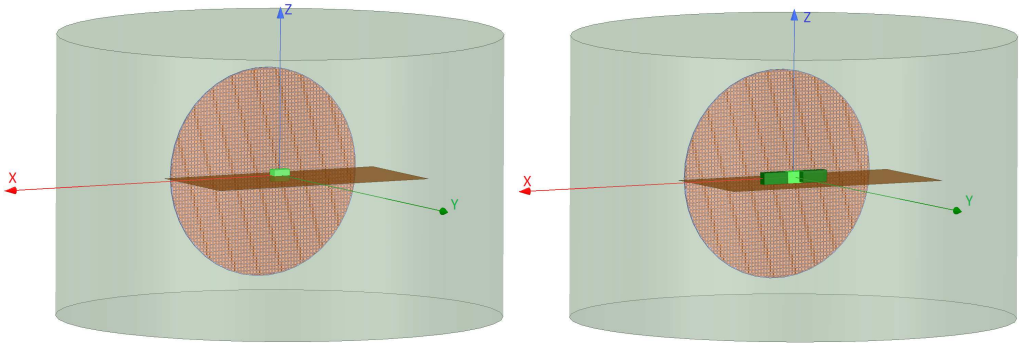

(a) Configuration I, Case I (b) Configuration I, Case II

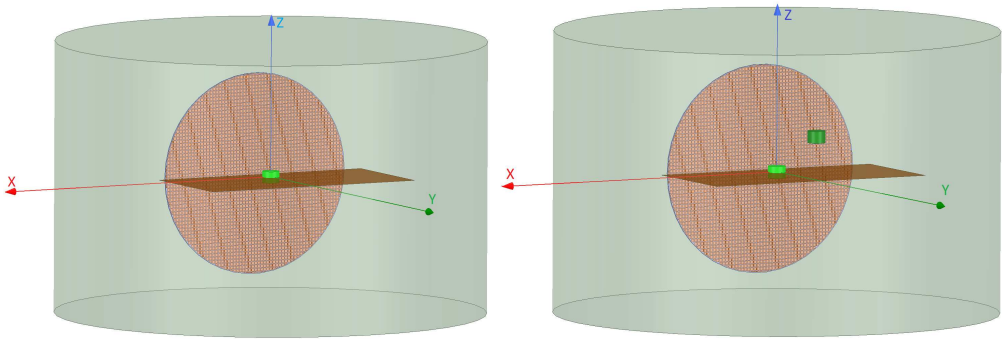

(c) Configuration I, Case III (d) Configuration I, Case IV

Fig. F.3: Summary of different case studies under Configuration I of the Bessel beam launcher setup.

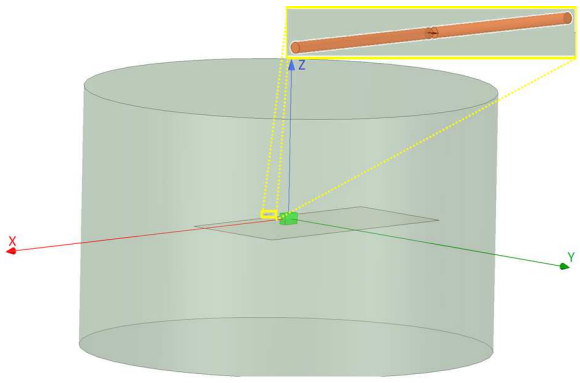

Fig. F.4: Configuration II in which a horizontal dipole antenna replaces the Bessel beam launcher for Case I.

G

Different Calibration Objects

This appendix is associated with Chapter 5. In Section 5.6.1, we have found α^{foc} and β^{foc} based on using a calibration object with the relative permittivity of 6.5. We have also investigated other calibration objects with different permittivities but having the same size of $\lambda/20 \times \lambda/10 \times \lambda/15$. The relative permittivities of these investigated calibration objects range from 5.5 to 10.5 with an increment of 0.5. For three of these calibration objects having relative permittivity values of 5.5, 6.5, and 10.5, we have presented the obtained values of α^{foc} and β^{foc} for Configuration IV in the last column of Tables G.1 and G.2. As expected, these values are similar, and are equal to $-0.03 - j0.04$ for α^{foc} and $0.02 - j0.06$ for β^{foc}. (These values of α^{foc} and β^{foc} are the values that we used in (5.14) to retrieve permittivity values in Section 5.6.) In addition, only for the sake of comparison, we have obtained α^{foc} and β^{foc} for Configurations I to III using the similar procedure used for Configuration IV.[1] These have also been reported in Tables G.1 and G.2.

[1] Note that since Configurations I to III are not as focused as Configuration IV, using the same notation as α^{foc} and β^{foc} is not appropriate for them. However, for simplicity and consistency, we have used the same notation for all configurations.

Tab. G.1: The obtained α^{foc} by the use of a calibration object with the size of $\lambda/20 \times \lambda/10 \times \lambda/15$ for three different relative permittivities $\epsilon_r' = 5.50$, $\epsilon_r' = 6.50$, and $\epsilon_r' = 10.50$ under the four configurations.

	$\boldsymbol{\alpha}^{\text{foc}}$			
Cal	Config. I	Config. II	Config. III	**Config. IV**
5.5	$0.01 - j0.05$	$0.01 - j0.03$	$0.02 - j0.12$	$-0.03 - j0.04$
6.5	$0.01 - j0.04$	$0.01 - j0.03$	$0.01 - j0.10$	$-0.03 - j0.04$
10.5	$0.01 - j0.04$	$0.01 - j0.03$	$0.01 - j0.05$	$-0.03 - j0.04$

Tab. G.2: The obtained β^{foc} by the use of a calibration object with the size of $\lambda/20 \times \lambda/10 \times \lambda/15$ for three different relative permittivities $\epsilon_r' = 5.50$, $\epsilon_r' = 6.50$, and $\epsilon_r' = 10.50$ under the four configurations.

	$\boldsymbol{\beta}^{\text{foc}}$			
Cal	Config. I	Config. II	Config. III	**Config. IV**
5.5	$0.07 - j0.05$	$0.05 - j0.05$	$0.10 - j0.03$	$0.02 - j0.06$
6.5	$0.07 - j0.05$	$0.05 - j0.05$	$0.09 - j0.03$	$0.02 - j0.06$
10.5	$0.07 - j0.05$	$0.05 - j0.05$	$0.04 - j0.01$	$0.02 - j0.06$

H

Reconstruction Comparison

This appendix is associated with Chapter 5. In this Appendix, the OI's reconstructed complex permittivity values for the example discussed in Section 5.6.2 using the four described configurations are presented. For the main configuration (Configuration IV) we used the methodology explained in Section 5.4 where the complex permittivity value is obtained from (5.14). For the other three configurations, we also use (5.14) but with their own α^{foc} and β^{foc} as tabulated in Appendix G for the calibration object having the relative permittivity of 6.5. The reconstruction results have been listed in Table H.1. As can be seen, the improvement in the accuracy of the reconstruction results is almost consistent when we are moving from our least localized imaging system (i.e., Configuration I) to our most localized imaging system (i.e., Configuration IV). The enhancement in the achievable reconstruction accuracy is mainly due to the accurate calculation of the two mapping operators, i.e., $\mathcal{G}_S$ and $\mathcal{G}_D$ represented by α^{foc} and β^{foc}.

Tab. H.1: The reconstructed complex permittivity values of the OI under our four configurations.

True ϵ'_r	Config. I	Config. II	Config. III	Config. IV
5.50	8.52 - 0.33j	7.02 + 0.15j	6.63 + 0.05j	5.69 + 0.00j
6.00	9.21 - 0.32j	7.72 + 0.22j	6.86 - 0.08j	6.01 + 0.05j
6.5	9.87 - 0.30j	8.40 + 0.31j	7.06 - 0.17j	6.69 + 0.05j
7.0	10.53 - 0.27j	9.10 + 0.40j	7.29 - 0.31j	7.23 + 0.05j
7.5	11.15 - 0.23j	9.80 + 0.52j	7.50 - 0.14j	7.74 + 0.06j
8.0	11.75 - 0.19j	10.47 + 0.66j	7.73 - 0.55j	8.23 + 0.08j
8.5	12.33 - 0.15j	11.15 + 0.80j	7.95 - 0.65j	8.79 + 0.10j
9.0	12.89 - 0.11j	11.85 + 0.96j	8.19 - 0.80j	9.55 + 0.11j
9.5	13.42 - 0.07j	12.54 + 1.14j	8.41 - 0.92j	10.12 + 0.16j
10.0	13.94 - 0.02j	13.24 + 1.34j	8.62 - 1.04j	10.71 + 0.18j
10.5	14.44 + 0.03j	13.89 + 1.54j	8.85 - 1.15j	11.27 + 0.22j

Bibliography

[1] J.-M. Geffrin, P. Sabouroux, and C. Eyraud, "Free space experimental scattering database continuation: experimental set-up and measurement precision," *Inverse Probl.*, vol. 21, pp. S117–S130, 2005.

[2] P. Mojabi and J. LoVetri, "Microwave biomedical imaging using the multiplicative regularized Gauss-Newton inversion," *IEEE Antennas Wireless Propag. Lett.*, vol. 8, pp. 645–648, 2009.

[3] A. Abubakar, T. M. Habashy, G. Pan, and M. K. Li, "Application of the multiplicative regularized Gauss Newton algorithm for three-dimensional microwave imaging," *IEEE Transactions on Antennas and Propagation*, vol. 60, no. 5, pp. 2431–2441, May 2012.

[4] "Tomography," https://en.wikipedia.org/wiki/Tomography.

[5] N. K. Nikolova, *Introduction to Microwave Imaging*. United Kingdom: Cambridge University Press, 2017.

[6] N. Bayat and P. Mojabi, "On an antenna design for 2D scalar near-field microwave tomography," *Applied Computational Electromagnetics Society Journal*, vol. 30, pp. 589–598, 2015.

[7] M. Pastorino, *Microwave Imaging*. New Jersey: John Wiley & Sons, 2010.

[8] O. M. Bucci, G. Bellizzi, A. Borgia, S. Costanzo, L. Crocco, G. D. Massa, and R. Scapaticci, "Experimental framework for magnetic nanoparticles enhanced breast cancer microwave imaging," *IEEE Access*, vol. 5, pp. 16 332–16 340, 2017.

[9] E. C. Fear, S. C. Hagness, P. M. Meaney, M. Okoniewski, and M. A. Stuchly, "Enhancing breast tumor detection with near-field imaging," *IEEE Microwave Mag.*, vol. 3, no. 1, pp. 48–56, Mar 2002.

[10] G. Oliveri, M. Salucci, N. Anselmi, and A. Massa, "Compressive sensing as applied to inverse problems for imaging: Theory, applications, current trends, and open challenges." *IEEE Antennas and Propagation Magazine*, vol. 59, no. 5, pp. 34–46, Oct 2017.

[11] M. Persson, A. Fhager, H. D. Trefna, Y. Yu, T. McKelvey, G. Pegenius, J. E. Karlsson, and M. Elam, "Microwave-based stroke diagnosis making global prehospital thrombolytic treatment possible," *IEEE Transactions on Biomedical Engineering*, vol. 61, no. 11, pp. 2806–2817, Nov 2014.

[12] A. T. Mobashsher, A. M. Abbosh, and Y. Wang, "Microwave system to detect traumatic brain injuries using compact unidirectional antenna and wideband transceiver with verification on realistic head phantom," *IEEE Transactions on Microwave Theory and Techniques*, vol. 62, no. 9, pp. 1826–1836, Sept 2014.

[13] Z. Wu and H. Wang, "Microwave tomography for industrial process imaging: Example applications and experimental results." *IEEE Antennas Propag. Mag.*, vol. 59, no. 5, pp. 61–71, Oct 2017.

[14] D. Gibbins, D. Byrne, T. Henriksson, B. Monsalve, and I. J. Craddock, "Less becomes more for microwave imaging: Design and validation of an ultrawide-band measurement array." *IEEE Antennas Propag. Mag.*, vol. 59, no. 5, pp. 72–85, Oct 2017.

[15] M. Hopfer, R. Planas, A. Hamidipour, T. Henriksson, and S. Semenov, "Electromagnetic tomography for detection, differentiation, and monitoring of brain stroke: A virtual data and human head phantom study." *IEEE Antennas Propag. Mag.*, vol. 59, no. 5, pp. 86–97, Oct 2017.

[16] M. Pastorino, S. Caorsi, and A. Massa, "A global optimization technique for microwave nondestructive evaluation," *IEEE. Trans. Instrum. and Meas.*, vol. 51, no. 4, pp. 666–673, Aug 2002.

[17] W. H. Weedon, W. C. Chew, and P. E. Mayes, "A step-frequency radar imaging system for microwave nondestructive evaluation," *Progress in Electromagnetic Research*, vol. 28, pp. 121–146, 2000.

[18] L. P. Song, C. Yu, and Q. H. Liu, "Through-wall imaging (TWI) by radar: 2-D tomographic results and analyses," *IEEE Trans. Geosci. Remote Sensing*, vol. 43, no. 12, pp. 2793–2798, Dec 2005.

[19] N. Firoozy, A. S. Komarov, J. Landy, D. G. Barber, P. Mojabi, and R. K. Scharien, "Inversion-based sensitivity analysis of snow-covered sea ice electromagnetic profiles," *IEEE Journal of Selected Topics in Applied Earth Observations and Remote Sensing*, vol. 8, no. 7, pp. 3643–3655, July 2015.

[20] P. Meaney, P. Kaufman, L. Muffly, M. Click, S. Poplack, W. Wells, G. Schwartz, R. M. di Florio-Alexander, T. Tosteson, Z. Li, S. Geimer, M. Fanning, T. Zhou, N. Epstein,

and K. Paulsen, "Microwave imaging for neoadjuvant chemotherapy monitoring: initial clinical experience," *Breast Cancer Research*, vol. 15, no. 8, pp. 2320–2331, Aug 2013.

[21] P. Mojabi and J. LoVetri, "Composite tissue-type and probability image for ultrasound and microwave tomography," *IEEE J. Multiscale and Multiphys. Comput. Techn.*, vol. 1, pp. 26–35, 2016.

[22] H. Jiang, C. Li, D. Pearlstone, and L. Fajardo, "Ultrasound-guided microwave imaging of breast cancer: tissue phantom and pilot clinical experiments," *Medical Physics*, vol. 32, no. 8, pp. 2528–2535, 2005.

[23] G. Boverman, C. Davis, S. Geimer, and P. M. Meaney, "Image registration for microwave tomography of the breast using priors from non-simultaneous previous magnetic resonance images," *IEEE Journal of Electromagnetics, RF and Microwaves in Medicine and Biology*, vol. PP, no. 99, pp. 1–1, 2017.

[24] N. Bayat, *On the Role of Antennas in the Achievable Resolution and Accuracy from Near-Field Microwave Tomography*, Master's thesis, University of Manitoba, Manitoba, Canada, 2014 [available online].

[25] P. C. Hansen, "The L-curve and its use in the numerical treatment of inverse problems," in *Computational Inverse Problems in Electrocardiology, Ed. P. Johnston, Advances in Computational Bioengineering*. WIT Press, 2000, pp. 119–142.

[26] A. J. Devaney and G. C. Sherman, "Nonuniqueness in inverse source and scattering problems," *IEEE Trans. Antennas Propag.*, vol. 30, no. 5, pp. 1034–1042, Sep 1982.

[27] N. Nikolova and Y. Rickard, "Nonradiating electromagnetic sources in a nonuniform medium," *Physical review. E, Statistical, nonlinear, and soft matter physics*, vol. 71, p. 016617, 02 2005.

[28] P. M. Meaney, M. W. Fanning, T. Raynolds, C. J. Fox., Q. Fang, C. A. Kogel, S. P. Poplack, and K. D. Paulsen, "Initial clinical experience with microwave breast imaging in women with normal mammography," *Acad Radiol.*, March 2007.

[29] J. D. Shea, P. Kosmas, S. C. Hagness, and B. D. V. Veen, "Three-dimensional microwave imaging of realistic numerical breast phantoms via a multiple-frequency inverse scattering technique," *Medical Physics*, vol. 37, no. 8, pp. 4210–4226, 2010.

[30] S. Semenov, J. Kellam, P. Althausen, T. Williams, A. Abubakar, A. Bulyshev, and Y. Sizov, "Microwave tomography for functional imaging of extremity soft tissues: feasibility assessment," *Phys. Med. Biol.*, vol. 52, pp. 5705–5719, 2007.

[31] T. J. Cui, W. C. Chew, X. X. Yin, and W. Hong, "Study of resolution and super resolution in electromagnetic imaging for half-space problems," *IEEE Trans. Antennas Propag.*, vol. 52, no. 6, pp. 1398–1411, June 2004.

[32] C. Gilmore, P. Mojabi, A. Zakaria, S. Pistorius, and J. LoVetri, "On super-resolution with an experimental microwave tomography system," *IEEE Antennas and Wireless Propagation Letters*, vol. 9, pp. 393–396, 2010.

[33] S. Semenov, R. Svenson, A. Bulyshev, A. Souvorov, A. Nazarov, Y. Sizov, V. Posukh, A. Pavlovsky, P. Repin, and G. Tatsis, "Spatial resolution of microwave tomography for detection of myocardial ischemia and infarction-experimental study on two-dimensional models," *IEEE Trans. Microwave Theory Tech.*, vol. 48, no. 4, pp. 538–544, Apr 2000.

[34] P. C. Hansen, M. E. Kilmer, and R. H. Kjeldsen, "Exploiting residual information in the parameter choice for discrete ill-posed problems," *BIT Numerical Mathematics*, vol. 46, pp. 41–59, 2006.

[35] A. Abubakar, T. M. Habashy, V. L. Druskin, L. Knizhnerman, and D. Alumbaugh, "2.5D forward and inverse modeling for interpreting low-frequency electromagnetic measurements," *Geophysics*, vol. 73, no. 4, pp. F165–F177, July–Aug 2008.

[36] P. Mojabi and J. LoVetri, "Enhancement of the Krylov subspace regularization for microwave biomedical imaging," *IEEE Transactions on Medical Imaging*, vol. 28, no. 12, pp. 2015–2019, Dec 2009.

[37] P. C. Hansen, "Numerical tools for analysis and solution of Fredholm integral equations of the first kind," *Inverse Probl.*, vol. 8, pp. 849–872, 1992.

[38] A. Abubakar, P. M. van den Berg, and S. Y. Semenov, "A robust iterative method for Born inversion," *IEEE Trans. Geosci. Remote Sensing*, vol. 42, no. 2, pp. 342–354, Feb 2004.

[39] N. Bayat and P. Mojabi, "The effect of antenna incident field distribution on microwave tomography reconstruction," *Progress In Electromagnetics Research*, vol. 145, pp. 153–161, 2014.

[40] T. Rubæk, P. M. Meaney, P. Meincke, and K. D. Paulsen, "Nonlinear microwave imaging for breast-cancer screening using Gauss-Newton's method and the CGLS inversion algorithm," *IEEE Trans. Antennas Propag.*, vol. 55, no. 8, pp. 2320–2331, Aug 2007.

[41] P. Mojabi, M. Ostadrahimi, L. Shafai, and J. LoVetri, "Microwave tomography techniques and algorithms: A review," in *Antenna Technology and Applied Electromagnetics (ANTEM), 2012 15th International Symposium on*, June 2012, pp. 1–4.

[42] P. M. Meaney, A. H. Golnabi, N. R. Epstein, S. D. Geimer, M. W. Fanning, J. B. Weaver, and K. D. Paulsen, "Integration of microwave tomography with magnetic resonance for improved breast imaging," *Medical Physics*, vol. 40, no. 10, p. 103101, 2013. [Online]. Available: https://aapm.onlinelibrary.wiley.com/doi/abs/10.1118/1.4820361

[43] A. H. Golnabi, P. M. Meaney, and K. D. Paulsen, "Tomographic microwave imaging with incorporated prior spatial information," *IEEE Transactions on Microwave Theory and Techniques*, vol. 61, no. 5, pp. 2129–2136, May 2013.

[44] ——, "3D microwave tomography of the breast using prior anatomical information," *Medical Physics*, vol. 43, no. 4, pp. 1933–1944, 2016. [Online]. Available: https://aapm.onlinelibrary.wiley.com/doi/abs/10.1118/1.4944592

[45] L. M. Neira, B. D. V. Veen, and S. C. Hagness, "High-resolution microwave breast imaging using a 3-D inverse scattering algorithm with a variable-strength spatial prior constraint," *IEEE Transactions on Antennas and Propagation*, vol. 65, no. 11, pp. 6002–6014, Nov 2017.

[46] M. Omer, P. Mojabi, D. Kurrant, J. LoVetri, and E. Fear, "Proof-of-concept of the incorporation of ultrasound-derived structural information into microwave radar imaging," *IEEE Journal on Multiscale and Multiphysics Computational Techniques*, vol. 3, pp. 129–139, 2018.

[47] N. Abdollahi, D. Kurrant, P. Mojabi, M. Omer, E. Fear, and J. LoVetri, "Incorporation of ultrasonic prior information for improving quantitative microwave imaging of breast," *IEEE Journal on Multiscale and Multiphysics Computational Techniques*, vol. 4, pp. 98–110, 2019.

[48] P. Mojabi and N. Bayat, "A multiplicative regularizer to incorporate prior spatial data in microwave imaging reconstruction," in *13th European Conference on Antennas and Propagation*, April 2019, pp. 1–5.

[49] A. Abubakar and P. M. van den Berg, "Iterative forward and inverse algorithms based on domain integral equations for three–dimensional electric and magnetic objects," *J. Comput. Phys.*, vol. 195, pp. 236–262, 2004.

[50] A. Abubakar, P. M. van den Berg, and J. J. Mallorqui, "Imaging of biomedical data using a multiplicative regularized contrast source inversion method," *IEEE Trans. Microwave Theory Tech.*, vol. 50, no. 7, pp. 1761–1777, July 2002.

[51] T. M. Habashy and A. Abubakar, "A general framework for constraint minimization for the inversion of electromagnetic measurements," *Progress in Electromagnetics Research*, vol. 46, pp. 265–312, 2004.

[52] P. Mojabi, "Investigation and development of algorithms and techniques for microwave tomography," Ph.D. dissertation, University of Manitoba, Winnipeg, Manitoba, Canada, 2010.

[53] M. Ostadrahimi, P. Mojabi, A. Zakaria, J. LoVetri, and L. Shafai, "Enhancement of gauss-newton inversion method for biological tissue imaging," *IEEE Transactions on Microwave Theory and Techniques*, vol. 61, no. 9, pp. 3424–3434, Sept 2013.

[54] P. Mojabi and J. LoVetri, "Overview and classification of some regularization techniques for the Gauss-Newton inversion method applied to inverse scattering problems," *IEEE Transactions on Antennas and Propagation*, vol. 57, no. 9, pp. 2658–2665, Sept 2009.

[55] A. Abubakar, P. M. van den Berg, T. M. Habashy, and H. Braunisch, "A multiplicative regularization approach for deblurring problems," *IEEE Trans. Image Processing*, vol. 13, no. 11, pp. 1524–1532, Nov 2004.

[56] P. Mojabi, J. LoVetri, and L. Shafai, "A multiplicative regularized Gauss–Newton inversion for shape and location reconstruction," *IEEE Transactions on Antennas and Propagation*, vol. 59, no. 12, pp. 4790–4802, 2011.

[57] W. C. Chew and J. H. Lin, "A frequency–hopping approach for microwave imaging of large inhomogeneous bodies," *IEEE Microwave and Guided Wave Letters*, vol. 5, no. 12, pp. 439–441, Dec. 1995.

[58] A. Abubakar, P. M. van den Berg, and T. M. Habashy, "Application of the multiplicative regularized contrast source inversion method on TM- and TE-polarized experimental Fresnel data," *Inverse Probl.*, vol. 21, pp. S5–S13, 2005.

[59] P. Mojabi and J. LoVetri, "A prescaled multiplicative regularized Gauss-Newton inversion," *IEEE Transactions on Antennas and Propagation*, vol. 59, no. 8, pp. 2954–2963, Aug 2011.

[60] M. Lazebnik and *et. al.*, "A large-scale study of the ultrawideband microwave dielectric properties of normal breast tissue obtained from reduction surgeries," *Physics in Medicine and Biology*, vol. 52, pp. 2637–2656, 2007.

[61] E. Zastrow, S. Davis, M. Lazebnik, F. Kelcz, B. V. Veen, and S. Hagness, "Database of 3D grid-based numerical breast phantoms for use in computational electromagnetics simulations," *Department of Electrical and Computer Engineering of University of Wisconsin-Madison*. [Online]. Available: http://uwcem.ece.wisc.edu/phantomRepository.html

[62] P. C. Hasen and D. P. O'leary, "The use of the l-curve in the regularization of discrete ill-posed problems," *SIAM J. Sci. Comput.*, vol. 14, no. 6, pp. 1487–1503, Nov 1993.

[63] R. Scapaticci, G. Bellizzi, I. Catapano, L. Crocco, and O. M. Bucci, "An effective procedure for mnp-enhanced breast cancer microwave imaging," *IEEE Transactions on Biomedical Engineering*, vol. 61, no. 4, pp. 1071–1079, April 2014.

[64] T. M. Grzegorczyk, P. M. Meaney, P. A. Kaufman, R. M. diFlorio Alexander, and K. D. Paulsen, "Fast 3-d tomographic microwave imaging for breast cancer detection," *IEEE Transactions on Medical Imaging*, vol. 31, no. 8, pp. 1584–1592, Aug 2012.

[65] J. De Zaeytijd, A. Franchois, C. Eyraud, and J. M. Geffrin, "Full-wave three-dimensional microwave imaging with a regularized Gauss Newton method; theory and experiment," *Antennas and Propagation, IEEE Transactions on*, vol. 55, no. 11, pp. 3279–3292, Nov 2007.

[66] R. Palmeri, M. T. Bevacqua, L. Crocco, T. Isernia, and L. D. Donato, "Microwave imaging via distorted iterated virtual experiments," *IEEE Transactions on Antennas and Propagation*, vol. 65, no. 2, pp. 829–838, Feb 2017.

[67] A. H. Golnabi, P. M. Meaney, and K. D. Paulsen, "Tomographic microwave imaging with incorporated prior spatial information," *IEEE Transactions on Microwave Theory and Techniques*, vol. 61, no. 5, pp. 2129–2136, May 2013.

[68] L. M. Neira, B. D. V. Veen, and S. C. Hagness, "High-resolution microwave breast imaging using a 3-D inverse scattering algorithm with a variable-strength spatial prior constraint," *IEEE Transactions on Antennas and Propagation*, IEEE Early Access.

[69] A. Baran, D. Kurrant, A. Zakaria, E. Fear, and J. LoVetri, "Breast cancer imaging using microwave tomography with radar-derived prior information," in *2014 USNC-URSI Radio Science Meeting (Joint with AP-S Symposium)*, July 2014, pp. 259–259.

[70] P. Mojabi, J. LoVetri, and L. Shafai, "A multiplicative regularized Gauss-Newton inversion for shape and location reconstruction," *IEEE Transactions on Antennas and Propagation*, vol. 59, no. 12, pp. 4790–4802, Dec 2011.

[71] K. D. P. Paul M. Meaney, Navin K. Yagnamurthy, "Pre-scaled two-parameter Gauss-Newton image reconstruction to reduce property recovery imbalance," *Phys Med Biol.*, vol. 47, no. 7, pp. 1101–1119, April 2002.

[72] N. Bayat and P. Mojabi, "A mathematical framework to analyze the achievable resolution from microwave tomography," *IEEE Trans. Antennas Propag.*, vol. 64, no. 6, pp. 1484–1489, April 2016.

[73] D. Li, P. M. Meaney, T. Raynolds, S. A. Pendergrass, M. W. Fanning, and K. D. Paulsen, "Parallel-detection microwave spectroscopy system for breast imaging," *Review of Scientific Instruments*, vol. 75, no. 7, pp. 2305–2313, July 2004.

[74] M. Ostadrahimi, P. Mojabi, C. Gilmore, A. Zakaria, S. Noghanian, S. Pistorius, and J. LoVetri, "Analysis of incident field modeling and incident/scattered field calibration techniques in microwave tomography," *IEEE Antennas Wireless Propag. Lett.*, vol. 10, pp. 900–903, 2011.

[75] P. Meaney, K. Paulsen, J. Chang, M. Fanning, and A. Hartov, "Nonactive antenna compensation for fixed-array microwave imaging. II. imaging results," *IEEE Trans. Med. Imag.*, vol. 18, no. 6, pp. 508–518, 1999.

[76] J. Bourqui, M. Okoniewski, and E. C. Fear, "Balanced antipodal Vivaldi antenna with dielectric director for near-field microwave imaging," *IEEE Transactions on Antennas and Propagation*, vol. 58, no. 7, pp. 2318–2326, July 2010.

[77] N. Bayat and P. Mojabi, "Near-field microwave imaging using focused near-field beams: An approach to mitigate undesired scattering effects," in *2nd URSI Atlantic Radio Science Meeting (URSI AT-RASC*, Gran Canaria, Spain, May 2018.

[78] G. G. Bellizzi, D. A. M. Iero, L. Crocco, and T. Isernia, "Three-dimensional field intensity shaping: The scalar case," *IEEE Antennas and Wireless Propagation Letters*, vol. 17, no. 3, pp. 360–363, March 2018.

[79] G. G. Bellizzi, M. T. Bevacqua, G. M. Battaglia, L. Crocco, and T. Isernia, "Advances in target conformal sar deposition for hyperthermia treatment planning," in *Second URSI Atlantic Radio Science Meeting*, Gran Canaria, Spain, June 2018.

[80] L. Crocco, L. D. Donato, D. A. M. Iero, and T. Isernia, "A new strategy to constrained focusing in unknown scenarios," *IEEE Antennas and Wireless Propagation Letters*, vol. 11, pp. 1450–1453, 2012.

[81] P. M. van den Berg and R. E. Kleinman, "A contrast source inversion method," *Inverse Probl.*, vol. 13, pp. 1607–1620, 1997.

[82] M. Oristaglio and H. Blok, "Wavefield imaging and inversion in electromagnetics and acoustics," *Lecture notes, Delft University*, 1995.

[83] W. C. Chew, Y. M. Wang, G. Otto, D. Lesselier, and J. C. Bolomey, "On the inverse source method of solving inverse scattering problems," *Inverse Problems*, vol. 10, no. 3, p. 547, 1994. [Online]. Available: http://stacks.iop.org/0266-5611/10/i=3/a=004

[84] C. Parini, S. Gregson, J. McCormick, and D. J. van Rensburg, *Theory and Practice of Modern Antenna Range Measurements*. United Kingdom: The Institution of Engineering and Technology, 2014.

[85] C. Balanis, *Antenna Theory: Analysis and Design*. New Jersey: John Wiley and Sons, 2005.

[86] O. M. Bucci and T. Isernia, "Electromagnetic inverse scattering: Retrievable information and measurement strategies," *Radio Science*, vol. 32, no. 6, pp. 2123–2137, Nov 1997.

[87] A. Grbic, L. Jiang, and R. Merlin, "Near-field plates: subdiffraction focusing with patterned surfaces," *Science*, vol. 320, pp. 511–513, 2008.

[88] M. Ettorre and A. Grbic, "Generation of propagating Bessel beams using leaky-wave modes," *IEEE Trans. Antennas Propag.*, vol. 60, no. 8, pp. 3605–3613, Aug 2012.

[89] M. Ettorre, S. M. Rudolph, and A. Grbic, "Generation of propagating Bessel beams using leaky-wave modes: Experimental validation," *IEEE Trans. Antennas Propag.*, vol. 60, no. 6, pp. 2645–2653, June 2012.

[90] Z. Bouchal, J. Wagner, and M. Chlup, "Self-reconstruction of a distorted nondiffracting beam," *Optics Communications*, vol. 151, no. 4, pp. 207 – 211, 1998. [Online]. Available: http://www.sciencedirect.com/science/article/pii/S0030401898000856

[91] N. Ahmed, M. P. J. Lavery, H. Huang, G. Xie, Y. Ren, Y. Yan, and A. E. Willner, "Experimental demonstration of obstruction-tolerant free-space transmission of two 50-Gbaud QPSK data channels using bessel beams carrying orbital angular momentum," in *2014 The European Conference on Optical Communication (ECOC)*, Sept 2014, pp. 1–3.

[92] T. Zvolensky, J. N. Gollub, D. L. Marks, and D. R. Smith, "Design and analysis of a W-band metasurface-based computational imaging system," *IEEE Access*, vol. 5, pp. 9911–9918, 2017.

[93] A. Epstein and G. V. Eleftheriades, "Huygens' metasurfaces via the equivalence principle: design and applications," *J. Opt. Soc. Am. B*, vol. 33, no. 2, pp. A31–A50, Feb 2016.

[94] M. Persson, A. Fhager, H. D. Trefna, Y. Yu, T. McKelvey, G. Pegenius, J. E. Karlsson, and M. Elam, "Microwave-based stroke diagnosis making global prehospital thrombolytic treatment possible," *IEEE Transactions on Biomedical Engineering*, vol. 61, no. 11, pp. 2806–2817, Nov 2014.

[95] M. Hopfer, R. Planas, A. Hamidipour, T. Henriksson, and S. Semenov, "Electromagnetic tomography for detection, differentiation, and monitoring of brain stroke: A virtual data and human head phantom study." *IEEE Antennas and Propagation Magazine*, vol. 59, no. 5, pp. 86–97, Oct 2017.

[96] T. Brown, I. Jeffrey, and P. Mojabi, "Multiplicatively regularized source reconstruction method for phaseless planar near-field antenna measurements," *IEEE Transactions on Antennas and Propagation*, vol. 65, no. 4, pp. 2020–2031, April 2017.

[97] T. Brown, C. Narendra, C. Niu, and P. Mojabi, "On the use of electromagnetic inversion for near-field antenna measurements: A review," in *2018 IEEE Conference on Antenna Measurements Applications (CAMA)*, Sep. 2018, pp. 1–4.

[98] M. Oristagalio and H. Blok, *Wavefield Imaging and Inversion in Electromagnetics and Acoustics*. Delft University Notes, 1995.

[99] N. Bayat and P. Mojabi, "On the use of focused incident near-field beams in microwave imaging," *Sensors*, vol. 18, 2018.

[100] P. C. Hansen, *Rank-deficient and discrete ill-posed problems: Numerical aspects of linear inversion*. Philadelphia, PA: SIAM, 1998.

[101] K. Belkebir and M. Saillard, "Testing inversion algorithms against experimental data: inhomogeneous targets," *Inverse Probl.*, vol. 21, pp. S1–S3, 2005.

[102] G. Lerosey, J. de Rosny, A. Tourin, and M. Fink, "Focusing beyond the diffraction limit with far-field time reversal," *Science*, vol. 315, no. 5815, pp. 1120–1122, 2007. [Online]. Available: https://science.sciencemag.org/content/315/5815/1120

[103] F. Chen and W. C. Chew, "Experimental verification of super resolution in nonlinear inverse scattering," *Applied Physics Letters*, vol. 72, June 1998.

[104] F-C. Chen and W. C. Chew, "Ultra-wideband radar imaging experiment for verifying super-resolution in nonlinear inverse scattering," in *IEEE Antennas and Propagation Society International Symposium and USNC URSI National Radio Science Meeting*, June 1998, pp. 1284–1287.

[105] A. A. Aydiner and W. C. Chew, "On the nature of super-resolution in inverse scattering," in *IEEE Antennas and Propagation Society International Symposium and USNC/CNC/URSI North American Radio Sci. Meeting*, June 2003, pp. 507–510.

[106] J. B. Pendry, "Negative refraction makes a perfect lens," *Phys. Rev. Lett.*, vol. 85, pp. 3966–3969, Oct 2000. [Online]. Available: https://link.aps.org/doi/10.1103/PhysRevLett.85.3966

[107] A. Grbic and G. V. Eleftheriades, "Overcoming the diffraction limit with a planar left-handed transmission-line lens," *Phys. Rev. Lett.*, vol. 92, p. 117403, Mar 2004. [Online]. Available: https://link.aps.org/doi/10.1103/PhysRevLett.92.117403

[108] A. Wong, "Sub-diffraction imaging using superoscillatory electromagnetic waves," Ph.D. dissertation, University of Toronto, Toronto, Canada, 2014.

[109] R. Merlin, "Radiationless electromagnetic interference: evanescent-field lenses and perfect focusing," *Science*, vol. 317, pp. 927–929, 2007.

[110] A. M. H. Wong and G. V. Eleftheriades, "Advances in imaging beyond the diffraction limit," *IEEE Photonics Journal*, vol. 4, no. 2, pp. 586–589, April 2012.

[111] N. Mohammadi Estakhri, B. Edwards, and N. Engheta, "Inverse-designed metastructures that solve equations," *Science*, vol. 363, no. 6433, pp. 1333–1338, 2019. [Online]. Available: https://science.sciencemag.org/content/363/6433/1333

[112] V. Okhmatovski, J. Aronsson, and L. Shafai, "A well-conditioned non-iterative approach to solution of the inverse problem," *IEEE Trans. Antennas Propag.*, vol. 60, no. 5, pp. 2418–2430, 2012.

[113] V. Okhmatovski, M. J. Feroj, and L. Shafai, "On use of inhomogeneous media for elimination of ill-posedness in the inverse problem," *IEEE Antennas and Wireless Propagation Letters*, vol. 17, no. 5, pp. 857–860, May 2018.

[114] J. Stang, M. Haynes, P. Carson, and M. Moghaddam, "A preclinical system prototype for focused microwave thermal therapy of the breast," *IEEE Transactions on Biomedical Engineering*, vol. 59, no. 9, pp. 2431–2438, Sep. 2012.

[115] P. M. van den Berg, "Nonlinear scalar inverse scattering: Algorithms and applications," in *Scattering and Inverse Scattering in Pure and Applied Science*, Eds : R. Pike and P. Sabatier. San Diego: Academic Press, 2002, pp. 142–161.

[116] N. Bayat and P. Mojabi, "Incorporating spatial priors in microwave imaging via multiplicative regularization," *IEEE Transactions on Antennas and Propagation (Early Access)*, pp. 1–12, 2019.

[117] A. Abubakar, T. Habashy, P. Berg, and A. Gisolf, "The diagonalized contrast source approach: An inversion method beyond the Born approximation," *Inverse Problems, 21 (2)*, vol. 21, 04 2005.

[118] M. Imani, "Theory and development of near-field plates," Ph.D. dissertation, University of Michigan, Ann Arbor, Michigan, USA, 2013.

[119] C. Gilmore, A. Zakaria, S. Pistorius, and J. LoVetri, "Microwave imaging of human forearms: Pilot study and image enhancement," *International Journal of Biomedical Imaging*, 2013.